Interaction of stress and phase transformations during thermochemical surface engineering

PhD Thesis

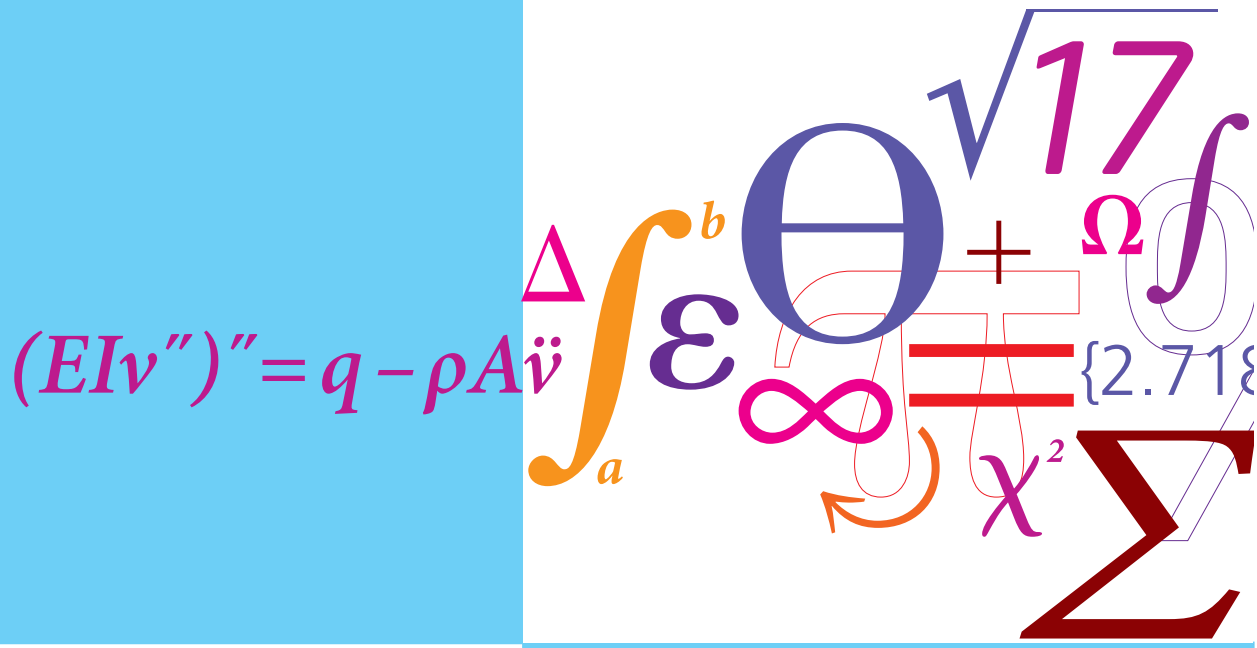

Freja N. Jespersen
September 2015

DTU Mechanical Engineering
Department of Mechanical Engineering

Interaction of stress and phase transformations during thermochemical surface engineering

PhD thesis

By Freja N. Jespersen

September 2015

Department of Mechanical Engineering

Technical University of Denmark

Dk-2800 Kgs. Lyngby, Denmark

Preface

The present thesis is submitted in candidacy for a Ph.D. degree at Technical University of Denmark (DTU).

The work presented in this thesis was done at the department of Mechanical engineering in the time period December 2011 – September 2015 under supervision of Professor Marcel Somers from section of materials and surface engineering, Professor Viggo Tvergaard from section of solid mechanics, and Professor Jesper Hattel from section of manufacturing engineering.

Part of the work presented in this thesis is submitted as articles, which are given in Appendix E.

Kgs. Lyngby, September 2015

Freja N. Jespersen

Abstract

Low temperature nitriding of austenitic stainless steel causes a surface zone of expanded austenite, which improves the wear resistance of the stainless steel while preserving the stainless behavior. During nitriding huge residual stresses are introduced in the treated zone, arising from the volume expansion that accompanies the dissolution of high nitrogen contents in expanded austenite. An intriguing phenomenon during low-temperature nitriding, is that the residual stresses evoked by dissolution of nitrogen in the solid state, affect the thermodynamics and the diffusion kinetics of nitrogen dissolution.

The present project is devoted to understanding the mutual interaction of stresses and phase transformations during thermochemical surface engineering by combining numerical modelling with experimental materials science.

The modelling was done by combining solid mechanics with thermodynamics and diffusion kinetics to simulate the evolution of composition-depth and stress-depth profiles resulting from nitriding of austenitic stainless steel. The model takes into account a composition-dependent diffusion coefficient of nitrogen in expanded austenite, short range ordering (trapping) of nitrogen atoms by chromium atoms, and the effect of composition-induced stress on surface concentration and diffusive flux. The effect of plasticity was also included.

Temperature and concentration dependencies of mechanical and diffusion material properties were studied, and the effect of incorporation in the model examined.

The effect of pre-stressing the sample was also tested, to investigate the effects of a residual stress-state that might be present from processing of the metal specimen.

Controlled thermochemical treatment of austenitic stainless steel was investigated experimentally by in-diffusion of nitrogen from a gaseous environment. Measurements of diffusion coefficient were conducted using thermogravimetry.

Resumé

Nitrering af austenitisk rustfrit stål ved lav temperatur skaber en overfladezone af ekspanderet austenit, der forbedrer overfladens slidegenskaber uden at fjerne den rustfrie egenskab fra materialet. Under nitrering opstår der store kompressive spændinger i det behandlede lag på grund af den volumetriske udvidelse der sker ved opløsning af store mængder nitrogen i ekspanderet austenit.

Et interessant fænomen under nitrering ved lav temperatur er, at de spændinger, der opstår på grund af opløsning af nitrogen i faststof, påvirker nitrogen opløsningens termodynamik og diffusions kinetik.

Dette projekt fokuserer på at forstå interaktionen af spændinger og fasetransformation under nitrering ved at kombinere numerisk modellering med eksperimentel materialeteknologi.

Modelleringen er lavet ved at kombinere fasstofmekanik med termodynamik og kinetik for at simulere udviklingen af de kompositions-dybde og spændings-dybde profiler der er et resultat af nitrering af austenitisk rustfrit stål. Modellen tager højde for en kompositionsafhængig diffusionskoefficient for nitrogen i ekspanderet austenit, interaktion mellem nitrogen og krom atomer, og effekten af kompositionsinducerede spændinger på overfladekoncentrationen og diffusionsfluxen. Effekten af plasticitet er også inkluderet i modellen.

Temperatur- og koncentrations-afhængigheder af mekaniske og diffusive materialeegenskaber er blevet studeret, og derefter er effekten af at inkorporere disse i modellen undersøgt.

Effekten af initielle spændinger er også testet, for at undersøge hvilken effekt residualspændinger fra foregående processer i produktion af metallet kan have.

Kontrolleret termo-kemisk behandling af austenitisk rustfrit stål blev undersøgt eksperimentelt ved at indføre nitrogen ved diffusion fra gas. Målinger af diffusionskoefficienter er lavet ved brug af en termovægt.

Guidance to the reader

In the present thesis the interactions of stresses and phase transformations during thermochemical treatment is investigated. The main purpose is the development of a model to predict composition- and stress-depth profiles during low temperature nitriding of stainless steel. The modelling activities are supplemented by experimental investigations.

Chapter 1 introduces the subject and gives background information about thermochemical surface treatment. Chapter 2 gives an overview over literature on modelling composition-profile development during low temperature nitriding of stainless steel.

In chapter 3 and 4 the basics behind the model are discussed, including topics such as kinetics and thermodynamics of the nitriding process.

In the following chapters the model is gradually expanded. In each chapter the theoretical background for the expansions are explained, and the effect of each addition on the predicted profiles is discussed. In chapter 5 the effect of a composition-dependent diffusion coefficient and the effect of short-range ordering of nitrogen and chromium are evaluated. In chapter 6 and 7 the interactions between stresses and composition are investigated while assuming purely elastic stresses, where chapter 6 introduces the evolution of composition induced stresses, and in chapter 7 the influence of the stresses on the development of the composition profiles is evaluated. In chapter 8 plasticity is included in the model and chapter 9 deals with the concentration dependency of mechanical properties.

In chapter 10 the effects of a stress state present before nitriding is evaluated by subjecting the model with all expansions to a pre-stress.

Chapter 11 and 12 deal with effects of temperature; in chapter 11 the temperature dependence of mechanical properties is explored and in chapter 12 effects of temperature variation from heating and cooling sequences is discussed.

Chapter 13 is about experimental investigations of nitriding, including measurements of nitrogen solubility and diffusion coefficient.

Finally; limitations of the model, conclusions to the work and outlook are given in chapters 14-16.

Acknowledgements

First I would like to thank main supervisor Marcel Somers, for ideas and guidance through the project and advice on kinetics and thermodynamics. I would also like to gratefully acknowledge supervisor Viggo Tvergaard for his expert advice on solid mechanics.

I owe a special thanks to supervisor Jesper Hattel for inspiring meetings with invaluable advice on the art of building a complex model, and on modelling of heat/concentration diffusion.

I would like to thank Thomas Christiansen for guidance in the area of experimental nitriding and denitriding, and Kristian Vinter Dahl and Jesper Thorborg for fruitful discussions about modelling.

I would also like to thank Federico Bottoli for cooperation on tensile testing experiments.

I also owe thanks to my PhD-colleague Morten Bakkedal for teaching me about C# programming, and to Trine Lomholt for inspiring me to believe that I could pursue a PhD-degree.

Thanks should also be given to Louise Laub Busk for assistance with double-checking numerous handcalculated differentiations, and to Mikkel Johnsen for general advice on optimizing programming.

Last I would like to thank my fiancée Morten Sjøgreen, who taught me a lot about project management, and provided support to get me all the way through.

Symbol list

Symbol	Unit	Description
a	m	Lattice parameter
a_N		Nitrogen activity
C_p	J/(kg.K)	Specific heat/ heat capacity at constant pressure
c	mol/m^3	Concentration
$\dot{c}$	mol/m^3	Concentration increment
$\bar{c}$	mol/m^3	Average concentration
c_0	mol/m^3	Concentration at start time
c_s	mol/m^3	Surface concentration
c_{Cr}	mol/m^3	Chromium concentration
c_N	mol/m^3	Nitrogen concentration
c_N^{eq}	mol/m^3	Equilibrium nitrogen concentration
c_{Cr}^{res}	mol/m^3	Concentration of residual chromium (The amount of free chromium after trapping)
c_N^{res}	mol/m^3	Concentration of residual nitrogen (The amount of free nitrogen after trapping)
c_N^{tot}	mol/m^3	Total concentration of nitrogen
c_{Cr}^{tr}	mol/m^3	Concentration of trapped chromium
c_N^{tr}	mol/m^3	Concentration of trapped nitrogen
c^S	mol/m^3	Surface concentration
c_N^s	mol/m^3	Nitrogen concentration at the surface
D	m^2/s	Diffusion coefficient
$\bar{D}$	m^2/s	Average diffusion coefficient
D_N	m^2/s	Diffusion coefficient of nitrogen
$D_N^{(c)}$	m^2/s	Concentration dependent diffusion coefficient of nitrogen
E	Pa	Young's modulus
E_T	Pa	Tangent modulus
Fo		Fourier number
f		Yield function
$\dot{f}$		Yield function increment

G		Gibbs energy
H		Enthalphy
HV	MPa	Vickers Hardness
i		Element number, used for finite difference discretization
J	mol/m^2	Flux
J_{surf}	mol/m^2	Flux through the surface
J_N	mol/m^2	Nitrogen flux
J_N^s	mol/m^2	Nitrogen flux through the surface
$J_N^{s,diss}$	mol/m^2	Flux of nitrogen atoms arriving at the surface from dissociation
$J_N^{s,diff}$	mol/m^2	Flux of nitrogen atoms leaving from the surface by diffusion
K_{CrN_n}		The solubility product of chromium and nitrogen
K_e		The thermodynamic solubility constant
K_N		Nitriding potential
K_N^{gas}		Nitriding potential in gas
K_T		Temperature and pressure dependent equilibrium constant for the reaction describing the dissolution of N into the solid phase from the gas phase
k		Reaction rate constant of the slowest step in the ammonia dissociation
k	W/(K.m)	Thermal conductivity
L	m	Half the sample thickness
L_{ijkl}		Incremental stiffness tensor
$M(t)$	mg	Diffusing mass as function of time
M_∞	mg	Amount of diffusing species that that entered or left after infinitely long time
M_{316}	g/mol	Molar mass of AISI 316 austenitic stainless steel
M_N	g/mol	Molar mass of nitrogen
M_N	(mol.m^2)/(J.s)	Nitrogen mobility
m	g	Mass
N_{av}	mol^{-1}	Avogadro's number
n		Hardening exponent for plasticity
n		Number of nitrogen atoms pr. chromium atoms for trapping
n		Number of atoms pr. unit-cell in the iron lattice
p	atm	Pressure

p_{H_2}	atm	Partial pressure of hydrogen
p_{NH_3}	atm	Partial pressure of ammonia
R	J/(mol.K)	Gas constant
S		Entropy
s_{ij}	Pa	Stress deviator tensor
T	K or °C	Temperature
$\dot{T}$	K	Temperature increment
T_{ref}	K or °C	Reference temperature
t	s	Time
V	m^3	volume
$V(c)$	m^3	Concentration-dependent volume of (expanded) austenite per metal atom
V_{ref}	m^3	Reference volume of austenite per metal atom
V_N		Partial molar volume of nitrogen
V_φ	m^3	Unitcell volume
y_N		Nitrogen content expressed as the fractional occupancy of the nitrogen sublattice
z	m	Depth
α	K^{-1}	Thermal expansion coefficient
α		Thermal diffusivity
β		Plasticity parameter (equal to 1 for plasticity, equal to 0 for elasticity)
$\Delta_r C_p$		Reaction change of heat capacity at constant pressure
$\Delta_r G$		Change of Gibbs energy for the reaction r
$\Delta_r H$		Standard enthalphy change for the reaction r
$\Delta_r S$		Entropy change for the reaction r
δ_{ij}		Kronecker's delta (equal to 1 if $i = j$, equal to zero if $i \neq j$)
ε_{ij}		Strain
ε_{ij}^{ch}		Chemical strain
$\dot{\varepsilon}_{ij}^{ch}$		Chemical strain increment
ε_{ij}^{mech}		Mechanical strain
$\dot{\varepsilon}_{ij}^{mech}$		Mechanical strain increment
$\dot{\varepsilon}_e^{pl}$		Equivalent plastic strain increment
$\dot{\varepsilon}_{ij}^{pl}$		Plastic strain increment

$\boldsymbol{\varepsilon_{ij}^{th}}$		Thermal strain
$\boldsymbol{\dot{\varepsilon}_{ij}^{th}}$		Thermal strain increment
$\boldsymbol{\varepsilon_{ij}^{tot}}$		Total strain
$\boldsymbol{\dot{\varepsilon}_{ij}^{tot}}$		Total strain increment
$\boldsymbol{\dot{\lambda}}$		Load parameter
$\boldsymbol{\mu}$	J/mol	Chemical potential
$\boldsymbol{\mu_0}$	J/mol	Reference chemical potential
$\boldsymbol{\mu_N}$	J/mol	Chemical potential of nitrogen
$\boldsymbol{\mu^{gas}}$	J/mol	Chemical potential in gas
$\boldsymbol{\upsilon}$		Poisson's ratio
$\boldsymbol{\rho}$	kg/m^3	Density
$\boldsymbol{\sigma_e}$	Pa	Von Mises equivalent stress
$\boldsymbol{\dot{\sigma}_e}$	Pa	Von Mises equivalent stress increment
$\boldsymbol{\sigma}$	Pa	Stress
$\boldsymbol{\sigma_{ij}}$	Pa	Stress tensor
$\boldsymbol{\dot{\sigma}_{ij}}$	Pa	Stress increment
$\boldsymbol{\sigma_{ij}^{el}}$	Pa	Elastic stress
$\boldsymbol{\sigma_H}$	Pa	Hydrostatic stress
$\boldsymbol{\sigma_Y}$	Pa	Yield stress
$\boldsymbol{\dot{\sigma}_Y}$	Pa	Incremental change of Yield stress

Contents

1. Introduction

Austenitic stainless steels are widely applied in structural applications due to the corrosion resistance of the material, which is caused by a very stable passive layer mainly formed from the alloying element chromium and oxygen from the surroundings [1]. However, austenitic stainless steels have poor tribological and wear performance, which can be problematic in some applications, for example in the food industry.

Low temperature thermochemical surface engineering by nitriding, carburizing and nitrocarburizing of stainless steel causes a surface zone of expanded austenite, which improves the wear resistance of the stainless steel while preserving the stainless behavior. The treatment can even improve the resistance against localized corrosion, as pitting and crevice corrosion [1][2][3].

Expanded austenite, sometimes referred to as the S-phase, is a supersaturated solid solution of nitrogen or carbon in the austenite phase, where nitrogen/carbon is dissolved interstitially in the octahedral sites of the f.c.c. iron lattice [1][4].

Dissolution of collosal amounts of carbon or nitrogen in solid solution is possible due to short range ordering with the alloying element chromium. For nitriding/carburizing at low temperatures, below 450°C, only short range ordering occurs, and nitrides/carbides are not formed due to limited substitutional mobility of the chromium and other metal atoms [5][6]. This means that the expanded austenite is metastable and will decompose with time. Expanded austenite resulting from nitriding will with time develop CrN [7][8] and carbon-expanded austenite will form chromium and iron-based carbides such as the Hägg carbide, M_5C_2, or M_7C_3 [9][10][11].

Christiansen and Somers [8] described the decomposition times for nitrogen expanded austenite, by an isothermal stability plot of nitrogen-expanded austenite of 316L and 304L stainless steels, shown in Figure 1, and they recommended an upper service temperature limit of 200-250°C for nitrogen-expanded austenite [1].

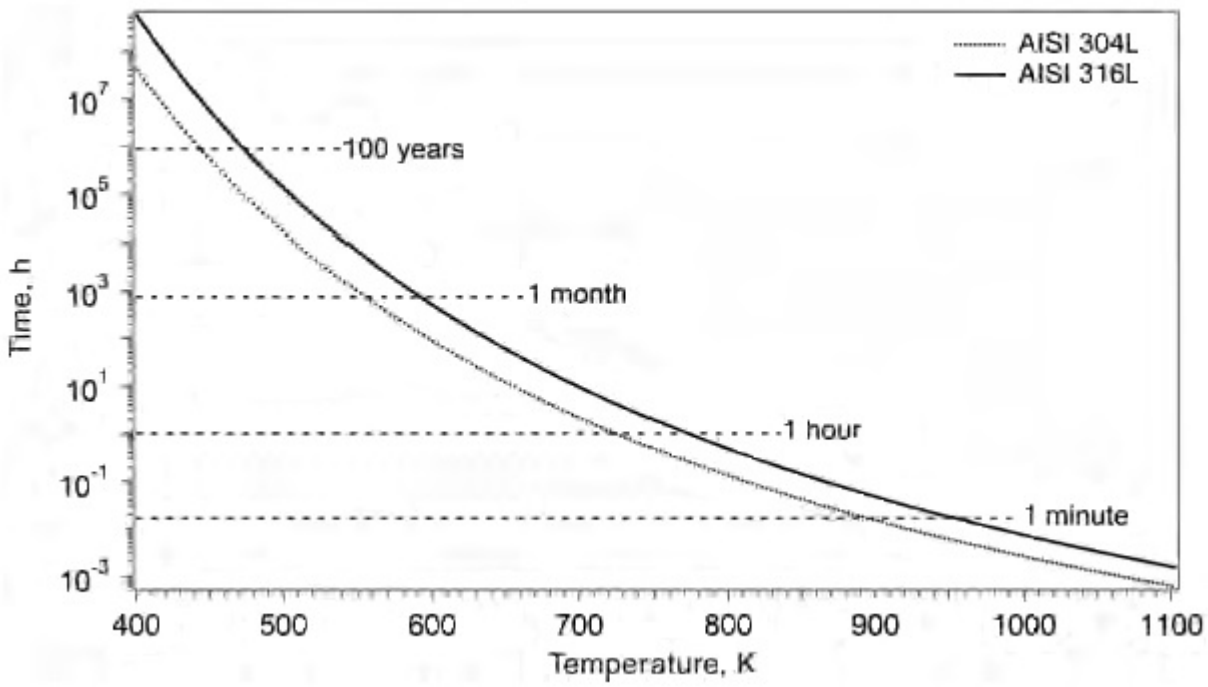

Figure 1 - Isothermal stability plot of nitrogen-expanded austenite of 316L and 304L stainless steels, based on isocronal annealing data. The graph shows the time to reach 50% decomposition. Source [1][8]

1.1 From history to state of the art

Traditionally, thermochemical surface treatments are carried out at temperatures above 500°C, but for stainless steel this results in a significant loss of corrosion resistance, due to formation of Chromium-nitrides/carbides [1]. See in this respect Figure 1; at 773K CrN develop within an hour.

The first indications of expanded austenite were seen by Lebrun in the 1970's [2][12], but the possibility of making the thermochemical treatments at lower temperatures, creating expanded austenite at the surface and keeping the corrosion resistant properties, was first scientifically recognised in the 1980's for plasma and ion based treatments by Zhang and Bell [13] and by Ichii [7]. They called the expanded austenite S-phase. Based on their works, and the work of Kolster [14], expanded austenite created by plasma and ion based treatments was investigated.

In the 1980's two commercial methods were developed; Kolsterizing by Kolster [14], which provided low temperature carburizing, and the plasma-based low temperature nitriding method provided by the company Nitruvid formed by Lebrun [1].

Plasma and ion-based treatments cannot be controlled as well as a gas-based treatment, and thus a method for gaseous treatment was pursued. The obstacle was that to create expanded austenite by nitriding/carburizing by gaseous methods, the very stable chromium rich oxide passivating layer has to be overcome for diffusion of nitrogen/carbon to take place.

The early attempts to overcome the passivating layer and making gas-based nitriding/carburising possible were done by trying to convert the passive film in to a permeable iron base oxide, as for example described by Gemma et al. [15], and later attempts involved removing the film with HCl and NF_3 gases, as in the Swagelock SAT 12 process presented by Collins et al. [16][17][18] and the NV Pionite process presented by Aioki et al. [19][20] respectively.

In the early 2000's two methods to replace the passivating layer by catalytic metal films were discovered; Somers et al. presented nickel as a coating prior to nitriding or carburizing [21] and Marx and Williams presented iron as a coating prior to carburizing [22][23]. These methods had the advantage that the activation was done ex-situ with the possibility of selective activation [23], and that the nickel-coated specimens can be stored before the thermochemical treatments [1].

Today, the current state of the art for activation prior to gas-based thermochemical surface treatments is patented by the company Expanite A/S [24] and involves the use of initially non-gaseous compounds, such as urea, that with the proper conditions will decompose and activate the surface and then create free nitrogen/carbon for the thermochemical treatment [1].

1.2 Development of microstructure and composition during low temperature thermochemical surface treatments

On low temperature thermochemical surface treatments expanded austenite is formed when nitrogen/carbon is dissolved in the lattice and forms a super-saturated solid solution of interstitials in the f.c.c lattice. Accordingly, no precipitation of a new phase occurs, but the austenitic f.c.c. iron lattice is preserved. During nitriding/ carburizing the nitrogen/carbon atoms diffuse into the material from the surface, resulting in a concentration gradient of nitrogen/carbon. The difference between the substrate austenite and the expanded austenite arises from a difference in composition, and the expanded austenite zone is seen in micrographs as a surface layer, as for example shown in Figure 2 for a nitrided austenitic steel sample. An example of glow discharge optical emission spectrometry measurements of nitrogen composition profiles resulting from thermochemical surface treatment are shown in Figure 3.

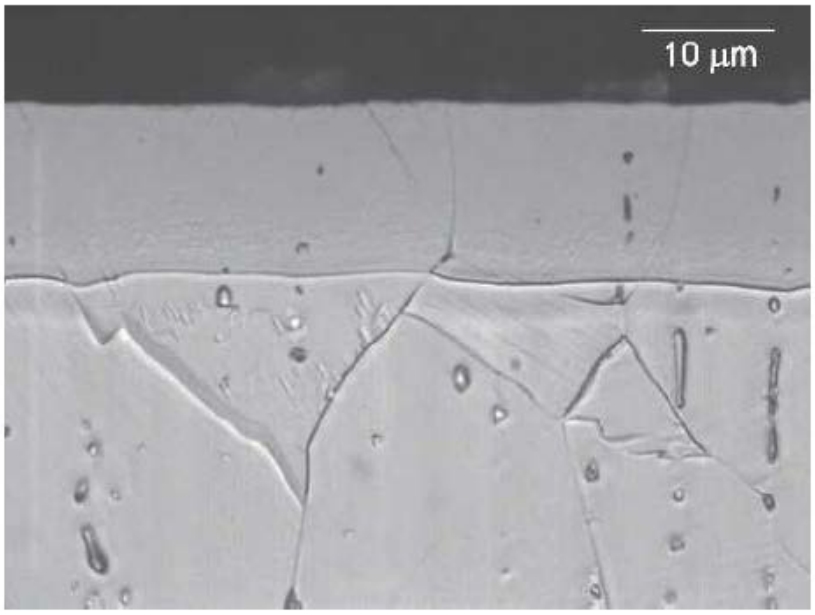

Figure 2 - Optical micrograph of nitrided AISI 316, from Christiansen and Somers [25]

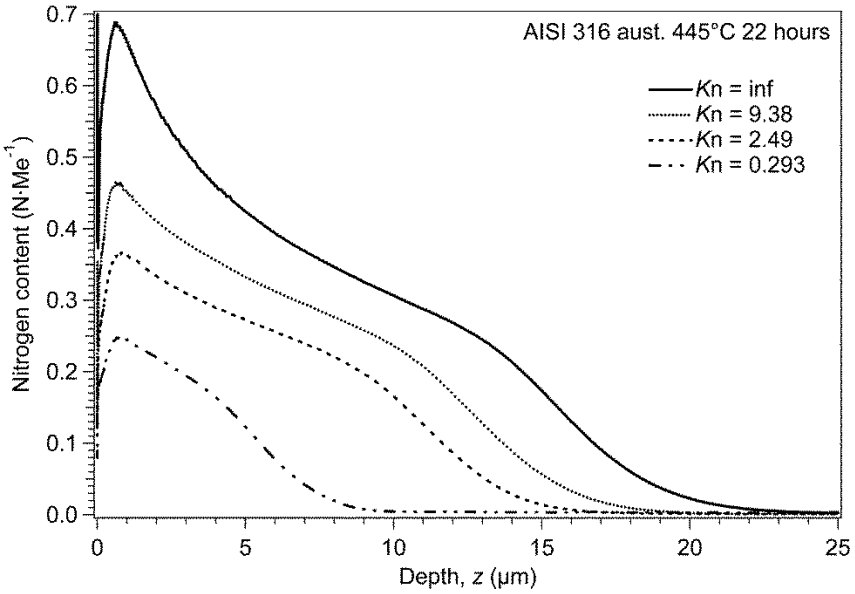

Figure 3 - Glow discharge optical emission spectrometry measurements of nitrogen concentration-depth profiles of nitride AISI 316, from Christiansen and Somers [2]

The improvement of wear resistance of the expanded austenite as compared to the substrate austenite is due to an increase in hardness, arising from the solid solution strengthening. Experimental hardness profiles, as for example shown in Figure 4, display a significantly increased hardness in the region where expanded austenite has developed.

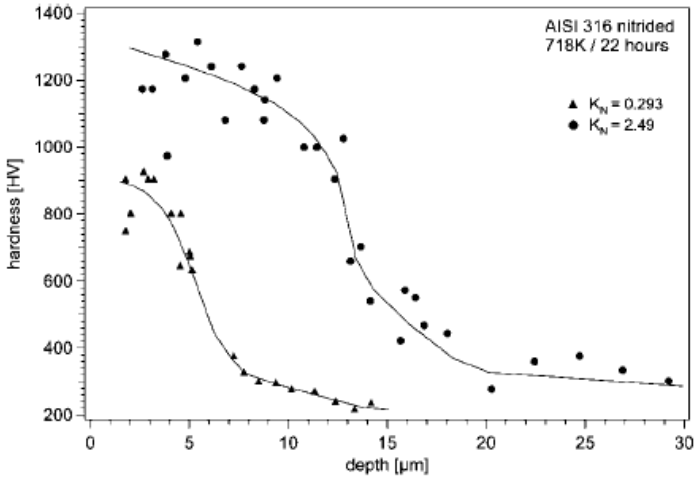

Figure 4 – Hardness depth profiles of nitrided AISI 316, from Christiansen and Somers [2] (see corresponding concentration depth profiles in Figure 3)

1.3 Process stresses

Besides the hardness gradient found in the nitrided/carburized samples there is also a residual compressive stress gradient in the expanded austenite zone. The residual stresses are introduced because of the concentration profile. Dissolution of large amounts of nitrogen/carbon is accompanied by a large volume expansion, which introduces residual stresses of several GPa's in the expanded austenite zone [2][4][26]. Examples of measured concentration-depth profiles and corresponding measured stress-depth profiles are presented in Figure 5.

Compressive stress levels of several GPa's clearly exceed the yield strength of austenitic stainless steel, which is around 290MPa [27]. Plastic deformation has been observed experimentally in nitrogen expanded austenite, both by lattice rotations and associated texture changes in expanded austenite and by enhanced surface roughness by grain push-out [25][28][29][30]. For carburizing the occurrence of plastic accommodation of composition-induced stresses has so far not been observed.

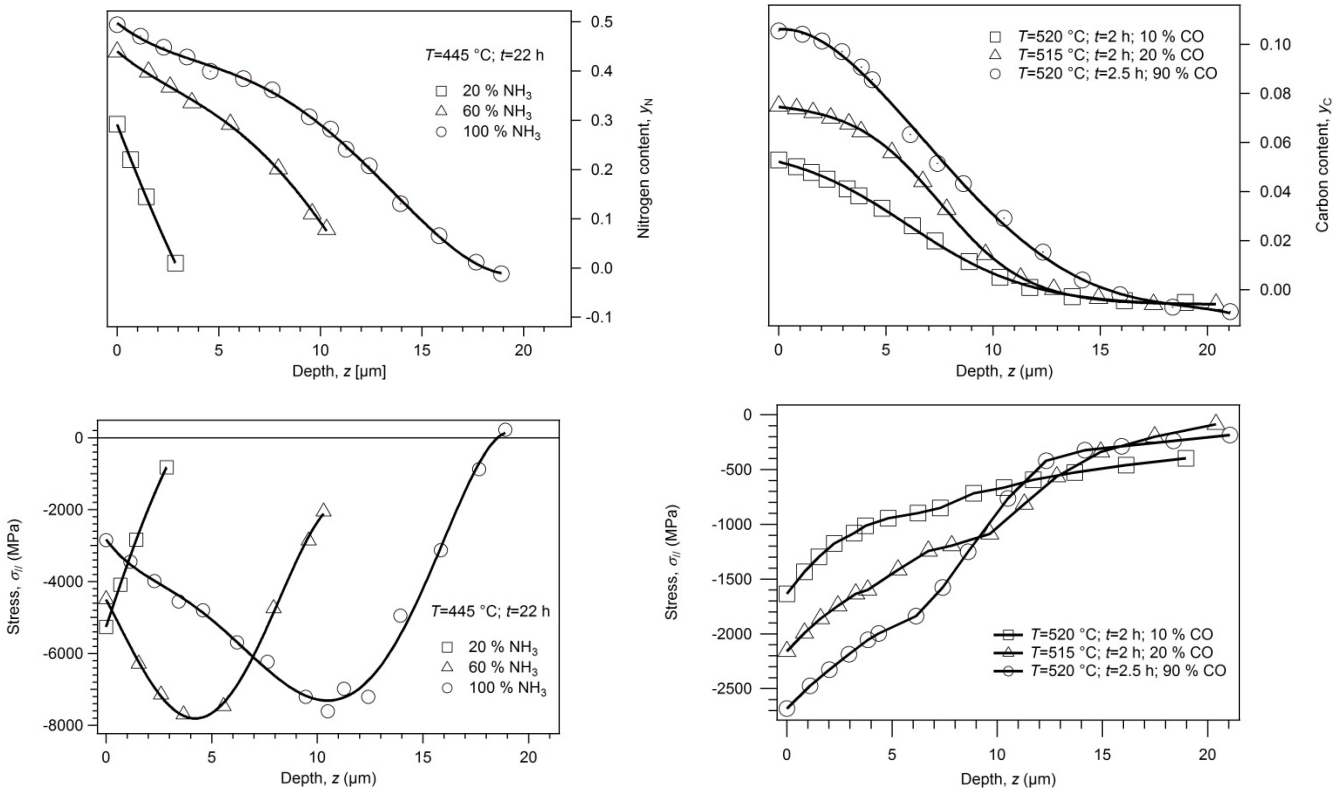

Figure 5 - Concentration-depth profiles and corresponding stress-depth profiles for nitrided and carburized samples from Christiansen and Somers [2]

1.4 Scope

The present work is concerned with the evolution of concentration-depth and residual stress-depth profiles in relation to the processing parameters of a thermochemical surface treatment of stainless steel: Low temperature nitriding. The aim of the work is to obtain a better understanding of the kinetics of the diffusion process and the effect of the resulting stresses, and to produce a model for the prediction of concentration- and stress-depth profiles.

Modelling of the concentration- and stress-depth profiles will be done based on the case of gaseous nitriding of austenitic stainless steels.

In this work only gas-based low-temperature nitriding will be considered, effects arising specifically for plasma-based processing, such as surface sputtering, will not be discussed.

Even though the case investigated is specific for gaseous nitriding, the concepts of the mechanisms governing the evolution of composition and residual stress are claimed to be applicable to (nitro)carburizing and plasma-assisted and liquid processing, as in Kolsterizing®, as well.

2. Literature review of composition profile modelling

Classical textbooks, e.g. [31], predict concentration depth-profile from interstitial diffusion (as for example carbon into iron/steel) by applying Fick's second law, and solving it, assuming an semi-infinite medium with a constant diffusion coefficient and constant surface concentration, using the complementary error function

$$c = c^S - (c^S - c_0) \cdot \mathrm{erf}\left(\frac{z}{2\sqrt{Dt}}\right) \quad (1)$$

where c^S is the surface concentration, D the diffusion coefficient, t the time, z the distance from the surface and c_0 the initial concentration in the specimen [31].

Using the error function solution implies many assumptions which are not in reality correct for nitriding of stainless steel, for example; that the stress state does not affect the concentration, that the diffusion coefficient is constant and that the nitrogen concentration is constant at the surface. In reality there are many factors influencing the concentration profile. The error-function predicted profiles, as shown in Figure 6, is also far from reality where concentration-depth profiles developing during low temperature nitriding are characterized by the shape shown in Figure 7: an initially steep decrease in nitrogen content followed by a plateau and a steep decline at the case-core transition.

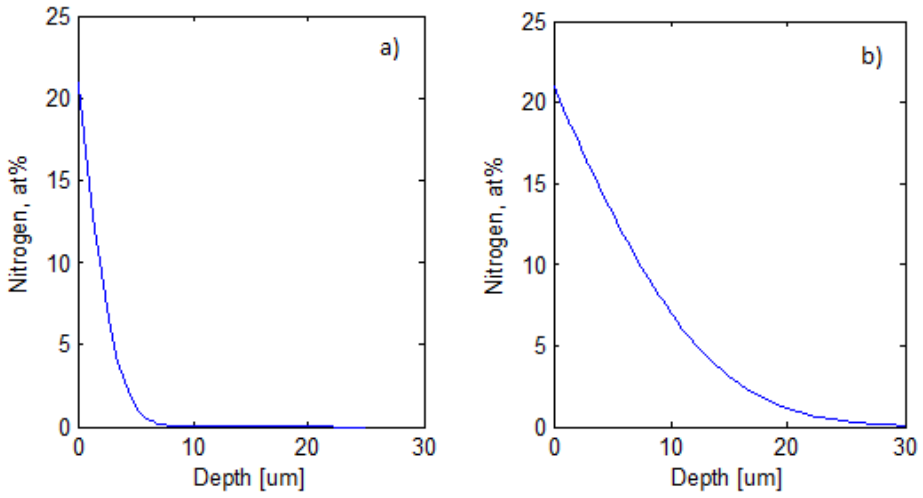

Figure 6 - concentration depth profiles after a) 1h and b) 15h predicted using the error-function solution using a diffusion coefficient of $10^{-15}\mathrm{m}^2/\mathrm{s}$

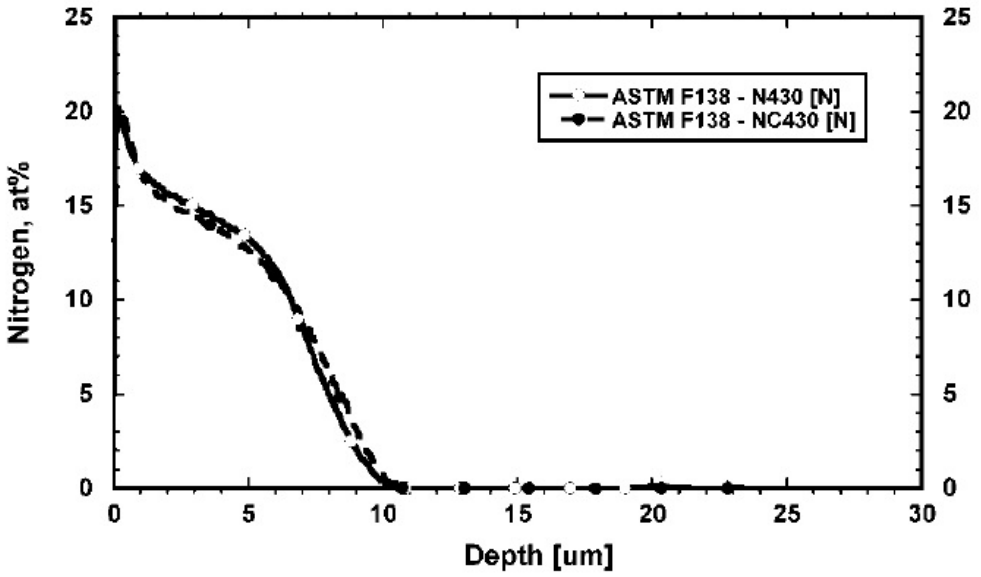

Figure 7 - Measured nitrogen concentration-depth profiles after 15h at 430°C. Source [3]

In the literature various approaches have been taken to predict and explain the composition-depth profile.

Parascandola et al. [32] modelled the concentration-depth profile of nitrogen during ion implantation, assuming a constant diffusion coefficient, using trapping and detrapping of nitrogen at trapsites formed by local chromium. This resulted in a satisfactory fitting to measured concentration-depth profiles. The same method was applied by Martinavicius et al. [33] to plasma-nitrided single crystals with various orientations.

In constrast, Christiansen and Somers [34] experimentally found that the diffusion coefficient of nitrogen in expanded austenite is not constant, but depends on the nitrogen concentration as shown in Figure 8. The increase of diffusion coefficient until a certain nitrogen concentration, displayed in Figure 8, can be explained by the expansion of the austenite f.c.c. lattice that occurs with increasing levels of nitrogen, since the expansion of the lattice will lower the activation energy for nitrogen to move from one interstitial site to another. However at some point the nitrogen concentration is so high that the falling probability of a unoccupied interstitial site that the nitrogen can jump to is no longer outweighed by faster diffusion, and that explains the lowering of diffusivity at higher nitrogen concentrations [1].

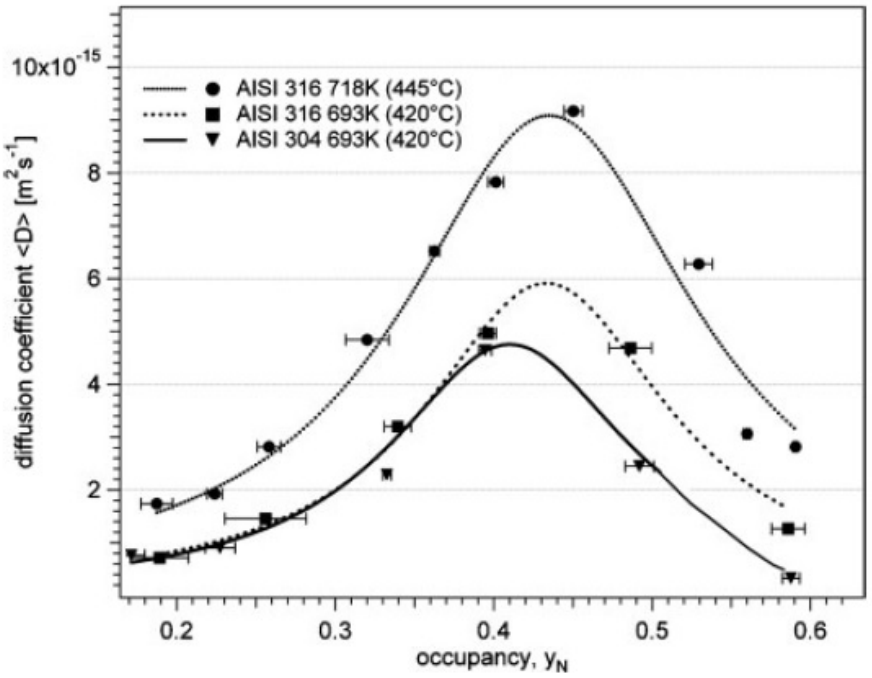

Figure 8 - Diffusion coefficient of nitrogen in austenite as function of nitrogen concentration measured by occupancy. Source [34]

Christiansen and Somers demonstrated that the composition dependence of the diffusion coefficient of nitrogen in expanded austenite can in principle explain the shape of the nitrogen concentration-depth profile developing during nitriding (seen in Figure 7) by calculating the concentration profile from Fick's 2nd law [34][35][36].

Another way of modeling the effect of short-range ordering with chromium is based on modeling of precipitation during nitriding by Sun and Bell [37] who looked at nitriding of iron. Their method was adapted by Christiansen and Somers in 2008 [34] to investigate the effect of trapping of nitrogen on the predicted concentration profile in stainless steel, combined with a concentration dependent diffusion coefficient and agreement with experimental results was found. The effect of trapping was also investigated by Moskaliovienne and Galdikas in 2011 [38].

Larche and Cahn [39][40] discussed the coupling between composition-induced stresses and the effect of stresses on diffusion. Building on this, Chu and Lee [41] included the effect of hydrostatic stress on the concentration profile using a constant diffusion coefficient, and incorporated it by making use of an effective diffusion coefficient, and calculated elastic stresses from

$$\sigma = \frac{E}{1-v}\frac{\bar{V}}{3}(c - \bar{c}) \tag{2}$$

where E is Youngs modulus, v is Poisson's ratio, $\bar{V}$ is the partial molal volume, $\bar{c}$ the average concentration in the specimen and c the current concentration for a specific depth. The approach from Chu and Lee was adopted by Christiansen and Somers [42], who showed that for a constant surface concentration the stress gradient arising from the concentration gradient causes a deeper penetration of the nitrogen. Yang [43] and Galdikas and Moskaliovienne [44][45][46] have also looked into the coupling between the stresses and diffusion inside the specimen, using an unphysical linear relation between the hydrostatic stress and the concentration, that was originally proposed by Christiansen and Somers to estimate fictitious stresses in X-ray diffraction stress measurements [47]. Galdikas and Moskaliovienne evaluated the diffusion coefficient from the Einstein-Smoluchowski relation, instead of using experimentally determined diffusion coefficients for the system.

Calculation of a surface flux, instead of using a constant surface concentration have been done by different approaches, one by Frieling and Somers [48][49] and another by Moskaliovienne and Galdikas [45][46]. The approach by Frieling and Somers will be applied in this work.

3. Process and kinetics of gaseous nitriding

Nitriding occurs by adsorption, dissolution and diffusion of nitrogen in the solid specimen. This process can be done by gaseous nitriding, where a gas mixture containing hydrogen and ammonia surrounds the specimen.

The adsorption and dissolution of nitrogen from the gas and into the solid specimen can be described by the following reaction

$$2NH_3 \rightleftarrows 2[N]_\varphi + 3H_2$$

where $[N]_\varphi$ represents nitrogen dissolved in the solid phase φ [49][50].

Dissolving of nitrogen takes place in steps. First ammonia is adsorbed at the surface of the specimen, then dissociation occurs, leading to adsorption of nitrogen at the surface and last there is dissolution of the adsorbed nitrogen in the solid phase.

The gas mixtures used for nitriding are NH_3/H_2 mixtures, and decomposition of the ammonia will occur by the following reaction

$$2NH_3 \rightleftarrows N_2 + 3H_2$$

giving nitrogen- and hydrogen gas [49],[50] .

At the surface of the specimen, a similar reaction occurs, but now the nitrogen is adsorbed, giving the following reaction

$$2NH_3 \rightleftarrows 2N_{\varphi,ad} + 3H_2$$

where $N_{\varphi,ad}$ is nitrogen adsorbed at the surface of phase φ of the solid specimen [49][50].

The adsorbed nitrogen then either dissolves in to the solid or forms nitrogen gas by the following reactions [49],[50]

$$N_{\varphi,ad} \rightleftarrows [N]_\varphi$$

$$N_{\varphi,ad} + N_{\varphi,ad} \rightleftarrows N_2$$

as illustrated in Figure 9.

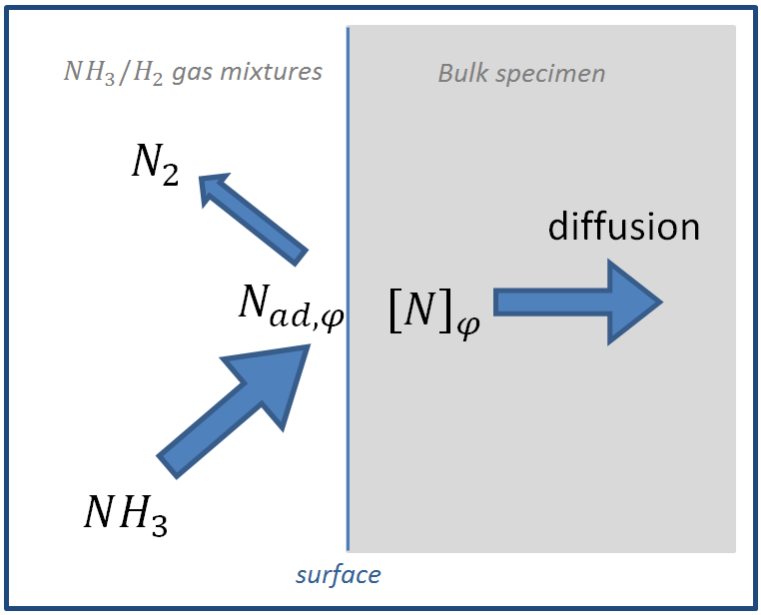

Figure 9 - Principle of gaseous nitriding [50]

The nitriding rate depends thus on three things; how fast the ammonia is transported to the surface of the specimen, the rate of the dissociation, adsorption and dissolving reactions at the surface of the specimen and the rate of solid state diffusion [48].

The first is usually disregarded, assuming that the transport of ammonia to the surface is fast enough not to be rate determining. However, under certain practical conditions, transport of ammonia (or desorption of N_2) from the surface can become rate-determining.

If the desorption of nitrogen from the surface is not considered, the flux of nitrogen through the surface J_{surf} of the specimen is given by the following equation [48][51]

$$J_{surf} = k \cdot \left(c_N^{eq} - c_N^s\right) \tag{3}$$

where c_N^s is the concentration of nitrogen just below the surface, c_N^{eq} is nitrogen concentration in the solid phase at the surface if a state of equilibrium was obtained, corresponding with the chemical potential of nitrogen in the gas-phase, and k is the reaction rate constant of the slowest step in the ammonia dissociation [48].

The ammonia dissociation, can be described by

$$2NH_3 \rightleftarrows 2N_{\varphi,ad} + 3H_2$$

and takes place in the following steps:

$$NH_3 \rightleftarrows NH_{3(ad)}$$

$$NH_{3(ad)} \rightleftarrows NH_{2(ad)} + H_{(ad)}$$

$$NH_{2(ad)} \rightleftarrows NH_{(ad)} + H_{(ad)}$$

$$NH_{(ad)} \rightleftarrows N_{(ad)} + H_{(ad)}$$

$$H_{(ad)} + H_{(ad)} \rightleftarrows H_2$$

For high hydrogen pressures the rate limiting step is the removal of hydrogen from NH_2 [52] and the constant k is thus the forward reaction constant of the reaction

$$NH_{2(ad)} \rightleftarrows NH_{(ad)} + H_{(ad)}$$

This constant is currently not known for nitriding of 316 stainless steel, but can be approached by using the value for Iron, which is calculated from [53]

$$k = k_0 \cdot p_{H_2} \cdot \exp\left(\frac{-Q_1}{RT}\right) \tag{4}$$

where p_{H_2} is the partial pressure of hydrogen in atm, R is the gas constant and T is the absolute temperature. k_0 and Q_1 are constants. For nitriding of 316 stainless steel the values of k_0 and Q_1 are unknown, but the values for nitriding of α-iron are known. For example for temperatures in the range of 770-870K (≈500-600 °C) and hydrogen partial pressures between 0.7 and 1atm, [53]:

$$k_0 = 9 \cdot 10^{-4}\ \mathrm{m/s \cdot atm}$$
$$Q_1 = 64220\ \mathrm{J/mol} \tag{5}$$

Values for nitriding of α-iron have also been reported by Grabke [52], who reported two different ranges since the reaction rate constant depends on the rate controlling step.

For low partial hydrogen pressure the reaction step

$$NH_{3(ad)} \rightleftarrows NH_{2(ad)} + H_{(ad)}$$

is rate controlling, giving one set of constants, and for higher pressures the reaction step

$$NH_{2(ad)} \rightleftarrows NH_{(ad)} + H_{(ad)}$$

is rate controlling. The boundary between the two rate controlling steps also depends on temperature [52].

The partial pressure of hydrogen can be found from the nitriding potential in the gas K_N^{gas}, which is defined as

$$K_N^{gas} \equiv \frac{p_{NH_3}}{{p_{H_2}}^{3/2}} \tag{6}$$

where p_{NH_3} and p_{H_2} are the partial pressure of ammonia and hydrogen respectively.

Using Daltons law of partial pressures, assuming ideal gasses the total pressure, p, is the sum of the partial pressures

$$p = p_{NH_3} + p_{H_2} \tag{7}$$

and assuming the total pressure is atmospheric pressure, 1 atm, the following form of eq. 6 can be found

$$K_N^{gas} = \frac{1 - p_{H_2}}{{p_{H_2}}^{3/2}} \tag{8}$$

From where the partial pressure of hydrogen can be determined.

4. Basic diffusion equations for internal diffusion

The diffusive flux of nitrogen atoms in the direction z, at constant temperature, under the influence of a chemical potential gradient in this species $\frac{\partial \mu_N}{\partial z}$ is defined [39] as

$$J = -M_N c_N \frac{\partial \mu_N}{\partial z} \tag{9}$$

where c_N is the nitrogen concentration in mol.m^{-3}, μ_N is the chemical potential of nitrogen in J.mol^{-1} and M_N is the mobility of nitrogen in m^2.s^{-1} given by [39]

$$M_N = \frac{D_N}{RT} \tag{10}$$

where D_N is the intrinsic diffusion coefficient of nitrogen in m^2.s^{-1}, R is the gas constant in J.mol^{-1}.K^{-1} and T is the temperature in K.

Generally, for constant temperature and pressure, the chemical potential, for an ideal solution, is assumed to depend on the concentration only

$$\mu(c_N) = \mu_0 + RT\ln(c_N) \tag{11}$$

In which case eq. 9 reduces to Fick's first law

$$J_N = -D_N \frac{\partial c_N}{\partial z} \tag{12}$$

More generally, for non-ideal solutions, the chemical potential is a function of the activity of nitrogen, a_N, and the hydrostatic stress (pressure), σ_H , and the temperature T [45][54]

$$\mu_N(a_N, \sigma_H, T) = \mu_{N,0} + RTln(a_N) - V_N \sigma_H \tag{13}$$

where $\mu_{N,0}$ is the chemical potential of nitrogen in the reference state with respect to which a_N is defined[1], V_N is the partial molar volume of nitrogen. It is noted that in principle a_N, V_N and σ_H depend on the temperature. The diffusive flux follows from inserting eq. 13 and eq. 10 into eq. 9, which results in

[1] Usually, for nitrogen in solid solution the reference state is taken as nitrogen gas at 1 bar at the temperature under consideration.

$$J_N = -\frac{D_N c_N}{RT}\left(\frac{\partial \mu_N}{\partial c_N}\frac{\partial c_N}{\partial z} + \frac{\partial \mu_N}{\partial \sigma_H}\frac{\partial \sigma_H}{\partial z}\right) \tag{14}$$

In a Fe-N phase the activity is linearly proportional to the nitriding potential, $K_N = \frac{p_{NH_3}}{{p_{H_2}}^{3/2}}$, by [55]

$$a = K_T K_N \tag{15}$$

where $K_T(T, p)$ is the temperature and pressure dependent equilibrium constant for the reaction describing the dissolution of N into the solid phase from the gas phase containing NH_3 and H_2.

Using eq. 13 the following expressions for the change of chemical potential with temperature and stress are obtained

$$\frac{\partial \mu_N}{\partial T} = R\ln(a) = R\ln(K_T K_N) \tag{16}$$

$$\frac{\partial \mu_N}{\partial \sigma_H} = V_N \tag{17}$$

Since the activity depends on the concentration

$$\frac{\partial \mu_N}{\partial c_N} = RT\frac{\partial \ln a}{\partial c_N} = \frac{RT}{c_N}\frac{\partial \ln(a_N)}{\partial \ln(c_N)} = \frac{RT}{c_N}\frac{\partial \ln(K_T K_N)}{\partial \ln(c_N)} \tag{18}$$

Realizing that K_T only depends on pressure and temperature and not on nitrogen concentration, it is obtained

$$\frac{\partial \mu_N}{\partial c_N} = \frac{RT}{K_N}\frac{\partial K_N}{\partial c_N} \tag{19}$$

Inserting eq. 16, eq. 17, and eq. 19 in eq. 14 the following generalized form of Fick's 1st law is obtained

$$J_N = -\frac{D_N c_N}{RT}\left(\frac{RT}{K_N}\frac{\partial K_N}{\partial c_N}\frac{\partial c_N}{\partial z} - V_N\frac{\partial \sigma_H}{\partial z}\right) \tag{20}$$

Accordingly, the generalized form of Fick's 2nd law is

$$\frac{\partial c_N}{\partial t} = -\frac{\partial}{\partial z}\left(-D_N^{(c)}.\frac{\partial c_N}{\partial z} + \frac{D_N.c_N}{RT}.V_N.\frac{\partial \sigma_H}{\partial z}\right) \tag{21}$$

where $D_N^{(c)}$ represents the concentration dependence of the diffusion coefficient of nitrogen, including the thermodynamic factor $\left(\frac{c_N}{K_N}\frac{\partial K_N}{\partial c_N}\right)$. When $D_N^{(c)}$ is a known explicit function of the concentration the equation can be rewritten to

$$\frac{\partial c_N}{\partial t} = -\frac{\partial}{\partial z}\left(-D_N^{(c)}.\frac{\partial c_N}{\partial z} + \frac{D_N^{(c)}}{\frac{\partial K_N}{\partial c_N}}.\frac{K_N}{RT}.V_N.\frac{\partial \sigma_H}{\partial z}\right) \tag{22}$$

and then the differentiation gives

$$\frac{\partial c_N}{\partial t} = \frac{\partial D_N^{(c)}}{\partial c_N}\cdot\left(\frac{\partial c_N}{\partial z}\right)^2 + D_N^{(c)}\cdot\frac{\partial^2 c_N}{\partial z^2} - \frac{\partial}{\partial z}\left(D_N^{(c)}\cdot\frac{K_N}{\frac{\partial K_N}{\partial c_N}}\right)\cdot\frac{V_N}{RT}\frac{\partial \sigma_H}{\partial z} - D_N^{(c)}\cdot\left(\frac{K_N}{\frac{\partial K_N}{\partial c_N}}\frac{V_N}{RT}\frac{\partial^2 \sigma_H}{\partial z^2}\right) \tag{23}$$

At the surface the concentration can then be found from the continuity equation for balancing the arriving and leaving nitrogen fluxes:

$$\frac{\partial c_N^s}{\partial t} = -\frac{\partial J_N^s}{\partial z} = -\left(\frac{\partial J_N^{s,diff}}{\partial z} - \frac{\partial J_N^{s,diss}}{\partial z}\right) \tag{24}$$

where $J_N^{s,diss}$ and $J_N^{s,diff}$ are the fluxes of nitrogen atoms arriving at the surface from dissociation and leaving from the surface by diffusion, respectively. Note that here the flux of nitrogen, from the surface by desorption of N_2, is omitted.

Combining eq. 24 with the expression for J_{surf}, given in eq. 3 and the expression for the flux, eq. 20 the nitrogen concentration in the surface cell follows from

$$\frac{\partial c_N^s}{\partial t} = \frac{\partial}{\partial z}\left(D_N^{(c)}.\frac{\partial c_N}{\partial z} - \frac{D_N^{(c)}}{\frac{\partial K_N}{\partial c_N}}.\frac{K_N}{RT}.V_N.\frac{\partial \sigma_H}{\partial z}\right) + \frac{\partial}{\partial z}\left(k\cdot\left(c_N^{eq} - c_N^s\right)\right) \tag{25}$$

which can be discretized using finite difference as

$$\frac{c_i^{t+\Delta t} - c_i^t}{\Delta t} = {D^*}_i^t \frac{c_{i+1}^t - c_i^t}{{\Delta z_i}^2} - {D^*}_i^t \cdot \frac{K_N}{\frac{\partial K_N}{\partial c}} \frac{1}{RT_i^t} V_N \frac{{\sigma_H}_{i+1}^t - {\sigma_H}_i^t}{{\Delta z_i}^2} + \frac{k}{\Delta z_i} \cdot \left(c_N^{eq} - c_i^t\right) \quad (26)$$

where i denotes the element number. Expressions for V_N, K_T and the relation between the nitriding potential K_N and the concentration, for the case examined in this work, nitriding of AISI 316 austenitic stainless steel, are derived in Appendix A.

5. Modelling of concentration depth-profiles using trapping and concentration dependent diffusion coefficient

5.1 Computational modelling of concentration profiles with constant temperature and no stress influence

Assuming constant temperature and no stress influence the diffusion equation, eq. 23, reduces to

$$\frac{\partial c_N}{\partial t} = \frac{\partial D_N^{(c)}}{\partial c_N} \cdot \left(\frac{\partial c_N}{\partial z}\right)^2 + D_N^{(c)} \cdot \frac{\partial^2 c_N}{\partial z^2} \tag{27}$$

For computations discretizing is done using central finite difference method

$$\frac{c_i^{t+\Delta t} - c_i^t}{\Delta t} = \frac{\partial D_N^{(c_i^t)}}{\partial c}\left(\frac{c_{i+1}^t - c_{i-1}^t}{2\Delta z}\right)^2 + D_N^{(c_i^t)} \cdot \frac{c_{i+1}^t - 2c_i^t + c_{i-1}^t}{\Delta z^2} \tag{28}$$

where $D_N^{(c_i^t)}$ is a known explicit function of the concentration, giving the possibility of calculating $\frac{\partial D}{\partial c}$ for a known concentration c_i^t.

The continuity equation at the surface to balance the fluxes of nitrogen atoms arriving at and leaving from the surface cell to calculate the actual surface concentration of nitrogen, described by eq. 24, can be discretized as

$$\frac{c_i^{t+\Delta t} - c_i^t}{\Delta t} = -\frac{J_{i\to i+1} - J_{surf}}{\Delta z} \tag{29}$$

Combining eq. 29 with the expression for J_{surf}, given in eq. 3 and the expression for the flux, (see eq. 20 and 21) the nitrogen concentration in the surface cell follows from

$$\frac{c_i^{t+\Delta t} - c_i^t}{\Delta t} = D_N^{(c_i^t)} \frac{c_{i+1}^t - c_i^t}{{\Delta z_i}^2} + \frac{k}{\Delta z_i} \cdot \left(c_{eq} - c_i^t\right) \tag{30}$$

Verification of program calculations for calculations with constant diffusion coefficient and with concentration dependent diffusion coefficient are given in Appendix C.3 and C.4 respectively.

5.2 Trapping

The short-range ordering of nitrogen atoms by chromium is referred to as trapping and is mathematically treated analogously to nitrogen precipitation as in [34][37][56]. It is assumed that trapping first occurs above a certain threshold probability for finding a Cr-N pair of atoms. Analogous to the solubility product of nitrogen and chromium contents above which CrN precipitation occurs, the thermodynamic solubility constant, K_e, is introduced to describe the solubility product of nitrogen and chromium contents above which trapping of nitrogen atoms occurs. Suppression of the actual precipitation of chromium nitride through sluggish diffusion kinetics of chromium diffusion is the very essence of supersaturated, metastable expanded austenite during low temperature nitriding (and/or carburizing) of stainless steel. Prolonged nitriding or subsequent ageing will eventually lead to the unintentional but unavoidable precipitation of CrN.

The equilibrium constant of trapping nitrogen by chromium is described by:

$$K_e = \frac{1}{c_{Cr} \cdot c_N^n} = \frac{1}{K_{CrN_n}} \rightarrow K_{CrN_n} = c_{Cr} \cdot c_N^n \tag{31}$$

where c_j is the concentration of the dissolved element *j* and K_{CrN_n} is the solubility product of Cr and N with *n* the number of nitrogen atoms per chromium atom, which is about Cr:N=1:0.9 for strong binding of nitrogen by chromium in AISI 316L [25].

5.2.1 Computational implementation of trapping

The amount of free nitrogen after trapping, i.e. concentration of residual nitrogen, c_N^{res}, can be found using eq. 31 from

$$K_{CrN_n} = c_{Cr}^{res} \cdot (c_N^{res})^n \tag{32}$$

Computationally the calculation of the residual nitrogen and chromium is done sequentially by calculating the residual nitrogen assuming that residual chromium in the equation above is equal to the free chromium before trapping, so

$$c_{Cr}^{res}{}_{before\ trapping} \cdot \left(c_N^{res}{}_{after\ trapping}\right)^n = K_{CrN_n} \tag{33}$$

The concentration of trapped nitrogen, c_N^{tr}, is then found by

$$c_N^{tr} = c_N(t,z) - c_N^{res} \tag{34}$$

and the trapped chromium, c_{Cr}^{tr}, by

$$c_{Cr}^{tr} = \frac{c_N^{tr}}{n} \tag{35}$$

The concentration of residual chromium after trapping, c_{Cr}^{res}, is then found as

$$c_{Cr}^{res} = c_{Cr}(t,z) - c_{Cr}^{tr} \tag{36}$$

It is noted that this sequential modeling induces a slight error, but for small time steps it is deemed negligible.

On incorporating trapping in the model for diffusion of nitrogen it is noted that only residual nitrogen is considered to diffuse, while the surface flux depends on the total concentration of nitrogen in the surface.

$$c_N^{tot} = c_N^{tr} + c_N^{res} \tag{37}$$

It should be noted that the diffusion coefficient depends on the total nitrogen concentration, because all nitrogen is in solid solution; no actual precipitation occurs.

5.3 Concentration dependence of diffusion coefficient

Christiansen et al. [34] measured the diffusion coefficient of nitrogen in expanded austenite, as was shown in Figure 8.

The following Lorentzian type expression for diffusion coefficient in m^2/s as a function of nitrogen concentration for the specific temperature of 445°C was obtained using the data of Christiansen et. al [34]

$$D(c_N) = 3.16 \cdot 10^{-15}\ [\mathrm{m^2/s}] \cdot \frac{1}{\pi} \cdot \frac{0.109}{(y_N(c_N) - 0.4365)^2 + 0.109^2} \tag{38}$$

where y_N is the nitrogen content expressed as the fractional occupancy of the nitrogen sublattice formed by the octahedral interstices, and c_N is the concentration in mol/m^3.

The relation between c_N and y_N depends on the volume of the unit cell [57]

$$c_N = \frac{n}{N_{av}} \cdot y_N \cdot \frac{1}{V_\varphi} \tag{39}$$

where n is the number of atoms pr. unit-cell in the iron lattice (equal to 4), N_{av} is Avogadros number and V_φ is the volume of the unit cell in m^3 at the given y_N.

$$c_N = \frac{4}{6.022 \cdot 10^{23}\mathrm{mol^{-1}}} \cdot y_N \cdot \frac{1}{V_\varphi} \tag{40}$$

To find the volume of the unit cell as a function of the concentration for expanded austenite $V(c_N)$, data from Christiansen and Somers [2] of the lattice parameter, *a,* corresponding to concentrations y_N was used. A plot showing the calculated volumes as function of the fractional occupancy are shown in Figure 10 below. Fitting a polynomium to the data gives a linear fit of

$$V_\varphi(y_N) = 2.8147 \cdot 10^{-29} \cdot y_N + 4.7134 \cdot 10^{-29} \tag{41}$$

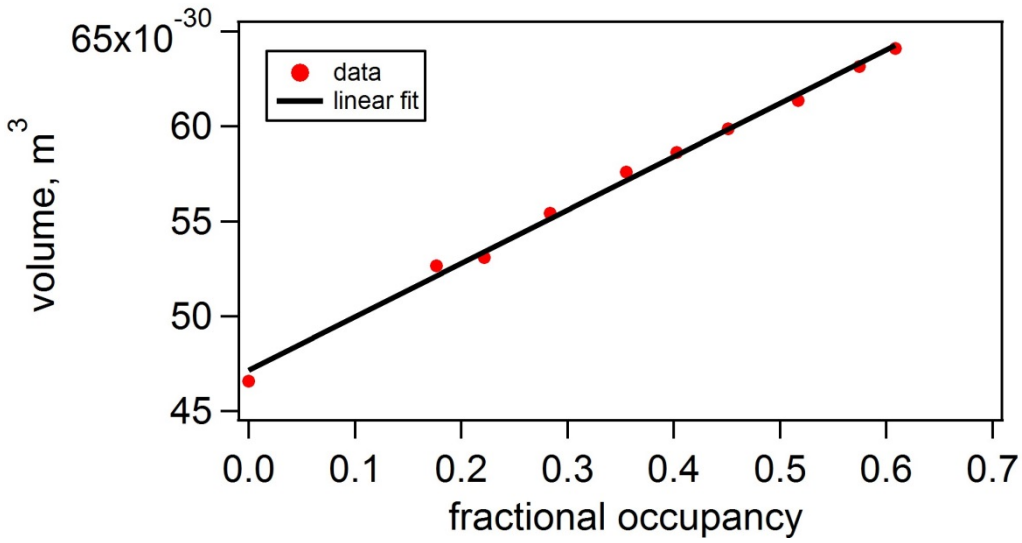

Figure 10 - Unit cell volume as function of nitrogen concentration expressed as fractional occupancy

Inserting the linear fit gives the following expression for calculating concentration in $\mathrm{mol/m^3}$ as function of fractional occupancy

$$c_N = \frac{4}{6.022 \cdot 10^{23}\mathrm{mol^{-1}}} \cdot \frac{y_N}{2.8147 \cdot 10^{-29}\mathrm{m^3} \cdot y_N + 4.7134 \cdot 10^{-29}\mathrm{m^3}} \tag{42}$$

Isolation of y_N and reducing gives the following expression for fractional occupancy as function of concentration

$$y_N = \frac{c_N}{140924\mathrm{mol/m^3} - c_N \cdot 0.59717} \tag{43}$$

Note that inserting eq. 43 in the expression for volume as function of fractional occupancy, eq. 41, gives the unitcell volume as function of concentration

$$V_\varphi(c_N) = 2.8147 \cdot 10^{-29}\mathrm{m^3} \cdot \frac{c_N}{140924\mathrm{mol/m^3} - c_N \cdot 0.59717} + 4.7134 \cdot 10^{-29}\mathrm{m^3} \tag{44}$$

and thus for $c_N = 0$ the reference volume is

$$V_{ref} = 4.7134 \cdot 10^{-29}\mathrm{m^3} \tag{45}$$

5.4 Effects of trapping and concentration dependent diffusion coefficient on concentration depth profiles

As described in section 5.2, trapping of nitrogen by chromium should be considered in the case of modelling diffusion of nitrogen during nitriding. The role of trapping on the developing concentration profile is thus investigated, while still considering the effect of a composition-dependent diffusion coefficient of nitrogen. For this purpose modelling of nitriding at 718 K for 22 hours is done, using a surface reaction rate constant $k = 5 \cdot 10^{-7}$ and a nitriding potential of K_N = 1000 $atm^{-1/2}$. For calculations with concentration dependent diffusion coefficient the expression for diffusion coefficient given in eq. 38 is applied, and for the calculations with a constant diffusion coefficient, the average value over the composition range is taken.

The nitrogen concentration-depth profiles were calculated for the case of no trapping, $K_{CrN} = \infty$, full trapping $K_{CrN} = 0$, and intermediate trapping for solubility products $K_{CrN} = 10^7$, $K_{CrN} = 10^8$ and $K_{CrN} = 10^9$. For these three cases of intermediate trapping, trapping occurs for nitrogen concentrations higher than approximately $700\mathrm{mol/m^3}$, $4600\mathrm{mol/m^3}$and $41600\mathrm{mol/m^3}$, respectively. The concentration profiles were calculated under the assumption that no composition-induced stress develops in the case, and that the sample could be assumed to be infinitely thick, compared to the diffusion depth range, thus the model calculates diffusion into a semi-infinite solid.

Figure 11 a) and b) displays the results of the calculations for constant diffusivity and concentration-dependent diffusivity, respectively. For the constant diffusion coefficient depicted in Figure 11a, the effect of trapping is easily seen, since full trapping leads to an abrupt transition to zero nitrogen concentration, whereas no trapping yields the usual complementary error-function profile, with a concentration gradient that decreases gradually with depth. Intermediate trapping results in a smoothening of the abrupt transition from high to low nitrogen concentration seen for full trapping. This is most clearly reflected by the profile for $K_{crN} = 10^7$. Not having the abrupt transition to zero concentration as the full trapping, the intermediate trapping curves shows a tail to the concentration profile beyond the depth where the solubility product is reached. The arrows in Figure 11a indicate the position of the discontinuity in the slope to the concentration profile occurs, that marks the concentration and depth below which no trapping occurs. The effect of a concentration-dependent diffusion coefficient that increases with nitrogen content, reaches a maximum and thereafter decreases with nitrogen content (see Figure 8) is reflected in Figure 11b. Analogous to the observations in Figure 11a a discontinuity in the slope is observed (marked by arrows) for the concentration and depth below which no trapping occurs.

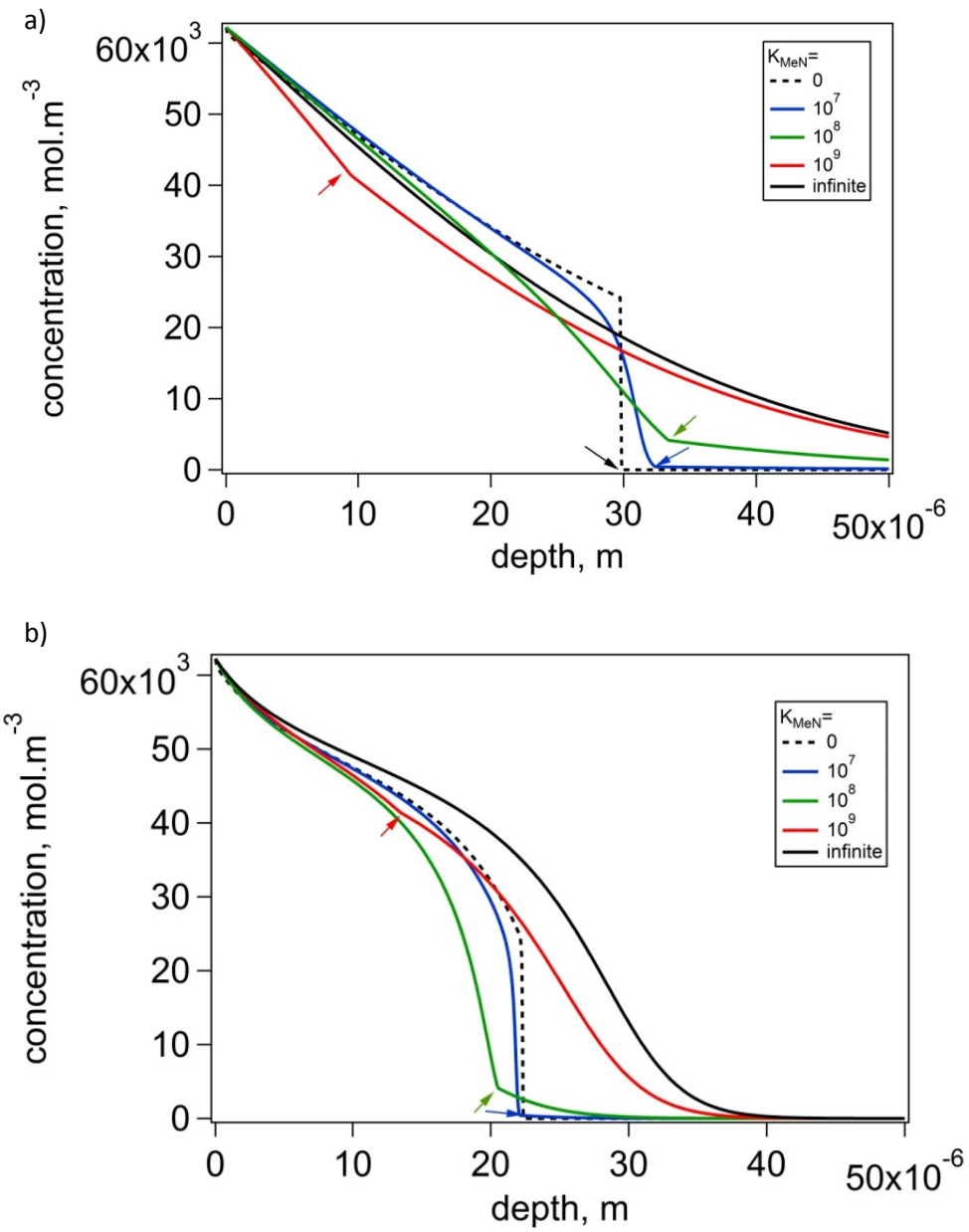

Figure 11 - Concentration-depth profiles calculated assuming a) constant diffusion coefficient and b) concentration dependent diffusion coefficient, for no trapping, $K_{CrN} = \infty$, full trapping $K_{CrN} = 0$, and intermediate trapping for solubility products $K_{CrN} = 10^7$, $K_{CrN} = 10^8$ and $K_{CrN} = 10^9$ of diffusing nitrogen atoms by chromium atoms. The arrows mark the discontinuity in the slope, at the depth below which no trapping occur.

5.6 The role of the surface reaction on evolution of composition-depth profiles

The competition of the fluxes of nitrogen arriving at and leaving from the surface is now evaluated, by including the surface reaction as described in eq. 3, which describes the flux of nitrogen through the surface. The evolution of the composition profile with time during nitriding at K_N= 1000 at 718 K was again considered using a concentration-dependent diffusivity, intermediate trapping $K_{CrN} = 10^7$ and $K_{CrN} = 10^9$ (cf. Figure 11b), and different values of the reaction-rate constant *k* in eq. 3 is now examined. The evolution of the concentration-depth profile with time is shown for k= $5 \cdot 10^{-7}$ in Figure 12a, and for k= $5 \cdot 10^{-10}$ in Figure 12b. As above, the role of composition-induced residual stress is omitted.

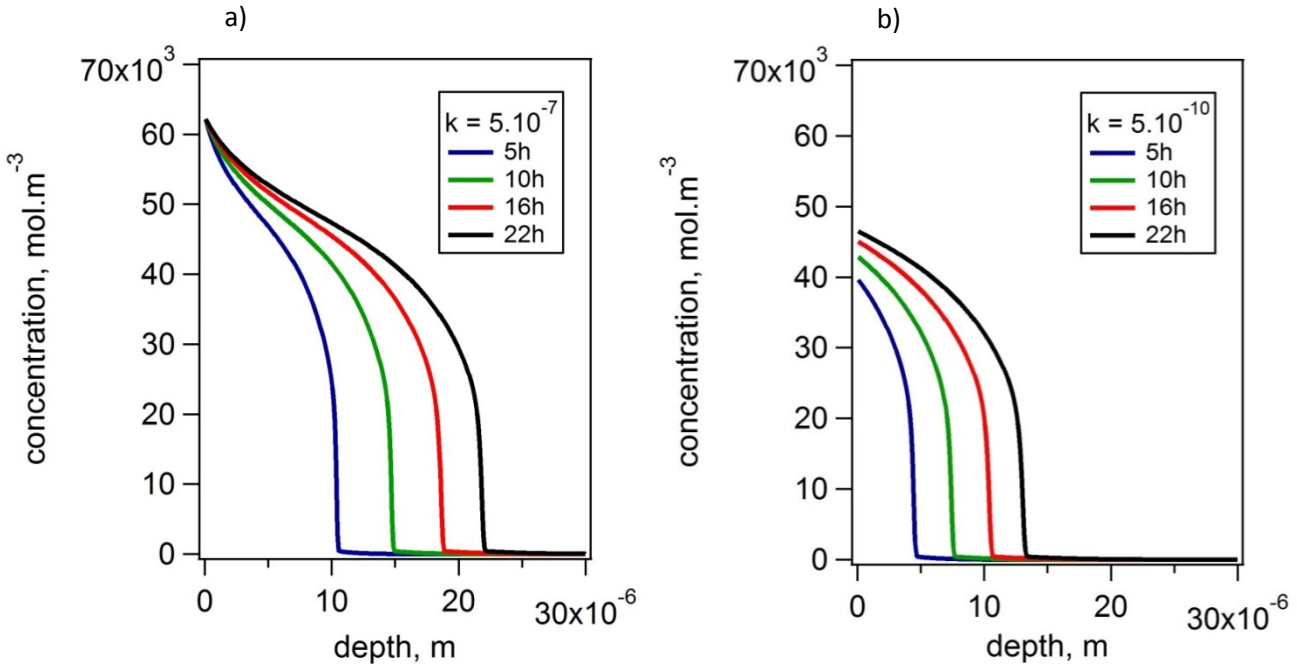

Figure 12 - Evolution of the concentration-depth profile with time for a) $k = 5 \cdot 10^{-7}$ and b) $k = 5 \cdot 10^{-10}$, for nitriding with a nitriding potential of 1000

The evolution of the concentration profile with time in Figure 12a shows that when the reaction rate constant of the surface reaction is k=5 10^{-7}, the same surface concentration is obtained for all times investigated. This indicates that local equilibrium of nitrogen in the gas phase and nitrogen in the solid phase is achieved at the surface. For the lower value of the reaction rate constant k=5 10^{-10}, shown in Figure 12b, the surface concentration increases gradually with nitriding time. In Figure 13 the concentration profiles obtained after nitriding for 22 h at 718 K are shown for various combinations of K_{CrN} and k. Examining the profiles in Figure 13 it is clearly seen that the surface concentration of nitrogen obtained after 22h decreases with a reduction of the reaction rate constant of the surface reaction. It is also observed that the incorporation of trapping and the value of K_{CrN} have an important influence on the total amount of nitrogen incorporated in the material. Stronger trapping leads to a lower amount of incorporated nitrogen and a steeper case-core transition.

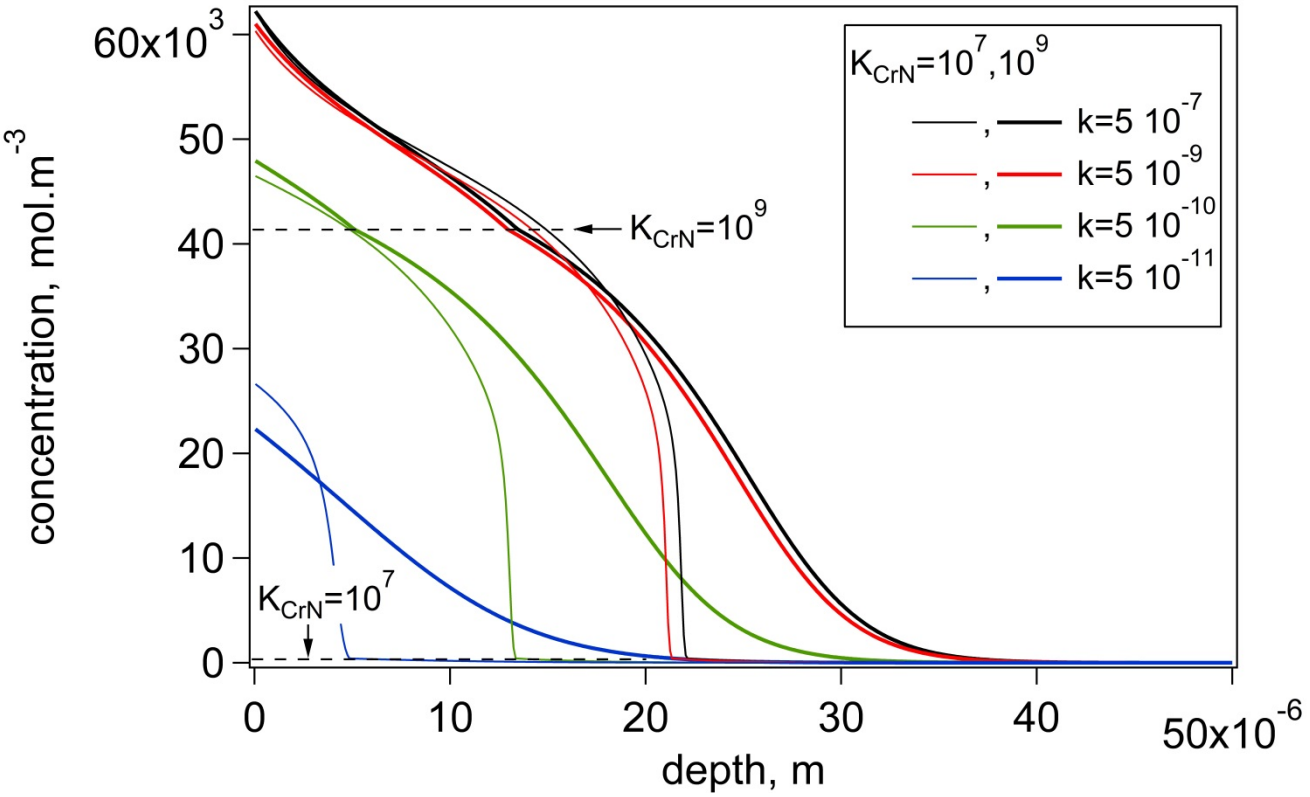

Figure 13 - Evolution of the surface concentration for various values of k, for $K_{CrN} = 10^7$ (thin lines) and $K_{CrN} = 10^9$ (thick lines) for nitriding of 22h at 718K.

6. Concentration-induced stresses

6.1 Calculation of concentration-induced stresses, assuming elasticity

The concentration induced stresses can be found from the chemical strain using mechanical equilibrium considerations as elaborated below.

6.1.1 Calculation of chemical strain

The strain arising from the expansion of the austenite lattice as caused by the dissolution of interstitial nitrogen, i.e. the chemical-induced strain, ε_{ij}^{ch}, is defined as

$$for\ i = j: \quad \varepsilon_{ij}^{ch}(c) = \frac{V(c)^{1/3} - V_{ref}^{1/3}}{V_{ref}^{1/3}} \tag{46}$$

$$for\ i \neq j: \quad \varepsilon_{ij}^{ch} = 0$$

where $V(c)$ is the concentration-dependent volume of (expanded) austenite per unitcell in m^3 and V_{ref} indicates the volume per unitcell of the interstitial-free lattice of austenite. A mathematical function of $V(c)$ was given in eq. 44 and a value for V_{ref} in eq. 45.

6.1.2 Calculation of stresses from strains

The total strain, ε_{ij}^{tot}, is given by [58]

$$\varepsilon_{ij}^{tot} = \varepsilon_{ij}^{mech} + \varepsilon_{ij}^{ch} + \varepsilon_{ij}^{th} \tag{47}$$

where ε_{ij}^{th} is the thermal strain and ε_{ij}^{mech} is the mechanical strain which is the sum of the elastic and plastic strain.

A simple description of the stress state in the surface can be found by applying a method equivalent to that of Hattel and Hansen [58] [59], with the following assumptions:

- The surface of the sample is homogeneous and can move freely: $\sigma_{33} = 0$ (σ_{33} is the stress normal to the surface).
- The stress state in the surface is rotationally symmetric, hence the normal stresses in the surface plane are equal $\sigma_{11} = \sigma_{22}$

- The specimen does not bend, hence uniform expansion at all depths: $\varepsilon_{11}^{tot} = \varepsilon_{22}^{tot}$ and $\varepsilon_{12}^{tot} = \varepsilon_{13}^{tot} = \varepsilon_{23}^{tot} = 0$, and thus $\sigma_{12} = \sigma_{13} = \sigma_{23} = 0$
- There are no temperature gradients in the sample, and no thermal strains.

For purely elastic stresses an equivalent to Hooke's generalized law where the chemical strain is added can be used

$$\sigma_{ij} = \frac{E}{1+\nu}\left(\varepsilon_{ij} + \frac{\nu}{1-2\nu}\delta_{ij}\varepsilon_{kk}\right) - \frac{E}{1-2\nu}\left(\varepsilon_{ij}^{th} + \varepsilon_{ij}^{ch}\right) \tag{48}$$

where E is Youngs modulus and ν is Poisson's ratio. The expression for σ_{33} becomes

$$\sigma_{33} = \frac{E}{1+\nu}\left(\varepsilon_{33}^{tot} + \frac{\nu}{1-2\nu}(\varepsilon_{11}^{tot} + \varepsilon_{22}^{tot} + \varepsilon_{33}^{tot})\right) - \frac{E}{1-2\nu}\left(\varepsilon_{33}^{th} + \varepsilon_{33}^{ch}\right) \tag{49}$$

With the assumptions $\sigma_{33} = 0$ and $\varepsilon_{22}^{tot} = \varepsilon_{11}^{tot}$ this gives

$$0 = \frac{E}{1+\nu}\left(\varepsilon_{33}^{tot} + \frac{\nu}{1-2\nu}(\varepsilon_{33}^{tot} + 2\varepsilon_{22}^{tot})\right) - \frac{E}{1-2\nu}\left(\varepsilon_{33}^{th} + \varepsilon_{33}^{ch}\right) \tag{50}$$

Isolating ε_{33} gives

$$\varepsilon_{33}^{tot} = \frac{1+\nu}{1-\nu}\left(\varepsilon_{33}^{th} + \varepsilon_{33}^{ch}\right) - \frac{2\nu}{1-\nu}\varepsilon_{22}^{tot} \tag{51}$$

$\sigma_{22} = \sigma_{11}$ can now be found as

$$\sigma_{22} = \frac{E}{1+\nu}\left(\varepsilon_{22}^{tot} + \frac{\nu}{1-2\nu}(\varepsilon_{11}^{tot} + \varepsilon_{22}^{tot} + \varepsilon_{33}^{tot})\right) - \frac{E}{1-2\nu}\left(\varepsilon_{22}^{th} + \varepsilon_{22}^{ch}\right) \tag{52}$$

applying $\varepsilon_{22}^{tot} = \varepsilon_{11}^{tot}$ it can be reduced to

$$\sigma_{22} = \frac{E}{(1+\nu)(1-2\nu)}\left(\nu\varepsilon_{33}^{tot} + \varepsilon_{22}^{tot} - (1+\nu)\left(\varepsilon_{22}^{th} + \varepsilon_{22}^{ch}\right)\right) \tag{53}$$

Inserting the expression for ε_{33}^{tot} (eq. 51) gives

$$\sigma_{22} = \frac{E}{(1+\nu)(1-2\nu)}\left(\nu\left(\frac{1+\nu}{1-\nu}\left(\varepsilon_{33}^{th}+\varepsilon_{33}^{ch}\right)-\frac{2\nu}{1-\nu}\varepsilon_{22}^{tot}\right)+\varepsilon_{22}^{tot} - (1+\nu)\left(\varepsilon_{22}^{th}+\varepsilon_{22}^{ch}\right)\right) \tag{54}$$

Using that $\varepsilon_{33}^{th} = \varepsilon_{22}^{th}$ and $\varepsilon_{33}^{ch} = \varepsilon_{22}^{ch}$ this can be reduced, as shown in Appendix B.1, to

$$\sigma_{22} = \frac{E}{1-\nu}\left(\varepsilon_{22}^{tot} - \varepsilon_{22}^{th} - \varepsilon_{22}^{ch}\right) \tag{55}$$

Assuming constant temperature and no thermal strains the expression reduces to

$$\sigma_{22}^{el} = \frac{E}{1-\nu}\left(\varepsilon_{22}^{tot} - \varepsilon_{22}^{ch}\right) \tag{56}$$

The total strain, ε_{22}^{tot}, can be found from considering mechanical equilibrium over the cross-section of the sample, which for the case that the stress state is mirror symmetrical with respect to the plane at half the sample thickness (total sample thickness is 2L)

$$\int_0^L \sigma_{22}^{el} dz = 0 \tag{57}$$

Inserting eq. 56 into eq. 57, and assuming that Young's modulus, E, and the Poisson ratio, ν, are independent of depth, yields

$$\frac{E}{1-\nu}\int_0^L \left(\varepsilon_{22}^{tot} - \varepsilon_{22}^{ch}\right) dz = 0 \tag{58}$$

Since it was assumed that $\varepsilon_{22}^{tot} = \varepsilon_{11}^{tot}$ is constant in space and varying in time this gives

$$\varepsilon_{22}^{tot} = \frac{1}{L}\int_0^L \left(\varepsilon_{22}^{ch}\right) dz \tag{59}$$

It is noted that a similar method was applied in [34][49][60], albeit that the total strain was taken equal to zero. This is a reasonable assumption, provided that the depth range where chemical strains apply is infinitely thin as compared to the depth range of the sample. This assumption simplifies the mathematical equations, resulting in the following equation for calculating the stress

$$\sigma_{22}^{el} = -\frac{E}{1-\nu}\varepsilon_{22}^{ch} \tag{60}$$

Tests to verify computational implementation of calculation for strains and stresses are shown in Appendix C.1 and C.2.

6.2 Composition induced stress profiles, calculated assuming elasticity

As the composition changes, the lattice expands and composition-induced strains is a result of this expansion of the lattice. From the relation between unitcell volume and nitrogen concentration given in eq. 44, the volumetric expansion of the lattice can be calculated, and from this the composition-induced strains introduced into the lattice can be calculated with eq. 46. As a first approach these strains are now assumed to be purely elastic and the elastic constants were assumed to be independent of the composition of austenite. Assuming an infinitely thick substrate, i.e. a total strain equal to zero, the composition-induced stresses were calculated with eq. 56 and are shown in Figure 14, for the composition profiles displayed in Figure 12. Comparing Figure 12 and Figure 14 it is seen that the elastic composition-induced compressive stress-depth profiles reflect the composition-depth profiles from which they were calculated. It is noted that the values of the stresses are five times as high as found experimentally with X-ray diffraction stress analysis [61]. The calculated stress values, assuming a purely elastic response, are unrealistically high and could never possibly be supported by the austenitic stainless steels under consideration.

Experimental observations of grain rotation and stacking fault generation shows that plastic deformation occurs as a result of nitriding of austenitic stainless steel [25][28][29][30]. The above assumption of pure elasticity is thus not valid, and applying this assumption gives an overestimation of the composition-induced stress.

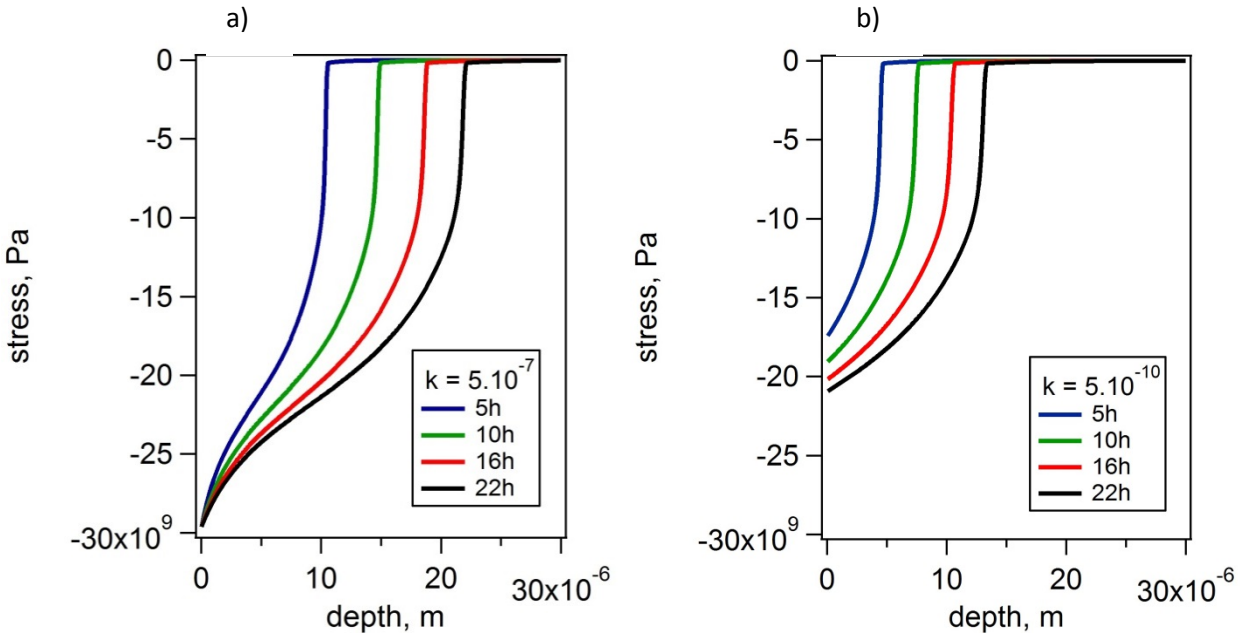

Figure 14 - Compressive composition-induced stress for an infinitely thick substrate, elastic accommodation of the volume expansion and K_{CrN}=10^7 and k=5 10^{-7}(a) and k=5 10^{-10} (b) for several diffusion times. The corresponding nitrogen concentration-depth profiles are given in Figs. 12a and 4b, respectively.

6.2.1 Effect of sample thickness on predicted stress depth profile

Above semi-infinite samples were assumed, and the total strain was assumed to be equal to zero. This is however only a valid assumption if the depth range where the chemical strain apply, is infinitely thin compared to the depth range of the sample. Thus the effect of sample thickness is now addressed in this section. The effect of the sample thickness on the stress distribution as calculated with eqs. 56-57 is shown in Figure 15 for several sample thicknesses, 2L. Only for relatively thin samples are there substantial tensile stresses present in the core to compensate for the high compressive stresses in the case. So since the stresses in the case are hugely overestimated by the assumption of pure elasticity, these results indicate that for most practical situations the tensile stresses in the core can be neglected.

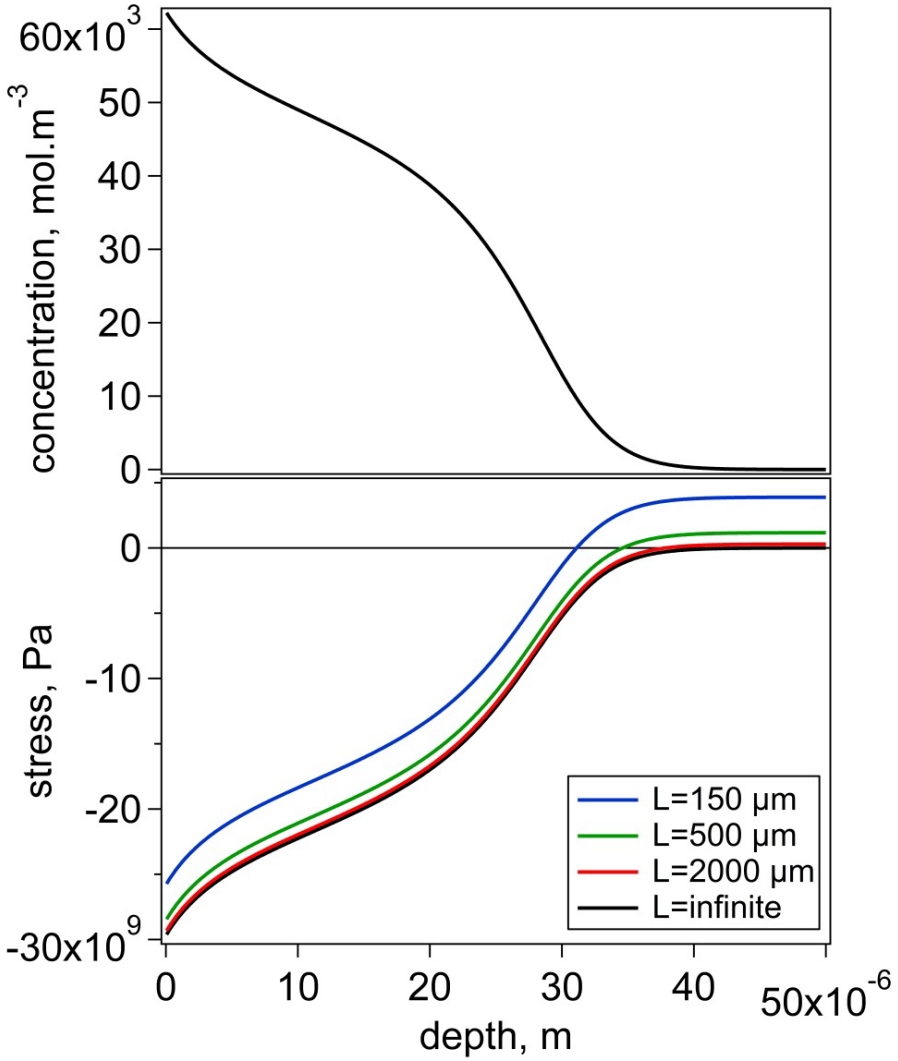

Figure 15 - Effect of thickness of the sample on the predicted stress profile, for 22h nitriding with a nitriding potential of 1000, k= $5 \cdot 10^{-7}$ and no trapping

7. Interaction of elastic stresses and concentration

7.1 Computational modelling of concentration profiles with stress influence at constant temperature

Including influence of stress on concentration flux, but assuming constant temperature, the expression for the concentration flux given by eq. 20, becomes

$$J_N = -\frac{D_N c_N}{RT}\left(\frac{RT}{K_N}\frac{\partial K_N}{\partial c_N}\frac{\partial c_N}{\partial z} - V_N\frac{\partial \sigma_H}{\partial z}\right) \tag{61}$$

Accordingly, the generalized form of Fick's 2nd law is

$$\frac{\partial c_N}{\partial t} = -\frac{\partial}{\partial z}\left(-D_N^{(c)}.\frac{\partial c_N}{\partial z} + \frac{D_N.c_N}{RT}.V_N.\frac{\partial \sigma_H}{\partial z}\right) \tag{62}$$

where $D_N^{(c)}$ represents the concentration dependence of the diffusion coefficient of nitrogen, including the thermodynamic factor $\left(\frac{c_N}{K_N}\frac{\partial K_N}{\partial c_N}\right)$. When $D_N^{(c)}$ is a known explicit function of the concentration, eq. 62 can be rewritten to

$$\frac{\partial c_N}{\partial t} = -\frac{\partial}{\partial z}\left(-D_N^{(c)}.\frac{\partial c_N}{\partial z} + \frac{D_N^{(c)}}{\frac{\partial K_N}{\partial c_N}}.\frac{K_N}{RT}.V_N.\frac{\partial \sigma_H}{\partial z}\right) \tag{63}$$

and then the differentiation gives

$$\frac{\partial c_N}{\partial t} = \frac{\partial D_N^{(c)}}{\partial c_N}\cdot\left(\frac{\partial c_N}{\partial z}\right)^2 + D_N^{(c)}\cdot\frac{\partial^2 c_N}{\partial z^2} - \frac{\partial}{\partial z}\left(D_N^{(c)}\cdot\frac{K_N}{\frac{\partial K_N}{\partial c_N}}\right)\cdot\frac{V_N}{RT}\frac{\partial \sigma_H}{\partial z} - D_N^{(c)} \cdot\left(\frac{K_N}{\frac{\partial K_N}{\partial c_N}}\frac{V_N}{RT}\frac{\partial^2 \sigma_H}{\partial z^2}\right) \tag{64}$$

Discretizing done using the central explicit finite difference method gives

$$\frac{c_i^{t+\Delta t}-c_i^t}{\Delta t}=\frac{\partial D_N^{(c_i^t)}}{\partial c}\left(\frac{c_{i+1}^t-c_{i-1}^t}{2\Delta z}\right)^2+D_N^{(c_i^t)}\cdot\frac{c_{i+1}^t-2c_i^t+c_{i-1}^t}{\Delta z^2}$$
$$-\frac{\left(D_N^{(c_{i+1}^t)}\cdot\frac{K_{N_{i+1}}}{\frac{\partial K_{N_{i+1}}}{\partial c_N}}-D_N^{(c_{i-1}^t)}\cdot\frac{K_{N_{i-1}}}{\frac{\partial K_{N_{i-1}}}{\partial c_N}}\right)}{2\Delta z}\frac{{\sigma_H}_{i+1}^t-{\sigma_H}_{i-1}^t}{2\Delta z}$$
$$-D_N^{(c_i^t)}\left(\frac{K_{N_i}}{\frac{\partial K_{N_i}}{\partial c_N}}\frac{V_N}{RT}\frac{{\sigma_H}_{i+1}^t-2{\sigma_H}_i^t+{\sigma_H}_{i-1}^t}{\Delta z^2}\right) \tag{65}$$

The continuity equation at the surface to balance the fluxes of nitrogen atoms arriving at and leaving from the surface cell to calculate the actual surface concentration of nitrogen, described by eq. 24, is discretized as

$$\frac{c_i^{t+\Delta t}-c_i^t}{\Delta t}=-\frac{J_{i\to i+1}-J_{surf}}{\Delta z} \tag{66}$$

Combining eq. 66 with the expression for J_{surf}, given in eq. 3, and the expression for the flux, in eq. 61, the nitrogen concentration in the surface cell follows from

$$\frac{c_i^{t+\Delta t}-c_i^t}{\Delta t}=D_N^{(c_i^t)}\frac{c_{i+1}^t-c_i^t}{{\Delta z_i}^2}-D_N^{(c_i^t)}\frac{K_{N_i}}{\frac{\partial K_{N_i}}{\partial c_N}}\frac{V_N}{RT}\frac{{\sigma_H}_{i+1}^t-{\sigma_H}_i^t}{{\Delta z_i}^2}+\frac{k}{\Delta z_i}\cdot\left(c_{eq}-c_i^t\right) \tag{67}$$

The computational sequence is illustrated by a flowchart in Figure 16.

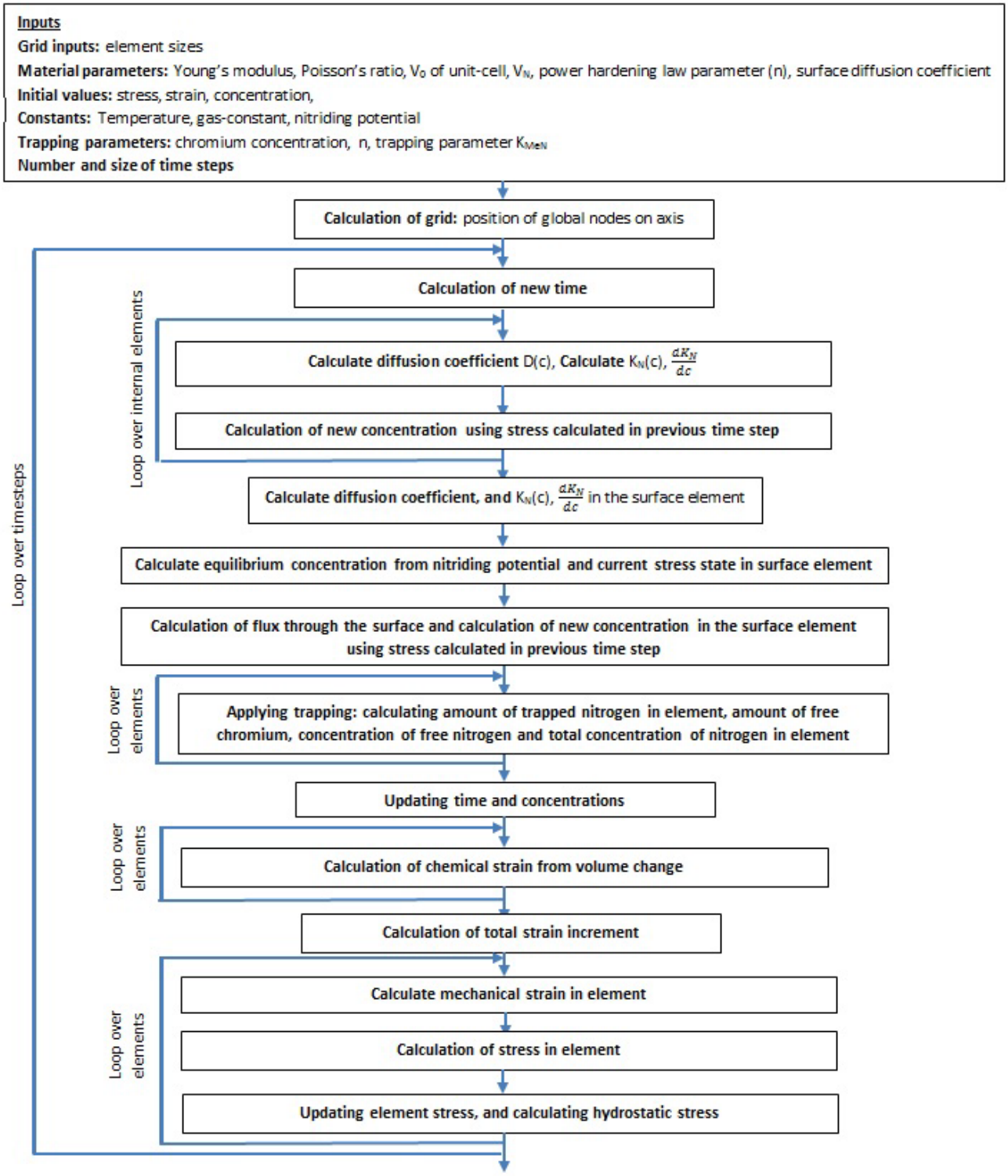

Figure 16 - Computational flowchart for calculation of concentration and stress-depth profiles, assuming purely elastic stresses

7.2 Stress effect on diffusion

7.2.1 Effect of composition induced stress profile on internal diffusion

The presence of a gradient in the composition-induced stress is equivalent to an additional driving force for the diffusion of nitrogen, see for example eq. 21. Since the composition-induced stress is a compressive stress decreasing with depth, (Figure 14), it implies a positive additional driving force for diffusion.

It should be noted that it is the stress changes with depth that increases the diffusion, not the level of stress. Adding a constant level of stress does not change the internal diffusion.

The effect of a stress-gradient induced driving force on the diffusion, when keeping the surface concentration constant, is demonstrated in Figure 17 for 22h nitriding at 718 K at K_N=1000. The lines obtained without considering an effect of the stress on the internal diffusion are reproduced from Figure 12a and Figure 14a. From Figure 17 it can be seen that for the extremely huge composition-induced stresses, predicted assuming purely elasticity, the driving force resulting from the stress-gradient results in a concentration profile that reaches about 3.5 times as deep as when the effect of the stress gradient on diffusion was not considered. This shows a potentially substantial contribution of stress-induced diffusion, albeit for the hugely overestimated stress.

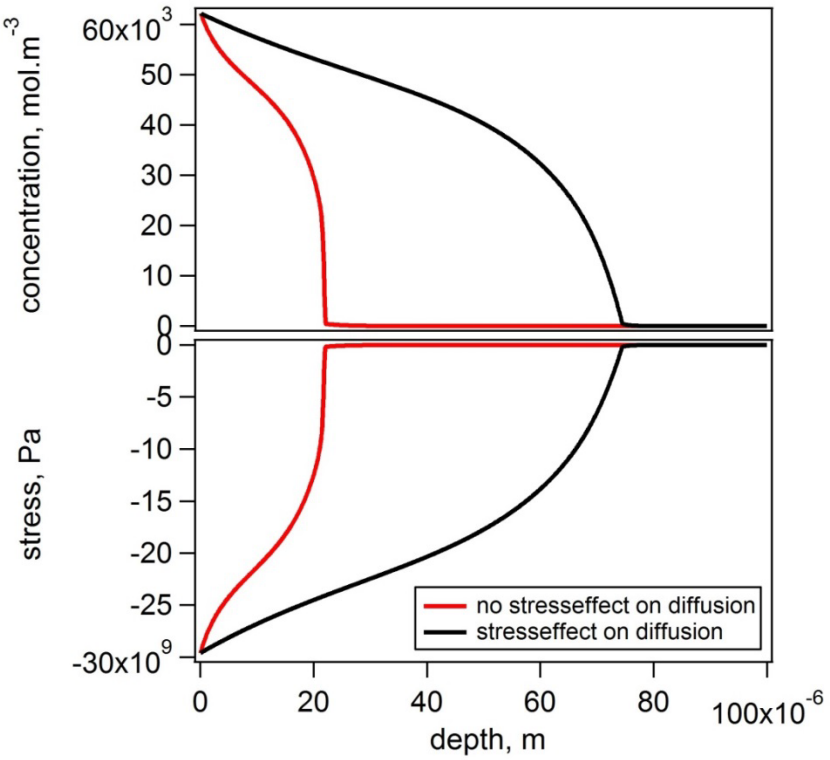

Figure 17 – Effect of taking into account stress on predicted concentration-depth profiles and stress-depth profiles for nitriding of 316 austenitic stainless steel after 22 hours at 445°C using a nitriding potential of 1000, K_{CrN}=10^7 and k=5 10^{-7}

7.3 Stress effect on surface

It was established in section 7.2 that the level of stress does not influence the internal diffusion, only the stress *gradient* does. However, compressive stress reduces the solubility of nitrogen in austenite under equilibrium conditions. This will be most clearly manifested by a reduction of the nitrogen concentration at the surface, which is the interface between the solid and gaseous phase, where local equilibrium is attempted to be imposed.

7.3.1 Influence of stress on the equilibrium concentration

The nitrogen content that can be dissolved in equilibrium with a chemical potential as imposed by a gas phase of known composition depends on the state of stress of the solid, as expressed by eq. 13. Consequently, the value of c_N^{eq}, i.e. the nitrogen content in the solid in equilibrium with the gas phase, decreases with the invoked compressive stress in the surface element. At its turn the flux of nitrogen through the surface as given by eq. 3 is affected as is the actual surface concentration. The concentration of nitrogen in a stressed solid in equilibrium with nitrogen in a gas of known composition follows from equating the chemical potentials of nitrogen in solid and in gas:

$$\mu^{gas} = \mu^{\sigma} \tag{68}$$

The chemical potentials in the solid with and without stress (σ=*0*) are given by

$$\mu^{\sigma=0} = \mu_0 + RT\ln(a) \tag{69}$$

$$\mu^{\sigma} = \mu_0 + RT\ln(a) - V_N\sigma_H$$

Hence, comparing the chemical potential in a stressed and a stress-free solid in equilibrium with the same gas leads to

$$\mu_0 + RTln(a^{\sigma}) - V_N\sigma_H = \mu_0 + RT\ln(a^{\sigma=0}) \tag{70}$$

$$\rightarrow a^{\sigma} = a^{\sigma=0} \cdot \exp\left(\frac{V_N\sigma_H}{RT}\right)$$

Inserting $a_N = K_T K_N$ and realizing that K_T depends on pressure, while K_N is independent of pressure, it follows

$$K_T{}^{\sigma} = K_T{}^{\sigma=0} \cdot \exp\left(\frac{V_N\sigma_H}{RT}\right) \tag{71}$$

The relation between the nitrogen concentration and the nitriding potential for a stressed solid follows from inserting eq. 71 for K_T in the relation between nitriding potential and concentration, which was given in Appendix A3 eq.A29,

$$K_N = 0.01125 \cdot \frac{c}{{K_T}^{\sigma=0} \cdot \exp\left(\frac{V_N \sigma_H}{RT}\right)} + \frac{102.5078}{{K_T}^{\sigma=0} \cdot \exp\left(\frac{V_N \sigma_H}{RT}\right)} \cdot \exp(0.0005129336 \cdot c_N - 24.60384) \tag{72}$$

Since the equation is non-linear and cannot be inverted analytically, the way to calculate the equilibrium concentration is by iteration. In this work Newton-Rhapson iterations was applied.

The dependence of the surface concentration on the hydrostatic component of the compressive stress is given in Figure 18, for stainless steel AISI 316 at 718 K and selected values of the nitriding potential[2], using eq. 72. From Figure 18 it is evident that the nitrogen solubility is very sensitive to the level of stress. Since a lower equilibrium concentration leads to a lower maximum flux through the surface, this indicates that a compressive stress resulting from the chemical strain reduces the nitrogen flux through the surface.

This means, that even though the level of stress does not affect the internal diffusion, it does affect the flux through the surface. So even though a stress profile with higher compressive stresses at the surface compared to the centre increases the internal diffusion, it also decreases the flux through the surface.

[2] The nitriding potential is proportional to the activity, and thus the chemical potential, of nitrogen in the gas phase (see Appendix A.3).

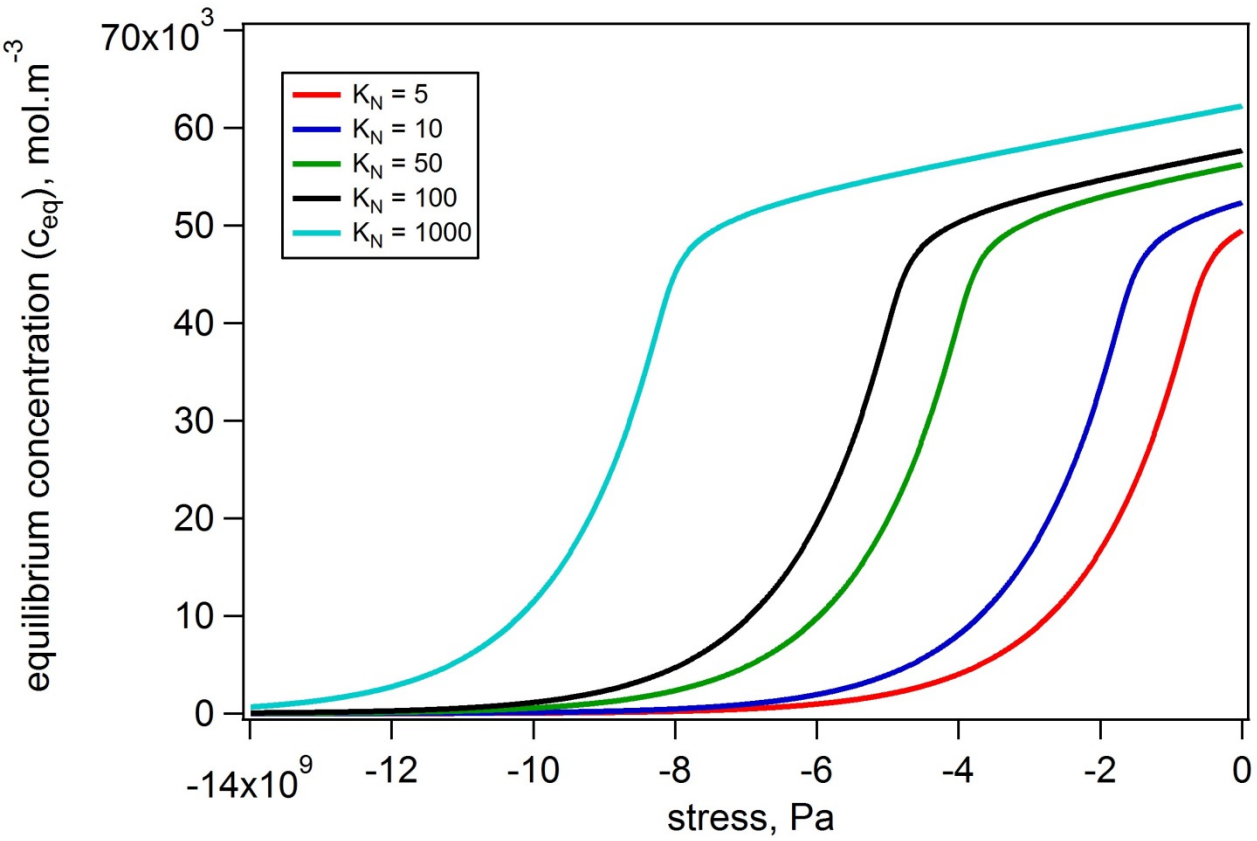

Figure 18 - Equilibrium concentrations as function of surface stress for varying nitriding potentials, K_N, (Note that negative values of stress denotes compressive stress)

7.3.2 Predicted concentration and stress-profiles when taking into account stress effect on surface

Implementing the effect of compressive stress on the local equilibrium at the surface, combined with the additional stress-induced driving force for diffusion, leads to the predicted concentration depth profile and stress-depth profile shown in Figure 19. Figure 19 also shows the profiles produced without considering an effect of the stress level on the surface flux (reproduced from Figure 17). Comparing the two profiles a reduction by about a factor 2 in the local nitrogen concentration is seen when the effect of stress on the surface concentration is taken into account. Nevertheless, the effect of a compressive stress gradient causes a penetration depth of the profile beyond the depth achieved without including the contribution of stress-induced diffusion, (see Figure 17) despite the substantially smaller chemical contribution to the driving force for diffusion.

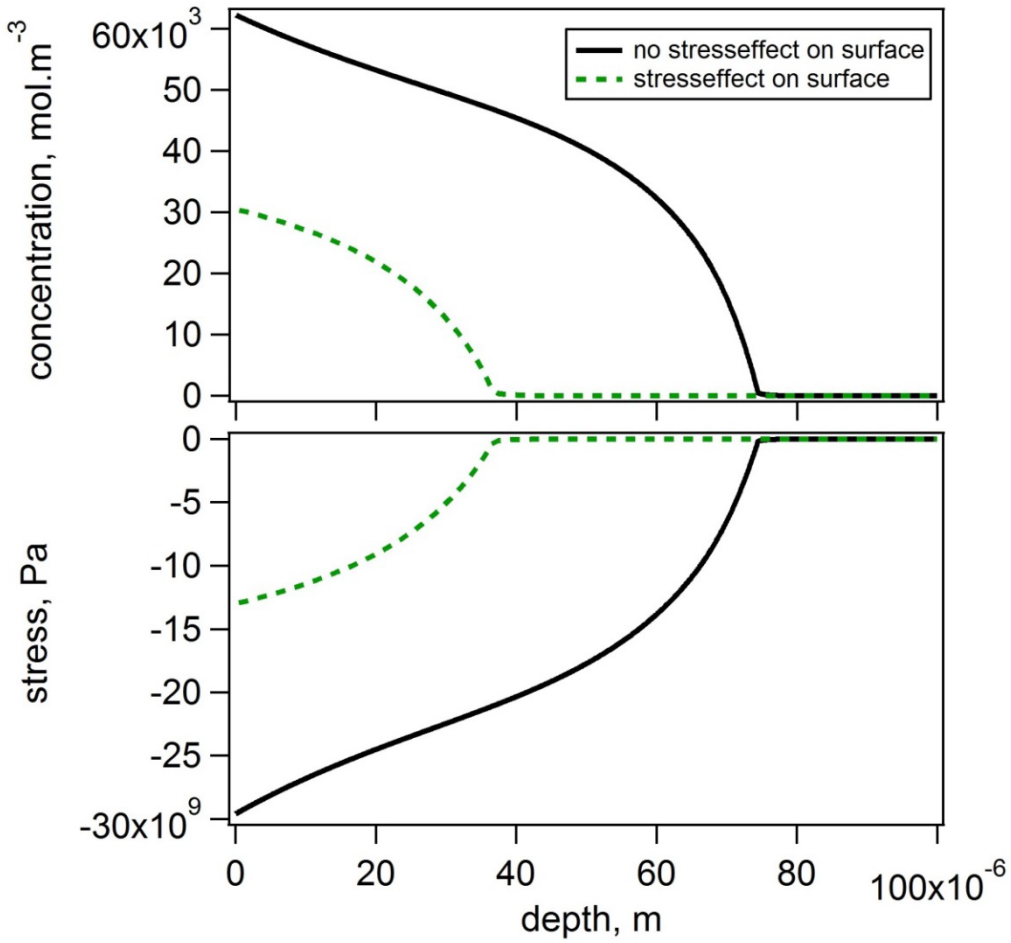

Figure 19 - Predicted concentration-depth profile and stress-depth profile for nitriding of 316 austenitic stainless steel after 22 hours at 445°C using a nitriding potential of 1000 K_{CrN}=10^7 and k=5 10^{-7}

8. Plasticity

As discussed in section 1.3, plastic deformation has been observed after nitriding, and since the stresses predicted assuming elasticity in section 7, are in the order of 13GPa, which is much higher than the yield stress of austenite, the assumption of pure elasticity is not very good for the case of nitriding. Thus the effect of taking into account plasticity in the model is investigated below.

8.1 Calculation of elastic-plastic stresses

For elastic-plastic stresses the stresses cannot be calculated directly, as was done for elasticity, since the stress depends on the path. Thus the incremental method is used. Where the relation between the incremental stress $\dot{\sigma}_{ij}$ and the incremental strain $\dot{\varepsilon}_{kl}$ is

$$\dot{\sigma}_{ij} = L_{ijkl}\dot{\varepsilon}_{kl} \tag{73}$$

where L_{ijkl} is the incremental stiffness tensor which is given according to J_2-flow theory [62] by

$$L_{ijkl} = \frac{E}{1+\nu}\left[\frac{1}{2}\left(\delta_{ik}\delta_{jl} + \delta_{il}\delta_{jk}\right) + \frac{\nu}{1-2\nu}\delta_{ij}\delta_{kl} - \beta\frac{3}{2}\frac{E/E_t - 1}{E/E_t - (1-2\nu)/3}\frac{s_{ij}s_{kl}}{\sigma_e^2}\right] \tag{74}$$

where E is Young's modulus, E_t is the tangent modulus, ν is Poisson's ratio and δ_{ij} is Kronecker's delta (which is =1 if i=j, and =0 if i≠j) and β = 0 for elastic unloading and β = 1 if there is plastic flow.

s_{ij} is the stress deviator tensor, which is given by [62]

$$s_{ij} = \sigma_{ij} - \delta_{ij}\frac{\sigma_{kk}}{3} \tag{75}$$

and the effective von Mises stress is given by [62]

$$\sigma_e^2 = \frac{3}{2}s_{ij}s_{ij} \tag{76}$$

If the Mises stress calculated in an element, i, exceeds the maximum Mises stress from previous increments, it is set to be the new maximum Mises stress:

$$if\ \sigma_e\ \geq\ \sigma_{e,max(i)}\ then\ \sigma_{e(i)} =\ \sigma_{e,max(i)} \tag{77}$$

The Mises stress increment $\dot{\sigma}_e$ is found from the incremental stresses in the element, i ($\dot{\sigma}_{kl}^{i}$) [62]:

$$\dot{\sigma}_e = \frac{3 \cdot s_{kl}^i \cdot \dot{\sigma}_{kl}^i}{2 \cdot \sigma_{e(i)}} \tag{78}$$

The β values, in eq. 74, can now be determined from the J_2 flow theory criteria [62]:

$$\begin{gathered} for\ \sigma_e = \sigma_{e,max}\ and\ \dot{\sigma}_e \geq 0 \quad \beta = 1 \\ if\ \sigma_e < \sigma_{e,max}\ or\ \dot{\sigma}_e < 0 \quad \beta = 0 \end{gathered} \tag{79}$$

Since β depends on the stresses it is used to calculate, the modelling made in this work is made so the program uses the β calculated in the previous step to determine the stresses in the next step. This means that a small overshoot will occur at the time of changing from elasticity to plasticity, but using sufficiently small increments it is tiny.

The tangent modulus is found using a power hardening law [62], which states that

$$for\ \sigma > \sigma_y, \varepsilon = \frac{\sigma_y}{E}\left(\frac{\sigma}{\sigma_y}\right)^n \tag{80}$$

Since $\frac{1}{E_t} = \frac{d\varepsilon}{d\sigma}$ this means that, applying this power hardening law, the tangent modulus (E_t) used in eq. 74 is given by:

$$E_t = \frac{E}{n}\left(\frac{\sigma_y}{\sigma_e}\right)^{n-1} \tag{81}$$

The new stress is found by adding the incremental stress to the stress from the previous step

$$\sigma_{ij} = \sigma_{ij} + \dot{\sigma}_{ij} \tag{82}$$

Applying the assumptions similar to the purely elastic case, using the equivalent method as Hattel and Hansen [58] [59], gives the following assumptions:

- Since the surface of the nitride specimen is free $\sigma_{33} = 0$,
- Since there is symmetry, the stresses in the surface plane are equal $\sigma_{11} = \sigma_{22}$
- Assuming no bending of the specimen, and hence uniform expansion through the material gives $\varepsilon_{11}^{tot} = \varepsilon_{22}^{tot}$ constant in space and varying in time, $\varepsilon_{12}^{tot} = \varepsilon_{13}^{tot} = \varepsilon_{23}^{tot} = 0$, and thus $\sigma_{12} = \sigma_{13} = \sigma_{23} = 0$

for no shear stresses, this gives

$$s_{11} = \sigma_{11} - \frac{\sigma_{11} + \sigma_{22} + \sigma_{33}}{3}$$

$$s_{22} = \sigma_{22} - \frac{\sigma_{11} + \sigma_{22} + \sigma_{33}}{3} \tag{83}$$

$$s_{33} = \sigma_{33} - \frac{\sigma_{11} + \sigma_{22} + \sigma_{33}}{3}$$

and then

$$\sigma_e^2 = \frac{3}{2}({s_{11}}^2 + {s_{22}}^2 + {s_{33}}^2) \tag{84}$$

Having no shear strains then gives

$$\dot{\sigma}_{11} = L_{1111}\dot{\varepsilon}_{11} + L_{1122}\dot{\varepsilon}_{22} + L_{1133}\dot{\varepsilon}_{33}$$

$$\dot{\sigma}_{22} = L_{2211}\dot{\varepsilon}_{11} + L_{2222}\dot{\varepsilon}_{22} + L_{2233}\dot{\varepsilon}_{33} \tag{85}$$

$$\dot{\sigma}_{33} = L_{3311}\dot{\varepsilon}_{11} + L_{3322}\dot{\varepsilon}_{22} + L_{3333}\dot{\varepsilon}_{33}$$

where

$$L_{1111} = \frac{E}{1+\nu}\left[\frac{1}{2}(\delta_{11}\delta_{11} + \delta_{11}\delta_{11}) + \frac{\nu}{1-2\nu}\delta_{11}\delta_{11} - \beta\frac{3}{2}\frac{E/E_t - 1}{E/E_t - (1-2\nu)/3}\frac{s_{11}s_{11}}{\sigma_e^2}\right] \tag{86}$$

$$= \frac{E}{1+\nu}\left[1 + \frac{\nu}{1-2\nu} - \beta\frac{3}{2}\frac{E/E_t - 1}{E/E_t - (1-2\nu)/3}\frac{s_{11}s_{11}}{\sigma_e^2}\right]$$

and

$$L_{1122} = \frac{E}{1+\nu}\left[\frac{1}{2}(\delta_{12}\delta_{12} + \delta_{12}\delta_{12}) + \frac{\nu}{1-2\nu}\delta_{11}\delta_{22} - \beta\frac{3}{2}\frac{E/E_t - 1}{E/E_t - (1-2\nu)/3}\frac{s_{11}s_{22}}{\sigma_e^2}\right] \tag{87}$$

$$= \frac{E}{1+\nu}\left[\frac{\nu}{1-2\nu} - \beta\frac{3}{2}\frac{E/E_t - 1}{E/E_t - (1-2\nu)/3}\frac{s_{11}s_{22}}{\sigma_e^2}\right]$$

and similar for the other incremental stiffness tensors, giving

$$\dot{\sigma}_{11} = \frac{E}{1+\nu}\left[1 + \frac{\nu}{1-2\nu} - \beta\frac{3}{2}\frac{E/E_t - 1}{E/E_t - (1-2\nu)/3}\frac{s_{11}s_{11}}{\sigma_e^2}\right]\dot{\varepsilon}_{11} + \frac{E}{1+\nu}\left[\frac{\nu}{1-2\nu} - \beta\frac{3}{2}\frac{E/E_t - 1}{E/E_t - (1-2\nu)/3}\frac{s_{11}s_{22}}{\sigma_e^2}\right]\dot{\varepsilon}_{22} + \frac{E}{1+\nu}\left[\frac{\nu}{1-2\nu} - \beta\frac{3}{2}\frac{E/E_t - 1}{E/E_t - (1-2\nu)/3}\frac{s_{11}s_{33}}{\sigma_e^2}\right]\dot{\varepsilon}_{33} \tag{88}$$

$$\dot{\sigma}_{22} = \frac{E}{1+\nu}\left[\frac{\nu}{1-2\nu} - \beta\frac{3}{2}\frac{E/E_t - 1}{E/E_t - (1-2\nu)/3}\frac{s_{22}s_{11}}{\sigma_e^2}\right]\dot{\varepsilon}_{11} + \frac{E}{1+\nu}\left[1 + \frac{\nu}{1-2\nu} - \beta\frac{3}{2}\frac{E/E_t - 1}{E/E_t - (1-2\nu)/3}\frac{s_{22}s_{22}}{\sigma_e^2}\right]\dot{\varepsilon}_{22} + \frac{E}{1+\nu}\left[\frac{\nu}{1-2\nu} - \beta\frac{3}{2}\frac{E/E_t - 1}{E/E_t - (1-2\nu)/3}\frac{s_{22}s_{33}}{\sigma_e^2}\right]\dot{\varepsilon}_{33} \tag{89}$$

$$\dot{\sigma}_{33} = \frac{E}{1+\nu}\left[\frac{\nu}{1-2\nu} - \beta\frac{3}{2}\frac{E/E_t - 1}{E/E_t - (1-2\nu)/3}\frac{s_{33}s_{11}}{\sigma_e^2}\right]\dot{\varepsilon}_{11} + \frac{E}{1+\nu}\left[\frac{\nu}{1-2\nu} - \beta\frac{3}{2}\frac{E/E_t - 1}{E/E_t - (1-2\nu)/3}\frac{s_{33}s_{22}}{\sigma_e^2}\right]\dot{\varepsilon}_{22} + \frac{E}{1+\nu}\left[1 + \frac{\nu}{1-2\nu} - \beta\frac{3}{2}\frac{E/E_t - 1}{E/E_t - (1-2\nu)/3}\frac{s_{33}s_{33}}{\sigma_e^2}\right]\dot{\varepsilon}_{33} \tag{90}$$

Since $\sigma_{11} = \sigma_{22}$ and $\varepsilon_{11} = \varepsilon_{22}$ then $\dot{\sigma}_{11} = \dot{\sigma}_{22}$ and $\dot{\varepsilon}_{11} = \dot{\varepsilon}_{22}$, at a given coordinate x_3 (depth) and since $\sigma_{33} = 0$ this gives

$$s_{11} = s_{22} = \frac{\sigma_{22}}{3} \tag{91}$$

$$s_{33} = -\frac{2\sigma_{22}}{3} \tag{92}$$

and having no shear stresses

$$\sigma_e^2 = \frac{3}{2}({s_{11}}^2 + {s_{22}}^2 + {s_{33}}^2) = \frac{3}{2}\left(\frac{{\sigma_{22}}^2}{9} + \frac{{\sigma_{22}}^2}{9} + 4\frac{{\sigma_{22}}^2}{9}\right) = {\sigma_{22}}^2 \tag{93}$$

The Mises stress increment is then

$$\dot{\sigma}_e = \frac{3(s_{11}\dot{\sigma}_{11} + s_{22}\dot{\sigma}_{22} + s_{33}\dot{\sigma}_{33})}{2 \cdot \sigma_e} = \frac{3\left(\frac{\sigma_{22}}{3}\dot{\sigma}_{22} + \frac{\sigma_{22}}{3}\dot{\sigma}_{22} - \frac{2\sigma_{22}}{3} \cdot 0\right)}{2 \cdot |\sigma_{22}|} \tag{94}$$

So if $\sigma_{22} > 0$

$$\dot{\sigma}_e = \dot{\sigma}_{22} \tag{95}$$

And if $\sigma_{22} < 0$

$$\dot{\sigma}_e = -\dot{\sigma}_{22} \tag{96}$$

Since $\varepsilon_{11} = \varepsilon_{22}$ then $\dot{\varepsilon}_{11} = \dot{\varepsilon}_{22}$ and then the expression for the incremental stress tensors can be reduced to

$$\begin{aligned}\dot{\sigma}_{11} = \dot{\sigma}_{22} = {} & \frac{E}{1+\nu}\left[\frac{\nu}{1-2\nu} - \beta\frac{1}{6}\frac{E/E_t - 1}{E/E_t - (1-2\nu)/3}\right]\dot{\varepsilon}_{22} \\ & + \frac{E}{1+\nu}\left[1 + \frac{\nu}{1-2\nu} - \beta\frac{1}{6}\frac{E/E_t - 1}{E/E_t - (1-2\nu)/3}\right]\dot{\varepsilon}_{22} \\ & + \frac{E}{1+\nu}\left[\frac{\nu}{1-2\nu} + \beta\frac{1}{3}\frac{E/E_t - 1}{E/E_t - (1-2\nu)/3}\right]\dot{\varepsilon}_{33}\end{aligned} \tag{97}$$

$$\begin{aligned}\dot{\sigma}_{33} = {} & \frac{E}{1+\nu}\left[\frac{\nu}{1-2\nu} - \beta\frac{3}{2}\frac{\frac{E}{E_t} - 1}{\frac{E}{E_t} - \frac{(1-2\nu)}{3}}\frac{-2}{9}\right]\dot{\varepsilon}_{22} \\ & + \frac{E}{1+\nu}\left[\frac{\nu}{1-2\nu} - \beta\frac{3}{2}\frac{E/E_t - 1}{E/E_t - (1-2\nu)/3}\frac{-2}{9}\right]\dot{\varepsilon}_{22} \\ & + \frac{E}{1+\nu}\left[1 + \frac{\nu}{1-2\nu} - \beta\frac{3}{2}\frac{E/E_t - 1}{E/E_t - (1-2\nu)/3}\frac{4}{9}\right]\dot{\varepsilon}_{33}\end{aligned} \tag{98}$$

Because of the free surface $\sigma_{33} = 0$ at all times thus $\dot{\sigma}_{33} = 0$ giving

$$\begin{aligned}0 = {} & \frac{E}{1+\nu}\left[\frac{\nu}{1-2\nu} - \beta\frac{3}{2}\frac{E/E_t - 1}{E/E_t - (1-2\nu)/3}\frac{-2}{9}\right]\dot{\varepsilon}_{22} \\ & + \frac{E}{1+\nu}\left[\frac{\nu}{1-2\nu} - \beta\frac{3}{2}\frac{E/E_t - 1}{E/E_t - (1-2\nu)/3}\frac{-2}{9}\right]\dot{\varepsilon}_{22} \\ & + \frac{E}{1+\nu}\left[1 + \frac{\nu}{1-2\nu} - \beta\frac{3}{2}\frac{E/E_t - 1}{E/E_t - (1-2\nu)/3}\frac{4}{9}\right]\dot{\varepsilon}_{33}\end{aligned} \tag{99}$$

Restructuring gives an expression for $\dot{\varepsilon}_{33}$ as function of $\dot{\varepsilon}_{22}$

$$\dot{\varepsilon}_{33} = -\frac{\left[2\frac{\nu}{1-2\nu} + \beta\frac{2}{3}\frac{E/E_t - 1}{E/E_t - (1-2\nu)/3}\right]}{\left[1 + \frac{\nu}{1-2\nu} - \beta\frac{2}{3}\frac{E/E_t - 1}{E/E_t - (1-2\nu)/3}\right]}\dot{\varepsilon}_{22} \tag{100}$$

In case of plasticity $\beta = 1$ and then

$$\begin{aligned}\dot{\sigma}_{11} = \dot{\sigma}_{22} = {} & \frac{E}{1+\nu}\left[\frac{\nu}{1-2\nu} - \frac{1}{6}\frac{E/E_t - 1}{E/E_t - (1-2\nu)/3}\right]\dot{\varepsilon}_{22} \\ & + \frac{E}{1+\nu}\left[1 + \frac{\nu}{1-2\nu} - \frac{1}{6}\frac{E/E_t - 1}{E/E_t - (1-2\nu)/3}\right]\dot{\varepsilon}_{22} \\ & + \frac{E}{1+\nu}\left[\frac{\nu}{1-2\nu} + \frac{1}{3}\frac{E/E_t - 1}{E/E_t - (1-2\nu)/3}\right]\dot{\varepsilon}_{33}\end{aligned} \tag{101}$$

And in case of no plasticity then $\beta = 0$ giving

$$\dot{\varepsilon}_{33} = -\frac{\left[2\frac{\nu}{1-2\nu}\right]}{\left[1 + \frac{\nu}{1-2\nu}\right]} = \frac{-2\nu}{1-\nu}\dot{\varepsilon}_{22} \tag{102}$$

Inserting these expressions (eq. 100 and 102) in the expression for the in-plane incremental stress tensors (eq. 97) gives

for plastic yielding

$$\begin{aligned}\dot{\sigma}_{11} = \dot{\sigma}_{22} = \frac{E}{1+\nu}\Bigg(& \left[1 + 2\frac{\nu}{1-2\nu} - \frac{1}{3}\frac{E/E_t - 1}{E/E_t - (1-2\nu)/3}\right] \\ & + \frac{-2\left[\frac{\nu}{1-2\nu} + \frac{1}{3}\frac{E/E_t - 1}{E/E_t - (1-2\nu)/3}\right]^2}{\left[1 + \frac{\nu}{1-2\nu} - \frac{2}{3}\frac{E/E_t - 1}{E/E_t - (1-2\nu)/3}\right]}\Bigg)\dot{\varepsilon}_{22}\end{aligned} \tag{103}$$

and for elasticity and elastic unloading

$$\begin{aligned}\dot{\sigma}_{11} = \dot{\sigma}_{22} = {} & \frac{E}{1+\nu}\left[\frac{\nu}{1-2\nu}\right]\dot{\varepsilon}_{22} + \frac{E}{1+\nu}\left[1 + \frac{\nu}{1-2\nu}\right]\dot{\varepsilon}_{22} + \frac{E}{1+\nu}\left[\frac{\nu}{1-2\nu}\right]\frac{-2\nu}{1-\nu}\dot{\varepsilon}_{22} \\ = {} & E\dot{\varepsilon}_{22}\left(\frac{1-\nu-2\nu\nu}{1-2\nu \quad 1+\nu \quad 1-\nu}\right) = \frac{E}{1-\nu}\dot{\varepsilon}_{22}\end{aligned} \tag{104}$$

which is the same result for the stress increment as found for the total stress using Hooke's law in section 6.1.

The increment strain $\dot{\varepsilon}_{22}$ as a function of depth can be found using equilibrium of the stress $\dot{\sigma}_{22}$ over the cross-section from the surface to the depth z_{max}

$$\int_0^{z_{max}} \dot{\sigma}_{22} dz = 0 \tag{105}$$

Inserting the expression for $\dot{\sigma}_{22}$ considering there might be both an elastic and a plastic region, and assuming that the Young's modulus, tangent modulus (an average value is used in the programming) and Poisson's ratio is constant with depth gives

$$\begin{aligned} \frac{E}{1+\nu}\Bigg(&\left[1+2\frac{\nu}{1-2\nu}-\frac{1}{3}\frac{E/E_t-1}{E/E_t-(1-2\nu)/3}\right] \\ &+\frac{-2\left[\frac{\nu}{1-2\nu}+\frac{1}{3}\frac{E/E_t-1}{E/E_t-(1-2\nu)/3}\right]^2}{\left[1+\frac{\nu}{1-2\nu}-\frac{2}{3}\frac{E/E_t-1}{E/E_t-(1-2\nu)/3}\right]}\Bigg)\int_0^{z_{max,plastic}} \dot{\varepsilon}_{22} dz \\ &+\frac{E}{1-\nu}\int_{z_{max,plastic}}^{z_{max}} \dot{\varepsilon}_{22} dz = 0 \end{aligned} \tag{106}$$

The mechanical strain increment $\dot{\varepsilon}_{22}$ was equal to $\dot{\varepsilon}_{22}^{tot} - \dot{\varepsilon}_{22}^{th} - \dot{\varepsilon}_{22}^{ch}$

$$\begin{aligned} \frac{E}{1+\nu}\Bigg(&\left[1+2\frac{\nu}{1-2\nu}-\frac{1}{3}\frac{E/E_t-1}{E/E_t-(1-2\nu)/3}\right] \\ &+\frac{-2\left[\frac{\nu}{1-2\nu}+\frac{1}{3}\frac{E/E_t-1}{E/E_t-(1-2\nu)/3}\right]^2}{\left[1+\frac{\nu}{1-2\nu}-\frac{2}{3}\frac{E/E_t-1}{E/E_t-(1-2\nu)/3}\right]}\Bigg)\int_0^{z_{max,plastic}} \left(\dot{\varepsilon}_{22}^{tot} - \dot{\varepsilon}_{22}^{th}\right. \\ &\left.- \dot{\varepsilon}_{22}^{ch}\right) dz + \frac{E}{1-\nu}\int_{z_{max,plastic}}^{z_{max}} \left(\dot{\varepsilon}_{22}^{tot} - \dot{\varepsilon}_{22}^{th} - \dot{\varepsilon}_{22}^{ch}\right) dz = 0 \end{aligned} \tag{107}$$

The total strain can now be determined. Since it was assumed that $\dot{\varepsilon}_{22}^{tot}$ is constant in space and varying in time this gives

$$\dot{\varepsilon}_{22}^{tot}\left[\frac{E}{1+\nu}\left(\left[1+2\frac{\nu}{1-2\nu}-\frac{1}{3}\frac{E/E_t-1}{E/E_t-(1-2\nu)/3}\right]\right.\right. \tag{108}$$

$$\left.\left.+\frac{-2\left[\frac{\nu}{1-2\nu}+\frac{1}{3}\frac{E/E_t-1}{E/E_t-(1-2\nu)/3}\right]^2}{\left[1+\frac{\nu}{1-2\nu}-\frac{2}{3}\frac{E/E_t-1}{E/E_t-(1-2\nu)/3}\right]}\right)\int_0^{z_{max,plastic}}dz+\frac{E}{1-\nu}\int_{z_{max,plastic}}^{z_{max}}dz\right]$$

$$=\frac{E}{1+\nu}\left(\left[1+2\frac{\nu}{1-2\nu}-\frac{1}{3}\frac{E/E_t-1}{E/E_t-(1-2\nu)/3}\right]\right.$$

$$\left.+\frac{-2\left[\frac{\nu}{1-2\nu}+\frac{1}{3}\frac{E/E_t-1}{E/E_t-(1-2\nu)/3}\right]^2}{\left[1+\frac{\nu}{1-2\nu}-\frac{2}{3}\frac{E/E_t-1}{E/E_t-(1-2\nu)/3}\right]}\right)\int_0^{z_{max,plastic}}\left(\dot{\varepsilon}_{22}^{th}+\dot{\varepsilon}_{22}^{ch}\right)dz$$

$$+\frac{E}{1-\nu}\int_{z_{max,plastic}}^{z_{max}}\left(\dot{\varepsilon}_{22}^{th}+\dot{\varepsilon}_{22}^{ch}\right)dz$$

$$\leftrightarrow$$

$$\dot{\varepsilon}_{22}^{tot} = \left[\frac{E}{1+\nu} \left(\left[1 + 2\frac{\nu}{1-2\nu} - \frac{1}{3}\frac{\frac{E}{E_t}-1}{\frac{E}{E_t}-\frac{(1-2\nu)}{3}} \right] + \frac{-2\left[\frac{\nu}{1-2\nu} + \frac{1}{3}\frac{\frac{E}{E_t}-1}{\frac{E}{E_t}-\frac{(1-2\nu)}{3}} \right]^2}{\left[1 + \frac{\nu}{1-2\nu} - \frac{2}{3}\frac{\frac{E}{E_t}-1}{\frac{E}{E_t}-\frac{(1-2\nu)}{3}} \right]} \right) \int_0^{z_{max,plastic}} \left(\dot{\varepsilon}_{22}^{th} + \dot{\varepsilon}_{22}^{ch} \right) dz + \frac{E}{1-\nu} \int_{z_{max,plastic}}^{z_{max}} \left(\dot{\varepsilon}_{22}^{th} + \dot{\varepsilon}_{22}^{ch} \right) dz \right] / \left[\frac{E}{1+\nu} \left(\left[1 + 2\frac{\nu}{1-2\nu} - \frac{1}{3}\frac{\frac{E}{E_t}-1}{\frac{E}{E_t}-\frac{(1-2\nu)}{3}} \right] + \frac{-2\left[\frac{\nu}{1-2\nu} + \frac{1}{3}\frac{\frac{E}{E_t}-1}{\frac{E}{E_t}-\frac{(1-2\nu)}{3}} \right]^2}{\left[1 + \frac{\nu}{1-2\nu} - \frac{2}{3}\frac{\frac{E}{E_t}-1}{\frac{E}{E_t}-\frac{(1-2\nu)}{3}} \right]} \right) z_{max,plastic} + \frac{E}{1-\nu}\left(z_{max} - z_{max,plastic} \right) \right] \tag{109}$$

where $\int_0^{z_{max,plastic}}\left(\dot{\varepsilon}_{22}^{th}+\dot{\varepsilon}_{22}^{ch}\right)dz$ and $\int_{z_{max,plastic}}^{z_{max}}\left(\dot{\varepsilon}_{22}^{th}+\dot{\varepsilon}_{22}^{ch}\right)dz$ can be calculated using finite difference discretization as $\sum_1^{i_{max,plastic}}\left[\dot{\varepsilon}_{22}^{th}(i)\cdot\Delta z(i)+\dot{\varepsilon}_{22}^{ch}(i)\cdot\Delta z(i)\right]$ and $\sum_{i_{max,plastic}}^{imax}\left[\dot{\varepsilon}_{22}^{th}(i)\cdot\Delta z(i)+\dot{\varepsilon}_{22}^{ch}(i)\cdot\Delta z(i)\right]$ respectively.

Computational sequence of the calculations when including plasticity is illustrated by a flowchart in Figure 20.

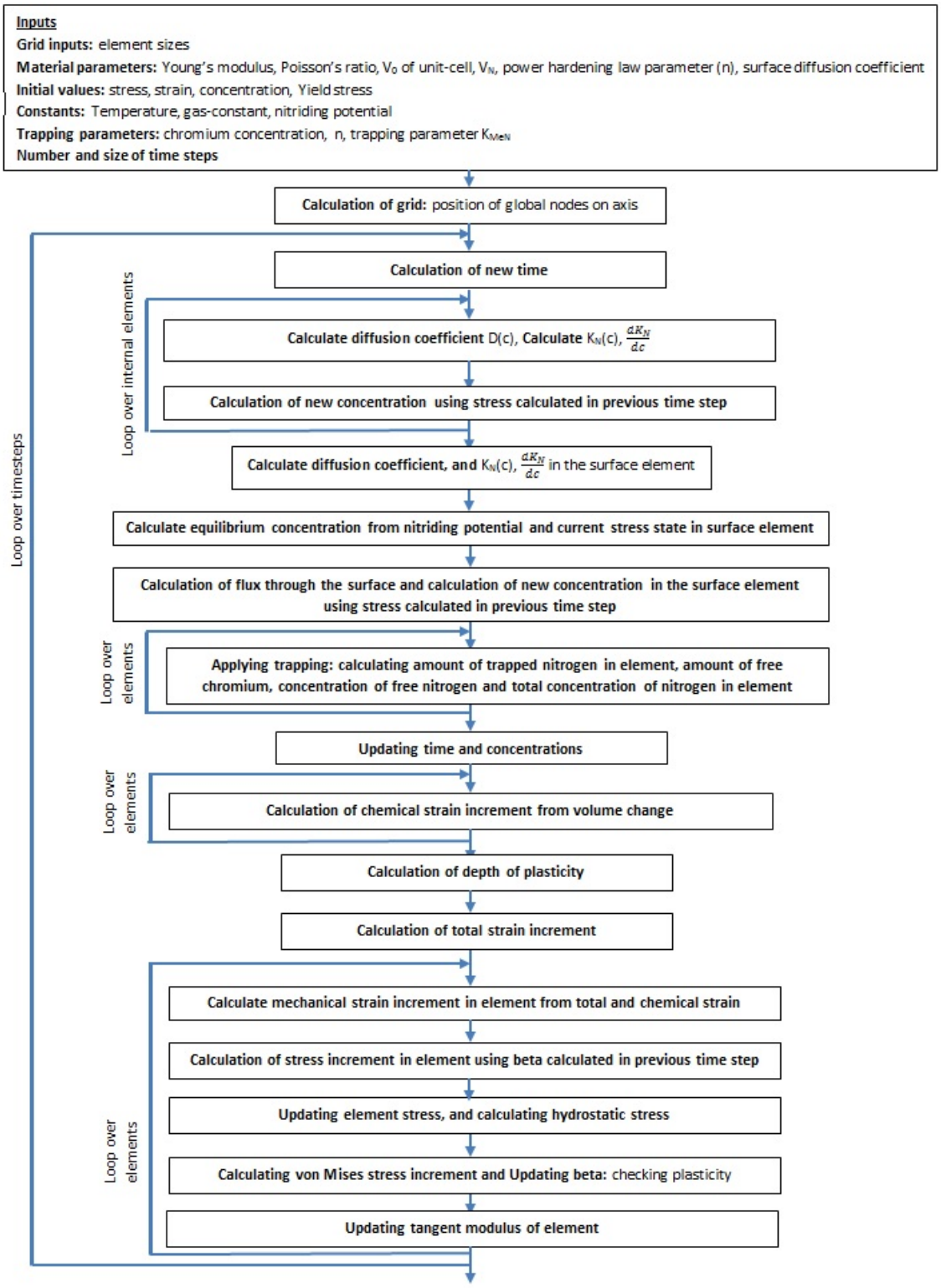

Figure 20 - Flowchart of computational sequence for calculating concentration and stress-depth profiles, when stresses are calculating with elasto-plasticity and constant yield stress

8.2 Effect on predicted concentration and stress profiles of plasticity

The difference between the predicted concentration- and stress-depth profiles calculated when assuming purely elasticity and when incorporating plasticity are displayed in Figure 21. For plasticity, a constant yield strength of 290MPa equal to the yield strength of 316 austenitic stainless steel at room temperature [63] was applied.

Comparison of the profiles shows that when plasticity is taken into account, the stress level in the expanded austenite zone is very low as compared to when assuming purely elasticity; as was expected. Consequently, for the case of plasticity with constant yield stress, the nitrogen surface concentration and the diffusive flux in the expanded austenite would be largely unaffected by the stress and thus a composition-depth profile reminiscent of that for no stress is obtained (cf. Figure 17).

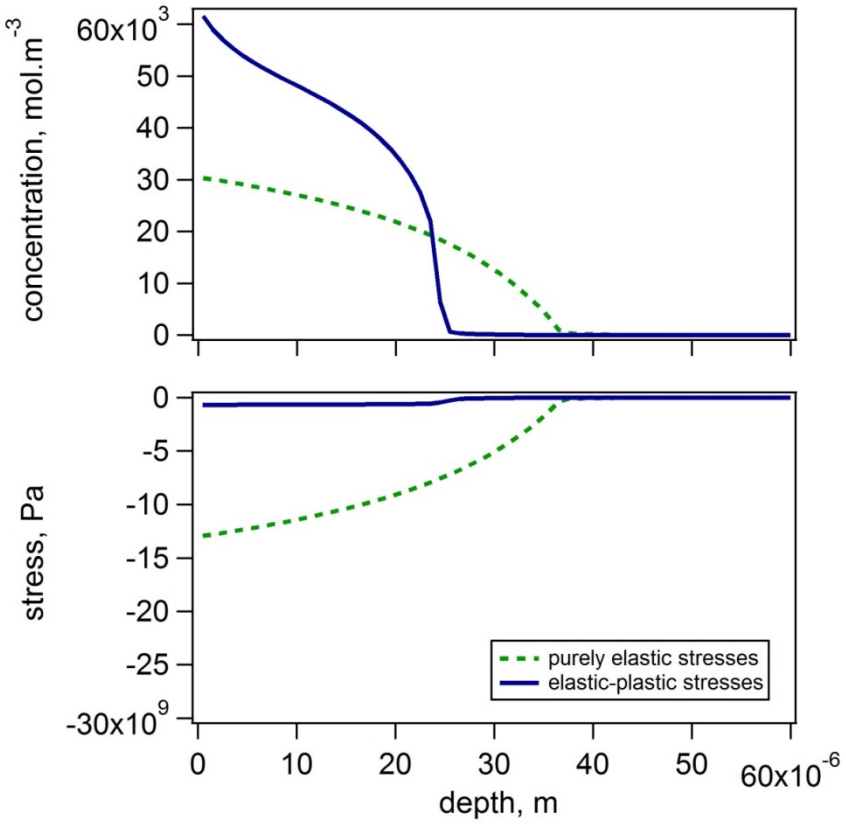

Figure 21 - Simulated concentration-depth profiles and stress-depth profiles using purely elastic accommodation of the lattice expansion or elastic-plastic accommodation using the const. yield stress of the austenitic material.

9. Concentration dependence of mechanical properties

9.1 Determination of concentration dependence of yield stress from experimental data

The relation between the yield stress and nitrogen content for austenitic stainless steel is not precisely known, particularly not for the high nitrogen contents of relevance for expanded austenite. Bottoli, et al. [64] investigated two qualities of austenitic stainless steel deformed to various degrees of equivalent strain, and found that the hardness (HV) and yield stress (σ_y) obey the following relation:

$$\sigma_y[\text{in MPa}] = -396 + 3.73 \cdot \text{HV} \tag{110}$$

Realizing that hardness and yield stress both are a measure for the resistance against plastic deformation, it is attempted to obtain an estimate for the concentration dependence of the yield stress from the hardness. Correlating hardness-depth and concentration-depth profiles for nitrided AISI 316 austenitic stainless steel from [65] and converting hardness into yield stress with eq. 110, the dependence displayed in Figure 22 was obtained. Obviously, the yield stress increases with the concentration until a point where a plateau is reached where the yield stress is independent on the concentration. Taking the yield stress of nitrogen free austenite as 290 MPa, a linear fit through the region (c<14796) where a steep increase in yield stress occurs, results in:

$$\sigma_y[\text{in MPa}] = 0.2424 \cdot c + 290 \tag{111}$$

For the plateau the average value is $\sigma_y = 3848\ \text{MPa}$, which is more than 10 times higher than the yield stress of the base material.

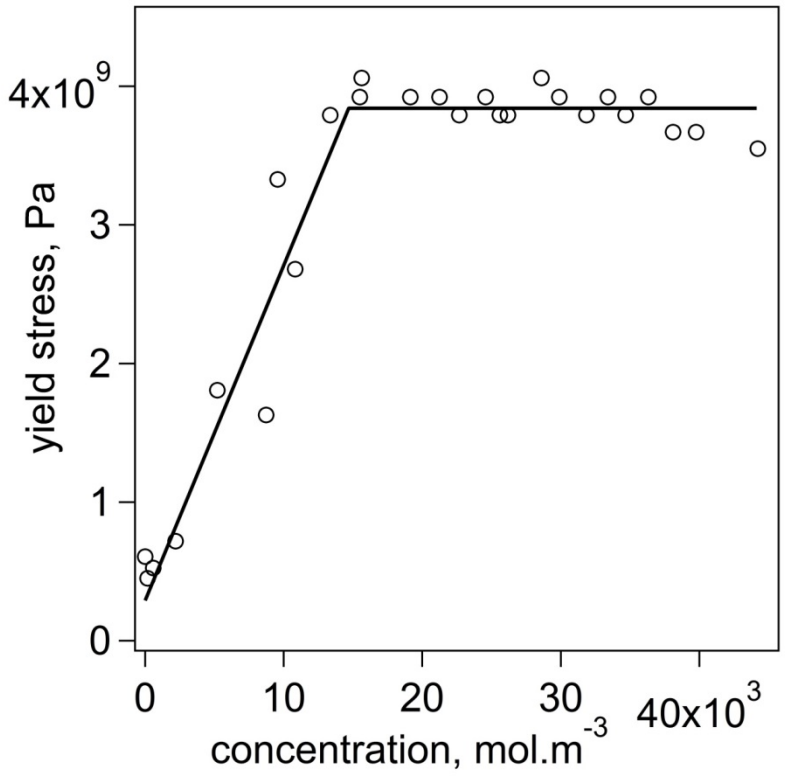

Figure 22 – Data and fit for relation between yield stress and nitrogen concentration for AISI 316 stainless steel

9.2 Plasticity criterion for non-constant yield strength

9.2.1 Basics for plasticity criterion for varying yield stress

For a mechanically sound solution, the plasticity criterion has to be calculated taking a non-constant yield stress into account.

The effect of yield stress temperature dependence on the plasticity criterion, was described by Hattel [58] and the concentration dependence can be treated similarly, as explained below.

The Von Mises stress was defined by eq. 76

$$\sigma_e^2 = \frac{3}{2} s_{ij} s_{ij} \tag{112}$$

and the yield stress is now assumed to be isotropic hardening and dependent on concentration and temperature

$$\sigma_Y(\varepsilon^{pl}, c, T) \tag{113}$$

The yield function is then defined as

$$f = \sigma_e^2 - \sigma_Y^2 = 0 \tag{114}$$

The elastic and plastic states are defined from the yield function as follows

$$\begin{aligned} f < 0 \quad & \text{elastic state} \\ f = 0 \quad & \text{plastic state} \end{aligned} \tag{115}$$

Note that the yield function cannot be larger than zero, since a stress state where the stress exceeds the current yield stress is impossible.

The associated flow rule states that the plastic strain rate is a function of the load parameter $\dot{\lambda}$ and the direction of the yield surface normal.

$$\dot{\varepsilon}_{ij}^{pl} = \dot{\lambda} \frac{\partial f}{\partial \sigma_{ij}} \tag{116}$$

According to Drucker's postulate, this direction is the outward normal to the yield surface, so using the Von Mises yield function

$$\frac{\partial f}{\partial \sigma_{ij}} = s_{ij} \tag{117}$$

Giving the following expression for the plastic strain rate, known as the Prandtl-Reuss expression:

$$\dot{\varepsilon}_{ij}^{pl} = \dot{\lambda} s_{ij} \tag{118}$$

The above is also the basis for the theory for constant yield stress, the difference comes from the consistency condition [58], that enforces the solution to stay on the yield surface in a plastic load increment:

$$\dot{f} = \frac{\partial f}{\partial s_{ij}} \dot{s}_{ij} + \left.\frac{\partial f}{\partial \varepsilon_e^{pl}}\right|_{T,c} \dot{\varepsilon}_e^{pl} + \left.\frac{\partial f}{\partial T}\right|_{\varepsilon_e^{pl},c} \dot{T} = 0 \tag{119}$$

where there is now an effect on the yield stress of the temperature to take into account.

$\dot{\varepsilon}_e^{pl}$ is the equivalent plastic strain increment, which can be calculated by

$$d\varepsilon_e^{pl} = \sqrt{\frac{2}{3} d\varepsilon_{ij}^{pl} d\varepsilon_{ij}^{pl}} \tag{120}$$

With no shear strains this gives

$$\dot{\varepsilon}_e^{pl} = \sqrt{\frac{2}{3}\left(\dot{\varepsilon}_{11}^{pl}\dot{\varepsilon}_{11}^{pl} + \dot{\varepsilon}_{22}^{pl}\dot{\varepsilon}_{22}^{pl} + \dot{\varepsilon}_{33}^{pl}\dot{\varepsilon}_{33}^{pl}\right)} \tag{121}$$

For the case where $\sigma_{11} = \sigma_{22}$ and $\sigma_{33} = 0$ this reduces to

$$\dot{\varepsilon}_e^{pl} = 2\dot{\varepsilon}_{22}^{pl} \tag{122}$$

9.2.3 Effect of concentration on consistency condition

When considering the consistency condition when there is an effect of concentration on yield stress, it is incorporated similarly to the effect of the temperature (see eq.119) giving

$$\dot{f} = \frac{\partial f}{\partial s_{ij}}\dot{s}_{ij} + \left.\frac{\partial f}{\partial \varepsilon_e^{pl}}\right|_{T,c} \dot{\varepsilon}_e^{pl} + \left.\frac{\partial f}{\partial T}\right|_{\varepsilon_e^{pl},c} \dot{T} + \left.\frac{\partial f}{\partial c}\right|_{\varepsilon_e^{pl},T} \dot{c} = 0 \tag{123}$$

The differentials can then be calculated from the yield function (eq. 114) as [58]

$$\frac{\partial f}{\partial s_{ij}}\dot{s}_{ij} = \frac{\partial(\sigma_e^2 - \sigma_Y^2)}{\partial s_{ij}}\dot{s}_{ij} = \left(\frac{\partial\left(\frac{3}{2}s_{ij}s_{ij}\right)}{\partial s_{ij}} + \frac{\partial(-\sigma_Y^2)}{\partial s_{ij}}\right)\dot{s}_{ij} = \left(3s_{ij} + 0\right)\dot{s}_{ij} = 3s_{ij}\dot{s}_{ij} \tag{124}$$

$$\left.\frac{\partial f}{\partial \varepsilon_e^{pl}}\right|_{T,c} \dot{\varepsilon}_e^{pl} = \left(\frac{\partial \sigma_e^2}{\partial \varepsilon_e^{pl}} + \frac{\partial(-\sigma_Y^2)}{\partial \varepsilon_e^{pl}}\right)\dot{\varepsilon}_e^{pl} = \left(0 + \frac{\partial(-\sigma_Y^2)}{\partial \sigma_Y}\frac{\partial \sigma_Y}{\partial \varepsilon_e^{pl}}\right)\dot{\varepsilon}_e^{pl} = -2\sigma_Y\frac{\partial \sigma_Y}{\partial \varepsilon_e^{pl}}\dot{\varepsilon}_e^{pl} \tag{125}$$

$$\left.\frac{\partial f}{\partial T}\right|_{\varepsilon_e^{pl},c} \dot{T} = \left(\frac{\partial \sigma_e^2}{\partial T} + \frac{\partial(-\sigma_Y^2)}{\partial T}\right)\dot{T} = \left(0 + \frac{\partial(-\sigma_Y^2)}{\partial \sigma_Y}\frac{\partial \sigma_Y}{\partial T}\right)\dot{T} = -2\sigma_Y\frac{\partial \sigma_Y}{\partial T}\dot{T} \tag{126}$$

$$\left.\frac{\partial f}{\partial c}\right|_{\varepsilon_e^{pl},T} \dot{c} = \left(\frac{\partial \sigma_e^2}{\partial c} + \frac{\partial(-\sigma_Y^2)}{\partial c}\right)\dot{c} = \left(0 + \frac{\partial(-\sigma_Y^2)}{\partial \sigma_Y}\frac{\partial \sigma_Y}{\partial c}\right)\dot{c} = -2\sigma_Y\frac{\partial \sigma_Y}{\partial c}\dot{c} \tag{127}$$

Inserting these in eq. 123 gives

$$\dot{f} = 3s_{ij}\dot{s}_{ij} - 2\sigma_Y\left.\frac{\partial \sigma_Y}{\partial \varepsilon_e^{pl}}\right|_{T,c} \dot{\varepsilon}_e^{pl} - 2\sigma_Y\frac{\partial \sigma_Y}{\partial T}\dot{T} - 2\sigma_Y\frac{\partial \sigma_Y}{\partial c}\dot{c} = 0 \tag{128}$$

The yield stress is affected both by the stress state, the temperature and the concentration, and thus the incremental change of yield stress is given by

$$\dot{\sigma}_Y = \left.\frac{\partial \sigma_Y}{\partial \varepsilon_e^{pl}}\right|_{T,c} \dot{\varepsilon}_e^{pl} + \left.\frac{\partial \sigma_Y}{\partial T}\right|_{\varepsilon_e^{pl},c} \dot{T} + \left.\frac{\partial \sigma_Y}{\partial c}\right|_{\varepsilon_e^{pl},T} \dot{c} \tag{129}$$

For constant temperature and concentration we simply get

$$\dot{\sigma}_Y = \left.\frac{\partial \sigma_Y}{\partial \varepsilon_e^{pl}}\right|_{T,c} \dot{\varepsilon}_e^{pl} \tag{130}$$

For constant temperature and concentration, the equivalent plastic strain increment can be related to the yields stress increment by [58]

$$\dot{\varepsilon}_e^{pl} = \frac{1}{E_T}\dot{\sigma}_Y - \frac{1}{E}\dot{\sigma}_Y \tag{131}$$

Rearranging gives

$$\frac{\dot{\varepsilon}_e^{pl}}{\dot{\sigma}_Y} = \frac{1}{E_T} - \frac{1}{E} \tag{132}$$

Inserting eq. 132 in eq. 130 and rearranging gives

$$\left.\frac{\partial \sigma_Y}{\partial \varepsilon_e^{pl}}\right|_{T,c} = \frac{\dot{\sigma}_Y}{\dot{\varepsilon}_e^{pl}} = \frac{1}{\left(\frac{1}{E_T} - \frac{1}{E}\right)} \tag{133}$$

Inserting this in the consistency condition as expressed in eq. 128 gives

$$\dot{f} = 3 s_{ij}\dot{s}_{ij} - 2\sigma_Y \left(\frac{1}{\left(\frac{1}{E_T} - \frac{1}{E}\right)} \dot{\varepsilon}_e^{pl} + \frac{\partial \sigma_Y}{\partial T}\dot{T} + \frac{\partial \sigma_Y}{\partial c}\dot{c} \right) = 0 \tag{134}$$

From the definition of s_{ij}, given in eq. 75, follows that

$$\dot{s}_{ij} = \dot{\sigma}_{ij} - \delta_{ij}\frac{\dot{\sigma}_{kk}}{3} \tag{135}$$

This means that

$$3s_{ij}\dot{s}_{ij} = 3s_{ij}\dot{\sigma}_{ij} - 3\delta_{ij}s_{ij}\frac{\dot{\sigma}_{kk}}{3} \tag{136}$$

Since the first invariant is equal to zero [62]

$$J_1 = s_{kk} = \delta_{ij}s_{ij} = 0 \tag{137}$$

this gives

$$3s_{ij}\dot{s}_{ij} = 3s_{ij}\dot{\sigma}_{ij} \tag{138}$$

Inserting this in the expression for the consistency condition, eq. 134, gives

$$\dot{f} = 3s_{ij}\dot{\sigma}_{ij} - 2\sigma_Y\left(\frac{1}{\left(\frac{1}{E_T} - \frac{1}{E}\right)}\dot{\varepsilon}_e^{pl} + \frac{\partial\sigma_Y}{\partial T}\dot{T} + \frac{\partial\sigma_Y}{\partial c}\dot{c}\right) = 0 \tag{139}$$

9.2.4 Derivation of load parameter

Using this form of the consistency condition an expression for the load parameter $\dot{\lambda}$ can be derived from the case of a uniaxial tensile testing similarly to what was described for temperature dependence in [58].

For the uniaxial tensile test the following applies

$$\sigma_{11} = \sigma_Y$$
$$\sigma_{22} = \sigma_{33} = 0 \tag{140}$$

and thus

$$s_{11} = \frac{2}{3}\sigma_Y \quad \wedge \quad s_{22} = s_{33} = -\frac{1}{3}\sigma_Y \tag{141}$$

Using the Prandtl-Reuss equation, eq. 118, gives

$$\dot{\varepsilon}_{11}^{pl} = \dot{\lambda}\frac{2}{3}\sigma_Y \quad \wedge \quad \dot{\varepsilon}_{22}^{pl} = \dot{\varepsilon}_{22}^{pl} = -\dot{\lambda}\frac{1}{3}\sigma_Y \tag{142}$$

which combines to

$$\dot{\varepsilon}_{22}^{pl} = \dot{\varepsilon}_{22}^{pl} = -\frac{1}{2}\dot{\varepsilon}_{11}^{pl} \tag{143}$$

Inserting this in the expression for the equivalent strain given by eq. 121 gives

$$\dot{\varepsilon}_e^{pl} = \sqrt{\frac{2}{3}\dot{\varepsilon}_{ij}^{pl}\dot{\varepsilon}_{ij}^{pl}} = \sqrt{\frac{2}{3}\left(\dot{\varepsilon}_{11}^{pl}\dot{\varepsilon}_{11}^{pl} + \frac{1}{4}\dot{\varepsilon}_{11}^{pl}\dot{\varepsilon}_{11}^{pl} + \frac{1}{4}\dot{\varepsilon}_{11}^{pl}\dot{\varepsilon}_{11}^{pl}\right)} = \dot{\varepsilon}_{11}^{pl} \tag{144}$$

Inserting this in eq. 142 gives

$$\dot{\varepsilon}_e^{pl} = \dot{\lambda}\frac{2}{3}\sigma_Y \tag{145}$$

Inserting this in the Prandtl-Reuss equation, eq. 118, gives

$$\dot{\varepsilon}_{ij}^{pl} = \dot{\lambda}s_{ij} = \frac{3}{2\sigma_Y}\dot{\varepsilon}_e^{pl}s_{ij} \tag{146}$$

Multiplying the consistency equation, eq. 139, with s_{kl} gives

$$\dot{f} \cdot s_{kl} = \left(3 s_{ij} \dot{\sigma}_{ij}\right) s_{kl} - 2\sigma_Y \left(\frac{1}{\left(\frac{1}{E_T} - \frac{1}{E}\right)} \dot{\varepsilon}_e^{pl} s_{kl} + \frac{\partial \sigma_Y}{\partial T} \dot{T} s_{kl} + \frac{\partial \sigma_Y}{\partial c} \dot{c} s_{kl} \right) = 0 \tag{147}$$

where we now can substitute $\dot{\varepsilon}_e^{pl} s_{kj}$ using eq. 146 giving

$$\left(3 s_{ij} \dot{\sigma}_{ij}\right) s_{kl} - 2\sigma_Y \left(\frac{1}{\left(\frac{1}{E_T} - \frac{1}{E}\right)} \frac{2}{3} \sigma_Y \dot{\varepsilon}_{kl}^{pl} + \frac{\partial \sigma_Y}{\partial T} \dot{T} s_{kl} + \frac{\partial \sigma_Y}{\partial c} \dot{c} s_{kl} \right) = 0 \tag{148}$$

Rearranging gives

$$\dot{\varepsilon}_{kl}^{pl} = \left(\frac{1}{E_T} - \frac{1}{E}\right) \frac{3}{2\sigma_Y} \left(\frac{3 s_{ij} \dot{\sigma}_{ij}}{2\sigma_Y} - \frac{\partial \sigma_Y}{\partial T} \dot{T} - \frac{\partial \sigma_Y}{\partial c} \dot{c} \right) s_{kl} \tag{149}$$

Combing with the Prandtl-Reuss equation, eq. 118, gives following expression for the load parameter

$$\dot{\lambda} = \left(\frac{1}{E_T} - \frac{1}{E}\right) \frac{3}{2\sigma_Y} \left(\frac{3 s_{ij} \dot{\sigma}_{ij}}{2\sigma_Y} - \frac{\partial \sigma_Y}{\partial T} \dot{T} - \frac{\partial \sigma_Y}{\partial c} \dot{c} \right) \tag{150}$$

For the nitriding case examined in this work, with the assumption of no shear stresses, $\dot{\sigma}_{11} = \dot{\sigma}_{22}$ and $\dot{\sigma}_{33} = 0$, then

$$s_{ij} \dot{\sigma}_{ij} = s_{11} \dot{\sigma}_{22} + s_{22} \dot{\sigma}_{22} \tag{151}$$

Using eq. 91, $s_{11} = s_{22} = \frac{\sigma_{22}}{3}$ leads to

$$s_{ij} \dot{\sigma}_{ij} = 2 \frac{\sigma_{22}}{3} \dot{\sigma}_{22} \tag{152}$$

Inserting this in the derived expression for the load parameter given in eq. 150, gives then for the assumption of no shear stresses, $\dot{\sigma}_{11} = \dot{\sigma}_{22}$ and $\dot{\sigma}_{33} = 0$

$$\dot{\lambda} = \left(\frac{1}{E_T} - \frac{1}{E}\right) \frac{3}{2\sigma_Y} \left(\frac{2\sigma_{22} \dot{\sigma}_{22}}{2\sigma_Y} - \frac{\partial \sigma_Y}{\partial T} \dot{T} - \frac{\partial \sigma_Y}{\partial c} \dot{c} \right) \tag{153}$$

9.2.5 Determination of the beta value

Plasticity and thus the β value is now determined from the following criteria [66]

$$for\ \sigma_e = \sigma_{e,max}\ and\ \dot{\lambda} \geq 0 \qquad \beta = 1$$
$$if\ \sigma_e < \sigma_{e,max}\ or\ \dot{\lambda} < 0 \qquad \beta = 0 \tag{154}$$

Note that if the yield stress was independent of temperature and concentration, eq. 150 would be reduced to

$$\dot{\lambda} = \left(\frac{1}{E_T} - \frac{1}{E}\right)\frac{3}{2\sigma_Y}\left(\frac{3s_{ij}\dot{\sigma}_{ij}}{2\sigma_Y}\right) \tag{155}$$

and then the criterion $\dot{\lambda} \geq 0$ would be fulfilled if

$$\frac{3s_{ij}\dot{\sigma}_{ij}}{2\sigma_Y} = \dot{\sigma}_e \geq 0 \tag{156}$$

which is the criterion for constant yield stress applied in section 8.1.

Computational sequence for calculating concentration and stress-depth profiles, using elastic-plastic stresses and a concentration-dependent yield stress is illustrated by a flowchart in Figure 23.

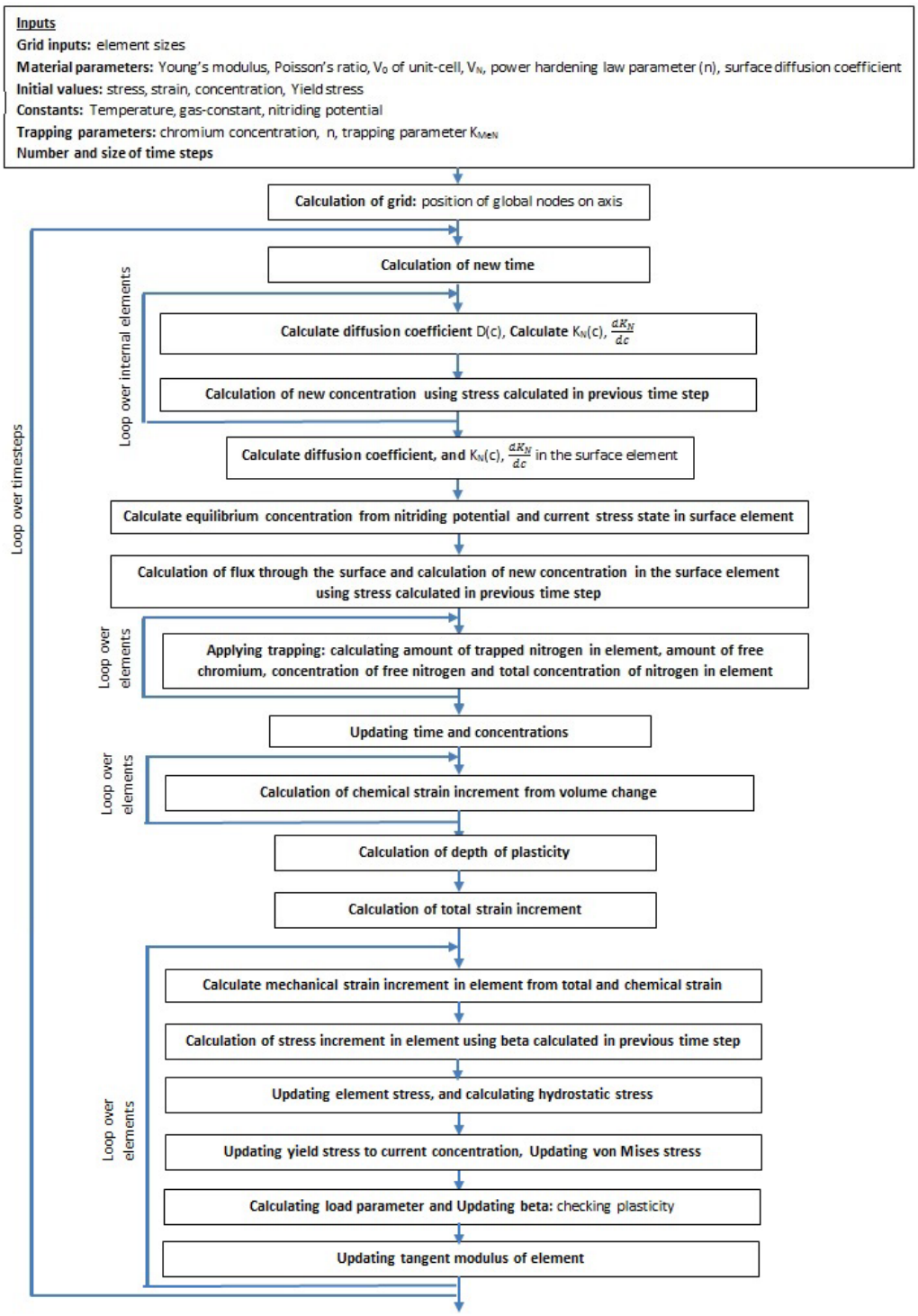

Figure 23 - Flowchart of computational sequence for calculating concentration and stress-depth profiles, when stresses are calculating with elasto-plasticity and concentration dependent yield stress

9.3 Effect on predicted concentration and stress profiles of concentration-dependent yield stress

The effect of the predicted concentration and stress-depth profiles on incorporating the concentration dependence of the yield strength compared to when using the constant yield strength of the base material (austenitic stainless steel 316) is shown in Figure 24. The increase of yield strength with concentration shown in section 9.1, results in surface stresses in the order of 10GPa, which is significantly higher than what is predicted using the constant yield strength, but still lower than the values predicted assuming purely elasticity (c.f. section 7). The increased stresses leads to deeper penetration of the concentration profile, and slightly lower surface concentrations, as compared to those predicted when using plasticity and constant yield stress. The combination of a rather high surface concentration and stress levels of approximately 10GPa at the surface leads to penetration depths even slightly higher than the ones predicted using purely elastic stresses (c.f.Figure 21).

The occurrence of plasticity in nitrogen-expanded austenite is seen to be the result of a competition between strengthening and stress build up. So for nitriding the stress build up clearly exceeds the yield strength achievable by solid solution strengthening, as is seen comparing the surface stress levels of around 10GPa to the maximum yield stress resulting from solid solution strengthening of 3.8GPa (c.f. Figure 22). For carburizing the strengthening effect presumably dominates the stress build up for the composition range under consideration, since plastic deformations are not observed experimentally.

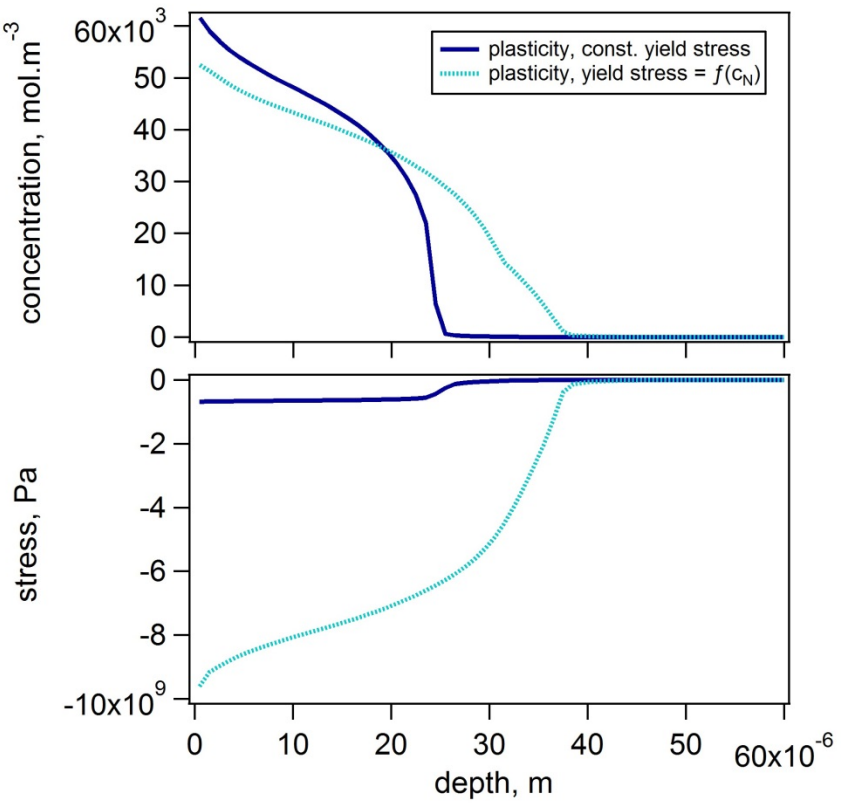

Figure 24 - Concentration and stress depth profile calculated assuming elasto-plasticity, with constant yields stress and with concentration dependent yield stress for nitriding of 316 austenitic stainless steel after 22 hours at 445°C using a nitriding potential of 1000 KMeN=10^7 and k=5 10^{-7}

9.3.1 Influence of sample thickness

The effect of the sample thickness on the predicted concentration- and stress-depth profiles, was discussed in section 6.2.1, but since there are now more interdependencies between profiles and properties it is re-evaluated and the effect of assumed sample thickness is shown in Figure 25. Similarly to what was seen in section 6.2.1 when purely elastic stresses were assumed, there is only a small difference in predicted stress values for the thicker samples and when assuming semi-infinite sample. Interestingly, for the thinner samples the highest stress is no longer at the surface but at a distance below the surface, which means that the sample thickness affects the shape of the stress-depth profile. Thus the thickness of the sample should be considered when evaluating the stress and composition profiles for the case of plasticity.

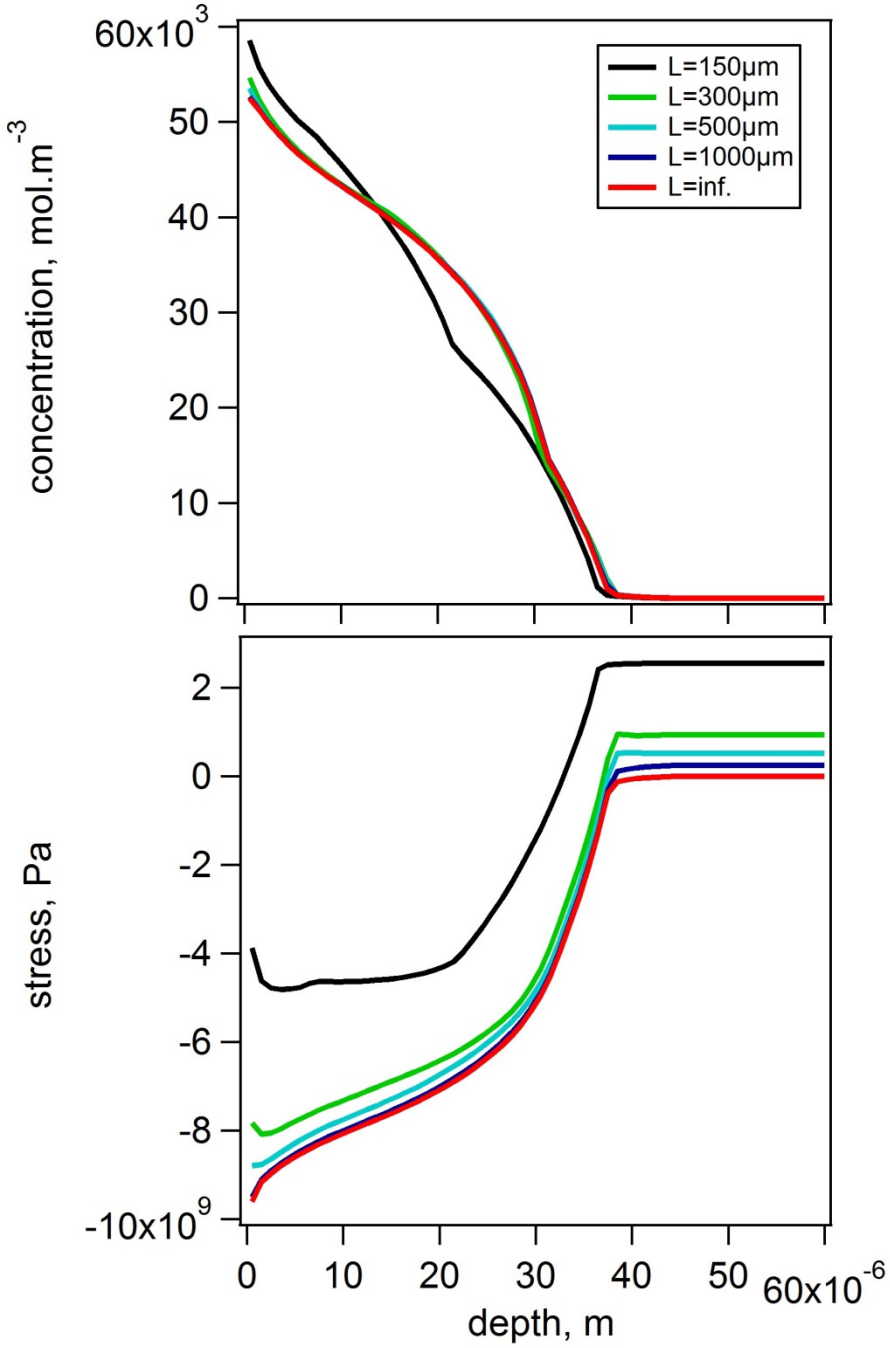

Figure 25 - Concentration and stress depth profile calculated for various sample thickness 2L, for nitriding of 316 austenitic stainless steel after 22 hours at 445°C using a nitriding potential of 1000 K_{CrN}=10^7 and k=5 10^{-7}

9.3.2 Influence of assumed element-size

To check convergence of the model the influence of assumed element-size has been investigated. First it was tested for the case when purely elastic stresses are assumed. When assuming purely elastic stresses decreasing the element size below 1µm did not result in significantly different results, but with the introduction of plasticity, the case could be different, and the effect of element-size is thus evaluated for this case too.

The effect of changing the element size used in the computational modelling incorporating plasticity is seen in Figure 26. Changing element size from 1µm to 0.1µm is seen to give similar concentration predictions at the surface, but a small change in the profiles with respect to penetration depth. Thus 0.1µm elements are used for subsequent calculations.

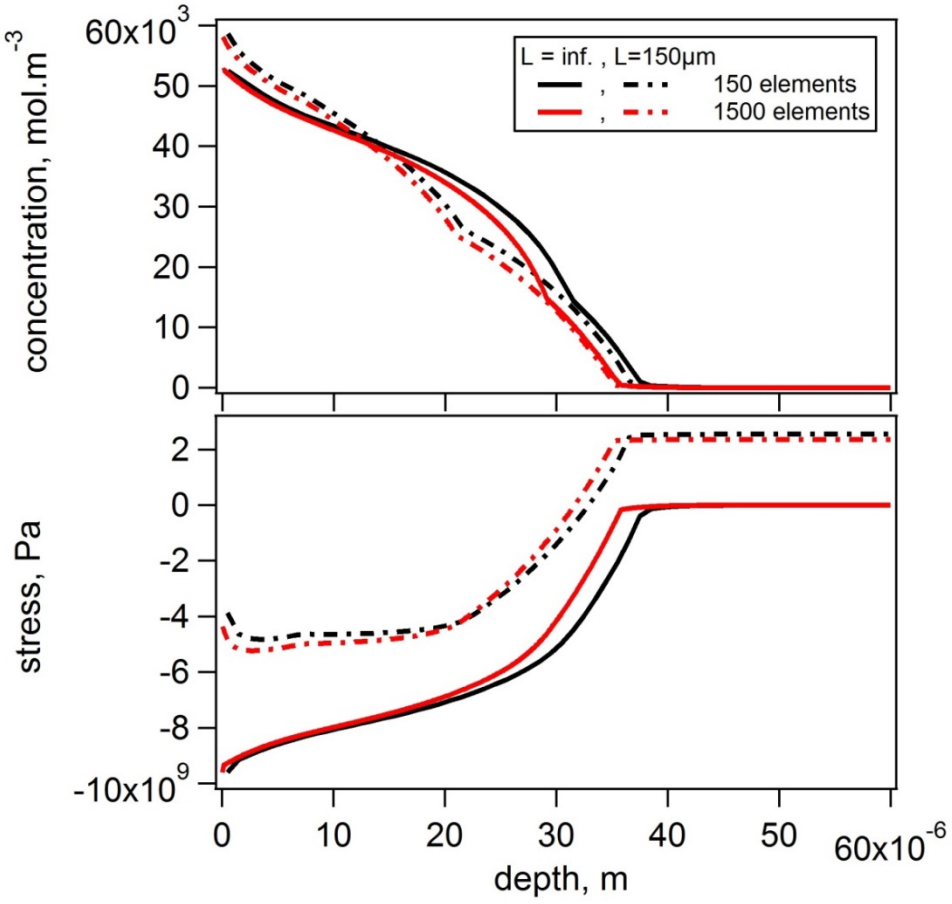

Figure 26 - Concentration and stress depth profile calculated for 2 sample thickness 2L, thin sample L=150µm and thick sample L=inf., and with two computational element sizes for nitriding of 316 austenitic stainless steel after 22 hours at 445°C using a nitriding potential of 1000 K_{CrN}=10^7 and k=5 10^{-7}

9.4 Experimental Determination of concentration dependence of Young's modulus from tensile tests

9.4.1 Experimental

To study the concentration dependence of Young's modulus, tensile testing of samples with varying nitrogen contents was performed. Choosing loading direction parallel to the rolling direction of the plate, tensile test specimens were cut in accordance with ASTM standard E 8M-04 [67].

In order to obtain uniform nitrogen contents throughout the samples, high temperature solution nitriding at 1150°C was applied on samples from three types of austenitic steels; AISI 304, AISI 316L and EN1.4369. Compositions of these are given in Table 1.

Table 1 - Composition of steels

	Cr	Ni	C	Si	Mn	Mo	N
AISI 304	18.5	10.5	0.08	0.75	2.0		
AISI 316L	16.26	10.05	0.019	0.40	1.47	2.02	0.067
EN 1.4369	18.58	7.11	0.09	0.74	5.92	0.18	0.23

After high temperature solution nitriding, the nitrogen distribution in the steels was found to be uniform, and concentrations were measured using inert gas fusion thermal conductivity detection with a LECO TN500 nitrogen analyzer.

Tensile testing was done using an Instron ASM tensile testing machine with a maximum load capacity of 100kN, using a constant strain rate of $6.67 \cdot 10^{-3} s^{-1}$. Three samples were tested for each concentration and average values of Young's modulus were found.

It should be noted, that this experimental work was done in cooperation with Bottoli, who used the tensile testing results to study plastic deformation and the effect of nitrogen content on yield strength [68].

9.4.1 Results and fit of data

Making a linear fit, as shown in Figure 27, the average change in Young's modulus with concentration, $\frac{\partial E}{\partial c_N}$, is

$$\frac{\partial E}{\partial c_N} = 1.9402 \cdot 10^5 \tag{157}$$

Only considering one material at the time gives

$$\frac{\partial E_{\mathrm{EN1.4369}}}{\partial c_N} = 1.547 \cdot 10^5 \tag{158}$$

$$\frac{\partial E_{304}}{\partial c_N} = 3.872 \cdot 10^5 \tag{159}$$

$$\frac{\partial E_{316L}}{\partial c_N} = 0.283 \cdot 10^5 \tag{160}$$

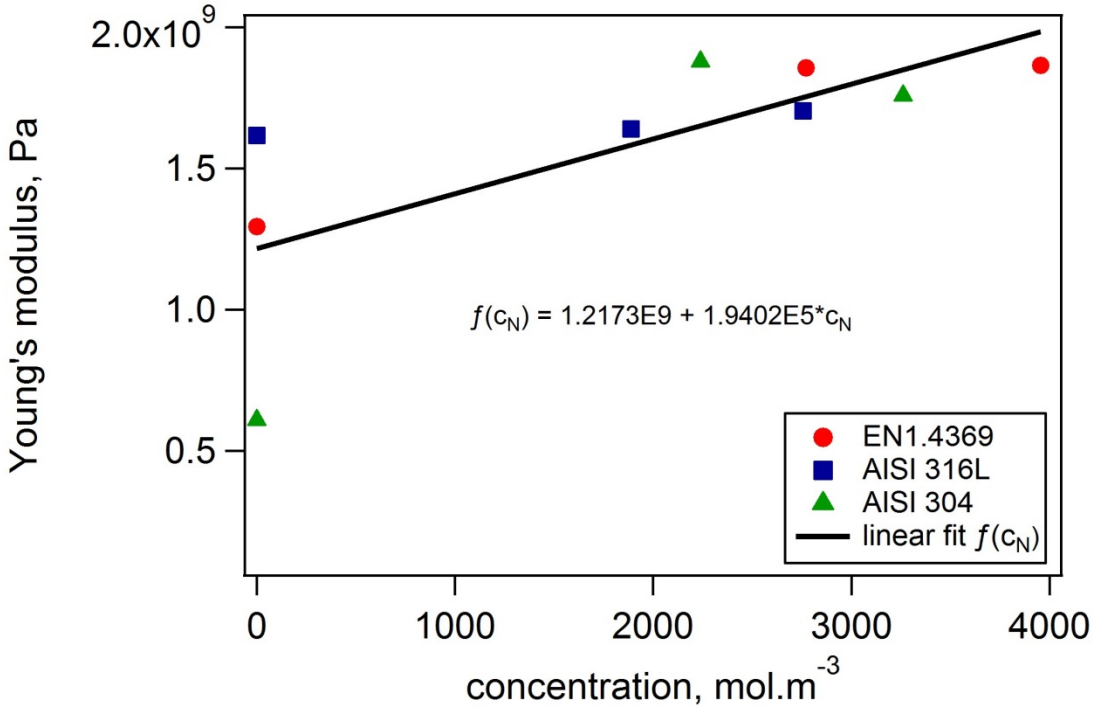

Figure 27 - Concentration dependence of Young's modulus

9.5 Calculation of elastic-plastic stresses for non-constant Young's modulus

Elastic-plastic stresses for non-constant Young's modulus is calculated as explained in section 8.1 from

$$\dot{\sigma}_{11} = \dot{\sigma}_{22} = \frac{E}{1+\nu}\left(\left[1 + 2\frac{\nu}{1-2\nu} - \frac{1}{3}\frac{E/E_t - 1}{E/E_t - (1-2\nu)/3}\right] + \frac{-2\left[\frac{\nu}{1-2\nu} + \frac{1}{3}\frac{E/E_t - 1}{E/E_t - (1-2\nu)/3}\right]^2}{\left[1 + \frac{\nu}{1-2\nu} - \frac{2}{3}\frac{E/E_t - 1}{E/E_t - (1-2\nu)/3}\right]}\right)\dot{\varepsilon}_{22}^{mech} \tag{161}$$

for plasticity,

and from

$$\dot{\sigma}_{11} = \dot{\sigma}_{22} = \frac{E}{1-\nu}\dot{\varepsilon}_{22}^{mech} \tag{162}$$

for elasticity, where

$$\dot{\varepsilon}_{22}^{mech} = \dot{\varepsilon}_{22}^{tot} - \dot{\varepsilon}_{22}^{th} - \dot{\varepsilon}_{22}^{ch} \tag{163}$$

This formulation will still be applied in this section, even though for changing Young's modulus additional terms in principle should be added to the expression for the stress increment. For a 1D elastic case a more correct formulation than $\dot{\sigma} = E\dot{\varepsilon}^{el}$ would be

$$\dot{\sigma} = E\dot{\varepsilon}^{el} + \dot{E}\varepsilon^{el} \tag{164}$$

For a plastic case it is however more complicated. The best approach would probably be using a formulation on the new time-level, rather than an incremental one, which could be convenient for the definition of a residual, and iterations could be done for non-linearities. This is however out of the scope for the current work, where focus is on an incremental explicit solution, and thus the effect of the Young's modulus increment on the stress increment is neglected in this work. A pragmatic approach where Young's modulus is adjusted after each time step is adopted, in this first attempt to evaluate the effect of a concentration dependent Young's modulus.

However, some change is done to the calculation of the total strain from the mechanical equilibrium, because if Young's modulus and Poisson's ratio are not constant with depth, but depend on temperature and/or concentration which changes with depth, the mechanical equilibrium integral to find the total strain (see eq. 105-106) must be redone, since now the material parameters cannot be set outside the integral

For the elastic case this gives

$$\int_0^{z_{max}} \frac{E}{1-\nu}\left(\dot{\varepsilon}_{22}^{tot} - \dot{\varepsilon}_{22}^{th} - \dot{\varepsilon}_{22}^{ch}\right)dz = 0 \tag{165}$$

Rearranging gives the expression for the total strain increment

$$\dot{\varepsilon}_{22}^{tot} = \frac{\int_0^{z_{max}} \frac{E}{1-\nu}\left(\dot{\varepsilon}_{22}^{th} + \dot{\varepsilon}_{22}^{ch}\right)dz}{\int_0^{z_{max}} \frac{E}{1-\nu}dz} \tag{166}$$

which can be discretised as

$$\dot{\varepsilon}_{22}^{tot} = \frac{\sum_1^{i_{max}} \left[\frac{E(i)}{1-\nu(i)}\left(\dot{\varepsilon}_{22}^{th}(i) + \dot{\varepsilon}_{22}^{ch}(i)\right)\cdot \Delta z(i)\right]}{\sum_1^{i_{max}} \left[\frac{E(i)}{1-\nu(i)}\Delta z(i)\right]} \tag{167}$$

For the plastic case the mecahnical equilibrium equation given by eq. 105 becomes

$$\begin{aligned}\int_0^{z_{max,plastic}} \frac{E}{1+\nu}\Bigg(&\left[1 + 2\frac{\nu}{1-2\nu} - \frac{1}{3}\frac{E/E_t - 1}{E/E_t - (1-2\nu)/3}\right] \\ &+ \frac{-2\left[\frac{\nu}{1-2\nu} + \frac{1}{3}\frac{E/E_t - 1}{E/E_t - (1-2\nu)/3}\right]^2}{\left[1 + \frac{\nu}{1-2\nu} - \frac{2}{3}\frac{E/E_t - 1}{E/E_t - (1-2\nu)/3}\right]}\Bigg)\left(\dot{\varepsilon}_{22}^{tot} - \dot{\varepsilon}_{22}^{th} - \dot{\varepsilon}_{22}^{ch}\right)dz \\ &+ \int_{z_{max,plastic}}^{z_{max}} \frac{E}{1-\nu}\left(\dot{\varepsilon}_{22}^{tot} - \dot{\varepsilon}_{22}^{th} - \dot{\varepsilon}_{22}^{ch}\right)dz = 0\end{aligned} \tag{168}$$

giving the following expression for the total strain

$$\varepsilon_{22}^{tot} = \left(\int_0^{z_{max,pl}} \frac{E}{1+\nu} \left(\left[1 + 2\frac{\nu}{1-2\nu} - \frac{1}{3}\frac{E/E_t - 1}{E/E_t - (1-2\nu)/3} \right] + \frac{-2\left[\frac{\nu}{1-2\nu} + \frac{1}{3}\frac{E/E_t - 1}{E/E_t - (1-2\nu)/3} \right]^2}{\left[1 + \frac{\nu}{1-2\nu} - \frac{2}{3}\frac{E/E_t - 1}{E/E_t - (1-2\nu)/3} \right]} \right) \left(\dot{\varepsilon}_{22}^{th} + \dot{\varepsilon}_{22}^{ch} \right) dz + \int_{z_{max,pl}}^{z_{max}} \frac{E}{1-\nu} \left(\dot{\varepsilon}_{22}^{th} + \dot{\varepsilon}_{22}^{ch} \right) dz \right) \Bigg/ \left(\frac{E}{1+\nu} \left(\left[1 + 2\frac{\nu}{1-2\nu} - \frac{1}{3}\frac{E/E_t - 1}{E/E_t - (1-2\nu)/3} \right] + \frac{-2\left[\frac{\nu}{1-2\nu} + \frac{1}{3}\frac{E/E_t - 1}{E/E_t - (1-2\nu)/3} \right]^2}{\left[1 + \frac{\nu}{1-2\nu} - \frac{2}{3}\frac{E/E_t - 1}{E/E_t - (1-2\nu)/3} \right]} \right) dz + \int_{z_{max,pl}}^{z_{max}} \frac{E}{1-\nu} dz \right) \tag{169}$$

which in the finite difference program is calculated as

$$\dot{\varepsilon}_{22}^{tot} = \sum_{1}^{i_{max,plastic}} \left[\frac{E(i)}{1+\nu(i)} \left(1 + 2\frac{\nu(i)}{1-2\nu(i)} - \frac{1}{3}\frac{E(i)/E_t(i)-1}{E(i)/E_t(i)-(1-2\nu(i))/3} + \frac{-2\left[\frac{\nu(i)}{1-2\nu(i)} + \frac{1}{3}\frac{E(i)/E_t(i)-1}{E(i)/E_t(i)-(1-2\nu(i))/3}\right]^2}{\left[1+\frac{\nu(i)}{1-2\nu(i)} - \frac{2}{3}\frac{E(i)/E_t(i)-1}{E(i)/E_t(i)-(1-2\nu)/3}\right]} \right) \cdot \left(\dot{\varepsilon}_{22}^{th}(i)\cdot\Delta z(i) + \dot{\varepsilon}_{22}^{ch}(i)\cdot\Delta z(i)\right) \right] + \sum_{i_{max,plastic}}^{i_{max}} \left[\frac{E(i)}{1-\nu(i)} \left(\dot{\varepsilon}_{22}^{th}(i)\cdot\Delta z(i) + \dot{\varepsilon}_{22}^{ch}(i)\cdot\Delta z(i)\right) \right] / \left\{ \sum_{1}^{i_{max,plastic}} \left[\frac{E(i)}{1+\nu(i)} \left(1 + 2\frac{\nu(i)}{1-2\nu(i)} - \frac{1}{3}\frac{E(i)/E_t(i)-1}{E(i)/E_t(i)-(1-2\nu(i))/3} + \frac{-2\left[\frac{\nu(i)}{1-2\nu(i)} + \frac{1}{3}\frac{E(i)/E_t(i)-1}{E(i)/E_t(i)-(1-2\nu(i))/3}\right]^2}{\left[1+\frac{\nu(i)}{1-2\nu(i)} - \frac{2}{3}\frac{E(i)/E_t(i)-1}{E(i)/E_t(i)-(1-2\nu)/3}\right]} \right) \Delta z(i) \right] + \sum_{i_{max,plastic}}^{i_{max}} \left[\frac{E(i)}{1-\nu(i)} \Delta z(i) \right] \right\} \tag{170}$$

9.6 Effect of concentration dependence of Young's modulus on concentration- and stress depth profiles

By tensile testing of stainless steel samples with various nitrogen concentrations, it was shown that Young's modulus increases with concentration. The effect of incorporating the change of Young's modulus with concentration, given by eq. 157, on the predicted concentration is shown in Figure 28, for the case where semi-infinity is assumed and for the case of L=150µm. When semi-infinity is assumed, the change of Young's modulus with concentration has only a small effect on the predicted stress depth profile and the effect on the concentration depth profile is insignificant, but for the case of a small sample thickness, there is significant change on the predicted stress-depth profile, where the increase of Young's modulus with concentration results in higher predicted compressive stresses.

From the tensile tests shown in section 9.4, the different types of austenitic stainless steels shows slightly varying changes of Young's modulus with concentration, see eq. 158-160, and since the measurements are made for concentrations in the range 0-4000mol/m^3 and the concentration levels when nitriding reaches up to 60000mol/m^3 resulting in a large extrapolation, it is thus important to check sensitivity of the model to variations in change of Young's modulus with concentration. The sensitivity of the model stress-depth profiles predictions to the variance in change of Young's modulus with concentration, is displayed in Figure 29, which shows that for both semi-infinite and thin samples (L = 150µm) the sensitivity of the model is insignificant for the variances in eq. 158-160.

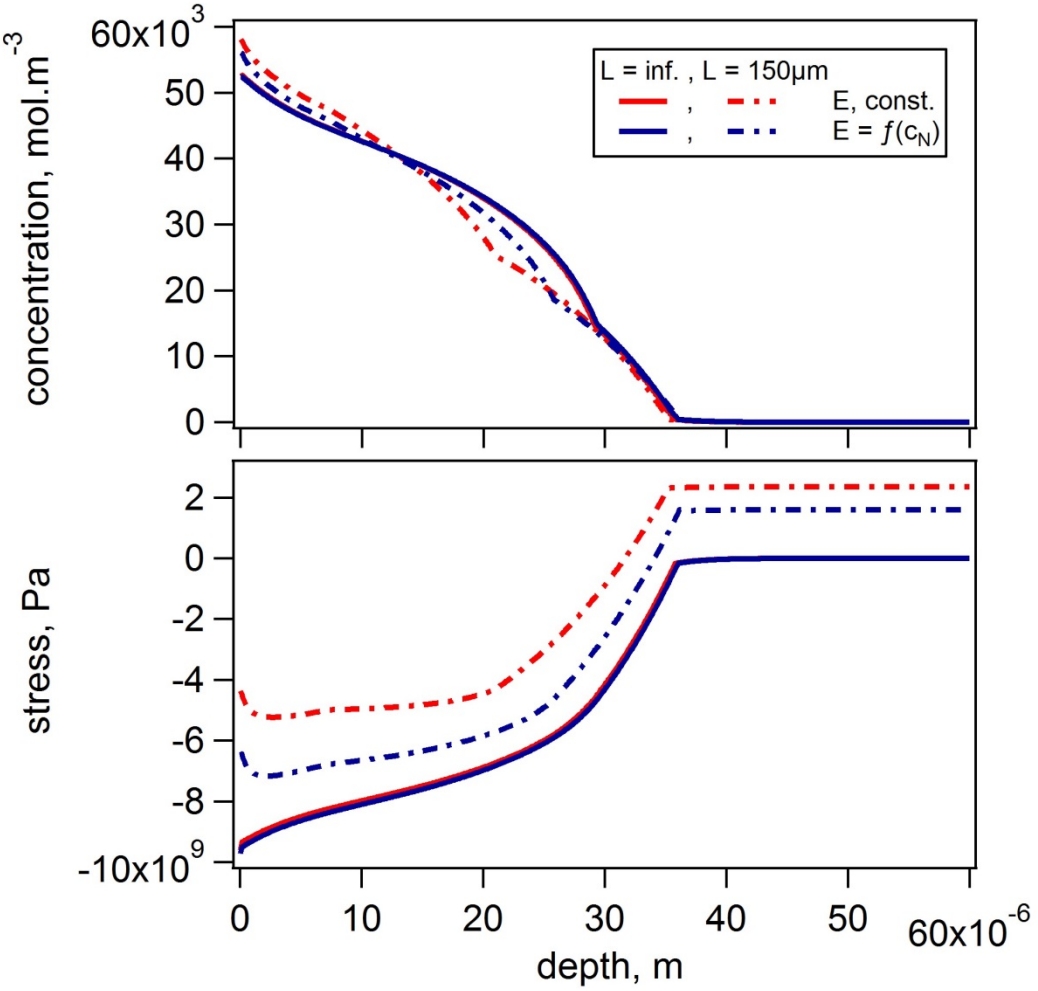

Figure 28 - Concentration, and stress depth profiles with constant Young's modulus, E, and with concentration dependent Young's modulus, $E = \mathfrak{f}(c_N)$, for nitriding at austenitic stainless steel after 22 hours at 445°C using a nitriding potential of 1000 $K_{CrN} = 10^7$ and k=5 10^{-7}.

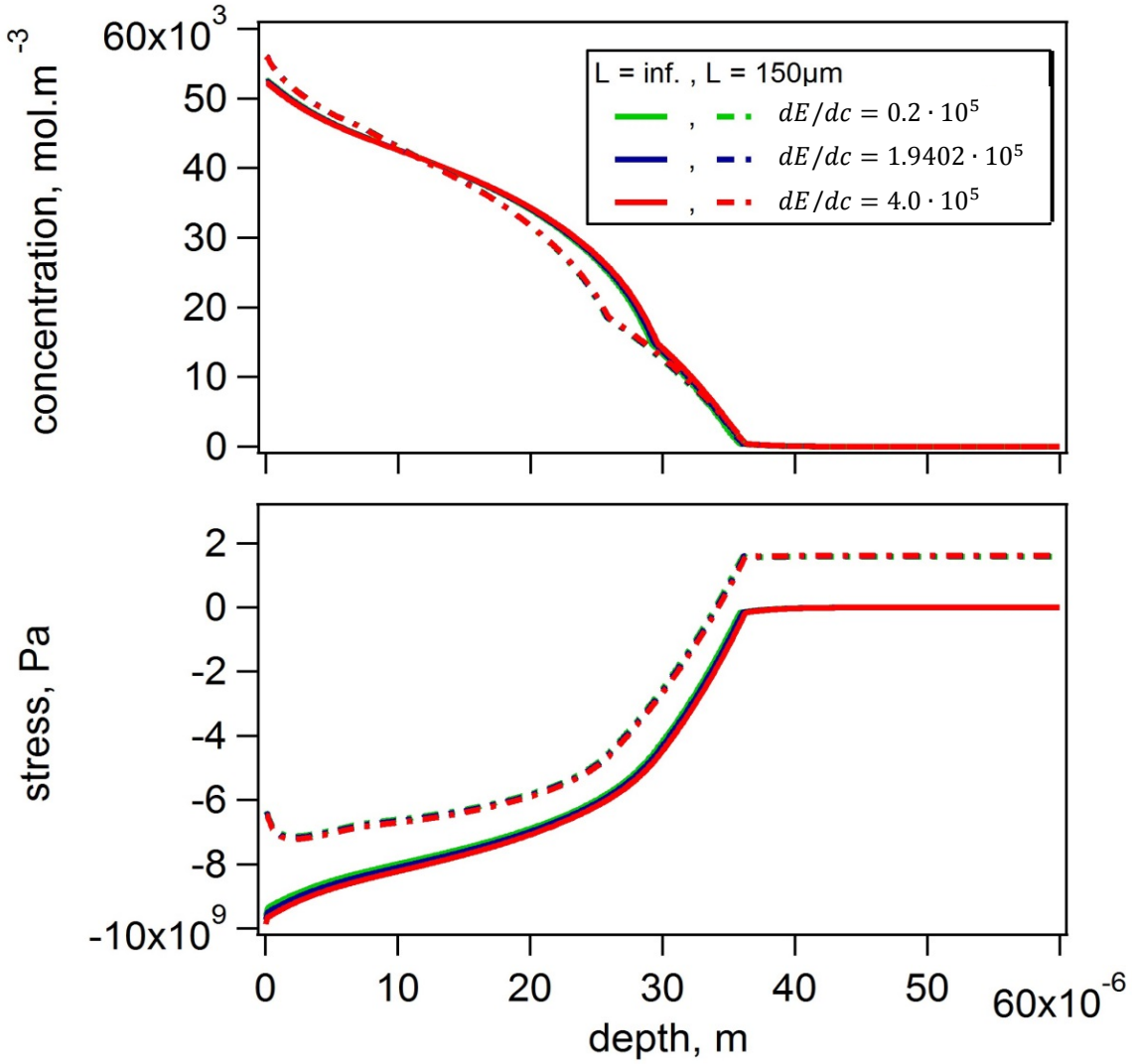

Figure 29 - Concentration, and stress depth profiles using various levels of change of Young's modulus with concentration, dEdc, for nitriding at austenitic stainless steel after 22 hours at 445°C using a nitriding potential of 1000 $K_{CrN} = 10^7$ and k=5 10^{-7}

10. Pre-stressing of sample before nitriding

In real life, specimens are not always stress free. Residual stresses are often found in the surface as a result of the processing history. Since a profound effect of stresses on nitrogen diffusion was demonstrated in the previous sections, it is intriguing to investigate the effect of pre-stressing of samples before nitriding.

From experiments with loading of austenite films during plasma carburizing Li et al. [69] demonstrated a substantial effect of pre-stressing on resulting expanded austenite case depth. This pre-stressing was done using uniaxial loading. The effect of applying a pre-stress on the predicted composition- and stress depth profiles will be examined below with the model developed in sections 4-9. It should be noted that the pre-stressing will be modelled assuming biaxial-pre-stressing, while the experiments were done using a uniaxial stress. This is due to the fact that the model is based on the assumption of rotational symmetry of the in-plane stresses. Attempts to expand the model beyond its limit, to incorporate uniaxial in-plane loading, is discussed in Appendix D.

10.1 Effect of pre-stressing on model predictions

The effect of pre-stressing on the predicted concentration- and stress-depth profiles is studied in this section. First biaxial pre-stressing for the case examined in this work; 22h nitriding with nitriding potential of 1000, is investigated. In Figure 30 the effect of biaxial pre-stressing of compressive stress of 500MPa to tensile stress of 1GPa on the concentration- and stress-depth profiles are shown for a sample of thickness (2L) of 300µm and a thick sample where semi-infinity is assumed. For both types of samples the effect of pre-stress is clearly seen in the depths above 40µm, where the nitrogen concentrations are zero. For the thick samples the pre-stressing hardly affects the predicted surface stresses, neither is the predicted concentration profile affected significantly. On the other hand, for the thin samples a significant difference is observed for predicted surface stresses and on the composition profile. The penetration depth is however not influenced much, unless pre-stressing is increased to 1GPa. In reality it does however not make sense to pre-stress with such a high pre-stress since the unexpanded austenite has a yield stress of around 290MPa which increases with the solid-solution strengthening from the nitrogen (see section 9.1).

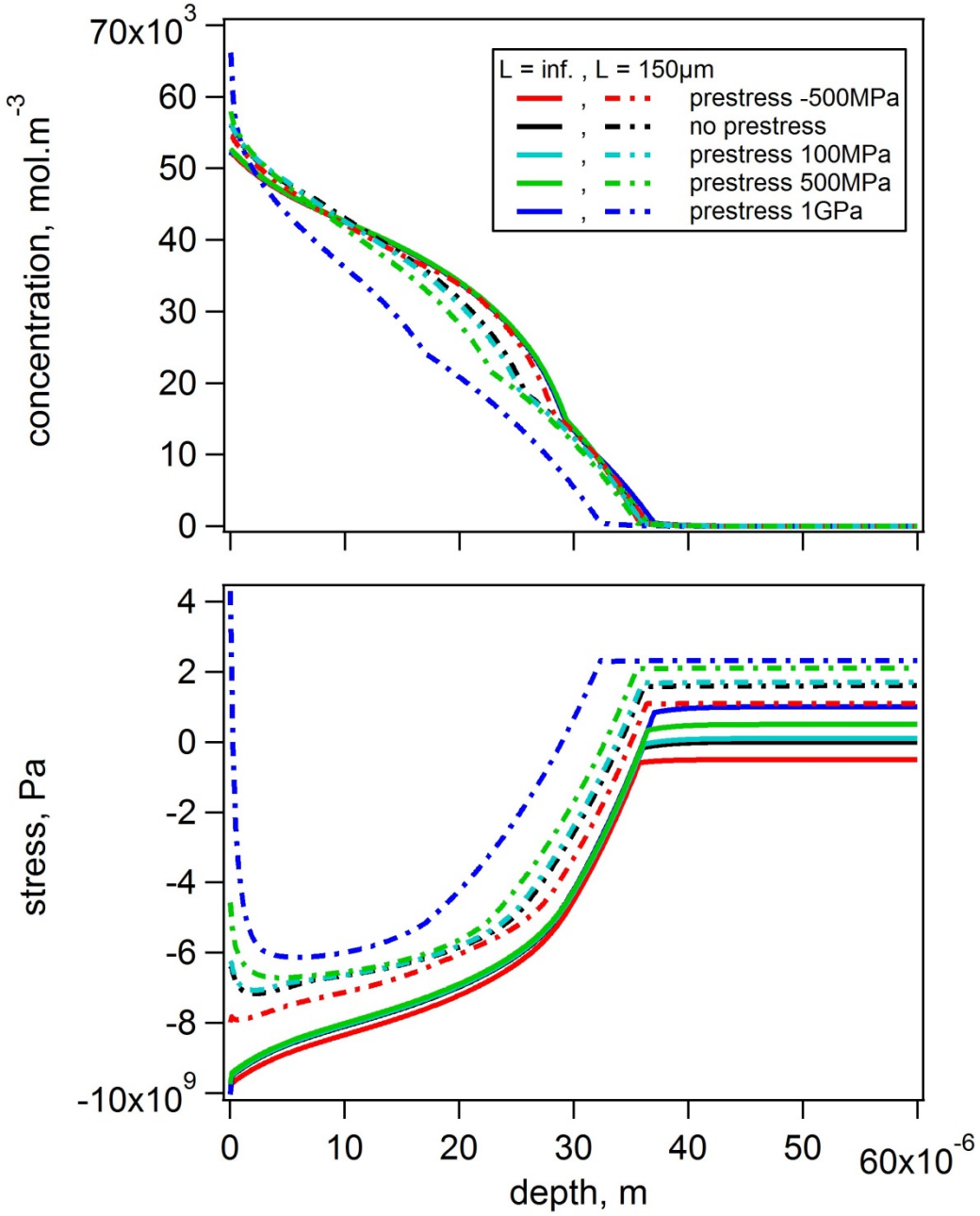

Figure 30 - Effect of biaxial pre-stressing on predicted concentration-depth and stress-depth profiles for nitriding 22h with nitriding potential K_N=1000

As discussed above, the model predicts that pre-stressing before nitriding does not increase the nitrogen penetration depth. This contradicts experimental findings for carburizing as reported by Li et al. [69], who found that application of a uniaxial tensile stress of only 20MPa during carburizing at 450°C for 10h almost doubled the layer thickness of expanded austenite and that application of tensile stress of 40 MPa almost tripled the penetration depth.

This difference in findings could be due to the differences between carburizing and nitriding, because compared to nitriding, carburizing has significantly lower surface concentrations and stresses, as seen in Figure 5. The carburized samples have surface concentrations of about 8000-13300mol/m^3 (y_N about 0.06-0.1) and surface stresses of about 1.5-2.5GPa. Plasticity has so far not been observed in carburized samples, contrary to the nitrided samples where plasticity does occur. Another difference is, that on carburizing trapping of interstitials by Cr is not as pronounced as in the case of nitriding [70]. To compare a simulation to the experiments on the effect of tensile stress on formation of expanded austenite during 10h of carburizing presented by Li et al. [69], without having input parameters for carburizing and thus using the nitriding data, a simulation is made of 10h nitriding with a nitriding potential of $K_N = 1$ to investigate the response of biaxial prestressing in the low concentration and low stress situation. The results are shown in Figure 31. Contrary to the experiments by Li et al., the model does not predict an effect on the penetration depth for the levels of pre-stressing used by Li et al. not even for the low stress, low concentration case.

This difference is intriguing, and testing the case of nitriding experimentally would be interesting for further research to investigate whether the difference arises from limitations in the model or from flaws in the experimental procedures.

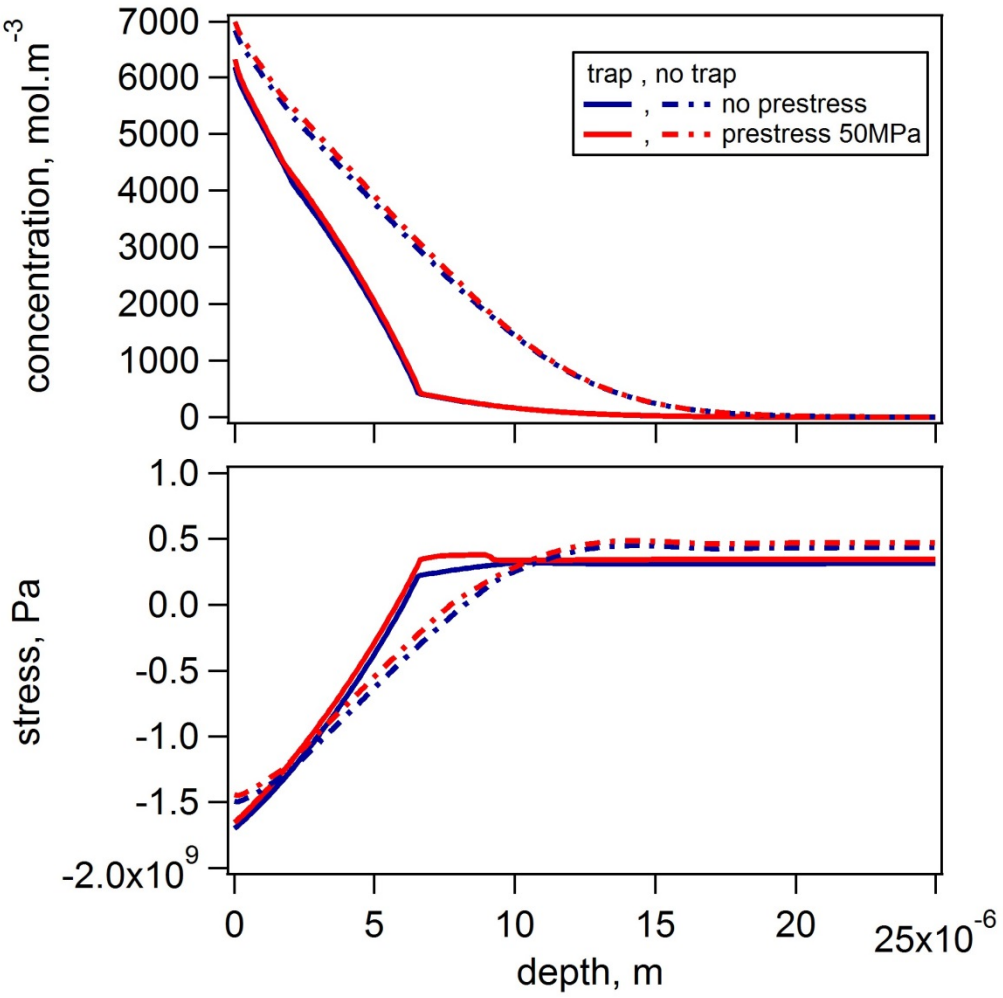

Figure 31 - Effect of biaxial pre-stressing on predicted concentration- and stress-depth profiles for nitriding at 445°C, 10h with nitriding potential K_N=1, for the case of trapping with $K_{CrN} = 10^7$ and the case of no trapping

11. Temperature dependence of mechanical properties

11.1 Determination of expression for temperature dependence of yield stress

Data for yield stress as a function of temperature was obtained from AK steel [63]. A fit of the data, as shown in Figure 32, gives the following relation for yield stress as function of temperature

$$\sigma_Y(T) = (8.128 \cdot 10^{-5} \cdot T^2 - 0.33 \cdot T + 379.98\,) \cdot 10^6 \text{ Pa} \tag{171}$$

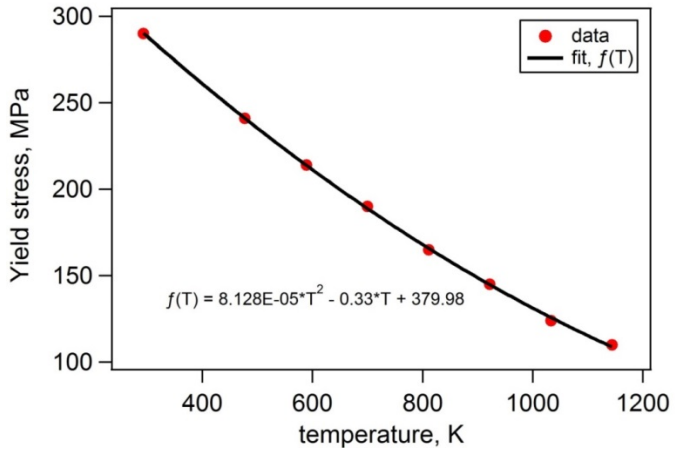

Figure 32 - Temperature dependence of yield stress

11.2 Determination of expression for temperature dependence of Young's modulus

Data for Young's modulus as a function of temperature was obtained from INCO [71]. A fit of the data as shown in Figure 33 gives the following relation for Young's modulus as function of temperature

$$E(T) = (-0.0808T + 226.42) \cdot 10^9 \text{ Pa} \tag{172}$$

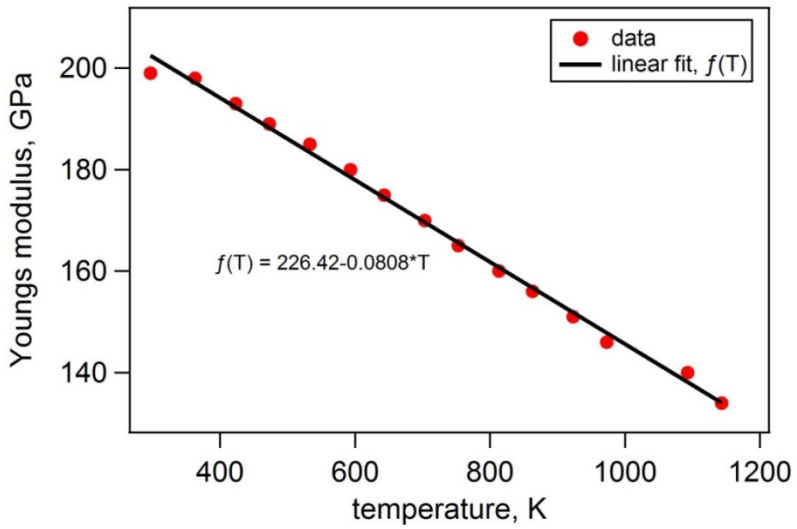

Figure 33 - Temperature dependence of Young's modulus

11.3 Temperature dependence of Poisson's ratio

Data for Poisson's ratio as function of temperature was obtained from INCO [71]. A fit of the data, as shown in Figure 34, gives an almost constant Poisson's ratio as function of temperature

$$\nu(T) = 0.29 \tag{173}$$

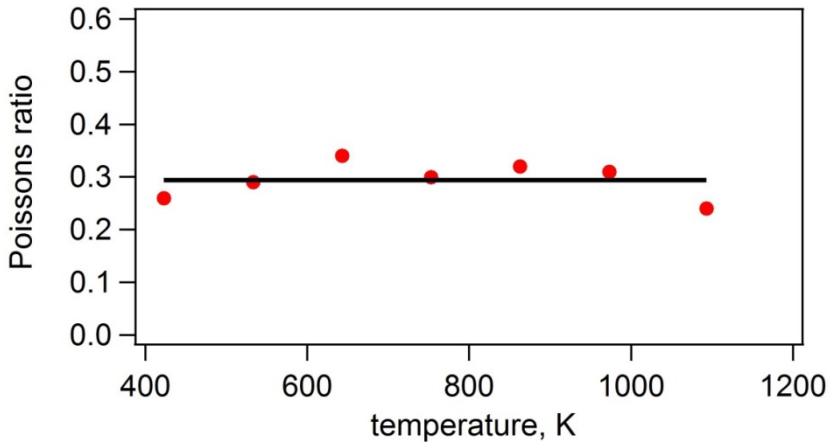

Figure 34 - Poisson ratio as function of temperature for 316 steel, measured datapoints from INCO [71] and linear fit

11.4 Effect on concentration and stress depth profiles of temperature dependence of mechanical properties

So far the modelling has been done using room temperature values of yield stress and Young's modulus. However, for nitriding at 445°C the temperature dependence of yield stress and Young's modulus should be taken into account. Expressions for temperature dependence of yield stress, (see. eq. 171), and Young's modulus, (see eq. 172) for 316 austenitic stainless steel, have been found from literature table values, see section 10.1-10.2. Both yield stress and Young's modulus decrease with increasing temperature. Poisson's ratio was found to be constant with temperature.

The effect of taking into account the temperature dependence of the yield stress and Young's modulus is shown in Figure 35, where it can be seen that using yield stress and Young's modulus at 445°C leads to predictions of lower values of compressive stress and slightly lower penetration depths, compared to when using yield stress and Young's modulus at room temperature.

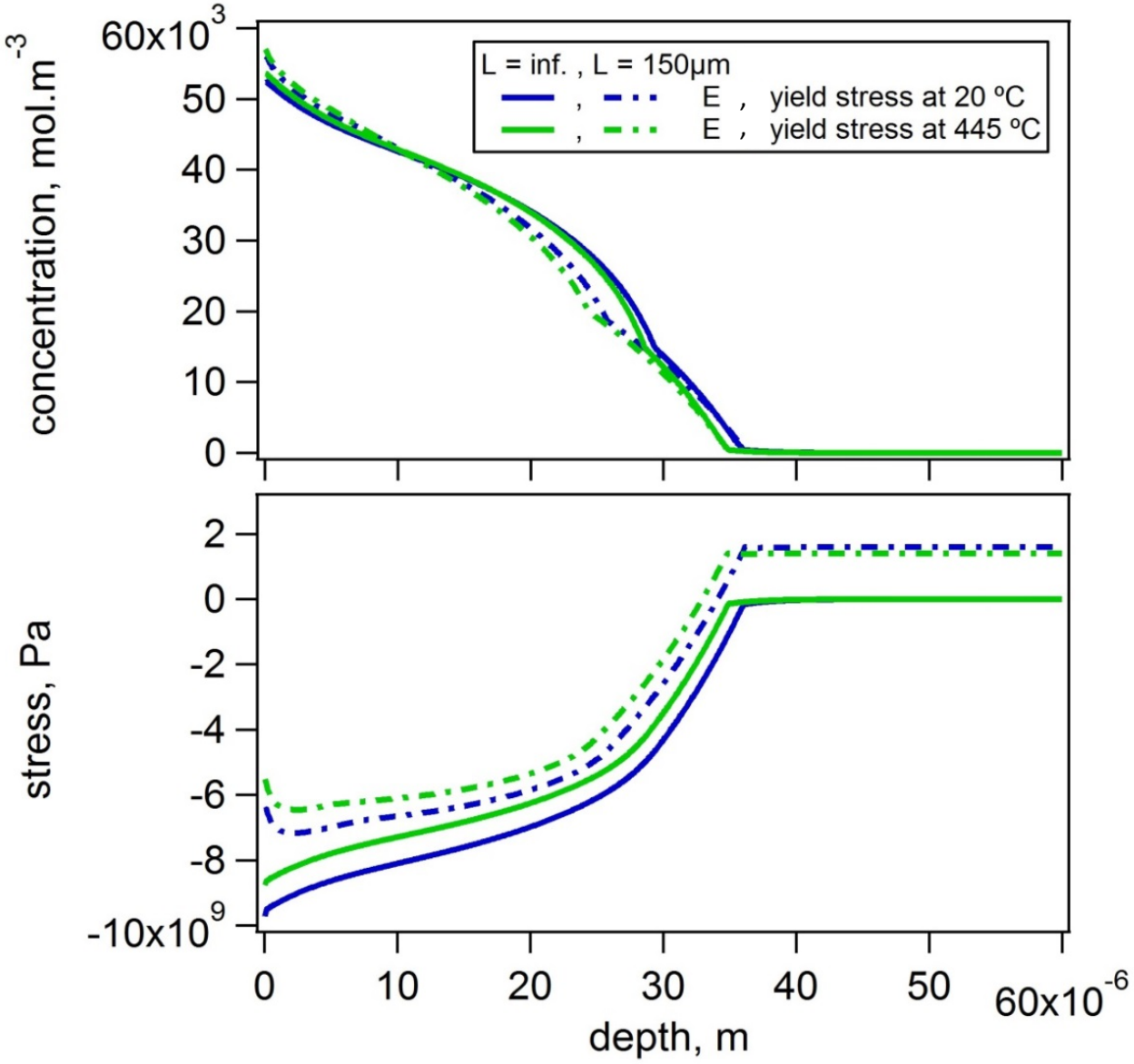

Figure 35 - Effect of temperature dependence of yield stress and Young's modulus on predicted concentration- and stress-depth-profiles for nitriding at austenitic stainless steel, using concentration dependent yield stress and Young's modulus after 22 hours at 445°C using a nitriding potential of 1000, $K_{CrN} = 10^7$ and k=5 10^{-7}

12. Temperature variations

When the temperature is no longer constant but varies, the temperature flow has to be considered and the effect of temperature variations on the stress and composition profiles should be considered.

12.1 Calculation of temperature flow

The governing equation for the thermal flow is Fourier's law [58]

$$\rho C_p \frac{\partial T}{\partial t} = \frac{\partial}{\partial z}\left(k \frac{\partial T}{\partial z}\right) \tag{174}$$

where *T* is the temperature, k is the thermal conductivity, C_p is the specific heat and ρ is the density. If the material parameters are assumed constant this can be written as [58]

$$\frac{\partial T}{\partial t} = \alpha \frac{\partial^2 T}{\partial z^2} \tag{175}$$

where α is the thermal diffusivity which can be calculated by

$$\alpha = \frac{k}{\rho C_p} \tag{176}$$

Calculating using explicit finite difference method gives

$$\frac{T_i^{t+\Delta t} - T_i^t}{\Delta t} = \alpha \frac{T_{i+1}^t - 2T_i^t + T_{i-1}^t}{\Delta z^2} \tag{177}$$

The boundary conditions are Diriclet at the surface (known Temperature = Temperature in oven) and Neumann at the centre (no flow due to symmetry boundary). For non-constant parameters

$$\frac{\partial T}{\partial t} = \frac{1}{\rho C_p}\frac{\partial}{\partial z}\left(k \frac{\partial T}{\partial z}\right) = \frac{1}{\rho C_p}\left(\frac{\partial k}{\partial z}\frac{\partial T}{\partial z} + k \frac{\partial^2 T}{\partial z^2}\right) \tag{178}$$

Discretizing using explicit finite difference gives

$$\frac{T_i^{t+\Delta t} - T_i^t}{\Delta t} = \frac{1}{\rho_i \cdot C_p(i)}\left(\frac{k_{i+1} - k_{i-1}}{2\Delta z} \cdot \frac{T_{i+1}^t - T_{i-1}^t}{2\Delta z} + k_i \frac{T_{i+1}^t - 2T_i^t + T_{i-1}^t}{\Delta z^2}\right) \tag{179}$$

Verification of computational calculation of temperature flow is shown in Appendix C.5.

12.2 Temperature dependence of density

Data for density as a function of temperature was obtained from INCO [71] A fit of the data, as shown in Figure 36, gives the following relation for density as function of temperature

$$\rho(T) = -0.0042T + 80.74\ \mathrm{kg/m^3} \tag{180}$$

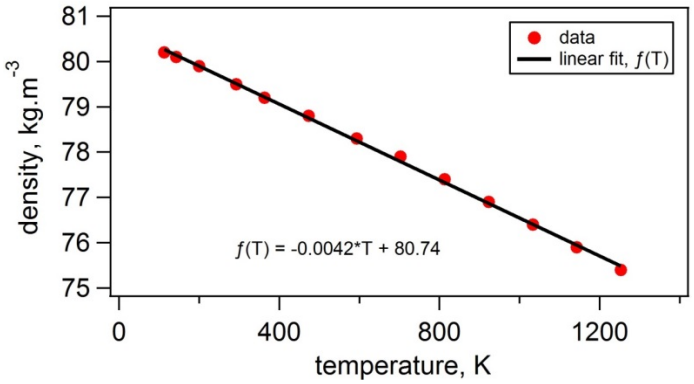

Figure 36 - Density as function of temperature for 316 steel, measured data-points from INCO [71] and linear fit

12.3 Temperature dependence of specific heat

Data for specific heat as a function of temperature was obtained from INCO [71]. A fit of the data, as shown in Figure 37, gives the following relation for specific heat as function of temperature

$$C_p(T) = 6 \cdot 10^{-7} \cdot T^3 - 0.0014T^2 + 1.1731T + 213.17\ \mathrm{J/kgK} \tag{181}$$

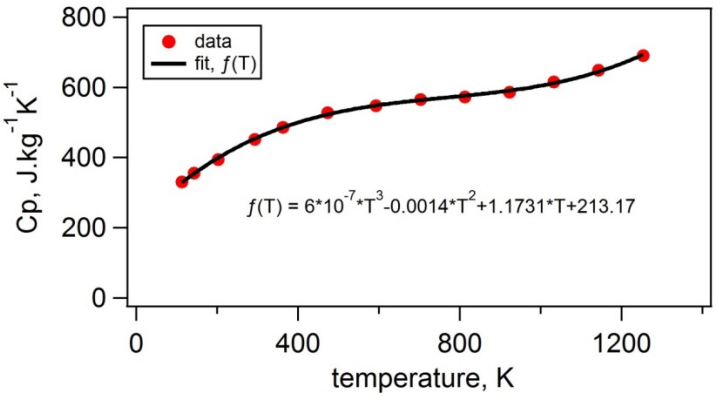

Figure 37 – Specific heat as function of temperature for 316 steel, measured datapoints from INCO [71] and polynomium fit

12.4 Temperature dependence of thermal conductivity

Data for thermal conductivity as a function of temperature was obtained by Ho and Chu [72]. A fit of the data, as shown in Figure 38, gives the following relation for thermal conductivity as function of temperature

$$k(T) = -2 \cdot 10^{-6} \cdot T^2 + 0.0179T + 8.3005 \text{ W/Km} \tag{182}$$

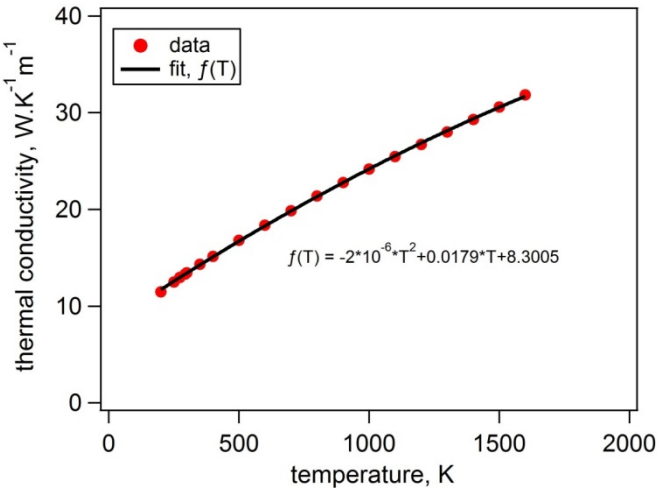

Figure 38 – Thermal conductivity as function of temperature for 316 steel, measured datapoints from Ho and Chu [72] and polynomium fit

12.5 Calculation of stress and strains taking into account temperature changes

The stress can be calculated as described for elastic-plastic stresses in section 8.1. However with varying temperatures the thermal strains are no longer equal to zero.

Thermal strain can be calculated from the temperature change, ΔT, by [58]

$$for\ i = j\ \ \varepsilon_{ij}^{th} = \alpha \Delta T, \qquad for\ i \neq j\ \varepsilon_{ij}^{th} = 0 \tag{183}$$

where α is the thermal expansion coefficient.

For austenitic stainless steel AISI 316 the average expansion coefficient for 385-920K is [73][74]

$$\alpha = 18.51 \cdot 10^{-6}\mathrm{K}^{-1} \tag{184}$$

The definition of the chemical-induced strain, ε_{ij}^{ch}, (see eq. 46) should also be considered

$$for\ i = j\text{:}\quad \varepsilon_{ij}^{ch}(c) = \frac{V(c)^{1/3} - V_{ref}^{1/3}}{V_{ref}^{1/3}} \tag{185}$$

$$for\ i \neq j\text{:}\quad \varepsilon_{ij}^{ch} = 0$$

Since the volume changes not only with concentration, but also with temperature.

The volume is found from the lattice parameter, a,

$$V = a^3 \tag{186}$$

and the change in the lattice parameter with temperature can be found from the thermal strain

$$\Delta a = \varepsilon^{th} \cdot a \tag{187}$$

The temperature dependence can thus be described using the thermal expansion coefficient

$$\Delta a = \alpha \cdot \Delta T \cdot a \tag{188}$$

and the volume as function of temperature can thus be found as

$$V(T) = \left(\alpha \cdot \Delta T \cdot a_{ref} + a_{ref}\right)^3 = \left((1 + \alpha \cdot \Delta T) \cdot a_{ref}\right)^3 = (1 + \alpha \cdot \Delta T)^3 V_{ref} \tag{189}$$

In section 5.3, the reference volume for zero concentration at room temperature was found to be

$$V_{ref}(20℃) = 4.7134 \cdot 10^{-29}\mathrm{m}^3 \tag{190}$$

Note that using this definition the volume arising from increasing concentration $V(c,T)$ becomes

$$V(c,T) = V(c,20℃)(1+\alpha \cdot \Delta T)^3 \tag{191}$$

Where the unitcell volume as function of nitrogen concentration $V(c_N, 20℃)$ was defined by eq. 44, to be

$$V(c_N,20℃) = 2.8147 \cdot 10^{-29}\mathrm{m}^3 \cdot \frac{c_N}{140924\mathrm{mol/m}^3 - c_N \cdot 0.59717} + 4.7134 \cdot 10^{-29}\mathrm{m}^3 \tag{192}$$

12.6 Calculation of composition profiles taking into account both influence from stress and varying temperatures

When a temperature gradient is present in the diffusion range, thermomigration should be considered, see for example Okafor et al. [83], Mathuni et al. [84] or Höglund and Ågren [85].

The diffusive flux of nitrogen atoms in te direction z under the influence of a temperature gradient $\frac{\partial T}{\partial z}$ and a chemical potential gradient in this species $\frac{\partial \mu_N}{\partial z}$ can be found from

$$J = -\frac{D_N c_N}{RT}\frac{\partial \mu_N}{\partial z} - \frac{D_N c_N Q^*}{RT^2}\frac{\partial T}{\partial z} \tag{193}$$

where $Q^*$is the heat of transport [83,84,85].

Giving the following generalized form of Fick's second law

$$\frac{\partial c_N}{\partial t} = \frac{\partial}{\partial z}\left(\frac{D_N c_N}{RT}\frac{\partial \mu_N}{\partial z} + \frac{D_N c_N Q^*}{RT^2}\frac{\partial T}{\partial z}\right) \tag{194}$$

12.7 Prediction of temperature profiles during heating or cooling

In reality when nitriding a sample, the furnace is heated, kept at the nitriding temperature, where nitrogen diffuses into the solid, and then subsequently cooled. Until now the heating and cooling have been ignored in this work.

Now, the temperature flow in the sample is calculated for a heating sequence.

To model the diffusive flow, very small elements of 0.1 µm were needed for a reasonable solution of the depths penetrated by nitrogen. These very small elements does however complicate using the explicit method for calculating the temperature profile described in section 12.1., since the thermal diffusivity is much faster than the nitrogen diffusivity. For a stable explicit calculation, the Fourier number has to be below 0.5 [58].

The Fourier number, *Fo*, is given by [58]

$$Fo = \frac{\alpha \Delta t}{\Delta z^2} \tag{197}$$

where, Δt is the timestep, Δz the element size and α is the thermal diffusivity which was given by eq. 176

$$\alpha = \frac{k}{\rho C_p} \tag{198}$$

To obtain $Fo < 0.5$ when using the data for specific heat, conductivity and density presented in section 12.2-12.4, for 445°C and using element sizes of 1 µm which is the largest value used in the concentration calculations, means that the time steps have to be

$$\Delta t < 1.07 \cdot 10^{-9} s \tag{199}$$

This would cause extreme calculation times, in order to obtain a number of steps that would provide representative nitriding times. Thus the temperatures are instead calculated using the implicit method where the equation used for calculating new temperatures, eq. 179, is changed to have the new time on the right side as well, so

$$\frac{T_i^{t+\Delta t} - T_i^t}{\Delta t} = \frac{1}{\rho_i \cdot C_p(i)} \left(\frac{k_{i+1} - k_{i-1}}{2\Delta z} \cdot \frac{T_{i+1}^{t+\Delta t} - T_{i-1}^{t+\Delta t}}{2\Delta z} + k_i \frac{T_{i+1}^{t+\Delta t} - 2T_i^{t+\Delta t} + T_{i-1}^{t+\Delta t}}{\Delta z^2} \right) \tag{200}$$

The equations are now solved simultaneously for all elements, with a Dirichlet condition at the surface; known temperature in the furnace, and a Neumann condition at the centre where we have a symmetry line and thus no flow. Details on implicit solving method are found in [58].

To test the how the temperature depth-profiles would be in the depths where diffusion occurs, a heating sequence was tested to the depth of 1000 μm, using time steps of 0.001 seconds. Note that diffusion depths have been seen to be below 100 μm. Figure 39 shows the temperature profile as function of time for the first second using an heating of the furnace of 400°C/hour, and what can be seen is that the heat travels so fast that the temperature is constant in the depths relevant to diffusion, when using the small time steps of 0.001 seconds.

A temperature-depth profile for a furnace heating of 400°C/s (which is unrealistically fast) is seen in Figure 40, and also here the heat penetrated fast enough that the surface and the depth of 1000 μm have the same temperature after each time-step.

It can thus be concluded that for the small depth ranges below 0.1 mm from the surface, relevant for the concentration depth profiles, the heat flow is so fast that the temperature can be considered constant even during heating and cooling. Thus the effect from a temperature gradient on the diffusion described in eqs. 193-196 can be neglected. The temperature level will however affect the diffusion coefficient during heating and cooling.

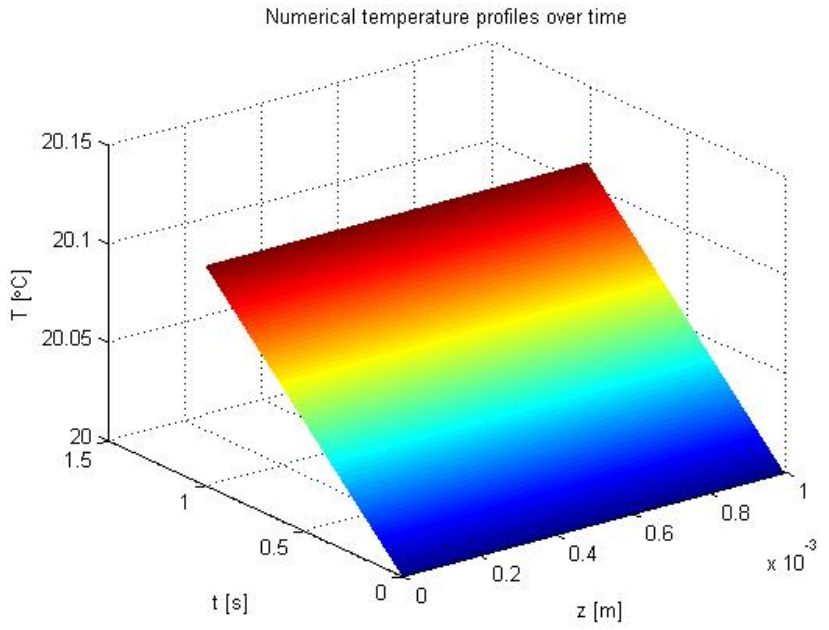

Figure 39 - Temperature-depth profiles inside the sample as function of time during the first second of simulation of a furnace heating of 400°C/hour.

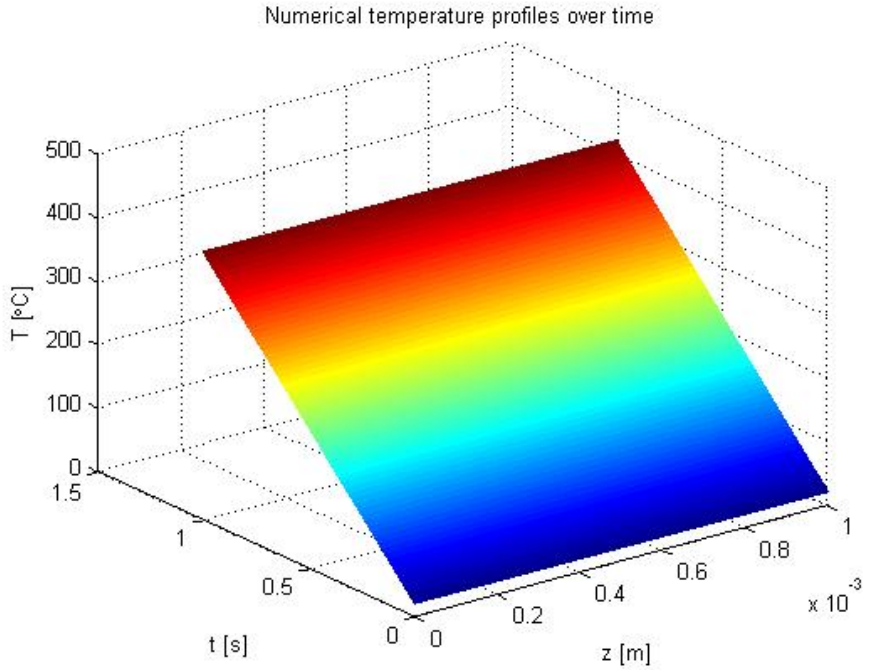

Figure 40 - Temperature-depth profiles inside the sample as function of time during the first second of simulation of an unrealistic extremely fast furnace heating of 400°C/s.

12.8 Prediction of concentration and stress-depth profiles when taking into account the expansion of the austenite lattice due to the temperature cycle in the furnace

In the previous section, it was shown that in the depth-ranges relevant to diffusion the temperature can be assumed constant with depth, and equal to the temperature in the furnace, since heat penetrates much faster than diffusion occurs.

Thus the heating and cooling which occur in a real thermochemical treatment can be included in the model, by assuming the temperature constant in space but varying with time for the depth range relevant for diffusion.

In reality the thermochemical treatment is usually done by heating from room temperature to the nitriding temperature, for example 445°C, and then holding the temperature constant for a specific nitriding time, after which the furnace is cooled to room temperature.

Modelling diffusion during heating and cooling would require knowledge of the dependency of the diffusion coefficient on temperature. Since the diffusion coefficient as function of concentration is only known at a few temperatures, a mathematical expression for the diffusion coefficient as function of both concentration and temperature is currently unknown. It is however known that the diffusion coefficient decreases with decreasing temperatures.

Thus for now, it will be assumed that no diffusion occurs during heating and cooling, implying that the composition only changes during the time where the temperature is kept constant at the nitriding temperature.

As described in section 12.5, the volume changes with temperature lead to a thermal strain.

In Figure 41, the resulting composition- and stress-depth profiles are shown for three cases. One where no heating or cooling is assumed, only a 22h holding period of 445°C, one with an initial heating sequence followed by a 22h holding period of 445°C, and one with an initial heating sequence, a 22h holding period of 445°C and then a 1h cooling period. In all cases the thermal expansion coefficient is assumed to be constant equal to the average value for austenite $\alpha = 18.51 \cdot 10^{-6}\mathrm{K}^{-1}$ [73].

Figure 41 displays that when assuming no composition change during heating or cooling, then the thermal strain, which is constant with depth, does not affect the predicted stress-depth profile. This is because the samples are assumed to be allowed to expand as long as it expands equally with depth, (i.e. a constant total strain with depth is assumed). Thus, since the temperature changes with time do not give rise to any temperature-depth gradients, there will not be any stresses predicted, just expansion arising from the temperature changes.

It should be noted here that if the samples are thick enough and the cooling proceeds fast enough, such that a temperature gradient occurs, additional residual stresses will occur as a result of the temperature gradient during cooling [59].

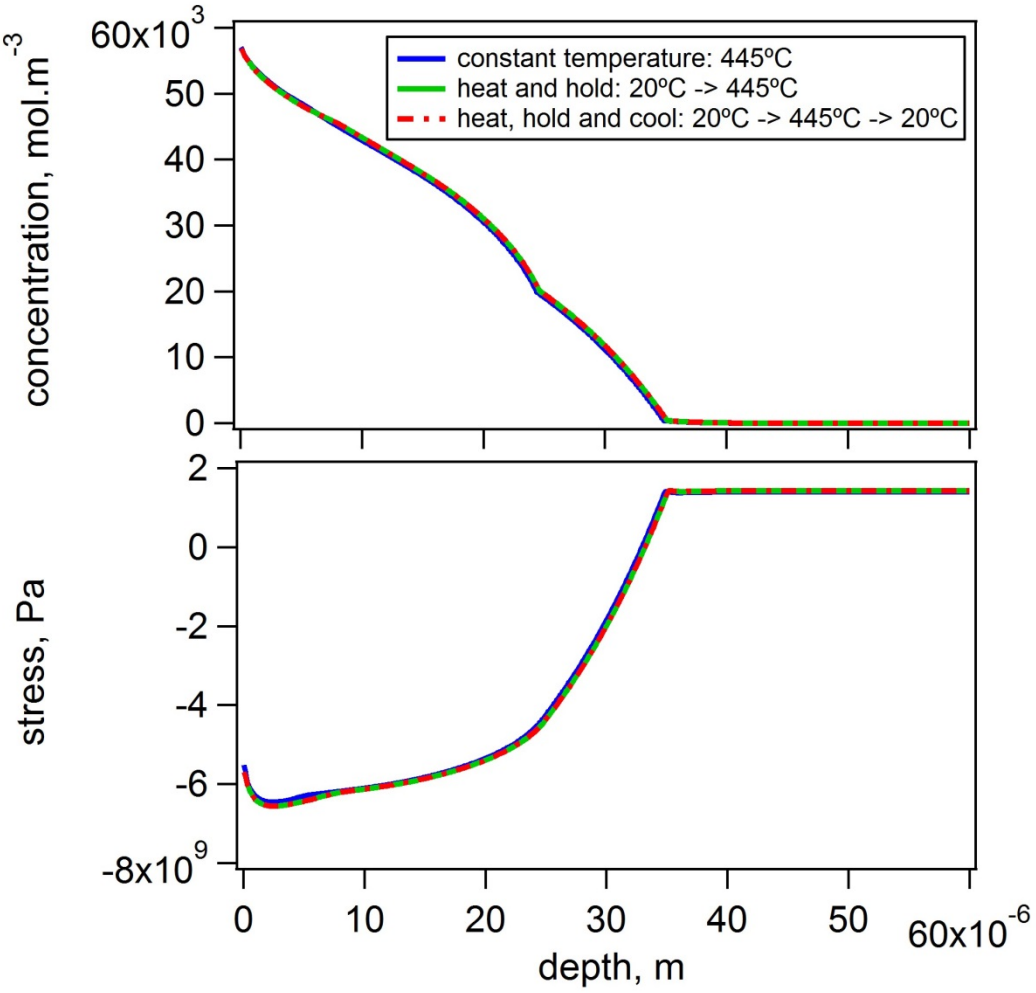

Figure 41 - concentration and stress-depth profiles resulting from simulation of nitriding with a nitriding potential of 1000, for various temperature cycles. For all temperature cycles the holding time at 445°C was 22h, heat and cooling times were 1h.

12.9 Effect of concentration on thermal expansion coefficient

Residual stresses resulting from thermal strains arise due to gradients in thermal strains. Gradients in the thermal strains can arise due to temperature gradients or due to gradients of the thermal expansion coefficient. For the depths in where diffusion occur, no temperature gradients was found, as discussed in section 12.7. However, thermally induced stresses should still be considered, since recent measurements by Brink [73] reveals that the thermal expansion coefficient in expanded austenite depends on the concentration. Given that a concentration gradient is present during cooling after nitriding, the dependency of the thermal expansion coefficient on concentration is now explored.

Experimental results, as determined with in situ heating during synchrotron X-ray diffraction from Brink [73], for nitrogen- and carbon-expanded austenite are given in Table 2 and Table 3 respectively. From the measurements it can be seen that for the fractional occupancy of 0.33 the thermal expansion coefficient depends on temperature. This is due to the difference between paramagnetic and ferromagnetic expanded austenite [73].

Table 2 - Thermal expansion coefficient for nitrogen expanded austenite. Source Brink [73]

Fractional occupancy, y_N	Temperature range, T [K]	Thermal expansion coefficient, α [K^{-1}]
0.0	385-920	$18.51 \cdot 10^{-6}$
0.14	385-787	$18.91 \cdot 10^{-6}$
0.33	341-549	$9.66 \cdot 10^{-6}$
0.33	572-808	$15.3 \cdot 10^{-6}$
0.56	385-657	$14.3 \cdot 10^{-6}$

Table 3 - Thermal expansion coefficient for carbon expanded austenite. Source Brink [73]

Fractional occupancy, y_C	Temperature range, T [K]	Thermal expansion coefficient, α [K^{-1}]
0.18	413-767	$18.2 \cdot 10^{-6}$
0.22	385-657	$18.4 \cdot 10^{-6}$

In order to mathematically describe the dependency of thermal expansion on concentration and temperature, a parametrization is done, as shown in Table 4. The Curie temperature, where the ferro-paramagnetic transition occurs, is here taken as 550K, consistent with magnetometry measurements on samples containing nitrogen levels in the relevant range [73]. It is noted that this parametrization is rough, and that future experimental work could massively improve the accuracy of the expressions. The data and parametrizations are displayed in Figure 42.

Table 4 – parametrization-functions for thermal expansion coefficients as function of concentration and temperature

Fractional occupancy, y_N	**Temperature range, T [K]**	**Thermal expansion coefficient, α [K^{-1}]**
0-0.22	all T	$\alpha = 18.51 \cdot 10^{-6}$
0.22-0.33	$T < 550$	$\alpha = 3.588 \cdot 10^{-5} - 7.9455 \cdot 10^{-5} \cdot y_N$
0.22-0.33	$T > 550$	$\alpha = 2.46 \cdot 10^{-5} - 2.8182 \cdot 10^{-5} \cdot y_N$
0.33-0.56	$T < 550$	$\alpha = 3.0026 \cdot 10^{-6} + 2.0174 \cdot 10^{-5} \cdot y_N$
0.33-0.56	$T > 550$	$\alpha = 1.6736 \cdot 10^{-5} - 4.3478 \cdot 10^{-6} \cdot y_N$
0.56 and up	all T	$\alpha = 14.3 \cdot 10^{-6}$

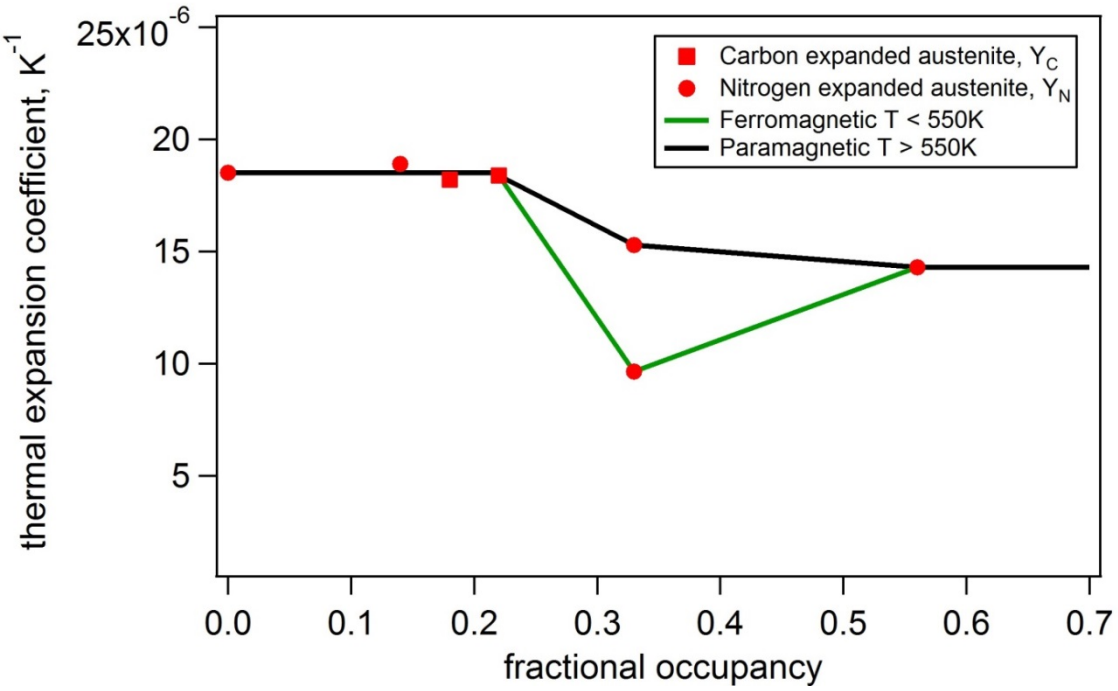

Figure 42 - Thermal expansion coefficients from [73] as function of concentration expressed as fractional occupancy, and lines representing a parametrization of the data.

12.10 Prediction of concentration and stress-depth profiles after temperature cycle in the furnace, taking into account effect of variation of thermal expansion coefficient

It was established in section 12.5 that a thermal strain gradient, can give rise to additional stresses besides the concentration-induced. Thermal strain gradient arises due to gradients in temperature or gradients in thermal expansion coefficient. It was shown in section 12.9 that variations in concentration lead to variations in thermal expansion coefficient. For the case of a thermal cycle in nitriding consisting of heating, holding at constant temperature where nitrogen diffuses into the sample and subsequent cooling, a concentration profile will be present during the cooling part, and thus a thermal strain gradient can arise due to the gradient in thermal expansion coefficient. A thermal expansion coefficient-depth profile corresponding to a concentration-depth profile resulting from 22h nitriding with nitriding potential of 1000 is shown in Figure 43.

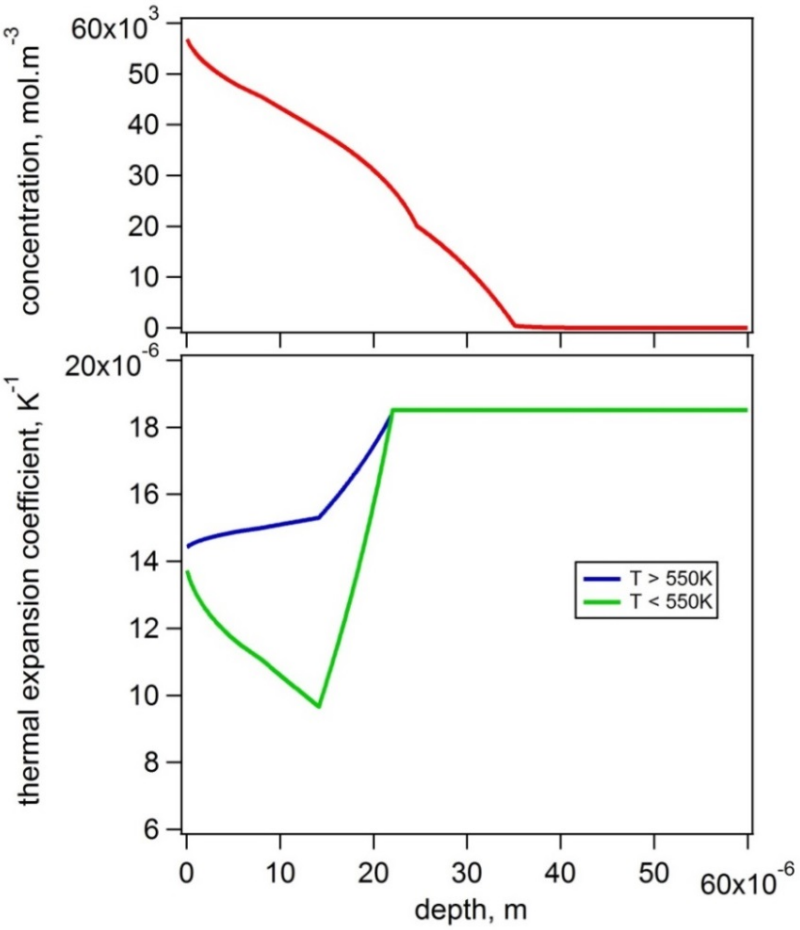

Figure 43 - Thermal expansion coefficient gradient resulting from concentration gradient. Concentration-depth profile is reproduced from Figure 41.

Examining Figure 43, it is seen that the concentration-depth gradient indeed leads to gradients in thermal expansion coefficient. So considering the case of nitriding with a thermal cycle of 1h heating from 20°C to 445°C, 22h nitriding at 445°C, and then 1h cooling to 20°C, taking into account the concentration dependence of the thermal expansion coefficient in the simulation, should thus lead to a change in the resulting stress-depth profile, compared to when assuming a constant thermal expansion coefficient. Results of such simulations are shown in Figure 44, where it can be seen that the thermal expansion coefficient gradient leads to a small change in the predicted stress-depth profile near the surface. Zooming in on the surface area, as shown in Figure 45, it can be seen that including the concentration dependency of the thermal expansion coefficient leads to an increase of compressive surface stresses in the order of 400MPa.

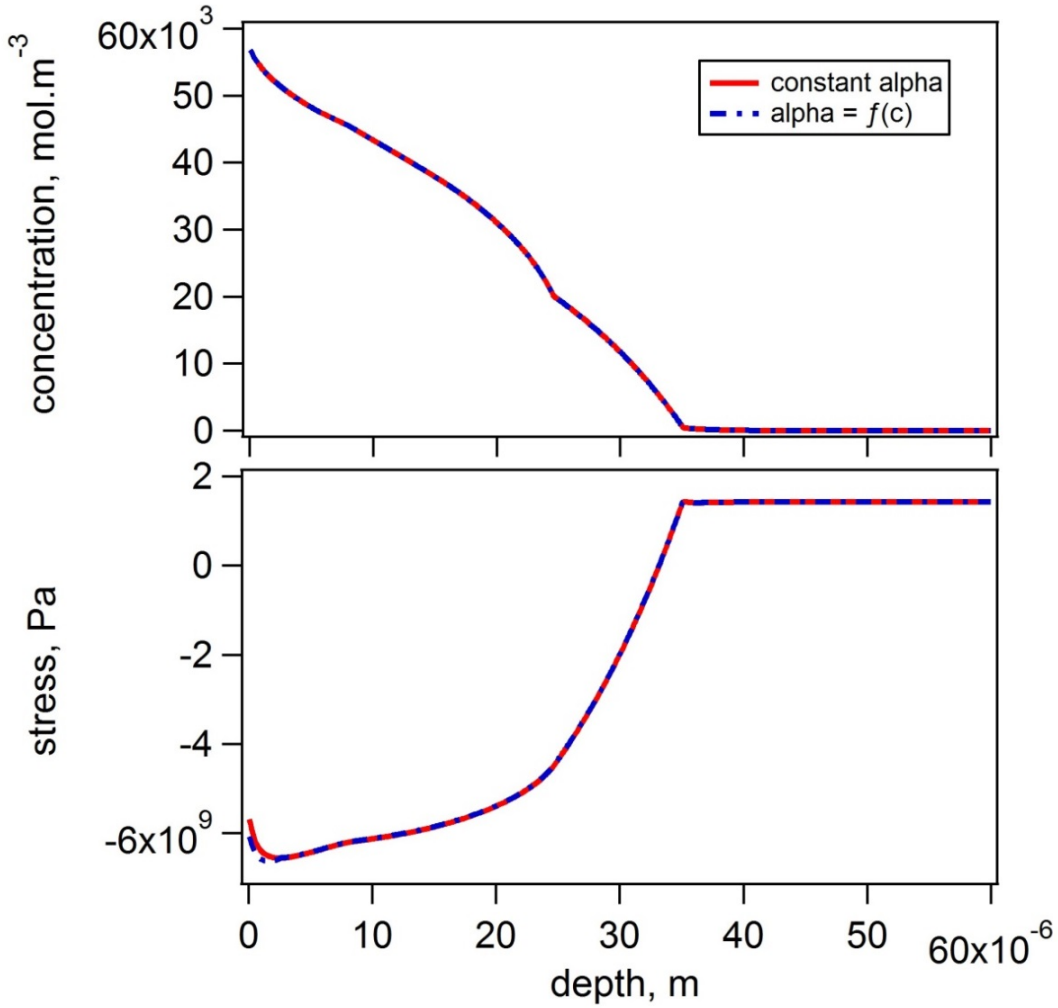

Figure 44 – Difference between assuming constant thermal expansion coefficient (constant alpha) and concentration dependent thermal expansion coefficient (alpha = f(c)). concentration and stress-depth profiles are resulting from simulation of nitriding with nitriding potential of 1000 on a sample of thickness 300µm, using a temperature cycle of 1h heating from 20°C to 445°C, then 22h nitriding at 445°C, and then 1h cooling to 20°C.

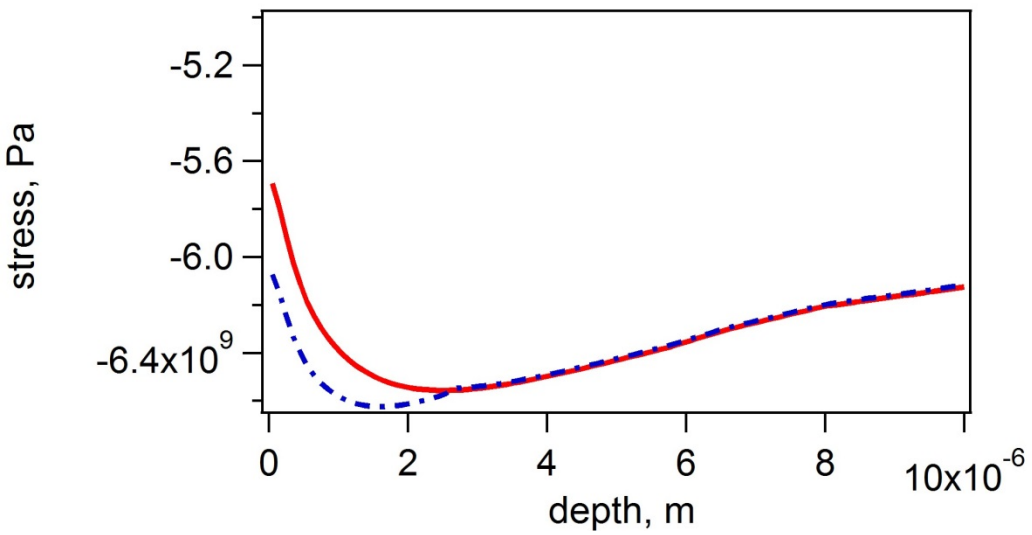

Figure 45 - Zoom in on surface region of stress-depth profiles shown in Figure 44

13. Denitriding experiments

As recognized in section 12.8 modelling of diffusion during the entire nitriding process including the heating and cooling sequence requires further knowledge about how the diffusion coefficient of nitrogen depends on temperature. To explore this and to obtain knowledge about solubility, nitriding-denitriding experiments were conducted.

13.1 Experimental

Samples were cut from 12.5µm thin foils of 316 austenitic stainless steel. Sample sizes were limited to approximately 15mm x 15mm due to the space in the thermobalance. A total mass of samples of approximately 700-900mg was used in each test.

Prior to nitriding, the samples were heat-treated at 1050°C in a hydrogen atmosphere in a horizontal tube furnace, in order to recrystallize and transform any martensite, that might have been introduced during cold rolling of the foils, into austenite.

Gaseous nitriding and subsequent stepwise denitriding were done in a Netzsch STA 449 F3 thermobalance, where temperature and gas-flow can be controlled simultaneously, while the sample mass is recorded.

Samples were heated and nitrided in an atmosphere of pure ammonia at 445°C. After saturation with nitrogen, the temperature was changed to the testing temperature and kept at the testing temperature until equilibrium was obtained. Then step-wise denitriding was carried out by changing the gas composition and thus the nitriding potential.

An example of a nitriding-denitriding curve is given in Figure 46.

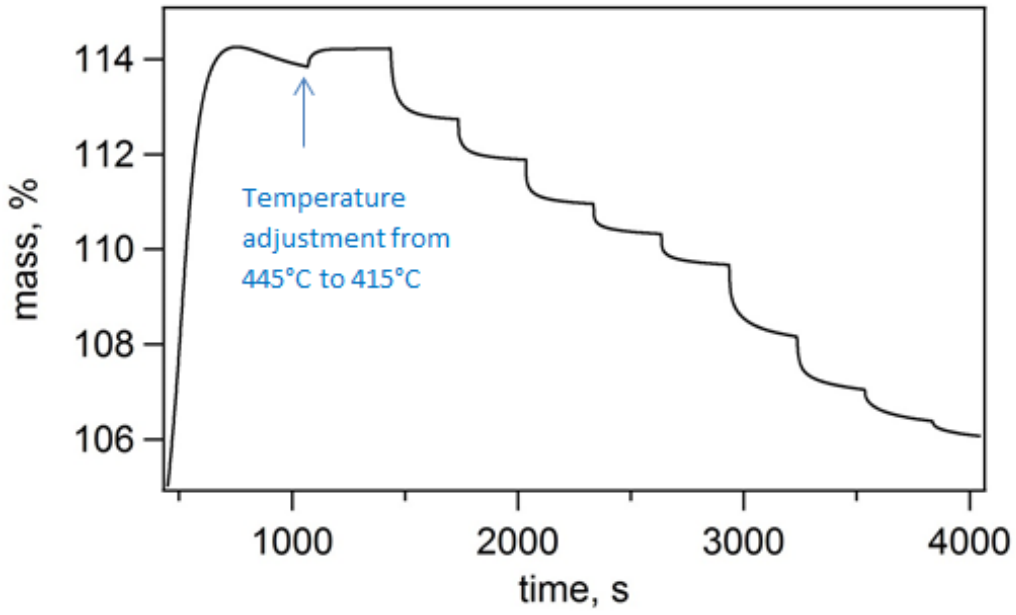

Figure 46 - Denitriding curve for nitriding at 445°C and subsequent denitriding at 415°C, mass is given as a percentage of original mass

13.2 Theoretical background for determining diffusion coefficient from denitriding experiments

To determine the concentration-dependent diffusion coefficient for different temperatures, the method of using denitriding data from thermogravimetric experiments described by Christiansen and Somers [34], [75] was applied.

Gaseous nitriding and denitriding can be described by equations for absorption and desorption in a plane sheet provided that diffusion of nitrogen in the solid state is the rate determining step. This diffusion in a plane sheet was described by Crank [76].

For a sheet with thickness $2L$, where the initial concentration of the diffusing species is c_0, and the surface concentration is c_s, the concentration as function of time and distance from the centreline $c(x,t)$ is

$$\frac{c(x,t)-c_0}{c_s-c_0} = 1 - \frac{4}{\pi}\sum_{n=0}^{\infty}\frac{(-1)^n}{2n+1}\cdot\exp\left(\frac{-\overline{D}(2n+1)^2\pi^2 t}{4L^2}\right)\cdot\cos\left(\frac{(2n+1)\pi x}{2L}\right) \quad (201)$$

where the centre-line of the sheet is defined as the $x = 0$ for the distance, thus $-L < x < L$, and where $\overline{D}$ is the average diffusion coefficient over the concentration range $c_s - c_0$, [75]

$$\overline{D} = \frac{1}{c_s - c_0} \int_{c_0}^{c_s} D(c) dc \tag{202}$$

where $D(c)$ is the concentration dependent diffusion coefficient as function of concentration.

The total amount of diffusing species which has entered or left at time, t, is then given by

$$\frac{M(t)}{M_\infty} = 1 - \sum_{n=0}^{\infty} \frac{8}{(2n+1)^2 \pi^2} \cdot \exp\left(\frac{-\overline{D}(2n+1)^2 \pi^2 t}{4L^2}\right) \tag{203}$$

where M_∞ is the total amount of diffusing species which has entered or left after infinitely long time.

During thermogravimetric experiments the mass of the sample is recorded as a function of time, and denitriding can be done in steps by controlling the gas-composition. For each of the denitriding steps the equation 203 can then be fitted, to find the average diffusion coefficient $\overline{D}$. As follows from eq. 202 the determination of the diffusion coefficient by approximation of $D(c)$ with $\overline{D}$ is better the narrower the concentration range over which it was experimentally measured.

Christiansen and Somers [75] noted, that since the gas concentration does not shift instantaneously and the surface reaction in denitriding is not infinitely rapid, eq. 203 does not apply at the very beginning of the profile steps. Accordingly, in this work fitting of eq. 203 to the denitriding curve was done in the time range 10minutes to 3hours after regulating the gas.

The concentration range can be calculated from the mass of nitrogen, m_N, and the initital mass of steel, using the molarmass of nitrogen, M_N, and the equivalent to molar mass for the 316 steel.

Since the atoms in the f.c.c. lattice equal the number of octahedral interstitial sites that the nitrogen can occupy, the fractional occupancy can be found from the fraction of nitrogen atoms to atoms in the original sample.

$$y_N = \frac{m_N / M_N}{m_{316} / M_{316}} \tag{204}$$

The concentration can then be found from the fraction occupancy using eq. 42.

Taking into account the major contributing elements in the 316 stainless steel, the composition in weight percent can be described as [27]; 77%Iron, 17%Chromium, 12%Nickel, 2%Molybdenum and 2%Manganese. This gives

$$M_{316} = 0.77 \cdot M_{Fe} + 0.17 \cdot M_{Cr} + 0.12 \cdot M_{Ni} + 0.02 \cdot M_{Mo} + 0.02 \cdot M_{Mn} = 61.9\text{g/mol} \quad (205)$$

13.3 Evaluation of experimentally determined diffusion coefficients

Determination of diffusion coefficients as a function of concentration and temperature was done from the denitriding curves as described in section 13.2. The resulting diffusion coefficients as function of concentration for varying temperatures are given in Figure 47.

For a constant temperature, the concentration dependence can be approximated by a Lorentzian type function,

$$D = y_0 + \frac{A}{(c - x_0)^2 + B} \quad (206)$$

where A, B, y_0 and x_0 are fitting parameters. The Lorentzian type fits are shown in Figure 47.

The data for 445°C shows an odd behavior, which is probably explained by formation of N_2 at the surface. N_2 formation could lead to porosities after prolonged time at the high temperature, which would cause a change of the maximum diffusion distance in the sample (L) and thus give wrong results from the fitting. The data measured at 445°C will thus not be considered when evaluating the diffusion coefficient results. The reason why porosity is suspected is that a loss of mass is observed after saturation is obtained at 445°C. When lowering the temperature for denitriding the saturation mass is obtained again after cooling to the denitriding temperature (see Figure 46). A temperature around 460°C is generally considered as the temperature where desorption of N_2 from an iron based surface can occur [77]. Then the amount of nitrogen in solid solution is the outcome of a balance of the dissociation of NH_3 and the desorption if N_2, i.e. a stationary state, rather than equilibrium. Frequently, the formation of N_2 has been observed to lead to N_2-filled holes, particularly for phases with a high nitrogen content as for example iron nitrides, (see [77]).

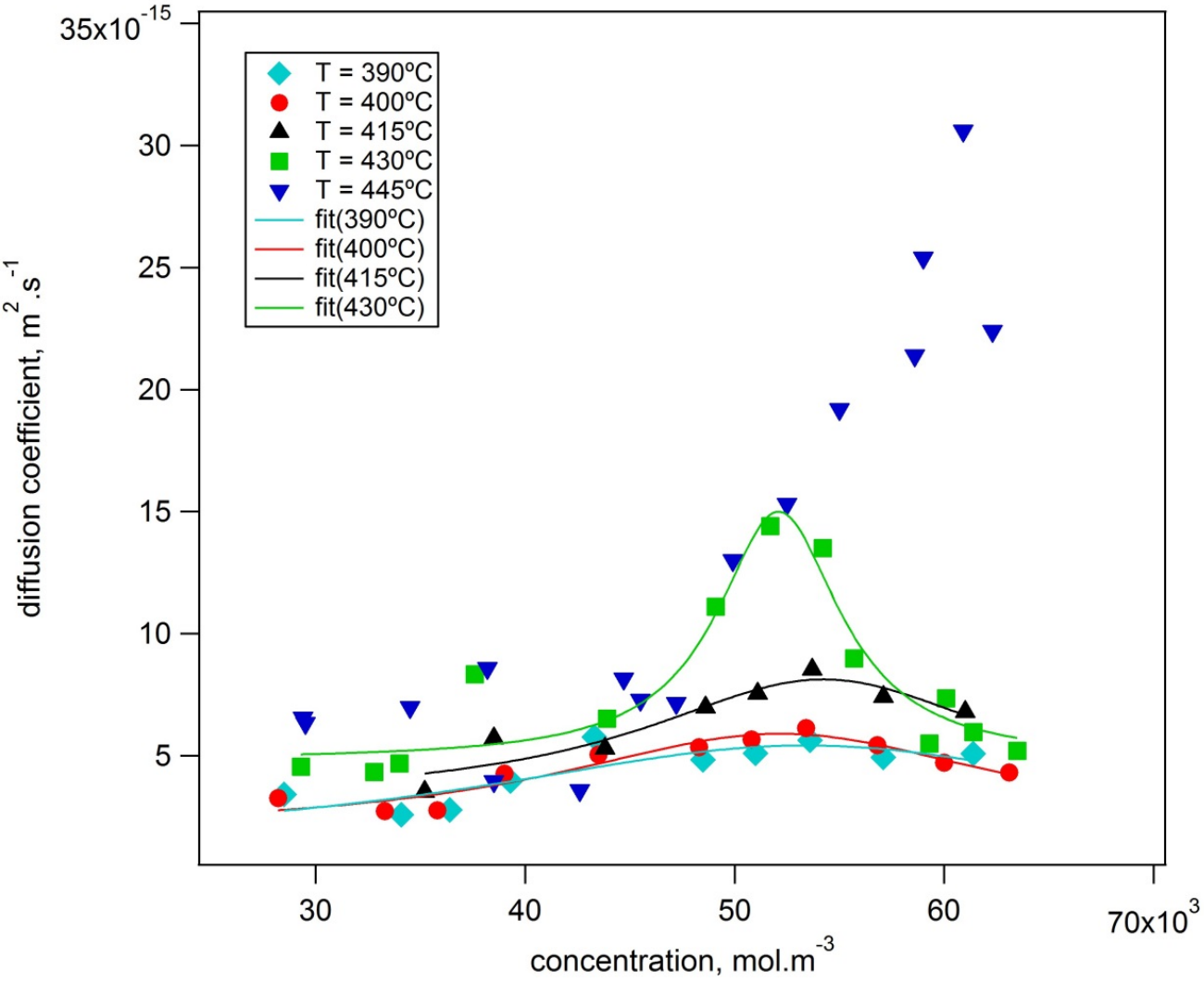

Figure 47 - Measured diffusion coefficients for varying temperatures and Lorentzian fits

Comparing the measured diffusion coefficients presented in Figure 47 to the ones measured by Christiansen and Somers [36], which were shown in Figure 8, (and applied in the previous chapters in this work) the same trend is seen with a Lorentzian type concentration dependency, with a maximum around 52000mol/m^3 for these measurements and around 50000mol/m^3 for the data in [36]. The absolute values differ by about a factor two, where the diffusion coefficients measured in this work are highest. Besides the insecurities arising from the fitting procedure, the differences might be explained by the fact that the samples in [36] were nickel coated, whereas the samples in this work were uncoated. The influence of the very thin (approximately 20nm) nickel coating could be discussed as follows. The rate of the surface reactions, i.e. N_2 and NH_3 formation, is determined by the condition at the surface. A difference in the rates of surface reactions and the occurrence of

mixed rate control of solid state diffusion and surface reaction, would lead to different apparent diffusion coefficients. Alternatively, for the nickel coated samples, the nitrogen atoms do not diffuse only through stainless steel, but at the 20nm closest to the surface diffusion occurs through Ni. The solubility of nitrogen in nickel is much lower than in expanded austenite, while the lattice parameter of f.c.c. nickel is smaller than for austenite. Then, it is anticipated that the diffusion of nitrogen in nickel proceeds more slowly than in expanded austenite. This is consistent with the relatively shallow case depth of expanded “austenite” on nickel-based alloys (see Eliasen et al. [78]). It is noted that, apart from the nickel coating, the main difference between present experiments and those described in [36] is the sample sizes. The use of larger samples in this work in principle should give more accurate results.

13.4 Determination of activation energies

For a certain concentration, the temperature dependence of the diffusion coefficient is expected to be described by the Arrhenius-type equation [31];

$$D(T) = D_0 \cdot \exp\left(\frac{-Q}{RT}\right) \tag{207}$$

where Q is activation energy and R is the gas constant.

To determine the activation energy and D_0, a linear fit of the type $y = ax + b$ is made to an Arrhenius plot of $\ln(D)$ as function of the reciprocal temperature, as seen in Figure 48.

Since

$$\ln(D) = \ln(D_0) - \left(\frac{Q}{R}\right) \cdot \left(\frac{1}{T}\right) \tag{208}$$

the activation energy and the pre-exponential factor, D_0, can be obtained from the slope and intersection of the linear fit. Using the fits for D for the temperatures 390, 400, 415 and 430°C, gives the Arrhenius plot shown in Figure 48.

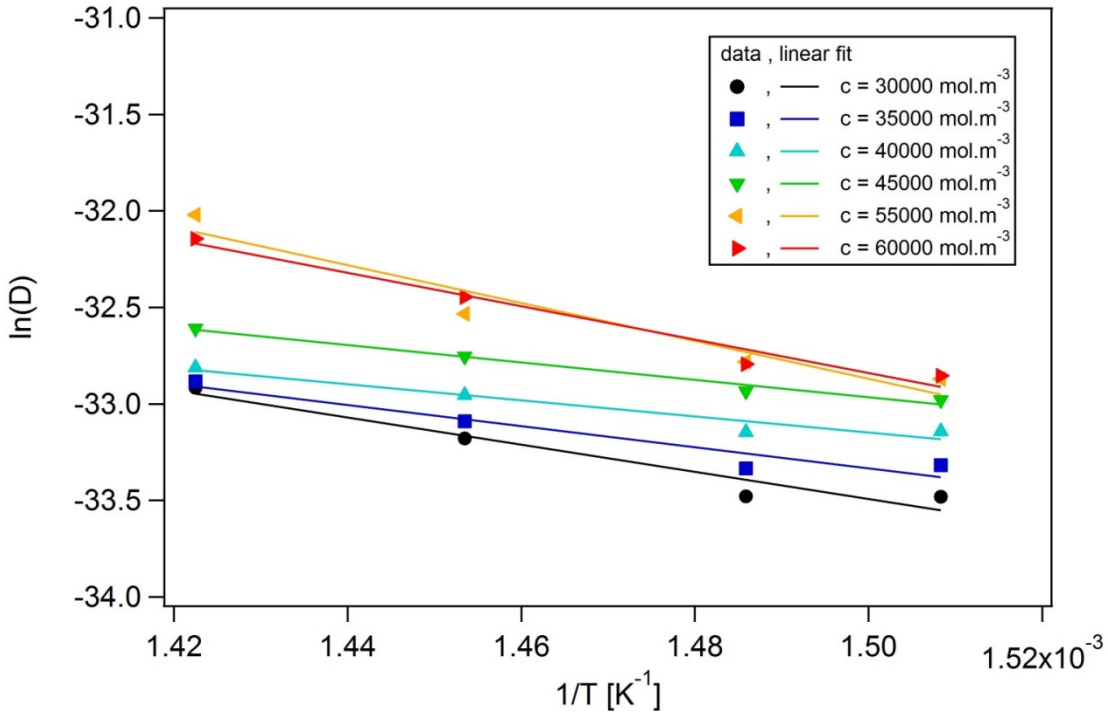

Figure 48 - Arrhenius plot using fits of diffusion coefficient data

The activation energies found, are given in Figure 49, which shows a decrease of the activation energy with increasing nitrogen concentration until a point where the activation energy increases again.

Eckel and Manning [79] reported activation energies of 108-120kJ (25800-28700cal) for low contents of nitrogen in austenitic stainless steel, and Wells et al. [80] reported activation energies decreasing from 150.6kJ (36000cal) to 117.2kJ (28000cal) with carbon contents increasing from 1at.% (1401mol/m^3) to 5at.% (6842mol/m^3). The initial trend of decreasing activation energy with increasing nitrogen concentration is thus consistent with previously published data. The increase of activation energy for high nitrogen concentrations could possibly be explained by a change in the diffusion mechanism, but further investigations should be made to examine this phenomenon.

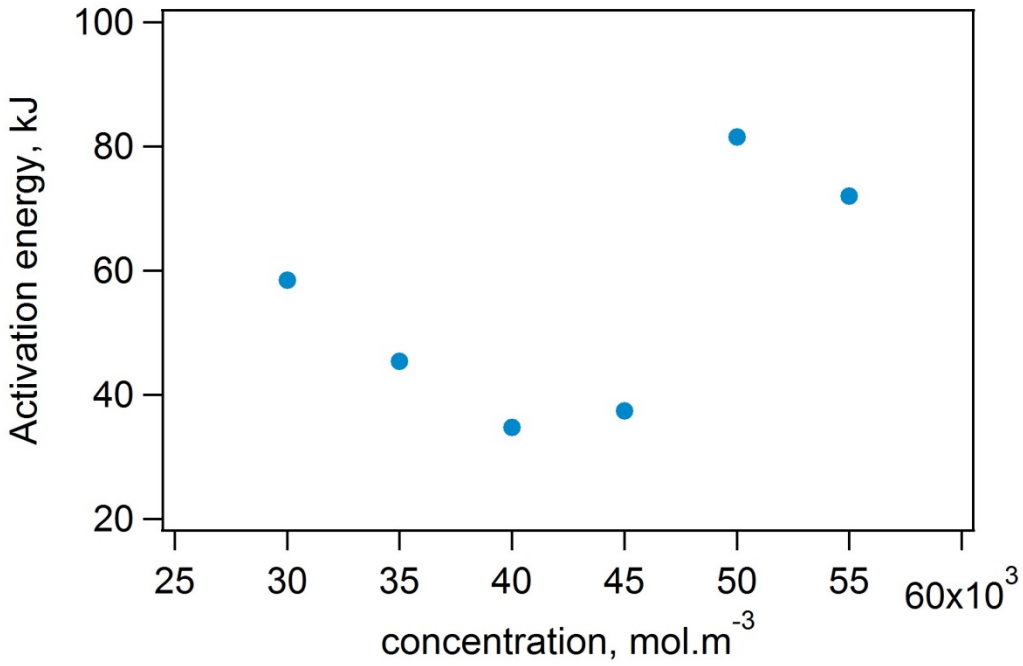

Figure 49 - Activation energies, Q, as function of concentration

13.5 Determination of expression for diffusion coefficient as function of concentration and temperature

For the temperatures evaluated the concentration dependence was seen, in section 13.3, to follow a Lorentzian type function,

$$D = y_0 + \frac{A}{(c - x_0)^2 + B} \tag{209}$$

where A, B, y_0 and x_0 , are fitting parameters which depends on temperature. The temperature dependences are evaluated below, in order to give an expression for diffusion coefficient as function of temperature and nitrogen concentration.

Figure 50 shows x_0 as function of temperature. x_0 seems to be largely temperature independent with an average value of

$$x_0(T) = 52961 \tag{210}$$

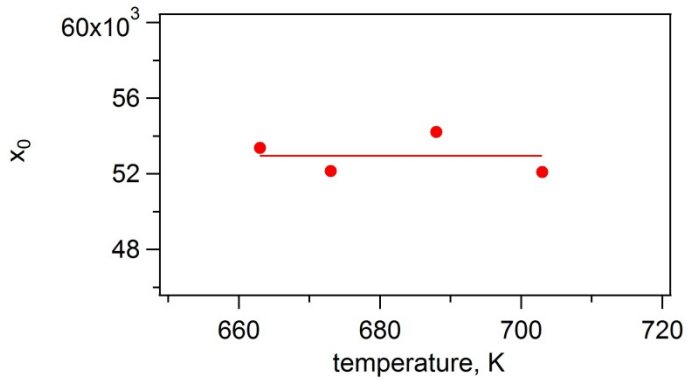

Figure 50 - x_0 as a function of temperature

Figure 51 shows y_0 as function of temperature [K]. y_0 is clearly temperature dependent and an exponential fit is done with the fitting function

$$y_0(T) = -1.4011 \cdot 10^{-15} + 1.5709 \cdot 10^{-15} \cdot \exp\big(0.022194(T - 641.31)\big) \tag{211}$$

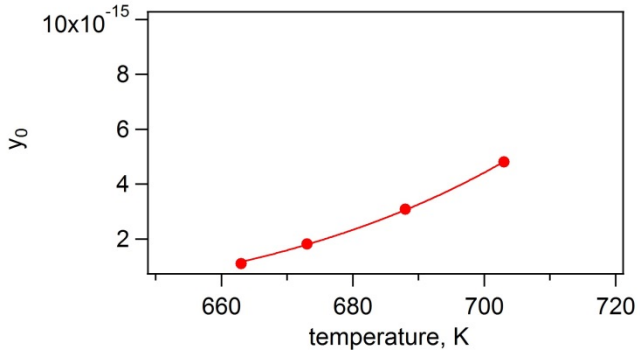

Figure 51 - y_0 as a function of temperature

Figure 52 shows A as function of temperature [K] and an exponential fit with the fitting function

$$A(T) = 2.04 \cdot 10^{-7} + 1.6497 \cdot 10^{-6} \cdot \exp\left(-0.085818(T - 661.28)\right) \tag{212}$$

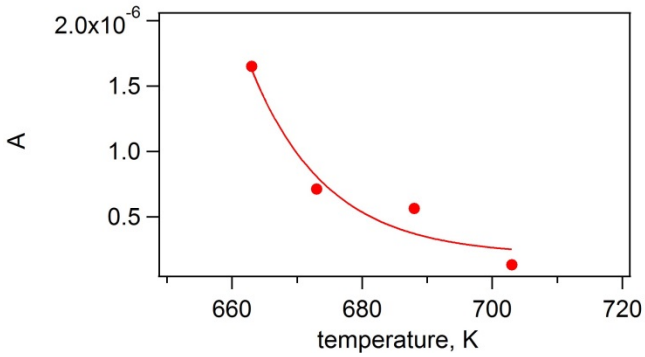

Figure 52 - A as a function of temperature

Figure 53 shows B as function of temperature [K] and an exponential fit with the fitting function

$$B(T) = 7.1091 \cdot 10^{6} + 4.1838 \cdot 10^{8} \cdot \exp\left(-0.066925(T - 661.12)\right) \tag{213}$$

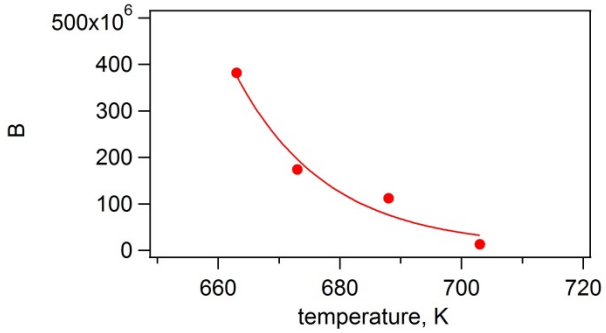

Figure 53 - B as a function of temperature

Inserting the fits of $x_0(T)$, $y_0(T)$, $A(T)$ and $B(T)$ gives the fit shown in Figure 54, for the diffusion coefficient as function of concentration and temperature.

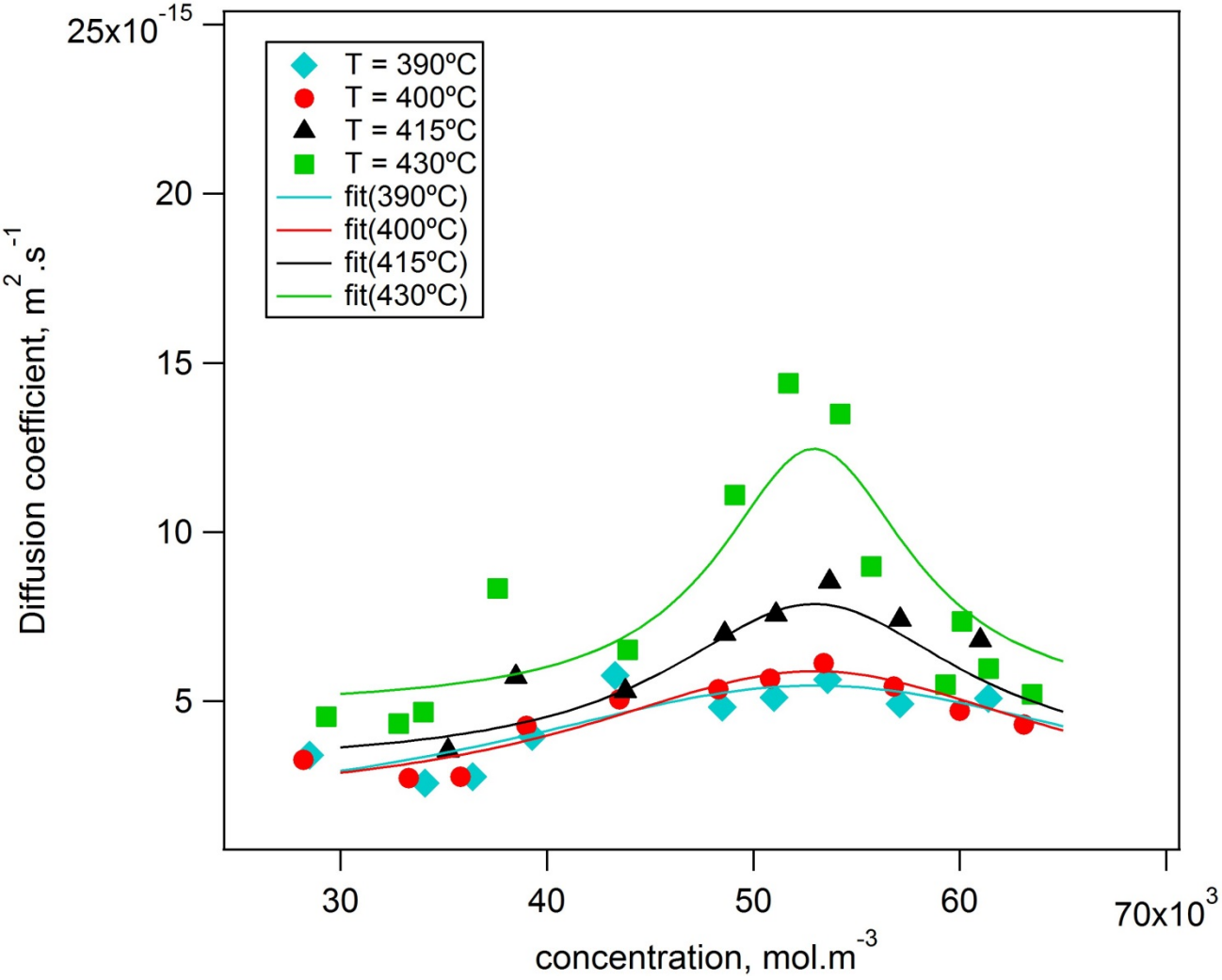

Figure 54 - Measured diffusion data and final fit of D as function of temperature and concentration

13.6 Solubility data

The absorption-desorption sequence for finding the diffusion coefficient, measured as described in section 13.1, also provides information about the equilibrium relation between the nitriding potential and the concentration of nitrogen in solid solution for a stress free sample of uniform composition.

The nitriding potential in each denitriding-step is determined from the gas composition in the step using eq. 8. From the mass-time curves measured (as for example Figure 46) the equilibrium mass can be determined at the end of each step, and the corresponding nitrogen concentration can then be found using eq. 204.

The nitriding concentration, expressed as fractional occupancy, is plotted as function of the activity in Figure 55. The activity is determined from the nitriding potential in the gas and the temperature dependent reaction equilibrium constant, K_T, using eq. 15.

The results are comparable to measurements reported by Christiansen and Somers in [25], for AISI 316 austenitic stainless steel at 693K and 718K which are also shown in Figure 55. So even for the larger temperature span examined in this work the trends are reproducible.

The differences observed between the results in [25] and those obtained in this work could be due to the use of not exactly the same expressions for K_T, or the fact that the measurements made in this work are made with thicker samples and larger sample sizes, which should theoretically provide more precise results.

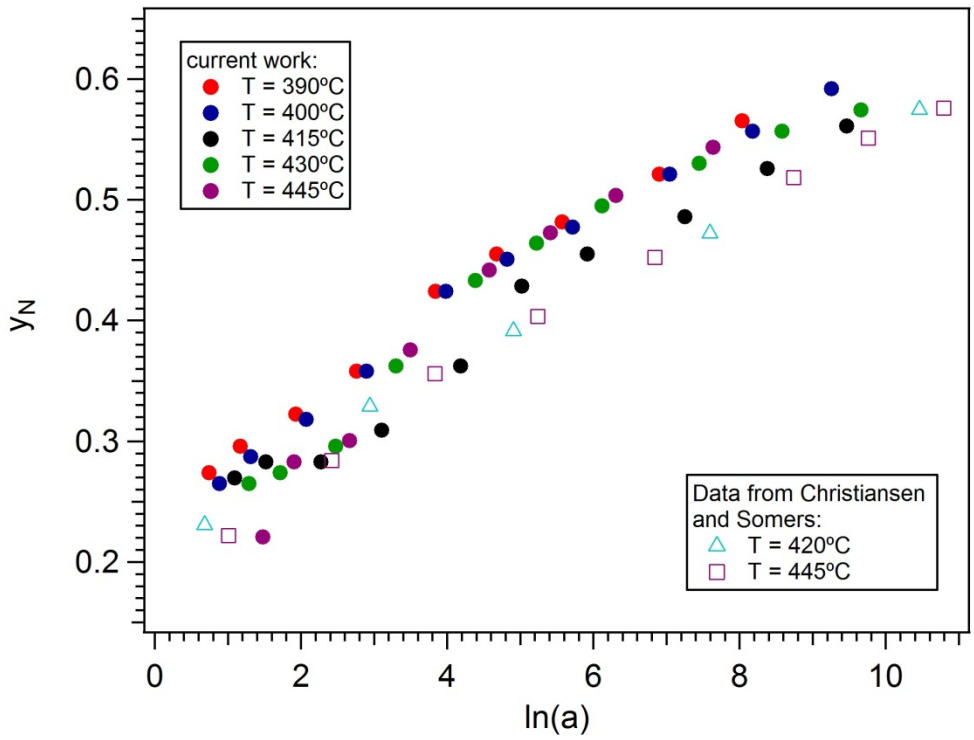

Figure 55 – Nitrogen solubility as function of activity in expanded austenite for nitriding of AISI 316 at various temperatures. Concentrations are given as fractional occupancy, y_N.

14. Limitations of the model and comparison to experimental work

The most important novel approaches in the model presented in this work are the coupling of composition and composition-induced stress (rather than a pragmatic linear relation between stress and concentration), and inclusion of plastic deformation, taking into account the occurrence of solid solution strengthening. Concentration and temperature dependency of material properties were explored, but some practical approaches were applied which limit the model. When examining the effect of stress-state present in the samples prior to nitriding, the assumption of rotational symmetry in the surface plane limits the applicability of the model, which cannot be applied to simulate cases such as uniaxial tensile loading.

In this work the nitrogen diffusion during heating and cooling sequence was ignored, due to insufficient knowledge about the diffusion behaviour at lower temperatures. So no diffusion was assumed to occur before the nitriding holding temperature was reached, and no diffusion was assumed during cooling. However, some diffusion will probably occur at the highest temperature during heating and cooling, especially if the heating/cooling is very slow. During cooling thermal stresses were shown to be the result of variation in the thermal expansion coefficient with nitrogen concentration. The interactions between thermal stresses, composition-induced stresses and diffusion occurring during heating/cooling might lead to changes in the predicted stress- and composition depth profiles.

Compressive surface stresses in the order of 6-10GPa, depending on the sample thickness assumed, are predicted by the model presented in this work. Experimentally, compressive stresses have been reported of 7-8 GPa for nitriding of austenitic stainless steel [1]. However, these values were very recently shown to be a consequence of inappropriate elastic constants, which appear to depend strongly on the nitrogen concentration, such that a reversal of the elastic anisotropy occurs over the composition range [37]. Thus when comparing the values predicted by the model to experimentally measured values, it should be kept in mind that both the simulation and the method used to determine stresses from measurements have limitations, and thus the correspondence between results is reasonable.

To examine the validity of the concentration-depth profiles predicted by the model developed in this work, experimentally determined concentration-depth profiles are compared to the profiles predicted from the model for the case of 22h hour nitriding. Compositions determined with X-ray diffraction analysis of AISI 316 nitrided for 22h at infinite nitriding potential and at 430°C are compared with predicted nitrogen concentration-depth profiles in Figure 56. Clearly, the nitrogen concentrations at the surface predicted by the model are in excellent agreement with the experimental values. However, the model appears to overestimate the case depth by about 80 %.

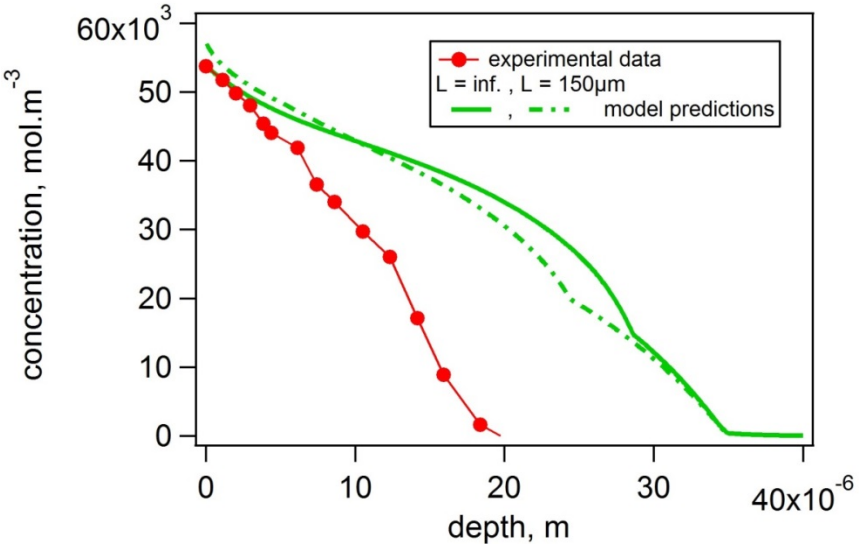

Figure 56 - comparison between experimentally determined concentration-depth profile from 22h nitriding with infinite nitriding potential from Christiansen and Somers [2] and concentration depth profile predicted by modelling 22h nitriding with nitriding potential of 1000.

In order to understand this overestimation, the experimental time-dependent nitrogen uptake in stainless steel during nitriding is compared to that for the model presented by Christiansen et al. in [34], assuming local equilibrium at the surface (see Figure 57). Also here the diffusion model overestimated the nitrogen uptake, for the case that the surface concentration was assumed to be reached instantaneously at the onset of nitriding. Evidently, experimentally the nitrogen uptake proceeds very slowly at the beginning of nitriding, most likely because the kinetics of the surface reaction dominate the nitrogen uptake in the early stage. After an acceleration of the experimental nitrogen uptake curve, is runs parallel with predicted nitrogen uptake (see Figure 57). A similar discrepancy can be expected for the present diffusion model and the experimental results (Figure 56). Attempts to account for the slow initial nitrogen uptake by including the influence of the kinetics of the surface reaction through adjusting the reaction rate constant, k, in eq. 3, did not lead to a perfect match

between predicted and experimental nitrogen concentration-depth profile. In Figure 57 the predicted nitrogen uptake after 22h is 1.85 times higher than the experimental nitrogen uptake, implying that the area under the corresponding nitrogen concentration profile should be 1.85 times deeper (for the corresponding N profiles see [34]). Adopting this factor of 1.85 to the present case, and accordingly extending the experimental concentration-depth profile along the depth axis by a factor 1.85, the model predictions and the experimental data are seen to agree excellently, as shown in Figure 58.

It is important to realize that apart from the scaling factor, which has its origin in actual experimental data, the present model has no fit parameters at all; all input data on solubility, kinetics and volume expansion was obtained on a series of homogeneous foils of expanded austenite of uniform composition. In this sense it is encouraging that including cross-effects between stress and diffusion, stress and solubility, as well as assuming an elastic-plastic approach and interstitial strengthening, leads to realistic composition-depth profiles that fit the experimental data within experimental accuracy. Future experimental work should concentrate on an experimental determination of the kinetics of the surface reactions.

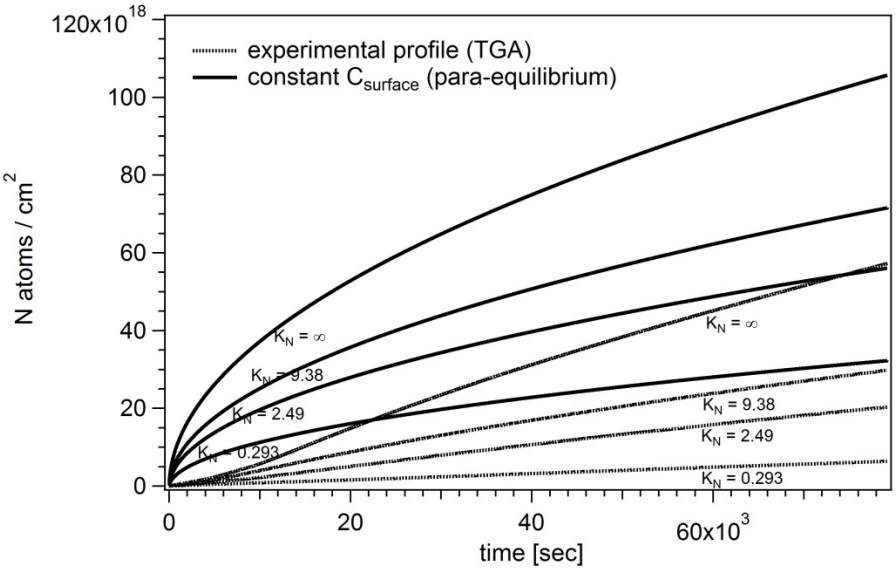

Figure 57 - Nitrogen uptake during nitriding at 718K experimental profile and calculated uptake [34]

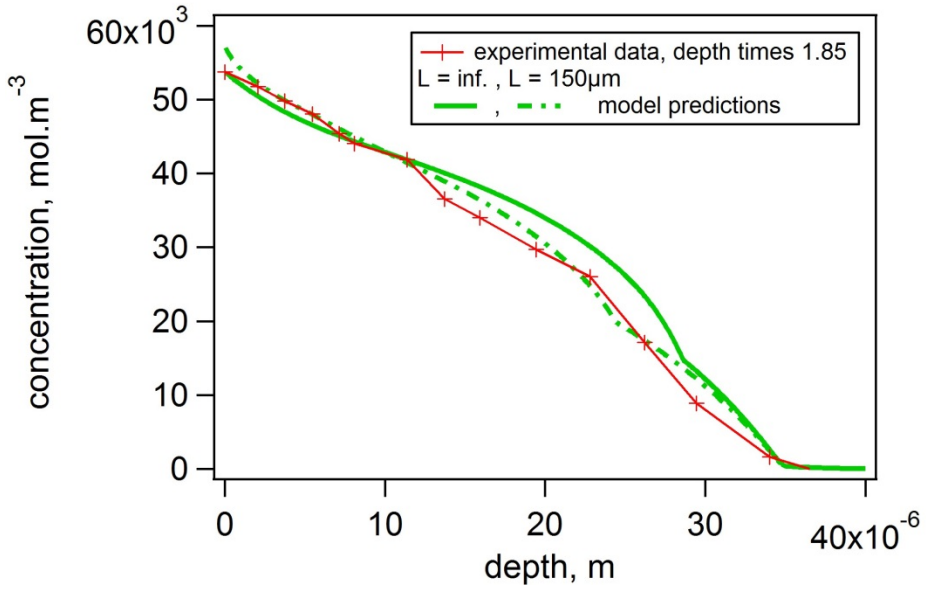

Figure 58 - Comparison between experimentally determined concentration-depth profile from 22h nitriding with infinite nitriding potential from Christiansen and Somers [2], which has been adjusted for depth with a factor 1.85, and concentration depth profile predicted by modelling 22h nitriding with nitriding potential

15. Conclusions

Nitriding of austenitic stainless steel was modelled taking into account a concentration-dependent diffusion coefficient and short-range ordering of chromium and nitrogen atoms (trapping). Stress-depth profiles were predicted from the lattice expansion caused by the interstitial nitrogen atoms. The interaction between the composition-induced stresses and the solid-state diffusion was examined for both purely elastic and elastic-plastic deformation. The effects of concentration and temperature dependent material properties were examined, as well as effects of pre-stressing. The effects of the thermal cycle of heating, holding and cooling were also discussed.

It can be concluded that:

- Solid state diffusion is enhanced by the compressive stress *gradient* resulting from the nitrogen concentration gradient.
- The flux of nitrogen through the surface is affected by the compressive stress level.
- Assuming purely elastic deformation, the interaction between stresses and diffusion results in surface stresses of around 13GPa (for thick samples), which results in faster predicted growth of the expanded austenite case.
- Assuming elastic-plastic deformation, and a constant yield stress, equal to the yield stress of the austenitic stainless steel, decreases the predicted surface stresses to stresses in the order of 1 GPa, and the predicted surface concentration is significantly increased compared to when assuming purely elastic stresses.
- Examining the effect of solid-solution strengthening, it is found that the yield stress increases with nitrogen concentration to a value more than ten times higher than the one of the austenite base material.
- Assuming elastic-plastic deformations, while taking into account the solid-solution strengthening, results in surface stresses of around 9-10GPa for thick samples and 4-5GPa for thin samples.
- Young's modulus increases with nitrogen concentration, and including this increases the predicted compressive surface stresses for thin samples to 6-7GPa.
- Stress states in the sample prior to nitriding can affect the predicted stress and concentration-depth profiles, but drastic changes in nitrogen penetration depths as observed experimentally for carburizing and reported in literature could not be verified by the model.

- Taking into account the nitriding temperature and considering dependence of mechanical properties, lowers the predicted surface concentrations for both thick and thin samples by around 1GPa.
- Including all of the above considerations of temperature and composition dependencies, surface stresses between 5-10GPa are predicted depending on sample thickness, where the highest stresses are predicted for thick samples. This is in accordance with experimental findings.
- Temperature flow is so much faster than diffusion flow, that there is no influence from temperature gradients on the predicted diffusive flux.
- The thermal expansion coefficient depends on the nitrogen concentration, which causes stress to arise from thermal strains during cooling due to the composition gradient. Associated additional compressive stress in the surface region is around 400MPa.
- Comparison with an experimental nitrogen-concentration profile indicated that the model overestimates the diffusion depth of nitrogen. It was demonstrated that this is most likely caused by unknown surface reaction kinetics. An effectively correction for this discrepancy shows that an excellent match of the shape of the calculated concentration-depth profile and the experimental result can be obtained. Further knowledge about the surface kinetics in the beginning of the nitriding process is needed for further improvement of the model.

Denitriding experiments were conducted to obtain more knowledge about solubility and diffusive behaviour as function of temperature. It can be concluded that:

- Solubility data confirms trends seen in literature for relations between nitrogen activity and concentration even for the larger temperature span examined in this work.
- Diffusion coefficient data confirms the trend, shown in literature, of a Lorentzian type concentration dependency, where diffusivity increases with nitrogen concentration until a concentration of about 52000mol/m^3 where after the diffusivity decreases again.
- Absolute values of diffusion coefficients determined in this work are a factor two higher than data earlier reported in the literature.

16. Outlook

Future works in modelling the concentration- and stress-depth profiles could be to incorporate the interdependencies in a full scale 3D finite element model, where stress states present before nitriding from manufacturing processes can be included.

Experimentally, future work should focus on determination of the kinetics of the surface reaction, as discussed in section 14.

Further work on denitriding curves to establish dependency of diffusion coefficient on both temperature and concentration would also be interesting, both to investigate the validity of the trends seen in this work for the activation energy, and to provide the basis for analyzing diffusion and stress development during heating and cooling. Further experimental work of determining thermal expansion coefficients as function of nitrogen concentration would also be of interest, in order to give a more accurate description of stress development during cooling after nitriding.

It would also be interesting to experimentally determine whether the literature results showing an effect of pre-stressing samples during carburizing can be verified, and to examine if similar trends are seen for nitriding experiments in order to investigate the discrepancy between the model predictions and the experiments.

Future works could also include measuring input parameters for modelling carburizing, by determining the carbon concentration dependencies of the diffusion coefficient, yield strength and Young's modulus.

Sources

[1] M. A. J. Somers and T. Christiansen, "Low-Temperature Surface Hardening og Stainless Steels," in *ASM Handbook - Heat treating of Iron And Steels*, vol. 4D, ASM International, 2014, pp. 439–450.

[2] T. L. Christiansen and M. A. J. Somers, "Low-temperature gaseous surface hardening of stainless steel: The current status," *Int. J. Mater. Res.*, vol. 100, no. 10, pp. 1361–1377, 2009.

[3] H. Dong, "S-phase surface engineering of Fe-Cr, Co-Cr and Ni-Cr alloys," *Int. Mater. Rev.*, no. 55, pp. 65–98, 2010.

[4] T. Christiansen, "Ph.D. thesis: Low temperature surface hardening of stainless steel." Department of Manufacturing engineering and Management - Technical University of Denmark, 2004.

[5] J. Oddershede, T. Christiansen, K. Ståhl, and M. A. J. Somers, "Extended X-ray absorption fine structure investigation of nitrogen stabilized expandend austenite," *Scr. Mater.*, no. 62, pp. 290–293, 2010.

[6] J. Oddershede, T. Christiansen, K. Ståhl, and M. A. J. Somers, "Extended X-ray Absorption Fine Structure Investigation of Carbon Stabilized Expanded Austenite and Carbides in Stainless Steel AISI 316," *Steel Res. Int*, vol. 82, no. 10, pp. 1248–1254, 2011.

[7] K. Ichii, K. Fujimura, and T. Takase, "Structure of the ion-nitrided layer of 18-8 stainless steel," *Technol. Rep. Kansai Univ.*, no. 27, pp. 135–144, 1985.

[8] T. Christiansen and M. A. J. Somers, "Decomposition kinetics of expanded austenite with high nitrogen contents," *Z. Für Met.*, no. 97, pp. 79–97, 2006.

[9] F. Ernst, Y. Cao, and G. M. Michal, "Carbides in low-temperature-carburized stainless steels," *Acta Mater.*, no. 52, pp. 1469–1477, 2004.

[10] Y. Cao, F. Ernst, and G. M. Michal, "Colossal carbon supersaturation in austenitic stainless steels carburized at low temperature," *Acta Mater.*, no. 51, pp. 4171–4181, 2003.

[11] K. Farrell, E. D. Specht, J. Pang, L. R. Walker, A. Rar, and J. R. Mayotte, "Characterization of a carburized surface layer on an austenitic stainless steel," *J. Nucl. Mater.*, no. 343, pp. 123–133, 2005.

[12] J. P. Lebrun, H. Michel, and M. Gantois, "Nitruration par bombardemnet ionique des aciers inoxydabales 18-10 (Nitriding of 18Cr10Ni type stainless steels by Ion Bombardement)," *Mem Sci Rev Met.*, vol. 69, no. 10, pp. 727–738, 1972.

[13] Z. L. Zhang and T. Bell, "Structure and corrosion resistance of plasma nitrided stainless steel," *Surf. Eng.*, vol. 1., no. 2, pp. 131–136, 1985.

[14] B. H. Kolster, "Versleiss- und korrosionsfeste Schichten auf austenitichen Stählen," *VDI-Berichte*, no. 506, pp. 107–113, 1983.

[15] K. Gemma, H. Kawakami, and M. Hagiwara, "Effect of NH3-O2 Gas mixtures on the protective Oxide film on High Chromium alloy steels," *Mater. Werkst.*, no. 24, pp. 378–385, 1993.

[16] S. R. Collins, G. H. Schiroky, S. V. Marx, and P. C. Williams, "Concurrent flow of activating gas in low temperature carburization," CA2861180 A1.

[17] S. R. Collins and P. C. Williams, "Low-temperature colossal supersaturation," *Adv. Mater. Process.*, vol. 164, no. 9, pp. 32–33, 2006.

[18] S. R. Collins, P. C. Williams, S. V. Marx, A. Heuer, and H. Kahn, "Low-Temperature Carburization of Austenitic Stainless Steels," in *ASM Handbook - Heat treating of Iron And Steels*, vol. 4D, ASM International, 2014, pp. 452–460.

[19] K. Aioki, T. Shirahata, M. Tahara, and K. Kitano, "Low Temperature Gas Carburising for Austenitic Stainless Steels: The NV-Pionite Process," in *Stainless Steel 2000*, Maney Publishing, 2002, pp. 389–405.

[20] K. Aioki and K. Kitano, "Surface hardening for austenitic stainless steels based on carbon solid solution," *Surf. Eng.*, vol. 18, no. 6, pp. 462–463, 2002.

[21] M. A. J. Somers, T. Christiansen, and P. Møller, "Case-hardening of stainless steel," EP1521861 B1.

[22] S. V. Marx and P. C. Williams, "Low temperature case hardening processes," EP1095170B1.

[23] P. C. Williams and S. V. Marx, "Selective case hardening processes at low temperature," US6165597 A.

[24] T. Christiansen, T. S. Hummelshøj, and M. A. J. Somers, “A Method of activating an article of passive ferrous or non-ferrous metal prior to carburising, nitriding and/or nitrocarburising,” WO2011009463 A1.
[25] T. Christiansen and M. A. J. Somers, “Controlled Dissolution of Colossal Quantitias of Nitrogen in Stainless Steel,” *Metall. Mater. Trans. A*, vol. 37A, pp. 675–682, 2006.
[26] T. Christiansen and M. A. J. Somers, “Stress and composition of carbon stabilized expanded austenite on stainless steel,” *Metall. Mater. Trans. A*, vol. 40A, pp. 1792–1798, 2009.
[27] “316-316L DataSheet - aksteel.com 24/1-2014.” .
[28] J. C. Stinville, C. Tromas, P. Villechaise, and C. Templier, “Anisotropy changes in hardness and indentation modulus induced by plasma nitriding of 316L polycrystalline stainless steel,” *Scr. Mater.*, no. 64, pp. 37–40, 2011.
[29] J. C. Stinville, P. Villechaise, C. Templier, J. P. Rivière, and M. Drouet, “Lattice rotation induced by plasma nitriding in a 316L polycrystalline stainless steel,” *Acta Mater.*, no. 58, pp. 2814–2821, 2010.
[30] C. Templier, J. C. Stinville, P. Villechaise, P. O. Renault, G. Abrasonis, J. P. Rivière, A. Martinavicius, and M. Drouet, “On lattice plane rotation and crystallographic structure of the expanded austenite in plasmanitrided AISI 316L steel,” *Surf. Coat. Technol.*, no. 204, pp. 2551–2558, 2010.
[31] D. A. Porter, K. E. Easterling, and M. Sherif, *Phase transformations in metals and alloys, third edition*. CRC press, Taylor and Francis Group, 2009.
[32] S. Parascandola, W. Möller, and D. L. Williamson, “The nitrogen transport in austenitic stainless steel at moderate temperatures,” *Appl. Phys. Lett.*, vol. 76, no. 16, pp. 2194–2196, 2000.
[33] A. Martinavicius, G. Abrasonis, and W. Möller, “Influence of crystal orientation and ion bombardment on thenitrogen diffusivity in single-crystalline austenitic stainless steel,” *J. Appl. Phys.*, no. 110, p. 074907, 2011.
[34] T. Christiansen, K. V. Dahl, and M. A. J. Somers, “Nitrogen diffusion and nitrogen depth profiles in expanded austenite: Experimental assessment, numerical simulation and role of stress,” *Mater. Sci. Technol.*, vol. 24, no. 2, pp. 159–167, 2008.
[35] T. Christiansen, K. V. Dahl, and M. A. J. Somers, “Simulation of nitrogen concentration depth profiles in low temperature nitrided stainless steels,” *Defect Diffus. Forum*, vol. 258–260, pp. 378–383, 2006.
[36] T. Christiansen and M. A. J. Somers, “Evaluation of diffusion coefficients from composition profiles - the influence of trapping,” *Defect Diffus. Forum*, vol. 258–260, pp. 384–389, 2006.
[37] Y. Sun and T. Bell, “A numerical model of plasma nitriding of low alloy steels,” *Mater. Sci. Eng. A*, no. 224, pp. 33–47, 1997.
[38] T. Moskalioviene and A. Galdikas, “Modeling of nitrogen pentration in polycrystalline AISI 316L stainless steel,” *Surf. Coat. Technol.*, no. 205, pp. 3301–3306, 2011.
[39] F. C. Larche and J. l. Cahn, “The effect of self-stress on diffusion in solids,” *Acta Metall.*, vol. 30, no. 10, pp. 1835–1845, 1982.
[40] F. C. Larche and J. W. Cahn, “Interactions of composition and stress in crystalline solids.,” *Acta Metall.*, vol. 33, no. 3, pp. 331–357, 1985.
[41] Chu and Sanboh Lee, “The effect of chemical stresses on diffusion,” *J. Appl. Phys.*, vol. 75, no. 6, pp. 2823–2829, 1994.
[42] T. L. Christiansen and M. A. J. Somers, “The influence of stress on interstitial diffusion- Carbon diffusion data in austenite revisited,” *Defect Diffus. Forum*, vol. 297–301, pp. 1408–1413, 2010.
[43] F. Yang, “Interaction between diffusion and chemical stresses,” *Mater. Sci. Eng. A*, vol. 409, no. 1–2, pp. 153–159, 2005.
[44] A. Galdikas and T. Moskalioviene, “Stress induced nitrogen diffusion during nitriding of austenitic stainless steel,” *Comput. Mater. Sci.*, no. 50, pp. 796–799, 2010.
[45] T. Moskalioviene and A. Galdikas, “Stress induced and concentration dependent diffusion of nitrogen in plasma nitrided austenitic stainless steel,” *Vacuum*, no. 86, pp. 1552–1557, 2012.

[46] A. Galdikas and T. Moskalioviene, “Swelling effect on stress induced and concentration dependent diffusion of nitrogen in plasma nitrided austenitic stainless steel,” *Comput. Mater. Sci.*, no. 72, pp. 140–145, 2013.
[47] T. Chistiansen and M. A. J. Somers, “Avoiding ghost stress on reconstruction of stress- and compostion-depth profiles from destructive X-ray diffration depth profiling,” *Mater. Sci. Eng. A*, no. 424, pp. 181–189, 2006.
[48] P. B. Friehling, F. W. Poulsen, and M. A. J. Somers, “Nucleation of iron nitrides during gaseous nitriding of iron; effect of a preoxidation treatment,” *Z. Für Met.*, vol. 92, no. 6, pp. 589–595.
[49] M. A. J. Somers, “Modelling nitriding of iron: From thermodynamics to residual stress,” *J. Phys. IV Proc.*, vol. 120, p. 13, 2004.
[50] M. A. J. Somers, “thermodynamics, Kinetics and microstructural evolution of the compound layer; a comparison of the states of knowledge of nitriding and nitrocarburising,” *Heat Treat. Met.*, vol. 200.4, pp. 92–102, 2000.
[51] E. J. Mittemeijer and M. A. J. Somers, “Thermodynamics, kinetics, and process control of nitriding,” *Surf. Eng.*, vol. 13, no. 6, pp. 483–497.
[52] H. J. Grabke, “Kinetics of Gas-Solid Interactions,” *Mater. Sci. Forum*, vol. 154, pp. 69–86, 1994.
[53] H. C. F. Rozendaal, E. J. Mittemeijer, P. F. Colijn, and P. J. Schaaf, “The development of nitrogen concentration profiles on nitriding iron,” *Metall. Trans. A*, vol. 14, no. 2, pp. 395–399, Feb. 1983.
[54] R. T. DeHoff, *Thermodynamics in materials science*. New York,N.Y.: McGraw-Hill, 1993.
[55] M. A. J. Somers, “IFHTSE Global 21: heat treatment and surface engineering in the twenty-first century† Part 14 - Development of compound layer during nitriding and nitrocarburising; current understanding and future challenges,” *Int. Heat Treat. Surf. Eng.*, vol. 5, no. 1, pp. 7–16, Mar. 2011.
[56] R. E. Schacherl, P. C. J. Graat, and E. J. Mittemeijer, “The Nitriding Kinetics of Iron-Chromium Alloys; The ROle of Excess Nitrogen: Experiments and Modelling,” *Metall. Mater. Trans. A*, vol. 35A, pp. 3387–3398, 2004.
[57] M. A. J. Somers and E. J. Mittemeijer, “Layer-growth kinetics on gaseous nitriding of pure iron: Evaluation of diffusion coefficients for nitrogen in iron nitrides,” *Metall. Mater. Trans. A*, vol. 26, no. 1, pp. 57–74, Jan. 1995.
[58] J. Hattel, *fundamentals of numerical modelling of casting processes*. Polyteknisk forlag, 2005.
[59] J. Hattel and P. N. Hansen, “A 1-D analytical model for the thermally induced stresses in the mold surface during die casting,” *Appl Math Model.*, vol. 18, no. october, 1994.
[60] M. A. J. Somers and E. J. Mittemeijer, “Development and relaxation of stress in surface layers; Composition and residual stress profiles in γ’-Fe4N1−x layers on α-Fe substrates,” *Metall. Trans. A*, vol. 21, no. 1, pp. 189–204, Jan. 1990.
[61] F. A. D. Fernandes, T. Christiansen, G. Winther, and M. A. J. Somers, “On the determination of stress profiles in expanded austenite by grazing incidence X-ray diffraction and successive layer removal,” *Acta Mater.*, no. 94, pp. 271–280, 2015.
[62] V. Tvergaard, *Plasticity and creep in structural materials*. Kgs. Lyngby, Denmark: Department of mechanical engineering, Technical University of Denmark, 2001.
[63] “316-316L data bulletin - aksteel.com 20/7 -2014.” .
[64] F. Bottoli, G. Winther, T. Christiansen, and M. A. J. Somers, “Influence of Plastic Deformation on LLow-Temperature Surface Hardening of Austenitic Stainless Steel by Gaseous Nitriding,” *Metall. Mater. Trans. A*, vol. 46A, pp. 2579–2590, 2015.
[65] F. A. D. Fernandes, M. A. J. Somers, and T. Christiansen, “Determination of stress profiles in expanded austenite by combining successive layer removal and GI-XRD,” *Adv. Mater. Res.*, vol. 996, pp. 155–161, 2014.
[66] V. Tvergaard, “Effect of thermally induced residual stresses on the failure of a whisker-reinforced metal,” *Mech. Mater.*, no. 11, pp. 149–161, 1991.

[67] “ASTM standard E 8M - 04: Standard test method for tension testing of metallic materials.” ASTM International.
[68] F. Bottoli, G. Winther, T. Christiansen, K. V. Dahl, and M. A. J. Somers, “Low temperature nitriding of deformed austenitic stainless steels with various nitrogen contents obtained by prior high temperature solution nitriding,” *Manuscr.*, 2015.
[69] W. Li, X. Li, and H. Dong, “Effect of tensile stress on the formation of S-phase during low-temperature plasma carburizing of 316L foil,” *Acta Mater.*, vol. 59, no. 14, pp. 5765–5774, 2011.
[70] J. Oddershede, T. Christiansen, K. Ståhl, and M. A. J. Somers, “Extended X-ray absorption fine structure investigation of annealed carbon expanded austenite,” *Steel Res. Int*, no. 83, pp. 162–168, 2012.
[71] INCO, “Austenitic chromium-nickel stainless steels - Engineering properties at elevated temperatures.” INCO databooks, reprint with metric conversions from from “Mechanical and physical properties of the austnitic chromium-nickel stainless steels at elevated temperatures” 1968 by the international Nickel company.
[72] C. Y. Ho and T. K. Chu, “Electrical resistivity and thermal conductivity of nine selected AISI stainless steels.” CINDAS for American iron and steel institute, 1977.
[73] B. Brink, “Ph.D. thesis: Sythesis and characterization of homogeneous interstitial solutions of nitrogen and carbon in iron-based lattices.” DTU Mechanics, 2015.
[74] B. Brink, K. Ståhl, T. Christiansen, and M. A. J. Somers, “Thermal expansion and phase transformations of nitrogen-expanded austenite studied with in situ synchotron x-ray diffraction,” *J. Appl. Crystallogr.*, no. 47, pp. 819–826, 2014.
[75] Thomas Christiansen, “Ph.D. Thesis: Low temperature surface hardening of stainless steel.” Department of Manufacturing engineering and Management - Technical University of Denmark, 2004.
[76] J. Crank, “Diffusion in a plane sheet,” in *The mathematics of diffusion*, Oxford University presss, 1956.
[77] M. A. J. Somers, “Chapter 8: Development of the compound layer during nitriding and nitrocarburising of iron and iron-carbon alloys,” in *Thermochemical surface engineering of steels*, .
[78] K. M. Eliasen, T. Christiansen, and M. A. J. Somers, “Low temperature gaseous nitriding of Ni based superalloys,” *Surf. Eng.*, vol. 26, no. 4, pp. 248–255, 2010.
[79] J. F. Eckel and C. R. Manning, “A study of Internal-friction Peaks in type 304 stainless steel containing nitrogen,” *Adv. Technol. Stainl. Steels Relat. Alloys*, vol. 1965, no. 369, pp. 342–347, 1965.
[80] C. Wells, W. Batz, and R. F. Mehl, “Diffusion coefficient of carbon in austenite,” *J. Met.*, vol. 188, pp. 553–560, 1950.
[81] P. Atkins and J. De Paula, *Atkins Physical chemistry*, 8th ed. Oxford University Press.
[82] W. J. Moore, *Physical Chemistry*. Longman, 1972.
[83] I. Okafor, O. Carlson and D. Martin; "Mass transport of carbon in One and two phase Iron-Nickel alloys in a temperature gradient" Metall. trans. A Vol. 13.A, 1982, pp. 1713-1719
[84] J. Mathuni, O. N. Carlson, E. Fromm and R. Kirchheim; "Electrotransport and Thermotransport of oxygen and Nitrogen in vanadium steel, Metall. trans. A Vol. 7A, 1976, pp. 977-981
[85] L. Höglund and J. Ågren; "Simulation of Carbon Diffusion in Steel Driven by a Temperature gradient", Journal of Phase Equilibria and Diffusion, 2010, Vol. 31, No 3, pp. 212-215

Appendix A – Determination of input parameters

A.1 Partial molar volume, V_N

The partial molar volume of nitrogen(/carbon) in the solid matrix, V_N [m^3/molN], can be found from the slope of the volume as function of the fractional occupancy y_N.

The volume as function of y_N is found from data from Christiansen et al. [2] in section 5.3 to be

$$V_\varphi(y_N) = 2.8147 \cdot 10^{-29} \cdot y_N + 4.7134 \cdot 10^{-29} \tag{A1}$$

Converting the slope to obtain the SI-units

$$V_N = 2.8147 \cdot 10^{-29} \frac{\mathrm{m}^3}{\mathrm{unitcell}} \frac{\mathrm{atomM}}{\mathrm{atomN}} \cdot \frac{1}{4} \frac{\mathrm{unitcell}}{\mathrm{atomM}} \cdot N_{av} \tag{A2}$$

$$V_N = 2.8147 \cdot 10^{-29} \frac{\mathrm{m}^3}{\mathrm{unitcell}} \frac{\mathrm{atomM}}{\mathrm{atomN}} \cdot \frac{1}{4} \frac{\mathrm{unitcell}}{\mathrm{atomM}} \cdot 6.022 \cdot 10^{23} \frac{\mathrm{atomN}}{\mathrm{molN}} \tag{A3}$$

$$V_N = 4.2376 \cdot 10^{-6}\ \mathrm{m}^3/\mathrm{molN} \tag{A4}$$

A.2 Temperature dependent equilibrium constant, K_T

K_T is the equilibrium constant for the reaction describing the dissolution of N into the solid phase from the gas phase containing NH_3 and H_2.

The reaction which determines K_T is the decomposition of the ammonia will occur by the following reaction

$$NH_3 \rightleftarrows N_{ad} + \frac{3}{2}H_2$$

At equilibrium the following equation is fulfilled for the equation [81]

$$0 = \Delta_r G + RT \cdot \ln(K_T) \tag{A5}$$

where $\Delta_r G$ is the change of Gibbs energy for the standard reaction, r, which in this case is given for a specific temperature, T, by [81]

$$\Delta_r G = \Delta_r H - T\Delta_r S \tag{A6}$$

where $\Delta_r H$ is the standard enthalphy change for the reaction and $\Delta_r S$ is the entropy change for the reaction.

The standard enthalphy change for the reaction at a specific temperature is [81]

$$\Delta_r H(T) = \Delta_r H\left(T_{ref}\right) + \int_{T_{ref}}^{T} \Delta_r C_p \, dT \tag{A7}$$

where $\Delta_r H\left(T_{ref}\right)$ is the standard enthalphy change for the reaction at a reference temperature, and $\Delta_r C_p$ is the reaction change of the heat capacity at constant pressure, which at for this specific reaction can be found from the following formula

$$\Delta_r C_p = \frac{1}{2} C_p(N_2) + \frac{3}{2} \cdot C_p(H_2) - C_p(NH_3) \tag{A8}$$

The heat capacity as function of temperature can be determined by [81]

$$C_p = a + bT + \frac{c}{T^2} \tag{A9}$$

where a, b and c are temperature independent material parameters. The values for the relevant gasses [81] are given in Table 5.

Table 5 –Material parameters for gases

Gas\parameters	a	b $(10^{-3}K^{-1})$	c $(10^{5}K^{2})$
H_2	27.28	3.26	0.50
NH_3	29.75	25.1	-1.55
N_2	28.58	3.77	-0.50

And thus

$$\Delta_r C_p = \Delta_r a + \Delta_r bT + \frac{\Delta_r c}{T^2} \tag{A10}$$

where

$$\Delta_r a = \frac{1}{2}\cdot a(N_2) + \frac{3}{2}\cdot a(H_2) - a(NH_3) = 25.46 \tag{A11}$$

$$\Delta_r b = \frac{1}{2}\cdot b(N_2) + \frac{3}{2}\cdot b(H_2) - b(NH_3) = -0.018325\ K^{-1} \tag{A12}$$

$$\Delta_r c = \frac{1}{2}\cdot c(N_2) + \frac{3}{2}\cdot c(H_2) - c(NH_3) = 2.05\cdot 10^5 K^2 \tag{A13}$$

Inserting in eq. A7 gives

$$\Delta_r H(T) = \Delta_r H\left(T_{ref}\right) + \int_{T_{ref}}^{T} \left(\Delta_r a + \Delta_r bT + \frac{\Delta_r c}{T^2}\right) dT \tag{A14}$$

Using 298K as the reference temperature the reference standard enthalpy changes, $\Delta_r H(T_{ref})$, can be calculated by

$$\Delta_r H(T_{ref}) = \frac{1}{2} \cdot H(298\text{K}, N_2) + \frac{3}{2} \cdot H(298\text{K}, H_2) - H(298\text{K}, NH_3) \tag{A15}$$

where the enthalpy values for the gasses are [81]

	N_2	H_2	NH_3
$H(298K)$ $[J/mol]$	0	0	-46110

Giving

$$\Delta_r H(T_{ref}) = 46110\ \text{J/mol} \tag{A16}$$

which gives the following expression for the standard enthalpy change of the reaction

$$\begin{aligned} \Delta_r H(T) &= \Delta_r H(298) + \int_{298}^{T} \left(\Delta_r a + \Delta_r bT + \frac{\Delta_r c}{T^2}\right) dT \\ &= \Delta_r H(T_{ref}) + \Delta_r a \cdot (T - 298) + \frac{1}{2}\Delta_r b(T^2 - 298^2) - \Delta_r c\left(\frac{1}{T} - \frac{1}{298}\right) \\ &= 46110 + 25.46 \cdot (T - 298) - \frac{1}{2}0.018325\ (T^2 - 298^2) - 2.05 \cdot 10^5\left(\frac{1}{T} - \frac{1}{298}\right) \\ &= 40024.5 + 25.46 \cdot T - 0.009163 \cdot T^2 - \frac{2.05 \cdot 10^5}{T} \end{aligned} \tag{A17}$$

The entropy change for the reaction at a specific temperature is [81]

$$\Delta_r S(T) = \Delta_r S(T_{ref}) + \int_{T_{ref}}^{T} \frac{\Delta_r C_p}{T}\ dT \tag{A18}$$

where $\Delta_r C_p$ is the reaction change of the heat capacity at constant pressure and $\Delta_r S(T_{ref})$ is the standard entrophy change for the reaction at a reference temperature, which using 298K as the reference temperature can be calculated by

$$\Delta_r S(T_{ref}) = \frac{1}{2} \cdot S(298\text{K}, N_2) + \frac{3}{2} \cdot S(298\text{K}, H_2) - S(298\text{K}, NH_3) \tag{A19}$$

where the entropy values for the gasses are [81]

	N_2	H_2	NH_3
$S(298K)$ $[J/(mol \cdot K)]$	191.61	130.684	192.45

Giving

$$\Delta_r S(T_{ref}) = 99.381 \text{ J/(mol} \cdot \text{K)} \tag{A20}$$

Using the expression for $\Delta_r C_p$ calculated when finding the enthalpy gives

$$\begin{aligned}
\Delta_r S(T) &= \Delta_r S(298) + \int_{298}^{T} \left(\frac{\Delta_r a}{T} + \Delta_r b + \frac{\Delta_r c}{T^3} \right) dT \\
&= \Delta_r S(298) + \Delta_r a \cdot (\ln(T) - \ln(298)) + \Delta_r b(T - 298) - \frac{\Delta_r c}{2} \left(\frac{1}{T^2} - \frac{1}{298^2} \right) \\
&= 99.381 \frac{J}{mol \cdot K} + 25.46 \cdot (\ln(T) - \ln(298)) - 0.018325(T - 298) \\
&\quad - \frac{2.05 \cdot 10^5}{2} \left(\frac{1}{T^2} - \frac{1}{298^2} \right) \\
&= -37.8977 + 25.46 \cdot \ln(T) - 0.018325 \cdot T - \frac{2.05 \cdot 10^5}{2 \cdot T^2}
\end{aligned} \tag{A21}$$

The change of Gibbs energy for the standard reaction, r, can now be found

$$\begin{aligned}
\Delta_r G &= \Delta_r H - T\Delta_r S \\
&= 40024.5 + 25.46 \cdot T - 0.009163 \cdot T^2 - \frac{2.05 \cdot 10^5}{T} \\
&\quad - T \left(-37.8977 + 25.46 \cdot \ln(T) - 0.018325 \cdot T - \frac{2.05 \cdot 10^5}{2 \cdot T^2} \right) \\
&= 40024.5 + 63.3577 \cdot T + 0.009162 \cdot T^2 - 25.46 \cdot T \cdot \ln(T) - \frac{2.05 \cdot 10^5}{2 \cdot T}
\end{aligned} \tag{A22}$$

Giving the following expression for the equilibrium constant

$$K_T = \exp\left(\frac{-\Delta_r G}{RT}\right) = \exp\left(\frac{-1}{R}\left(\frac{40024.5}{T} + 63.3577 + 0.009162 \cdot T - 25.46 \cdot \ln(T) - \frac{2.05 \cdot 10^5}{2 \cdot T^2}\right)\right) \quad \text{(A23)}$$

Using the gas-constant $R = 8.314\text{J}/(\text{mol} \cdot \text{K})$ gives the equilibrium constant in J/mol N.

$$K_T = \exp\left(-\frac{4814.11}{T} - 7.6206 - 0.001102 \cdot T + 3.0623 \cdot \ln(T) + \frac{12328.6}{T^2}\right) \quad \text{(A24)}$$

The change of the equilibrium constant with pressure is given by [82]

$$\frac{\partial \ln(K_T)}{\partial p} = \frac{\Delta V}{RT} \quad \text{(A25)}$$

and it can then be written

$${K_T}^{\sigma} = {K_T}^{\sigma=0} \cdot \exp\left(\frac{V_N \sigma_H}{RT}\right) \quad \text{(A26)}$$

which gives the final expression for the equilibrium constant

$$K_T = \exp\left(-\frac{4814.11}{T} - 7.6206 - 0.001102 \cdot T + 3.0623 \cdot \ln(T) + \frac{12328.6}{T^2}\right) \cdot \exp\left(\frac{V_N \sigma_H}{RT}\right) \quad \text{(A27)}$$

A.3 Relation between nitriding potential, K_N, and concentration

The relation between nitriding potential of an NH_3/H_2 gas mixture, i.e. $K_N = {p_{NH_3}}/{p_{H_2}^{\frac{3}{2}}}$, and the nitrogen concentration, c_N, is determined from the absorption isotherms relation between the equilibrium nitrogen content, expressed as the fractional occupancy of the nitrogen sub-lattice, y_N, in stress-free austenite and the nitrogen activity applied by the gas mixture from Christiansen [2]. Converting the fractional occupancy, y_N , to concentration, c_N, using eq. 42, Figure 59, is obtained. For equilibrium between nitrogen in solid state and imposed nitriding potential the activity of nitrogen in the solid state is linearly proportional to the nitriding potential, K_N by [55]

$$a_N = K_T K_N \tag{A28}$$

where K_T is the equilibrium constant for the dissolution reaction of N into the solid state from the gas phase, and is a function of temperature and pressure. For dilute solutions Henrian behaviour can be assumed, implying linear proportionality between the nitrogen activity and the nitrogen concentration: $a_N = \gamma \cdot c_N$. This condition can be assumed only for nitrogen concentrations approaching nil.

Since K_T is not a function of concentration, it follows from the above for small concentrations $K_N = \gamma \cdot \frac{c_N}{K_T}$. The raw data suggest an exponential relation between K_N and c_N. A function of the following form obeys Henrian behaviour for small c_N, and was used to parametrize the data

$$K_N = k1 \cdot \frac{c}{K_T} + \frac{k2}{K_T} \cdot \exp(k3 \cdot c_N + k4) \tag{A29}$$

where $k1$, $k2$, $k3$ and $k4$ are fitting parameters.

Calculating K_T for 316 stainless steel the temperature of the measurements 445°C = 718.15K, and no hydrostatic stress Gives $K_T = 155.738$.

For AISI 316 a satisfactory fit of the data at 445°C was obtained with the following parameters

$k1$	$k2$	$k3$	$k4$
0.01125	102.5078	0.0005129336	-24.60384

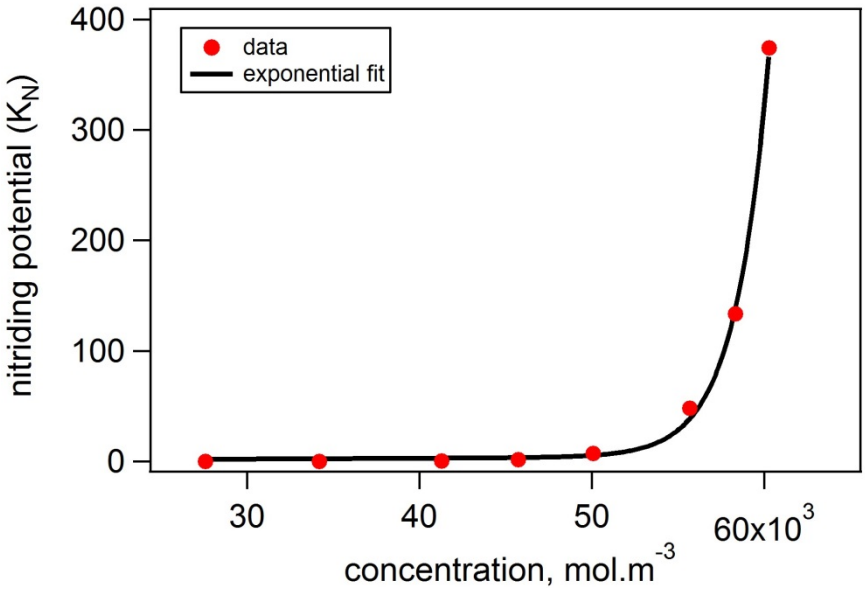

Figure 59 – Fit and - raw data of nitriding potential as function of concentration at 445°C

Appendix B – Extended calculations

B.1 Reduction of stress expression

$$\sigma_{yy} = \frac{E}{(1+\nu)(1-2\nu)}\left(\frac{\nu^2+\nu}{1-\nu}\left(\varepsilon_{yy}^{th}+\varepsilon_{yy}^{ch}\right) - \frac{2\nu^2}{1-\nu}\varepsilon_{yy} + \varepsilon_{yy} - (1+\nu)\left(\varepsilon_{yy}^{th}+\varepsilon_{yy}^{ch}\right)\right) \tag{B1}$$

$$\leftrightarrow\ \sigma_{yy} = \frac{E}{(1+\nu)(1-2\nu)}\left(\frac{\nu^2+\nu\left(\varepsilon_{yy}^{th}+\varepsilon_{yy}^{ch}\right) - 2\nu^2\varepsilon_{yy} + (1-\nu)\varepsilon_{yy} - (1+\nu)(1-\nu)\left(\varepsilon_{yy}^{th}+\varepsilon_{yy}^{ch}\right)}{1-\nu}\right) \tag{B2}$$

$$\leftrightarrow\ \sigma_{yy} = \frac{E}{(1+\nu)(1-2\nu)}\left(\frac{(1-\nu-2\nu^2)\varepsilon_{yy} + \left(\nu^2+\nu-(1+\nu)(1-\nu)\right)\left(\varepsilon_{yy}^{th}+\varepsilon_{yy}^{ch}\right)}{1-\nu}\right) \tag{B3}$$

$$\leftrightarrow\ \sigma_{yy} = \frac{E}{(1-\nu-2\nu^2)}\left(\frac{(1-\nu-2\nu^2)\varepsilon_{yy} + (2\nu^2+\nu-1)\left(\varepsilon_{yy}^{th}+\varepsilon_{yy}^{ch}\right)}{1-\nu}\right) \tag{B4}$$

$$\leftrightarrow\ \sigma_{yy} = \frac{E}{(1-\nu-2\nu^2)}\left(\frac{(1-\nu-2\nu^2)\varepsilon_{yy} - (1-\nu-2\nu^2)\left(\varepsilon_{yy}^{th}+\varepsilon_{yy}^{ch}\right)}{1-\nu}\right) \tag{B5}$$

$$\leftrightarrow\ \sigma_{yy} = E\left(\frac{\varepsilon_{yy} - \left(\varepsilon_{yy}^{th}+\varepsilon_{yy}^{ch}\right)}{1-\nu}\right) \tag{B6}$$

$$\leftrightarrow\ \sigma_{yy} = \frac{E}{1-\nu}\left(\varepsilon_{yy} - \varepsilon_{yy}^{th} - \varepsilon_{yy}^{ch}\right) \tag{B7}$$

B.2 isolation of total strain expression for uneven strains

Isolating ε_{11}^{tot} in the equation from $\int_0^{z_{max}} \dot{\sigma}_{11} dz = 0$ gives

$$\int_0^{z_{max,plastic}} \frac{E}{1+\nu} \left\{ \left(\left[1 + \frac{\nu}{1-2\nu} - \frac{3}{2} \frac{E/E_t - 1}{E/E_t - (1-2\nu)/3} \frac{\frac{1}{9}\left(4{\sigma_{11}}^2 + {\sigma_{22}}^2 - 4\sigma_{22}\sigma_{11}\right)}{{\sigma_{11}}^2 + {\sigma_{22}}^2 - \sigma_{22}\sigma_{11}} \right] \right.\right.$$

$$\left. - \frac{\left[\frac{\nu}{1-2\nu} - \frac{3}{2} \frac{\frac{E}{E_t} - 1}{\frac{E}{E_t} - \frac{(1-2\nu)}{3}} \frac{\frac{1}{9}\left(-2{\sigma_{11}}^2 + {\sigma_{22}}^2 - \sigma_{22}\sigma_{11}\right)}{{\sigma_{11}}^2 + {\sigma_{22}}^2 - \sigma_{22}\sigma_{11}} \right] \left[\frac{\nu}{1-2\nu} - \frac{3}{2} \frac{\frac{E}{E_t} - 1}{\frac{E}{E_t} - \frac{(1-2\nu)}{3}} \frac{\frac{1}{9}\left(-2{\sigma_{11}}^2 + {\sigma_{22}}^2 - \sigma_{22}\sigma_{11}\right)}{{\sigma_{11}}^2 + {\sigma_{22}}^2 - \sigma_{22}\sigma_{11}} \right]}{\left[1 + \frac{\nu}{1-2\nu} - \frac{3}{2} \frac{\frac{E}{E_t} - 1}{\frac{E}{E_t} - \frac{(1-2\nu)}{3}} \frac{\frac{1}{9}\left({\sigma_{11}}^2 + {\sigma_{22}}^2 + 2\sigma_{22}\sigma_{11}\right)}{{\sigma_{11}}^2 + {\sigma_{22}}^2 - \sigma_{22}\sigma_{11}} \right]} \right) \cdot \left(\dot{\varepsilon}_{11}^{tot} - \dot{\varepsilon}_{11}^{th} - \dot{\varepsilon}_{11}^{ch} \right)$$

$$+ \left(\left[\frac{\nu}{1-2\nu} - \frac{3}{2} \frac{E/E_t - 1}{E/E_t - (1-2\nu)/3} \frac{\frac{1}{9}\left(-2{\sigma_{11}}^2 - 2{\sigma_{22}}^2 + 5\sigma_{22}\sigma_{11}\right)}{{\sigma_{11}}^2 + {\sigma_{22}}^2 - \sigma_{22}\sigma_{11}} \right] \right.$$

$$\left. - \frac{\left[\frac{\nu}{1-2\nu} - \frac{3}{2} \frac{\frac{E}{E_t} - 1}{\frac{E}{E_t} - \frac{(1-2\nu)}{3}} \frac{\frac{1}{9}\left(-2{\sigma_{11}}^2 + {\sigma_{22}}^2 - \sigma_{22}\sigma_{11}\right)}{{\sigma_{11}}^2 + {\sigma_{22}}^2 - \sigma_{22}\sigma_{11}} \right] \left[\frac{\nu}{1-2\nu} - \frac{3}{2} \frac{\frac{E}{E_t} - 1}{\frac{E}{E_t} - \frac{(1-2\nu)}{3}} \frac{\frac{1}{9}\left({\sigma_{11}}^2 - 2{\sigma_{22}}^2 - \sigma_{22}\sigma_{11}\right)}{{\sigma_{11}}^2 + {\sigma_{22}}^2 - \sigma_{22}\sigma_{11}} \right]}{\left[1 + \frac{\nu}{1-2\nu} - \frac{3}{2} \frac{\frac{E}{E_t} - 1}{\frac{E}{E_t} - \frac{(1-2\nu)}{3}} \frac{\frac{1}{9}\left({\sigma_{11}}^2 + {\sigma_{22}}^2 + 2\sigma_{22}\sigma_{11}\right)}{{\sigma_{11}}^2 + {\sigma_{22}}^2 - \sigma_{22}\sigma_{11}} \right]} \right) \cdot \left(\dot{\varepsilon}_{22}^{tot} - \dot{\varepsilon}_{22}^{th} - \dot{\varepsilon}_{22}^{ch} \right) \Bigg\} dz$$

$$+ \int_{z_{max,plastic}}^{z_{max}} \frac{E}{1+\nu} \left(\left(\left[1 + \frac{\nu}{1-2\nu} \right] - \frac{\left[\frac{\nu}{1-2\nu} \right]^2}{\left[1 + \frac{\nu}{1-2\nu} \right]} \right) \left(\dot{\varepsilon}_{11}^{tot} - \dot{\varepsilon}_{11}^{th} - \dot{\varepsilon}_{11}^{ch} \right) + \left(\left[\frac{\nu}{1-2\nu} \right] - \frac{\left[\frac{\nu}{1-2\nu} \right]^2}{\left[1 + \frac{\nu}{1-2\nu} \right]} \right) \left(\dot{\varepsilon}_{22}^{tot} - \dot{\varepsilon}_{22}^{th} - \dot{\varepsilon}_{22}^{ch} \right) \right) dz = 0$$

Isolating $\dot{\varepsilon}_{11}^{tot}$

$$\int_0^{z_{max,plastic}} \frac{E}{1+\nu}\left\{\left(\left[1+\frac{\nu}{1-2\nu}-\frac{3}{2}\frac{E/E_t-1}{E/E_t-(1-2\nu)/3}\frac{\frac{1}{9}\left(4{\sigma_{11}}^2+{\sigma_{22}}^2-4\sigma_{22}\sigma_{11}\right)}{{\sigma_{11}}^2+{\sigma_{22}}^2-\sigma_{22}\sigma_{11}}\right]\right.\right.$$

$$\left.\left.-\frac{\left[\frac{\nu}{1-2\nu}-\frac{3}{2}\frac{\frac{E}{E_t}-1}{\frac{E}{E_t}-\frac{(1-2\nu)}{3}}\frac{\frac{1}{9}\left(-2{\sigma_{11}}^2+{\sigma_{22}}^2-\sigma_{22}\sigma_{11}\right)}{{\sigma_{11}}^2+{\sigma_{22}}^2-\sigma_{22}\sigma_{11}}\right]\left[\frac{\nu}{1-2\nu}-\frac{3}{2}\frac{\frac{E}{E_t}-1}{\frac{E}{E_t}-\frac{(1-2\nu)}{3}}\frac{\frac{1}{9}\left(-2{\sigma_{11}}^2+{\sigma_{22}}^2-\sigma_{22}\sigma_{11}\right)}{{\sigma_{11}}^2+{\sigma_{22}}^2-\sigma_{22}\sigma_{11}}\right]}{\left[1+\frac{\nu}{1-2\nu}-\frac{3}{2}\frac{\frac{E}{E_t}-1}{\frac{E}{E_t}-\frac{(1-2\nu)}{3}}\frac{\frac{1}{9}\left({\sigma_{11}}^2+{\sigma_{22}}^2+2\sigma_{22}\sigma_{11}\right)}{{\sigma_{11}}^2+{\sigma_{22}}^2-\sigma_{22}\sigma_{11}}\right]}\right)\right\}dz$$

$$\cdot\,\dot{\varepsilon}_{11}^{tot}$$

$$-\int_0^{z_{max,plastic}} \frac{E}{1+\nu}\left\{\left(\left[1+\frac{\nu}{1-2\nu}-\frac{3}{2}\frac{E/E_t-1}{E/E_t-(1-2\nu)/3}\frac{\frac{1}{9}\left(4{\sigma_{11}}^2+{\sigma_{22}}^2-4\sigma_{22}\sigma_{11}\right)}{{\sigma_{11}}^2+{\sigma_{22}}^2-\sigma_{22}\sigma_{11}}\right]\right.\right.$$

$$\left.\left.-\frac{\left[\frac{\nu}{1-2\nu}-\frac{3}{2}\frac{\frac{E}{E_t}-1}{\frac{E}{E_t}-\frac{(1-2\nu)}{3}}\frac{\frac{1}{9}\left(-2{\sigma_{11}}^2+{\sigma_{22}}^2-\sigma_{22}\sigma_{11}\right)}{{\sigma_{11}}^2+{\sigma_{22}}^2-\sigma_{22}\sigma_{11}}\right]\left[\frac{\nu}{1-2\nu}-\frac{3}{2}\frac{\frac{E}{E_t}-1}{\frac{E}{E_t}-\frac{(1-2\nu)}{3}}\frac{\frac{1}{9}\left(-2{\sigma_{11}}^2+{\sigma_{22}}^2-\sigma_{22}\sigma_{11}\right)}{{\sigma_{11}}^2+{\sigma_{22}}^2-\sigma_{22}\sigma_{11}}\right]}{\left[1+\frac{\nu}{1-2\nu}-\frac{3}{2}\frac{\frac{E}{E_t}-1}{\frac{E}{E_t}-\frac{(1-2\nu)}{3}}\frac{\frac{1}{9}\left({\sigma_{11}}^2+{\sigma_{22}}^2+2\sigma_{22}\sigma_{11}\right)}{{\sigma_{11}}^2+{\sigma_{22}}^2-\sigma_{22}\sigma_{11}}\right]}\right)\right\}$$

$$\cdot\left(\dot{\varepsilon}_{11}^{th}+\dot{\varepsilon}_{11}^{ch}\right)\Bigg\}\,dz$$

$$+\int_0^{z_{max,plastic}} \frac{E}{1+\nu}\left\{\left(\left[\frac{\nu}{1-2\nu}-\frac{3}{2}\frac{E/E_t-1}{E/E_t-(1-2\nu)/3}\frac{\frac{1}{9}\left(-2{\sigma_{11}}^2-2{\sigma_{22}}^2+5\sigma_{22}\sigma_{11}\right)}{{\sigma_{11}}^2+{\sigma_{22}}^2-\sigma_{22}\sigma_{11}}\right]\right.\right.$$

$$\left.\left.-\frac{\left[\frac{\nu}{1-2\nu}-\frac{3}{2}\frac{\frac{E}{E_t}-1}{\frac{E}{E_t}-\frac{(1-2\nu)}{3}}\frac{\frac{1}{9}\left(-2{\sigma_{11}}^2+{\sigma_{22}}^2-\sigma_{22}\sigma_{11}\right)}{{\sigma_{11}}^2+{\sigma_{22}}^2-\sigma_{22}\sigma_{11}}\right]\left[\frac{\nu}{1-2\nu}-\frac{3}{2}\frac{\frac{E}{E_t}-1}{\frac{E}{E_t}-\frac{(1-2\nu)}{3}}\frac{\frac{1}{9}\left({\sigma_{11}}^2-2{\sigma_{22}}^2-\sigma_{22}\sigma_{11}\right)}{{\sigma_{11}}^2+{\sigma_{22}}^2-\sigma_{22}\sigma_{11}}\right]}{\left[1+\frac{\nu}{1-2\nu}-\frac{3}{2}\frac{\frac{E}{E_t}-1}{\frac{E}{E_t}-\frac{(1-2\nu)}{3}}\frac{\frac{1}{9}\left({\sigma_{11}}^2+{\sigma_{22}}^2+2\sigma_{22}\sigma_{11}\right)}{{\sigma_{11}}^2+{\sigma_{22}}^2-\sigma_{22}\sigma_{11}}\right]}\right)\right\}dz\cdot\dot{\varepsilon}_{22}^{tot}$$

$$-\int_0^{z_{max,plastic}} \frac{E}{1+\nu}\left\{\left(\left[\frac{\nu}{1-2\nu}-\frac{3}{2}\frac{E/E_t-1}{E/E_t-(1-2\nu)/3}\frac{\frac{1}{9}\left(-2{\sigma_{11}}^2-2{\sigma_{22}}^2+5\sigma_{22}\sigma_{11}\right)}{{\sigma_{11}}^2+{\sigma_{22}}^2-\sigma_{22}\sigma_{11}}\right]\right.\right.$$

$$\left.\left.-\frac{\left[\frac{\nu}{1-2\nu}-\frac{3}{2}\frac{\frac{E}{E_t}-1}{\frac{E}{E_t}-\frac{(1-2\nu)}{3}}\frac{\frac{1}{9}\left(-2{\sigma_{11}}^2+{\sigma_{22}}^2-\sigma_{22}\sigma_{11}\right)}{{\sigma_{11}}^2+{\sigma_{22}}^2-\sigma_{22}\sigma_{11}}\right]\left[\frac{\nu}{1-2\nu}-\frac{3}{2}\frac{\frac{E}{E_t}-1}{\frac{E}{E_t}-\frac{(1-2\nu)}{3}}\frac{\frac{1}{9}\left({\sigma_{11}}^2-2{\sigma_{22}}^2-\sigma_{22}\sigma_{11}\right)}{{\sigma_{11}}^2+{\sigma_{22}}^2-\sigma_{22}\sigma_{11}}\right]}{\left[1+\frac{\nu}{1-2\nu}-\frac{3}{2}\frac{\frac{E}{E_t}-1}{\frac{E}{E_t}-\frac{(1-2\nu)}{3}}\frac{\frac{1}{9}\left({\sigma_{11}}^2+{\sigma_{22}}^2+2\sigma_{22}\sigma_{11}\right)}{{\sigma_{11}}^2+{\sigma_{22}}^2-\sigma_{22}\sigma_{11}}\right]}\right)\cdot\left(\dot{\varepsilon}_{22}^{th}+\dot{\varepsilon}_{22}^{ch}\right)\right\}dz$$

$$+\int_{z_{max,plastic}}^{z_{max}} \frac{E}{1+\nu}\left(\left[1+\frac{\nu}{1-2\nu}\right]-\frac{\left[\frac{\nu}{1-2\nu}\right]^2}{\left[1+\frac{\nu}{1-2\nu}\right]}\right)dz\cdot\dot{\varepsilon}_{11}^{tot}$$

$$-\int_{z_{max,plastic}}^{z_{max}} \frac{E}{1+\nu}\left(\left[1+\frac{\nu}{1-2\nu}\right]-\frac{\left[\frac{\nu}{1-2\nu}\right]^2}{\left[1+\frac{\nu}{1-2\nu}\right]}\right)(\dot{\varepsilon}_{11}^{th}+\dot{\varepsilon}_{11}^{ch})dz$$

$$+\int_{z_{max,plastic}}^{z_{max}} \frac{E}{1+\nu}\left(\left[\frac{\nu}{1-2\nu}\right]-\frac{\left[\frac{\nu}{1-2\nu}\right]^2}{\left[1+\frac{\nu}{1-2\nu}\right]}\right)dz\cdot\dot{\varepsilon}_{22}^{tot}$$

$$-\int_{z_{max,plastic}}^{z_{max}} \frac{E}{1+\nu}\left(\left[\frac{\nu}{1-2\nu}\right]-\frac{\left[\frac{\nu}{1-2\nu}\right]^2}{\left[1+\frac{\nu}{1-2\nu}\right]}\right)(\dot{\varepsilon}_{22}^{th}+\dot{\varepsilon}_{22}^{ch})dz=0$$

Simplifying

$$A_{int} \cdot \dot{\varepsilon}_{11}^{tot} + B_{int} + C_{int} \cdot \dot{\varepsilon}_{22}^{tot} + D_{int} + E_{int} \cdot \dot{\varepsilon}_{11}^{tot} + F_{int} + G_{int} \cdot \dot{\varepsilon}_{22}^{tot} + H_{int} = 0$$

$$A_{int} \cdot \dot{\varepsilon}_{11}^{tot} + E_{int} \cdot \dot{\varepsilon}_{11}^{tot} = -B_{int} - C_{int} \cdot \dot{\varepsilon}_{22}^{tot} - D_{int} - F_{int} - G_{int} \cdot \dot{\varepsilon}_{22}^{tot} - H_{int}$$

$$(A_{int} + E_{int}) \cdot \dot{\varepsilon}_{11}^{tot} = -(C_{int} + G_{int}) \cdot \dot{\varepsilon}_{22}^{tot} - B_{int} - D_{int} - F_{int} - H_{int}$$

$$\dot{\varepsilon}_{11}^{tot} = -\frac{(C_{int} + G_{int})}{(A_{int} + E_{int})} \cdot \dot{\varepsilon}_{22}^{tot} - \frac{B_{int} + D_{int} + F_{int} + H_{int}}{(A_{int} + E_{int})}$$

where

$$A_{int} = \int_0^{z_{max,plastic}} \frac{E}{1+\nu} \left\{ \left(\left[1 + \frac{\nu}{1-2\nu} - \frac{3}{2} \frac{E/E_t - 1}{E/E_t - (1-2\nu)/3} \frac{\frac{1}{9}\left(4{\sigma_{11}}^2 + {\sigma_{22}}^2 - 4\sigma_{22}\sigma_{11}\right)}{{\sigma_{11}}^2 + {\sigma_{22}}^2 - \sigma_{22}\sigma_{11}} \right] \right. \right.$$
$$\left. \left. - \frac{\left[\frac{\nu}{1-2\nu} - \frac{3}{2} \frac{\frac{E}{E_t} - 1}{\frac{E}{E_t} - \frac{(1-2\nu)}{3}} \frac{\frac{1}{9}\left(-2{\sigma_{11}}^2 + {\sigma_{22}}^2 - \sigma_{22}\sigma_{11}\right)}{{\sigma_{11}}^2 + {\sigma_{22}}^2 - \sigma_{22}\sigma_{11}} \right] \left[\frac{\nu}{1-2\nu} - \frac{3}{2} \frac{\frac{E}{E_t} - 1}{\frac{E}{E_t} - \frac{(1-2\nu)}{3}} \frac{\frac{1}{9}\left(-2{\sigma_{11}}^2 + {\sigma_{22}}^2 - \sigma_{22}\sigma_{11}\right)}{{\sigma_{11}}^2 + {\sigma_{22}}^2 - \sigma_{22}\sigma_{11}} \right]}{\left[1 + \frac{\nu}{1-2\nu} - \frac{3}{2} \frac{\frac{E}{E_t} - 1}{\frac{E}{E_t} - \frac{(1-2\nu)}{3}} \frac{\frac{1}{9}\left({\sigma_{11}}^2 + {\sigma_{22}}^2 + 2\sigma_{22}\sigma_{11}\right)}{{\sigma_{11}}^2 + {\sigma_{22}}^2 - \sigma_{22}\sigma_{11}} \right]} \right) \right\} dz$$

$$B_{int} = -\int_0^{z_{max,plastic}} \frac{E}{1+\nu} \left\{ \left(\left[1 + \frac{\nu}{1-2\nu} - \frac{3}{2} \frac{E/E_t - 1}{E/E_t - (1-2\nu)/3} \frac{\frac{1}{9}\left(4{\sigma_{11}}^2 + {\sigma_{22}}^2 - 4\sigma_{22}\sigma_{11}\right)}{{\sigma_{11}}^2 + {\sigma_{22}}^2 - \sigma_{22}\sigma_{11}} \right] \right. \right.$$
$$\left. \left. - \frac{\left[\frac{\nu}{1-2\nu} - \frac{3}{2} \frac{\frac{E}{E_t} - 1}{\frac{E}{E_t} - \frac{(1-2\nu)}{3}} \frac{\frac{1}{9}\left(-2{\sigma_{11}}^2 + {\sigma_{22}}^2 - \sigma_{22}\sigma_{11}\right)}{{\sigma_{11}}^2 + {\sigma_{22}}^2 - \sigma_{22}\sigma_{11}} \right] \left[\frac{\nu}{1-2\nu} - \frac{3}{2} \frac{\frac{E}{E_t} - 1}{\frac{E}{E_t} - \frac{(1-2\nu)}{3}} \frac{\frac{1}{9}\left(-2{\sigma_{11}}^2 + {\sigma_{22}}^2 - \sigma_{22}\sigma_{11}\right)}{{\sigma_{11}}^2 + {\sigma_{22}}^2 - \sigma_{22}\sigma_{11}} \right]}{\left[1 + \frac{\nu}{1-2\nu} - \frac{3}{2} \frac{\frac{E}{E_t} - 1}{\frac{E}{E_t} - \frac{(1-2\nu)}{3}} \frac{\frac{1}{9}\left({\sigma_{11}}^2 + {\sigma_{22}}^2 + 2\sigma_{22}\sigma_{11}\right)}{{\sigma_{11}}^2 + {\sigma_{22}}^2 - \sigma_{22}\sigma_{11}} \right]} \right) \right.$$
$$\left. \cdot \left(\dot{\varepsilon}_{11}^{th} + \dot{\varepsilon}_{11}^{ch} \right) \right\} dz$$

$$C_{int} = \int_0^{z_{max,plastic}} \frac{E}{1+\nu} \left\{ \left(\left[\frac{\nu}{1-2\nu} - \frac{3}{2} \frac{E/E_t - 1}{E/E_t - (1-2\nu)/3} \frac{\frac{1}{9}\left(-2{\sigma_{11}}^2 - 2{\sigma_{22}}^2 + 5\sigma_{22}\sigma_{11}\right)}{{\sigma_{11}}^2 + {\sigma_{22}}^2 - \sigma_{22}\sigma_{11}} \right] \right. \right.$$
$$\left. \left. - \frac{\left[\frac{\nu}{1-2\nu} - \frac{3}{2} \frac{\frac{E}{E_t} - 1}{\frac{E}{E_t} - \frac{(1-2\nu)}{3}} \frac{\frac{1}{9}\left(-2{\sigma_{11}}^2 + {\sigma_{22}}^2 - \sigma_{22}\sigma_{11}\right)}{{\sigma_{11}}^2 + {\sigma_{22}}^2 - \sigma_{22}\sigma_{11}} \right] \left[\frac{\nu}{1-2\nu} - \frac{3}{2} \frac{\frac{E}{E_t} - 1}{\frac{E}{E_t} - \frac{(1-2\nu)}{3}} \frac{\frac{1}{9}\left({\sigma_{11}}^2 - 2{\sigma_{22}}^2 - \sigma_{22}\sigma_{11}\right)}{{\sigma_{11}}^2 + {\sigma_{22}}^2 - \sigma_{22}\sigma_{11}} \right]}{\left[1 + \frac{\nu}{1-2\nu} - \frac{3}{2} \frac{\frac{E}{E_t} - 1}{\frac{E}{E_t} - \frac{(1-2\nu)}{3}} \frac{\frac{1}{9}\left({\sigma_{11}}^2 + {\sigma_{22}}^2 + 2\sigma_{22}\sigma_{11}\right)}{{\sigma_{11}}^2 + {\sigma_{22}}^2 - \sigma_{22}\sigma_{11}} \right]} \right) \right\} dz$$

$$D_{int} = -\int_0^{z_{max,plastic}} \frac{E}{1+\nu} \left\{ \left(\left[\frac{\nu}{1-2\nu} - \frac{3}{2} \frac{E/E_t - 1}{E/E_t - (1-2\nu)/3} \frac{\frac{1}{9}\left(-2{\sigma_{11}}^2 - 2{\sigma_{22}}^2 + 5\sigma_{22}\sigma_{11}\right)}{{\sigma_{11}}^2 + {\sigma_{22}}^2 - \sigma_{22}\sigma_{11}} \right] \right. \right.$$
$$\left. \left. - \frac{\left[\frac{\nu}{1-2\nu} - \frac{3}{2} \frac{\frac{E}{E_t} - 1}{\frac{E}{E_t} - \frac{(1-2\nu)}{3}} \frac{\frac{1}{9}\left(-2{\sigma_{11}}^2 + {\sigma_{22}}^2 - \sigma_{22}\sigma_{11}\right)}{{\sigma_{11}}^2 + {\sigma_{22}}^2 - \sigma_{22}\sigma_{11}} \right] \left[\frac{\nu}{1-2\nu} - \frac{3}{2} \frac{\frac{E}{E_t} - 1}{\frac{E}{E_t} - \frac{(1-2\nu)}{3}} \frac{\frac{1}{9}\left({\sigma_{11}}^2 - 2{\sigma_{22}}^2 - \sigma_{22}\sigma_{11}\right)}{{\sigma_{11}}^2 + {\sigma_{22}}^2 - \sigma_{22}\sigma_{11}} \right]}{\left[1 + \frac{\nu}{1-2\nu} - \frac{3}{2} \frac{\frac{E}{E_t} - 1}{\frac{E}{E_t} - \frac{(1-2\nu)}{3}} \frac{\frac{1}{9}\left({\sigma_{11}}^2 + {\sigma_{22}}^2 + 2\sigma_{22}\sigma_{11}\right)}{{\sigma_{11}}^2 + {\sigma_{22}}^2 - \sigma_{22}\sigma_{11}} \right]} \right) \right.$$
$$\left. \cdot \left(\dot{\varepsilon}_{22}^{th} + \dot{\varepsilon}_{22}^{ch} \right) \right\} dz$$

$$E_{int} = \int_{z_{max,plastic}}^{z_{max}} \frac{E}{1+\nu} \left(\left[1 + \frac{\nu}{1-2\nu} \right] - \frac{\left[\frac{\nu}{1-2\nu} \right]^2}{\left[1 + \frac{\nu}{1-2\nu} \right]} \right) dz$$

$$F_{int} = -\int_{z_{max,plastic}}^{z_{max}} \frac{E}{1+\nu} \left(\left[1 + \frac{\nu}{1-2\nu} \right] - \frac{\left[\frac{\nu}{1-2\nu} \right]^2}{\left[1 + \frac{\nu}{1-2\nu} \right]} \right) \left(\dot{\varepsilon}_{11}^{th} + \dot{\varepsilon}_{11}^{ch} \right) dz$$

$$G_{int} = \int_{z_{max,plastic}}^{z_{max}} \frac{E}{1+\nu} \left(\left[\frac{\nu}{1-2\nu} \right] - \frac{\left[\frac{\nu}{1-2\nu} \right]^2}{\left[1 + \frac{\nu}{1-2\nu} \right]} \right) dz$$

$$H_{int} = -\int_{z_{max,plastic}}^{z_{max}} \frac{E}{1+\nu} \left(\left[\frac{\nu}{1-2\nu} \right] - \frac{\left[\frac{\nu}{1-2\nu} \right]^2}{\left[1 + \frac{\nu}{1-2\nu} \right]} \right) \left(\dot{\varepsilon}_{22}^{th} + \dot{\varepsilon}_{22}^{ch} \right) dz$$

The integral over $\dot{\sigma}_{22}$ is then:

$$\int_0^{z_{max,plastic}} \frac{E}{1+\nu}\left\{\left(\left[\frac{\nu}{1-2\nu}-\frac{3}{2}\frac{E/E_t-1}{E/E_t-(1-2\nu)/3}\frac{\frac{1}{9}\left(-2{\sigma_{11}}^2-2{\sigma_{22}}^2+5\sigma_{22}\sigma_{11}\right)}{{\sigma_{11}}^2+{\sigma_{22}}^2-\sigma_{22}\sigma_{11}}\right]\right.\right.$$

$$\left.\left.-\frac{\left[\frac{\nu}{1-2\nu}-\frac{3}{2}\frac{E/E_t-1}{E/E_t-(1-2\nu)/3}\frac{\frac{1}{9}\left({\sigma_{11}}^2-2{\sigma_{22}}^2-\sigma_{22}\sigma_{11}\right)}{{\sigma_{11}}^2+{\sigma_{22}}^2-\sigma_{22}\sigma_{11}}\right]\left[\frac{\nu}{1-2\nu}-\frac{3}{2}\frac{\frac{E}{E_t}-1}{\frac{E}{E_t}-\frac{(1-2\nu)}{3}}\frac{\frac{1}{9}\left(-2{\sigma_{11}}^2+{\sigma_{22}}^2-\sigma_{22}\sigma_{11}\right)}{{\sigma_{11}}^2+{\sigma_{22}}^2-\sigma_{22}\sigma_{11}}\right]}{\left[1+\frac{\nu}{1-2\nu}-\frac{3}{2}\frac{\frac{E}{E_t}-1}{\frac{E}{E_t}-\frac{(1-2\nu)}{3}}\frac{\frac{1}{9}\left({\sigma_{11}}^2+{\sigma_{22}}^2+2\sigma_{22}\sigma_{11}\right)}{{\sigma_{11}}^2+{\sigma_{22}}^2-\sigma_{22}\sigma_{11}}\right]}\right)\cdot\left(\dot{\varepsilon}_{11}^{tot}-\dot{\varepsilon}_{11}^{th}-\dot{\varepsilon}_{11}^{ch}\right)$$

$$+\left(\left[1+\frac{\nu}{1-2\nu}-\frac{3}{2}\frac{E/E_t-1}{E/E_t-(1-2\nu)/3}\frac{\frac{1}{9}\left({\sigma_{11}}^2+4{\sigma_{22}}^2-4\sigma_{22}\sigma_{11}\right)}{{\sigma_{11}}^2+{\sigma_{22}}^2-\sigma_{22}\sigma_{11}}\right]\right.$$

$$\left.-\frac{\left[\frac{\nu}{1-2\nu}-\frac{3}{2}\frac{E/E_t-1}{E/E_t-(1-2\nu)/3}\frac{\frac{1}{9}\left({\sigma_{11}}^2-2{\sigma_{22}}^2-\sigma_{22}\sigma_{11}\right)}{{\sigma_{11}}^2+{\sigma_{22}}^2-\sigma_{22}\sigma_{11}}\right]\left[\frac{\nu}{1-2\nu}-\frac{3}{2}\frac{\frac{E}{E_t}-1}{\frac{E}{E_t}-\frac{(1-2\nu)}{3}}\frac{\frac{1}{9}\left({\sigma_{11}}^2-2{\sigma_{22}}^2-\sigma_{22}\sigma_{11}\right)}{{\sigma_{11}}^2+{\sigma_{22}}^2-\sigma_{22}\sigma_{11}}\right]}{\left[1+\frac{\nu}{1-2\nu}-\frac{3}{2}\frac{\frac{E}{E_t}-1}{\frac{E}{E_t}-\frac{(1-2\nu)}{3}}\frac{\frac{1}{9}\left({\sigma_{11}}^2+{\sigma_{22}}^2+2\sigma_{22}\sigma_{11}\right)}{{\sigma_{11}}^2+{\sigma_{22}}^2-\sigma_{22}\sigma_{11}}\right]}\right)\cdot\left(\dot{\varepsilon}_{22}^{tot}-\dot{\varepsilon}_{22}^{th}-\dot{\varepsilon}_{22}^{ch}\right)\Bigg\}dz$$

$$+\int_{z_{max,plastic}}^{z_{max}}\frac{E}{1+\nu}\left(\left(\left[\frac{\nu}{1-2\nu}\right]-\frac{\left[\frac{\nu}{1-2\nu}\right]^2}{\left[1+\frac{\nu}{1-2\nu}\right]}\right)\left(\dot{\varepsilon}_{11}^{tot}-\dot{\varepsilon}_{11}^{th}-\dot{\varepsilon}_{11}^{ch}\right)\right.$$

$$\left.+\left(\left[1+\frac{\nu}{1-2\nu}\right]-\frac{\left[\frac{\nu}{1-2\nu}\right]^2}{\left[1+\frac{\nu}{1-2\nu}\right]}\right)\left(\dot{\varepsilon}_{22}^{tot}-\dot{\varepsilon}_{22}^{th}-\dot{\varepsilon}_{22}^{ch}\right)\right)dz=0$$

Isolating $\dot{\varepsilon}_{11}^{tot}$ and $\dot{\varepsilon}_{22}^{tot}$ gives

$$\int_0^{z_{max,plastic}} \frac{E}{1+\nu}\left\{\left(\left[\frac{\nu}{1-2\nu}-\frac{3}{2}\frac{E/E_t-1}{E/E_t-(1-2\nu)/3}\frac{\frac{1}{9}\left(-2{\sigma_{11}}^2-2{\sigma_{22}}^2+5\sigma_{22}\sigma_{11}\right)}{{\sigma_{11}}^2+{\sigma_{22}}^2-\sigma_{22}\sigma_{11}}\right]\right.\right.$$

$$\left.\left.-\frac{\left[\frac{\nu}{1-2\nu}-\frac{3}{2}\frac{E/E_t-1}{E/E_t-(1-2\nu)/3}\frac{\frac{1}{9}\left({\sigma_{11}}^2-2{\sigma_{22}}^2-\sigma_{22}\sigma_{11}\right)}{{\sigma_{11}}^2+{\sigma_{22}}^2-\sigma_{22}\sigma_{11}}\right]\left[\frac{\nu}{1-2\nu}-\frac{3}{2}\frac{\frac{E}{E_t}-1}{\frac{E}{E_t}-\frac{(1-2\nu)}{3}}\frac{\frac{1}{9}\left(-2{\sigma_{11}}^2+{\sigma_{22}}^2-\sigma_{22}\sigma_{11}\right)}{{\sigma_{11}}^2+{\sigma_{22}}^2-\sigma_{22}\sigma_{11}}\right]}{\left[1+\frac{\nu}{1-2\nu}-\frac{3}{2}\frac{\frac{E}{E_t}-1}{\frac{E}{E_t}-\frac{(1-2\nu)}{3}}\frac{\frac{1}{9}\left({\sigma_{11}}^2+{\sigma_{22}}^2+2\sigma_{22}\sigma_{11}\right)}{{\sigma_{11}}^2+{\sigma_{22}}^2-\sigma_{22}\sigma_{11}}\right]}\right)\right\}dz$$

$$\cdot\,\dot{\varepsilon}_{11}^{tot}$$

$$-\int_0^{z_{max,plastic}} \frac{E}{1+\nu}\left\{\left(\left[\frac{\nu}{1-2\nu}-\frac{3}{2}\frac{E/E_t-1}{E/E_t-(1-2\nu)/3}\frac{\frac{1}{9}\left(-2{\sigma_{11}}^2-2{\sigma_{22}}^2+5\sigma_{22}\sigma_{11}\right)}{{\sigma_{11}}^2+{\sigma_{22}}^2-\sigma_{22}\sigma_{11}}\right]\right.\right.$$

$$\left.\left.-\frac{\left[\frac{\nu}{1-2\nu}-\frac{3}{2}\frac{E/E_t-1}{E/E_t-(1-2\nu)/3}\frac{\frac{1}{9}\left({\sigma_{11}}^2-2{\sigma_{22}}^2-\sigma_{22}\sigma_{11}\right)}{{\sigma_{11}}^2+{\sigma_{22}}^2-\sigma_{22}\sigma_{11}}\right]\left[\frac{\nu}{1-2\nu}-\frac{3}{2}\frac{\frac{E}{E_t}-1}{\frac{E}{E_t}-\frac{(1-2\nu)}{3}}\frac{\frac{1}{9}\left(-2{\sigma_{11}}^2+{\sigma_{22}}^2-\sigma_{22}\sigma_{11}\right)}{{\sigma_{11}}^2+{\sigma_{22}}^2-\sigma_{22}\sigma_{11}}\right]}{\left[1+\frac{\nu}{1-2\nu}-\frac{3}{2}\frac{\frac{E}{E_t}-1}{\frac{E}{E_t}-\frac{(1-2\nu)}{3}}\frac{\frac{1}{9}\left({\sigma_{11}}^2+{\sigma_{22}}^2+2\sigma_{22}\sigma_{11}\right)}{{\sigma_{11}}^2+{\sigma_{22}}^2-\sigma_{22}\sigma_{11}}\right]}\right)\right\}$$

$$\cdot\left(\dot{\varepsilon}_{11}^{th}+\dot{\varepsilon}_{11}^{ch}\right)\Bigg\}dz$$

$$+\int_0^{z_{max,plastic}} \frac{E}{1+\nu}\left\{\left(\left[1+\frac{\nu}{1-2\nu}-\frac{3}{2}\frac{E/E_t-1}{E/E_t-(1-2\nu)/3}\frac{\frac{1}{9}(\sigma_{11}{}^2+4\sigma_{22}{}^2-4\sigma_{22}\sigma_{11})}{\sigma_{11}{}^2+\sigma_{22}{}^2-\sigma_{22}\sigma_{11}}\right]\right.\right.$$

$$\left.\left.-\frac{\left[\frac{\nu}{1-2\nu}-\frac{3}{2}\frac{E/E_t-1}{E/E_t-(1-2\nu)/3}\frac{\frac{1}{9}(\sigma_{11}{}^2-2\sigma_{22}{}^2-\sigma_{22}\sigma_{11})}{\sigma_{11}{}^2+\sigma_{22}{}^2-\sigma_{22}\sigma_{11}}\right]\left[\frac{\nu}{1-2\nu}-\frac{3}{2}\frac{\frac{E}{E_t}-1}{\frac{E}{E_t}-\frac{(1-2\nu)}{3}}\frac{\frac{1}{9}(\sigma_{11}{}^2-2\sigma_{22}{}^2-\sigma_{22}\sigma_{11})}{\sigma_{11}{}^2+\sigma_{22}{}^2-\sigma_{22}\sigma_{11}}\right]}{\left[1+\frac{\nu}{1-2\nu}-\frac{3}{2}\frac{\frac{E}{E_t}-1}{\frac{E}{E_t}-\frac{(1-2\nu)}{3}}\frac{\frac{1}{9}(\sigma_{11}{}^2+\sigma_{22}{}^2+2\sigma_{22}\sigma_{11})}{\sigma_{11}{}^2+\sigma_{22}{}^2-\sigma_{22}\sigma_{11}}\right]}\right)\right\}dz$$

$$\cdot\,\dot{\varepsilon}_{22}^{tot}$$

$$-\int_0^{z_{max,plastic}} \frac{E}{1+\nu}\left\{\left(\left[1+\frac{\nu}{1-2\nu}-\frac{3}{2}\frac{E/E_t-1}{E/E_t-(1-2\nu)/3}\frac{\frac{1}{9}(\sigma_{11}{}^2+4\sigma_{22}{}^2-4\sigma_{22}\sigma_{11})}{\sigma_{11}{}^2+\sigma_{22}{}^2-\sigma_{22}\sigma_{11}}\right]\right.\right.$$

$$\left.\left.-\frac{\left[\frac{\nu}{1-2\nu}-\frac{3}{2}\frac{E/E_t-1}{E/E_t-(1-2\nu)/3}\frac{\frac{1}{9}(\sigma_{11}{}^2-2\sigma_{22}{}^2-\sigma_{22}\sigma_{11})}{\sigma_{11}{}^2+\sigma_{22}{}^2-\sigma_{22}\sigma_{11}}\right]\left[\frac{\nu}{1-2\nu}-\frac{3}{2}\frac{\frac{E}{E_t}-1}{\frac{E}{E_t}-\frac{(1-2\nu)}{3}}\frac{\frac{1}{9}(\sigma_{11}{}^2-2\sigma_{22}{}^2-\sigma_{22}\sigma_{11})}{\sigma_{11}{}^2+\sigma_{22}{}^2-\sigma_{22}\sigma_{11}}\right]}{\left[1+\frac{\nu}{1-2\nu}-\frac{3}{2}\frac{\frac{E}{E_t}-1}{\frac{E}{E_t}-\frac{(1-2\nu)}{3}}\frac{\frac{1}{9}(\sigma_{11}{}^2+\sigma_{22}{}^2+2\sigma_{22}\sigma_{11})}{\sigma_{11}{}^2+\sigma_{22}{}^2-\sigma_{22}\sigma_{11}}\right]}\right)\right\}$$

$$\cdot\,(\dot{\varepsilon}_{22}^{th}+\dot{\varepsilon}_{22}^{ch})\Bigg\}dz$$

$$+\int_{z_{max,plastic}}^{z_{max}} \frac{E}{1+\nu}\left(\left[\frac{\nu}{1-2\nu}\right]-\frac{\left[\frac{\nu}{1-2\nu}\right]^2}{\left[1+\frac{\nu}{1-2\nu}\right]}\right)dz\cdot\dot{\varepsilon}_{11}^{tot}-\int_{z_{max,plastic}}^{z_{max}} \frac{E}{1+\nu}\left(\left[\frac{\nu}{1-2\nu}\right]-\frac{\left[\frac{\nu}{1-2\nu}\right]^2}{\left[1+\frac{\nu}{1-2\nu}\right]}\right)(\dot{\varepsilon}_{11}^{th}+\dot{\varepsilon}_{11}^{ch})dz$$

$$+\int_{z_{max,plastic}}^{z_{max}} \frac{E}{1+\nu}\left(\left[1+\frac{\nu}{1-2\nu}\right]-\frac{\left[\frac{\nu}{1-2\nu}\right]^2}{\left[1+\frac{\nu}{1-2\nu}\right]}\right)dz\cdot\dot{\varepsilon}_{22}^{tot}$$

$$-\int_{z_{max,plastic}}^{z_{max}} \frac{E}{1+\nu}\left(\left[1+\frac{\nu}{1-2\nu}\right]-\frac{\left[\frac{\nu}{1-2\nu}\right]^2}{\left[1+\frac{\nu}{1-2\nu}\right]}\right)(\dot{\varepsilon}_{22}^{th}+\dot{\varepsilon}_{22}^{ch})dz=0$$

which can be shortened to

$$I_{int} \cdot \dot{\varepsilon}_{11}^{tot} + J_{int} + K_{int} \cdot \dot{\varepsilon}_{22}^{tot} + L_{int} + M_{int} \cdot \dot{\varepsilon}_{11}^{tot} + N_{int} + O_{int} \cdot \dot{\varepsilon}_{22}^{tot} + P_{int} = 0$$

where

$$I_{int} = \int_0^{z_{max,plastic}} \frac{E}{1+\nu} \left\{ \left(\left[\frac{\nu}{1-2\nu} - \frac{3}{2} \frac{E/E_t - 1}{E/E_t - (1-2\nu)/3} \frac{\frac{1}{9}\left(-2{\sigma_{11}}^2 - 2{\sigma_{22}}^2 + 5\sigma_{22}\sigma_{11}\right)}{{\sigma_{11}}^2 + {\sigma_{22}}^2 - \sigma_{22}\sigma_{11}} \right] \right. \right.$$
$$\left. \left. - \frac{\left[\frac{\nu}{1-2\nu} - \frac{3}{2} \frac{E/E_t - 1}{E/E_t - (1-2\nu)/3} \frac{\frac{1}{9}\left({\sigma_{11}}^2 - 2{\sigma_{22}}^2 - \sigma_{22}\sigma_{11}\right)}{{\sigma_{11}}^2 + {\sigma_{22}}^2 - \sigma_{22}\sigma_{11}} \right] \left[\frac{\nu}{1-2\nu} - \frac{3}{2} \frac{\frac{E}{E_t} - 1}{\frac{E}{E_t} - \frac{(1-2\nu)}{3}} \frac{\frac{1}{9}\left(-2{\sigma_{11}}^2 + {\sigma_{22}}^2 - \sigma_{22}\sigma_{11}\right)}{{\sigma_{11}}^2 + {\sigma_{22}}^2 - \sigma_{22}\sigma_{11}} \right]}{\left[1 + \frac{\nu}{1-2\nu} - \frac{3}{2} \frac{\frac{E}{E_t} - 1}{\frac{E}{E_t} - \frac{(1-2\nu)}{3}} \frac{\frac{1}{9}\left({\sigma_{11}}^2 + {\sigma_{22}}^2 + 2\sigma_{22}\sigma_{11}\right)}{{\sigma_{11}}^2 + {\sigma_{22}}^2 - \sigma_{22}\sigma_{11}} \right]} \right) \right\} dz$$

$$J_{int} = -\int_0^{z_{max,plastic}} \frac{E}{1+\nu} \left\{ \left(\left[\frac{\nu}{1-2\nu} - \frac{3}{2} \frac{E/E_t - 1}{E/E_t - (1-2\nu)/3} \frac{\frac{1}{9}\left(-2{\sigma_{11}}^2 - 2{\sigma_{22}}^2 + 5\sigma_{22}\sigma_{11}\right)}{{\sigma_{11}}^2 + {\sigma_{22}}^2 - \sigma_{22}\sigma_{11}} \right] \right. \right.$$
$$\left. - \frac{\left[\frac{\nu}{1-2\nu} - \frac{3}{2} \frac{E/E_t - 1}{E/E_t - (1-2\nu)/3} \frac{\frac{1}{9}\left({\sigma_{11}}^2 - 2{\sigma_{22}}^2 - \sigma_{22}\sigma_{11}\right)}{{\sigma_{11}}^2 + {\sigma_{22}}^2 - \sigma_{22}\sigma_{11}} \right] \left[\frac{\nu}{1-2\nu} - \frac{3}{2} \frac{\frac{E}{E_t} - 1}{\frac{E}{E_t} - \frac{(1-2\nu)}{3}} \frac{\frac{1}{9}\left(-2{\sigma_{11}}^2 + {\sigma_{22}}^2 - \sigma_{22}\sigma_{11}\right)}{{\sigma_{11}}^2 + {\sigma_{22}}^2 - \sigma_{22}\sigma_{11}} \right]}{\left[1 + \frac{\nu}{1-2\nu} - \frac{3}{2} \frac{\frac{E}{E_t} - 1}{\frac{E}{E_t} - \frac{(1-2\nu)}{3}} \frac{\frac{1}{9}\left({\sigma_{11}}^2 + {\sigma_{22}}^2 + 2\sigma_{22}\sigma_{11}\right)}{{\sigma_{11}}^2 + {\sigma_{22}}^2 - \sigma_{22}\sigma_{11}} \right]} \right) \cdot \left(\dot{\varepsilon}_{11}^{th} + \dot{\varepsilon}_{11}^{ch} \right) \right\} dz$$

$$K_{int} = \int_0^{z_{max,plastic}} \frac{E}{1+\nu} \left\{ \left(\left[1 + \frac{\nu}{1-2\nu} - \frac{3}{2} \frac{E/E_t - 1}{E/E_t - (1-2\nu)/3} \frac{\frac{1}{9}\left({\sigma_{11}}^2 + 4{\sigma_{22}}^2 - 4\sigma_{22}\sigma_{11}\right)}{{\sigma_{11}}^2 + {\sigma_{22}}^2 - \sigma_{22}\sigma_{11}} \right] \right. \right.$$
$$\left. \left. - \frac{\left[\frac{\nu}{1-2\nu} - \frac{3}{2} \frac{E/E_t - 1}{E/E_t - (1-2\nu)/3} \frac{\frac{1}{9}\left({\sigma_{11}}^2 - 2{\sigma_{22}}^2 - \sigma_{22}\sigma_{11}\right)}{{\sigma_{11}}^2 + {\sigma_{22}}^2 - \sigma_{22}\sigma_{11}} \right] \left[\frac{\nu}{1-2\nu} - \frac{3}{2} \frac{\frac{E}{E_t} - 1}{\frac{E}{E_t} - \frac{(1-2\nu)}{3}} \frac{\frac{1}{9}\left({\sigma_{11}}^2 - 2{\sigma_{22}}^2 - \sigma_{22}\sigma_{11}\right)}{{\sigma_{11}}^2 + {\sigma_{22}}^2 - \sigma_{22}\sigma_{11}} \right]}{\left[1 + \frac{\nu}{1-2\nu} - \frac{3}{2} \frac{\frac{E}{E_t} - 1}{\frac{E}{E_t} - \frac{(1-2\nu)}{3}} \frac{\frac{1}{9}\left({\sigma_{11}}^2 + {\sigma_{22}}^2 + 2\sigma_{22}\sigma_{11}\right)}{{\sigma_{11}}^2 + {\sigma_{22}}^2 - \sigma_{22}\sigma_{11}} \right]} \right) \right\} dz$$

$$L_{int} = -\int_0^{z_{max,plastic}} \frac{E}{1+\nu}\left\{\left(\left[1+\frac{\nu}{1-2\nu}-\frac{3}{2}\frac{E/E_t-1}{E/E_t-(1-2\nu)/3}\frac{\frac{1}{9}(\sigma_{11}{}^2+4\sigma_{22}{}^2-4\sigma_{22}\sigma_{11})}{\sigma_{11}{}^2+\sigma_{22}{}^2-\sigma_{22}\sigma_{11}}\right]\right.\right.$$

$$\left.\left.-\frac{\left[\frac{\nu}{1-2\nu}-\frac{3}{2}\frac{E/E_t-1}{E/E_t-(1-2\nu)/3}\frac{\frac{1}{9}(\sigma_{11}{}^2-2\sigma_{22}{}^2-\sigma_{22}\sigma_{11})}{\sigma_{11}{}^2+\sigma_{22}{}^2-\sigma_{22}\sigma_{11}}\right]\left[\frac{\nu}{1-2\nu}-\frac{3}{2}\frac{\frac{E}{E_t}-1}{\frac{E}{E_t}-\frac{(1-2\nu)}{3}}\frac{\frac{1}{9}(\sigma_{11}{}^2-2\sigma_{22}{}^2-\sigma_{22}\sigma_{11})}{\sigma_{11}{}^2+\sigma_{22}{}^2-\sigma_{22}\sigma_{11}}\right]}{\left[1+\frac{\nu}{1-2\nu}-\frac{3}{2}\frac{\frac{E}{E_t}-1}{\frac{E}{E_t}-\frac{(1-2\nu)}{3}}\frac{\frac{1}{9}(\sigma_{11}{}^2+\sigma_{22}{}^2+2\sigma_{22}\sigma_{11})}{\sigma_{11}{}^2+\sigma_{22}{}^2-\sigma_{22}\sigma_{11}}\right]}\right)\right.$$

$$\left.\cdot(\dot{\varepsilon}_{22}^{th}+\dot{\varepsilon}_{22}^{ch})\right\}dz$$

$$M_{int} = \int_{z_{max,plastic}}^{z_{max}} \frac{E}{1+\nu}\left(\left[\frac{\nu}{1-2\nu}\right]-\frac{\left[\frac{\nu}{1-2\nu}\right]^2}{\left[1+\frac{\nu}{1-2\nu}\right]}\right)dz$$

$$N_{int} = -\int_{z_{max,plastic}}^{z_{max}} \frac{E}{1+\nu}\left(\left[\frac{\nu}{1-2\nu}\right]-\frac{\left[\frac{\nu}{1-2\nu}\right]^2}{\left[1+\frac{\nu}{1-2\nu}\right]}\right)(\dot{\varepsilon}_{11}^{th}+\dot{\varepsilon}_{11}^{ch})dz$$

$$O_{int} = \int_{z_{max,plastic}}^{z_{max}} \frac{E}{1+\nu}\left(\left[1+\frac{\nu}{1-2\nu}\right]-\frac{\left[\frac{\nu}{1-2\nu}\right]^2}{\left[1+\frac{\nu}{1-2\nu}\right]}\right)dz$$

$$P_{int} = -\int_{z_{max,plastic}}^{z_{max}} \frac{E}{1+\nu}\left(\left[1+\frac{\nu}{1-2\nu}\right]-\frac{\left[\frac{\nu}{1-2\nu}\right]^2}{\left[1+\frac{\nu}{1-2\nu}\right]}\right)(\dot{\varepsilon}_{22}^{th}+\dot{\varepsilon}_{22}^{ch})dz$$

Inserting expression for $\dot{\varepsilon}_{11}^{tot}$ derived from the integral over $\dot{\sigma}_{11}$

$$\dot{\varepsilon}_{11}^{tot} = -\frac{(C_{int}+G_{int})}{(A_{int}+E_{int})}\cdot\dot{\varepsilon}_{22}^{tot} - \frac{B_{int}+D_{int}+F_{int}+H_{int}}{(A_{int}+E_{int})}$$

in the expression resulting from the integral over $\dot{\sigma}_{22}$

$$I_{int}\cdot\dot{\varepsilon}_{11}^{tot} + J_{int} + K_{int}\cdot\dot{\varepsilon}_{22}^{tot} + L_{int} + M_{int}\cdot\dot{\varepsilon}_{11}^{tot} + N_{int} + O_{int}\cdot\dot{\varepsilon}_{22}^{tot} + P_{int} = 0$$

Gives (omitting the subscript *int* for convenience)

$$I \cdot \left(-\frac{(C+G)}{(A+E)} \cdot \dot{\varepsilon}_{22}^{tot} - \frac{B+D+F+H}{(A+E)} \right) + J + K \cdot \dot{\varepsilon}_{22}^{tot} + L + M \cdot \left(-\frac{(C+G)}{(A+E)} \cdot \dot{\varepsilon}_{22}^{tot} - \frac{B+D+F+H}{(A+E)} \right) + N + O \cdot \dot{\varepsilon}_{22}^{tot} + P = 0$$

Isolating $\dot{\varepsilon}_{22}^{tot}$ gives

$$-I \cdot \frac{(C+G)}{(A+E)} \cdot \dot{\varepsilon}_{22}^{tot} - I \cdot \frac{B+D+F+H}{(A+E)} + J + K \cdot \dot{\varepsilon}_{22}^{tot} + L - M \cdot \frac{(C+G)}{(A+E)} \cdot \dot{\varepsilon}_{22}^{tot} - M \cdot \frac{B+D+F+H}{(A+E)} + N + O \cdot \dot{\varepsilon}_{22}^{tot} + P = 0$$

$$\leftrightarrow$$

$$-I \cdot \frac{(C+G)}{(A+E)} \cdot \dot{\varepsilon}_{22}^{tot} + K \cdot \dot{\varepsilon}_{22}^{tot} - M \cdot \frac{(C+G)}{(A+E)} \cdot \dot{\varepsilon}_{22}^{tot} + O \cdot \dot{\varepsilon}_{22}^{tot} = I \cdot \frac{B+D+F+H}{(A+E)} - J - L + M \cdot \frac{B+D+F+H}{(A+E)} - N - P$$

$$\leftrightarrow$$

$$\left(-\frac{(I+M) \cdot (C+G)}{(A+E)} + K + O \right) \cdot \dot{\varepsilon}_{22}^{tot} = \frac{(I+M) \cdot (B+D+F+H)}{(A+E)} - J - L - N - P$$

$$\leftrightarrow$$

$$\dot{\varepsilon}_{22}^{tot} = \frac{\frac{(I+M) \cdot (B+D+F+H)}{(A+E)} - J - L - N - P}{\left(-\frac{(I+M) \cdot (C+G)}{(A+E)} + K + O \right)}$$

Appendix C - Verification of program calculations

C.1 - Verification of strain calculation

Verification of calculation of total strain from chemical strain

To verify the calculation of the chemical and total strains, a constant temperature test case is run where the concentration initially is set to zero, $\left(c_i^0 = 0\right)$ throughout the specimen and then in one time step is raised to a fixed value $\left(c_i^1 = \bar{c}\right)$.

This gives the same chemical strain in all elements; for $i = j$ $\varepsilon_{ij}^{che,\varphi}(c) = \frac{1}{3} \cdot \frac{V(c)_\varphi - V_{\varphi,ref}}{V_{\varphi,ref}}$, where

$V_\varphi(c) = 2.7603 \cdot 10^{-34} \cdot \bar{c} + 4.6197 \cdot 10^{-29}$ and $V_{\varphi,ref} = 4.6197 \cdot 10^{-29}$ was applied for this test case.

The expression for the total strain,

$$\varepsilon_{yy} = \frac{1}{x_{max}} \sum_{1}^{imax} \left[\varepsilon_{yy}^{th}(i) \cdot \Delta x(i) + \varepsilon_{yy}^{ch}(i) \cdot \Delta x(i)\right] \tag{C1}$$

can then be reduced to

$$\varepsilon_{yy} = \varepsilon_{yy}^{ch}(i) \tag{C2}$$

which reduces the expression for the stress to

$$\sigma_{yy} = \frac{E}{1-\nu}\left(\varepsilon_{yy} - \varepsilon_{yy}^{th} - \varepsilon_{yy}^{ch}\right) = 0 \tag{C3}$$

Using $\bar{c} = 5000, E = 200\text{GPa}, \nu = 0.3$ the following results were obtained

	Chemical strain: $\boldsymbol{\varepsilon_{yy}^{ch}(i)}$	**Total strain:** $\boldsymbol{\varepsilon_{yy}}$	**Elastic strain:**	**Stress:** $\boldsymbol{\sigma_{yy}}$
Calculated analytically from above expressions	0.009958	0.009958	0	0
Result from test-run of program	0.009958	0.009958	$-1.7347 \cdot 10^{-18}$ (numeric zero)	$-4.9564 \cdot 10^{-7}$Pa (numeric zero)

Resulting curves from the simulation, shown in Figure 60 shows the intended horizontal linear profiles. Since the analytically calculated results and the simulation results are the same, the calculation of total strain in the simulation is verified.

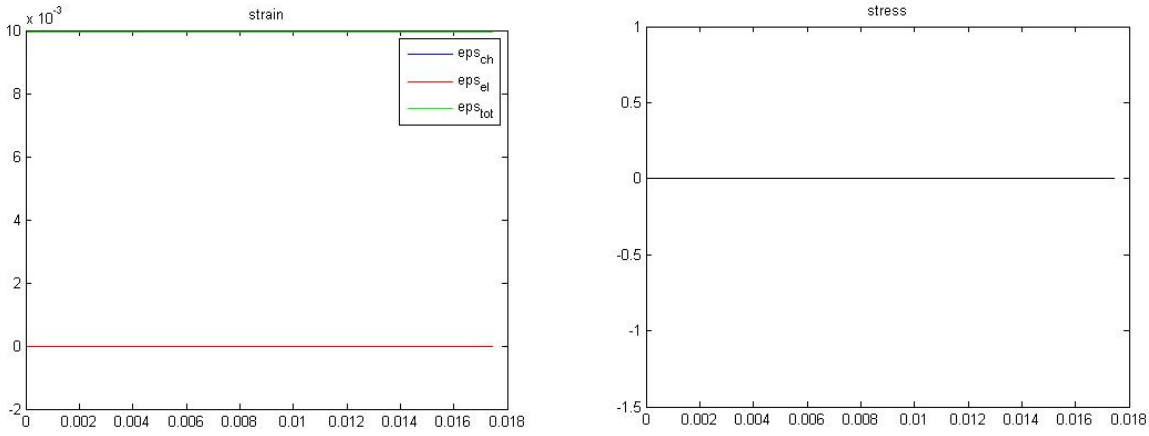

Figure 60 - strains and stresses predicted by test simulation, calculating total strain (eps_{tot}) from chemical strain (eps_{ch})

Verification of calculation of total strain from thermal strain

To verify the calculation of the thermal and total strains, a zero concentration test case is run where the temperature initially is set to zero, $\left(T_i^0 = 0\right)$ throughout the specimen and then in one time step is raised to a fixed value $\left(T_i^1 = \bar{T}\right)$.

This gives the same chemical strain in all elements $for\ i = j\ \varepsilon_{ij}^{th}(c) = \alpha\Delta T$,

The expression for the total strain

$$\varepsilon_{yy} = \frac{1}{x_{max}} \sum_{1}^{imax} \left[\varepsilon_{yy}^{th}(i) \cdot \Delta x(i) + \varepsilon_{yy}^{ch}(i) \cdot \Delta x(i)\right] \tag{C4}$$

Can then be reduced to

$$\varepsilon_{yy} = \varepsilon_{yy}^{th}(i) \tag{C5}$$

which reduces the expression for the stress to

$$\sigma_{yy} = \frac{E}{1-\nu}\left(\varepsilon_{yy} - \varepsilon_{yy}^{th} - \varepsilon_{yy}^{ch}\right) = 0 \tag{C6}$$

Using $\bar{T} = 200K, E = 200\text{GPa}, \nu = 0.3, \alpha = 10^{-5}$ the following results were obtained

	Thermal strain: $\boldsymbol{\varepsilon_{yy}^{th}(i)}$ for all i	**Total strain: $\boldsymbol{\varepsilon_{yy}}$**	**Elastic strain:**	**Stress: $\boldsymbol{\sigma_{yy}}$**
Calculated analytically from above expressions	0.002	0.002	0	0
Result from test-run of program	0.002	0.002	$-8.6736 \cdot 10^{-19}$ (numeric zero)	$-2.4782 \cdot 10^{-07}$Pa (numeric zero)

Analytically calculated results and the simulation results are the same, the calculation of total strain from thermal strain in the simulation is verified.

C.2 - Verification of stress calculation

Concentration differences test

To verify the calculation of the stress, a constant temperature test case is run where the concentration initially is set to zero, $\left(c_i^0 = 0\right)$ throughout the specimen and then in one time step is raised so that the first half of the specimen is set to a fixed value $\left(c_i^1 = \bar{c}\right)$, and the second half is kept at zero $c_i^1 = c_i^0$.

This gives, analytically, a chemical strain of zero in the second half, and in the elements of the first half; for $i = j$ $\varepsilon_{ij}^{che,\varphi}(c) = \frac{1}{3} \cdot \frac{V(c)_\varphi - V_{\varphi,ref}}{V_{\varphi,ref}}$, where

$V_\varphi(c) = 2.7603 \cdot 10^{-34} \cdot \bar{c} + 4.6197 \cdot 10^{-29}$ and $V_{\varphi,ref} = 4.6197 \cdot 10^{-29}$ was applied.

The total strain is then found to be half of the chemical strain in the second half of the specimen,

$$\varepsilon_{yy} = \frac{1}{x_{max}} \sum_{1}^{imax} \left[0 \cdot \frac{x_{max}}{2} + \varepsilon_{yy}^{ch} \cdot \frac{x_{max}}{2}\right] = \frac{\varepsilon_{yy}^{ch}}{2} \tag{C7}$$

inducing a compressive stress in the first half of the specimen of

$$\sigma_{yy} = \frac{E}{1-\nu}\left(\frac{\varepsilon_{yy}^{ch}}{2} - \varepsilon_{yy}^{ch}\right) = -\frac{E}{1-\nu}\frac{\varepsilon_{yy}^{ch}}{2} \tag{C8}$$

and a tensile stress in the second half of the specimen of

$$\sigma_{yy} = \frac{E}{1-\nu}\left(\frac{\varepsilon_{yy}^{ch}}{2} - 0\right) = \frac{E}{1-\nu}\frac{\varepsilon_{yy}^{ch}}{2} \tag{C9}$$

Using $\bar{c} = 10000, E = 200\text{GPa}, \nu = 0.3$ the following results were obtained

	Chemical strain first half: $\varepsilon_{yy}^{ch}(i)$	**Chemical strain 2nd half:** $\varepsilon_{yy}^{ch}(i)$	**Total strain:** ε_{yy}	**Stress first half:** σ_{yy}	**Stress 2nd half:** σ_{yy}
Calculated analytically from above expressions	0.01992	0	0.009958	-2.8453 GPa	2.8453 GPa
Result from test-run of program	0.01992	0	0.009958	-2.8453 GPa	2.8453 GPa

The total strain is now the same as the one found in the strain check example as would be expected since the concentration average was the same.

Resulting curves from program, seen in Figure 61, shows the expected profiles

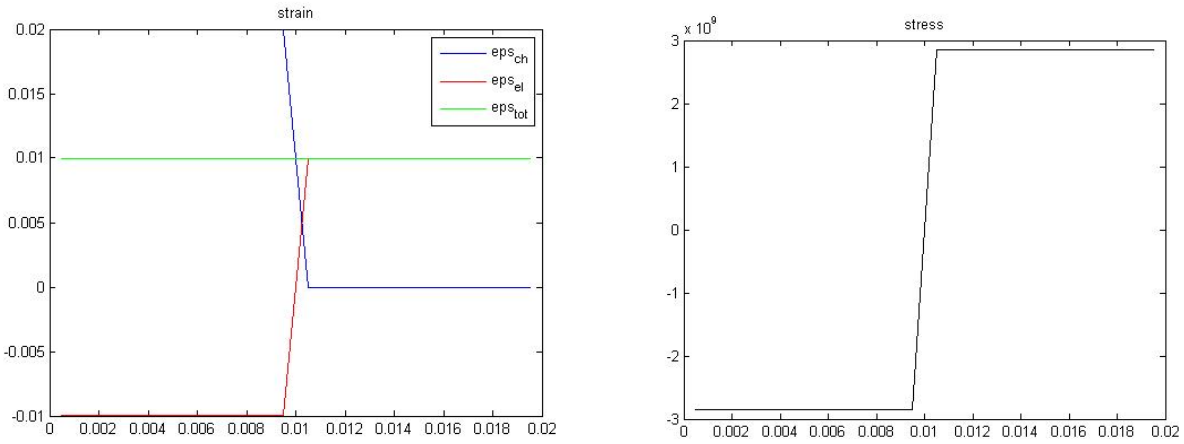

Figure 61 - strains and stresses predicted by test simulation; varying concentrations

Analytically the residual from the stress should be

$$R = \int_0^{x_{max}} \sigma_{yy} dx = 0 \tag{C10}$$

In the numerical code this is implemented as

$$R = \sum_{i}^{imax} \sigma_i \cdot \Delta z_i \tag{C11}$$

For this test example $R = -3.45 \cdot 10^{-8}$ (numerical zero).

Linear varying concentration test

Verifying the stress and strain calculation the program is now subjected to a linear decreasing concentration profile with concentrations going from 10000 to 0. This still gives the same concentration average as in the two previous tests and thus the same average strain should be found. Since the concentration at the surface cell and the centre cell are the same as in the concentration differences test, the same stress levels should be found in these cells as in the concentration differences test, and a linear stress profile is expected.

The resulting curves from the program run are seen below in Figure 62, and the expected linear profiles are achieved.

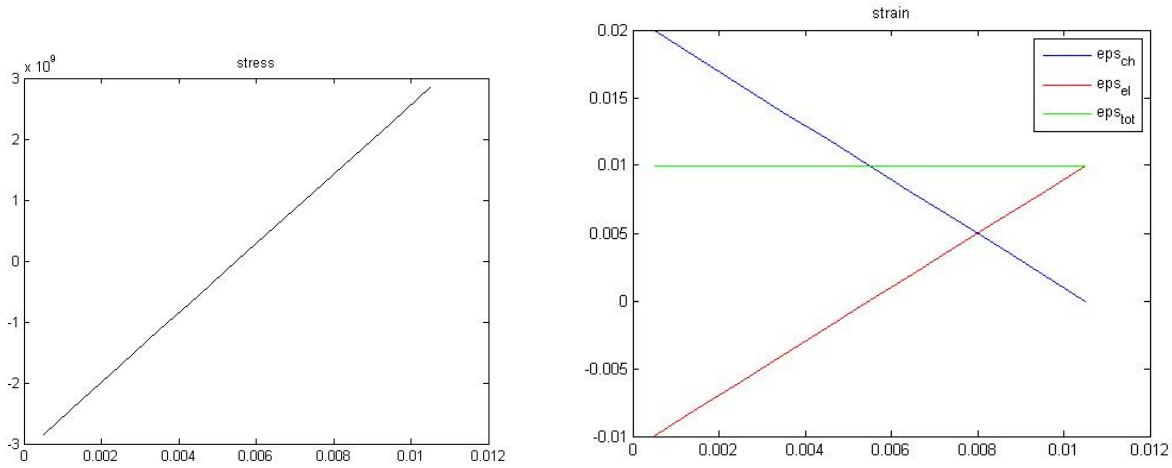

Figure 62 - strains and stresses predicted by test simulation; linear varying concentrations

Comparing the results with the ones from the concentration differences test it is seen that they are the same.

	Chemical strain first cell: $\boldsymbol{\varepsilon_{yy}^{ch}(i)}$	**Total strain:** $\boldsymbol{\varepsilon_{yy}}$	**Stress first cell:** $\boldsymbol{\sigma_{yy}}$	**Stress center cell:** $\boldsymbol{\sigma_{yy}}$
Concentration differences test	0.01992	0.009958	-2.8453 GPa	2.8453 GPa
Result from test-run of program (linear variation concentration)	0.01992	0.009958	-2.8453 GPa	2.8453 GPa

The residual for this test examples stress calculation was found to be $R = -2.79 \cdot 10^{-9}$ (numerical zero).

Temperature differences test

To verify the calculation of the stress, a zero concentration test case is run where the temperature initially is set to zero, $\left(T_i^0 = 0\right)$ throughout the specimen and then in one time step is raised so that the first half of the specimen is set to a fixed value $\left(T_i^1 = \bar{T}\right)$, and the second half is kept at zero $T_i^1 = T_i^0$.

This gives analytically a thermal strain of zero in the second half, and in the elements of the first half; for $i = j$ $\varepsilon_{ij}^{th}(c) = \alpha\Delta\bar{T}$,

The total strain is then found to be half of the thermal strain in the second half,

$$\varepsilon_{yy} = \frac{1}{x_{max}} \sum_{1}^{imax} \left[\varepsilon_{yy}^{th} \cdot \frac{x_{max}}{2} + 0 \cdot \frac{x_{max}}{2}\right] = \frac{\varepsilon_{yy}^{th}}{2} \tag{C12}$$

inducing a compressive stress in the first half of

$$\sigma_{yy} = \frac{E}{1-\nu}\left(\frac{\varepsilon_{yy}^{th}}{2} - \varepsilon_{yy}^{th}\right) = -\frac{E}{1-\nu}\frac{\varepsilon_{yy}^{th}}{2} \tag{C13}$$

And a tensile stress in the second half of

$$\sigma_{yy} = \frac{E}{1-\nu}\left(\frac{\varepsilon_{yy}^{th}}{2} - 0\right) = \frac{E}{1-\nu}\frac{\varepsilon_{yy}^{th}}{2} \tag{C14}$$

Using $\bar{T} = 400K, E = 200\text{GPa}, \nu = 0.3, \alpha = 10^{-5}$ the following results were obtained

	Thermal strain first half: $\varepsilon_{yy}^{th}(i)$	**Thermal strain 2nd half: $\varepsilon_{yy}^{th}(i)$**	**Total strain: ε_{yy}**	**Stress first half: σ_{yy}**	**Stress 2nd half: σ_{yy}**
Calculated analytically from above expressions	0.004	0	0.002	-571.4 MPa	571.4 MPa
Result from test-run of program	0.004	0	0.002	-571.4 MPa	571.4 MPa

The total strain is now the same as the one found in the strain check example as would be expected since the temperature average was the same.

Resulting curves from simulation, seen in Figure 63, shows the expected profiles

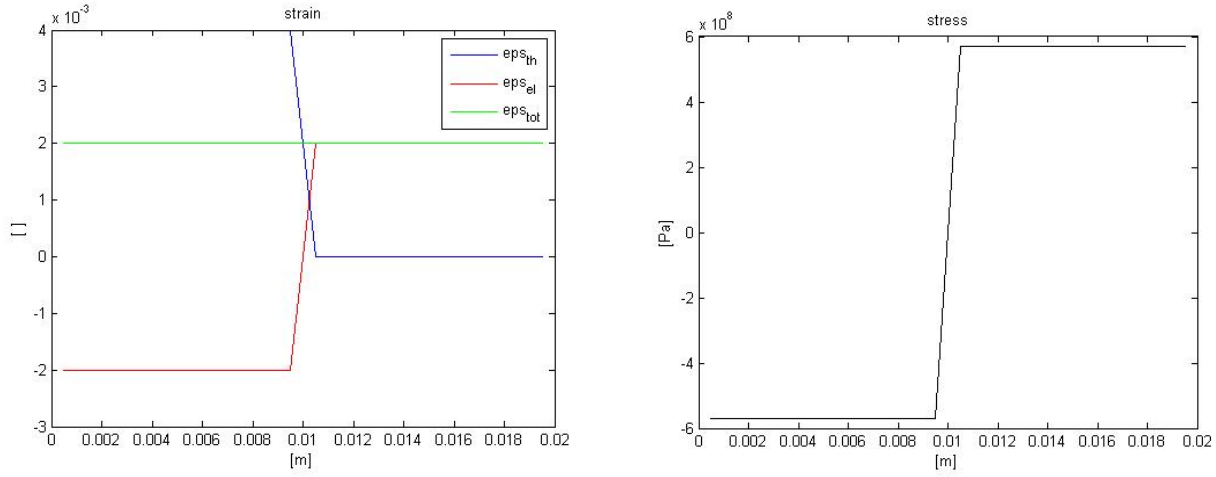

Figure 63 - strains and stresses predicted by test simulation; temperature variations

Linear varying temperature test

Verifying the stress and strain calculation the program is now subjected to a linear decreasing temperature profile with temperatures going from 400K to 0K. This still gives the same temperature average as in the previous temperature test and thus the same average strain should be found. Since the temperature at the surface cell and the centre cell are the same as in the temperature differences test, the same stress levels should be found in these cells as in the temperature differences test, and a linear stress profile is expected.

The resulting curves from the program run are seen below in Figure 64, and the expected linear profiles are achieved.

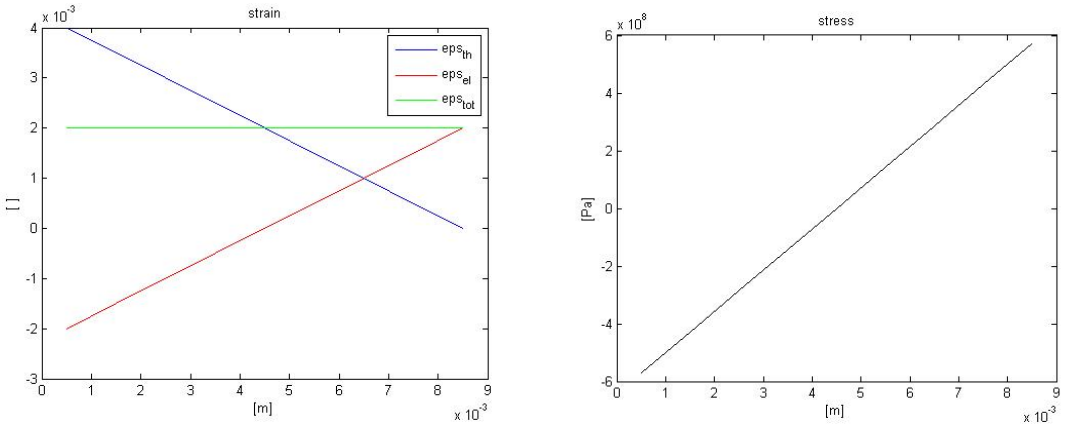

Figure 64 - strains and stresses predicted by test simulation; linear varying temperatures

Comparing the results with the ones from the temperature differences test it is seen that they are the same.

	Thermal strain first cell: $\boldsymbol{\varepsilon_{yy}^{th}(i)}$	**Total strain:** $\boldsymbol{\varepsilon_{yy}}$	**Stress first cell:** $\boldsymbol{\sigma_{yy}}$	**Stress center cell:** $\boldsymbol{\sigma_{yy}}$
Temperature differences test	0.004	0.002	-571.4 MPa	571.4 MPa
Result from test-run of program (linear variation temperature)	0.004	0.002	-571.4 MPa	571.4 MPa

The residual for this test examples stress calculation was found to be $R = -1.164 \cdot 10^{-9}$ (numerical zero).

C.3 - Verification of concentration calculation by Fick's law

The concentration calculated by Fick's law can be verified by comparing with the analytical solution, testing the case where there is a constant concentration at the surface and zero concentration in the specimen to begin with.

The analytical solution is given by eq. 1;

$$c = c_s - (c_s - c_0) \cdot \mathrm{erf}\left(\frac{z}{2\sqrt{Dt}}\right) \tag{C15}$$

where c_s is the surface concentration, D the diffusion coefficient, t the time, z the distance from the surface and c_0 the initial concentration in the specimen, which in this case is zero giving

$$c = c_s - c_s \cdot \mathrm{erf}\left(\frac{z}{2\sqrt{Dt}}\right) \tag{C16}$$

Running this test, and plotting the analytical and numerically found solutions, as shown in Figure 65, it is seen that the same composition profile is obtained.

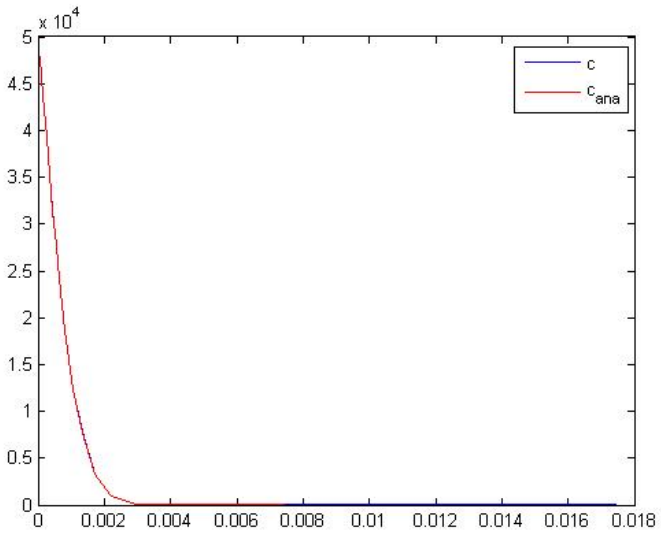

Figure 65 - concentration depth profiles, calculated analytically and explicit numerical. The two curves are seen to be identical.

C.4 - Verification of Non-constant diffusion coefficient calculation by comparison to model by Christiansen et al.

Christiansen et al. [34] modeled concentration profiles for non-constant diffusion coefficients. Using the fractional occupancies, *y*, thus modeled

$$\frac{\partial y}{\partial t} = \frac{\partial D}{\partial z}\frac{\partial y}{\partial z} + D\frac{\partial^2 y}{\partial z^2} \tag{C17}$$

Comparing results from the model presented in this work to their model, using the same input parameters, gives the same output, as shown in Figure 66.

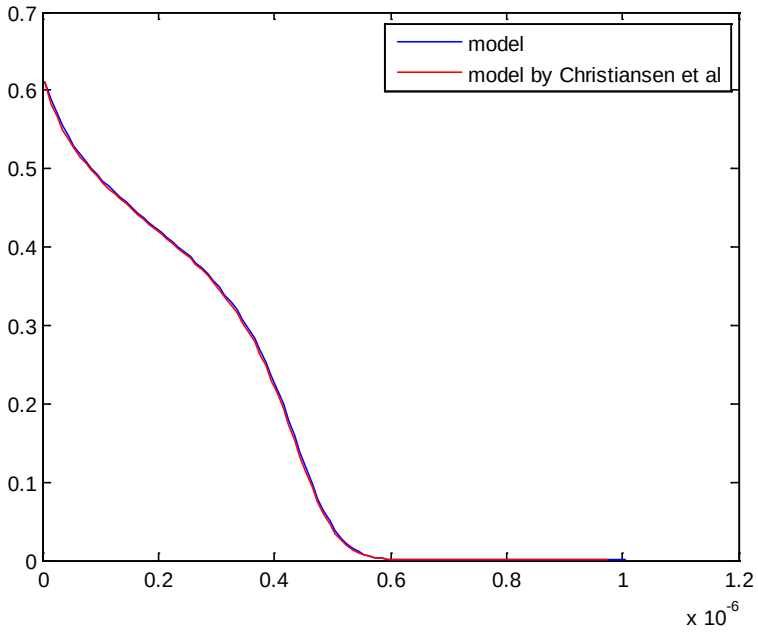

Figure 66 – fractional occupancy-depth profiles predicted by the model of Christiansen et al. and the model presented in this work

However, running a simulation where the input was transformed from fractional occupancies to concentrations and then running the simulations with concentrations;

$$\frac{\partial c}{\partial t} = \frac{\partial D}{\partial z}\frac{\partial c}{\partial z} + D\frac{\partial^2 c}{\partial z^2} \tag{C18}$$

and comparing to the concentration profile found from the y-profile calculated by their model did not give the same output as shown in Figure 67.

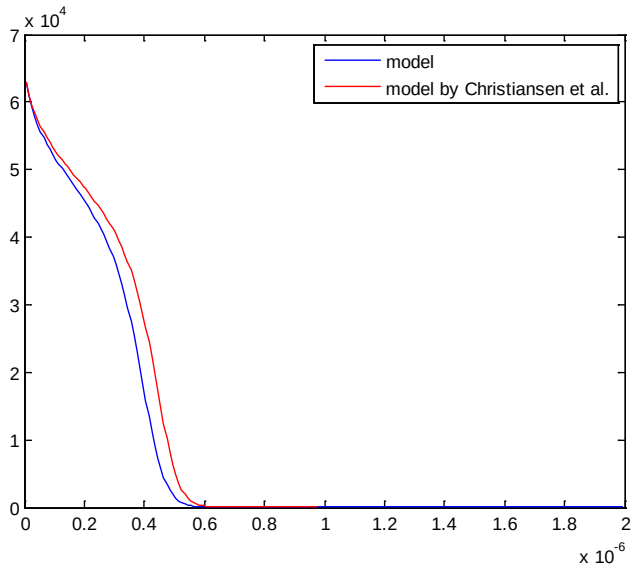

Figure 67 - concentration-depth profiles predicted by the model of Christiansen et al. and the model in this work

This however is explained by the following:

Their model is based on the equation

$$\frac{\partial y}{\partial t} = \frac{\partial D}{\partial z}\frac{\partial y}{\partial z} + D\frac{\partial^2 y}{\partial z^2} \tag{C19}$$

Using the chain rule since the fractional occupancy, y, depends on the concentration c gives

$$\frac{\partial y}{\partial c}\frac{\partial c}{\partial t} = \frac{\partial D}{\partial z}\frac{\partial y}{\partial c}\frac{\partial c}{\partial z} + D\cdot\frac{\partial}{\partial z}\left(\frac{\partial y}{\partial c}\frac{\partial c}{\partial z}\right) \tag{C20}$$

which leads to

$$\frac{\partial y}{\partial c}\frac{\partial c}{\partial t} = \frac{\partial D}{\partial z}\frac{\partial y}{\partial c}\frac{\partial c}{\partial z} + D\cdot\left(\frac{\partial}{\partial z}\left(\frac{\partial y}{\partial c}\right)\frac{\partial c}{\partial z} + \frac{\partial y}{\partial c}\frac{\partial^2 c}{\partial z^2}\right) \tag{C21}$$

$$\leftrightarrow$$

$$\frac{\partial y}{\partial c}\frac{\partial c}{\partial t} = \frac{\partial D}{\partial z}\frac{\partial y}{\partial c}\frac{\partial c}{\partial z} + D\cdot\left(\frac{\partial^2 y}{\partial c^2}\left(\frac{\partial c}{\partial z}\right)^2 + \frac{\partial y}{\partial c}\frac{\partial^2 c}{\partial z^2}\right) \tag{C22}$$

and finally gives

$$\frac{\partial c}{\partial t} = \frac{\partial D}{\partial z}\frac{\partial c}{\partial z} + D \cdot \frac{\frac{\partial^2 y}{\partial c^2}}{\frac{\partial y}{\partial c}}\left(\frac{\partial c}{\partial z}\right)^2 + D\frac{\partial^2 c}{\partial z^2} \tag{C23}$$

Since the relation between y and c is

$$y = \frac{c}{a - bc} \tag{C24}$$

where $a = \frac{140924\text{mol}}{\text{m}^3}$, $b = 0.59717$ (see eq. 43)

$$\frac{\partial y}{\partial c} = \frac{a}{(a - bc)^2} \tag{C25}$$

$$\frac{\partial^2 y}{\partial c^2} = \frac{a \cdot 2 \cdot (a - bc) \cdot b}{(a - bc)^4} \tag{C26}$$

$$\frac{\frac{\partial^2 y}{\partial c^2}}{\frac{\partial y}{\partial c}} = \frac{\frac{a \cdot 2 \cdot (a - bc) \cdot b}{(a - bc)^4}}{\frac{a}{(a - bc)^2}} = \frac{2 \cdot (a - bc) \cdot b}{(a - bc)^2} = \frac{2b}{a - bc} \tag{C27}$$

Thus

$$\frac{\partial c}{\partial t} = \frac{\partial D}{\partial z}\frac{\partial c}{\partial z} + D \cdot \frac{2b}{a - bc}\left(\frac{\partial c}{\partial z}\right)^2 + D\frac{\partial^2 c}{\partial z^2} \tag{C28}$$

And this is different compared to

$$\frac{\partial c}{\partial t} = \frac{\partial D}{\partial z}\frac{\partial c}{\partial z} + D\frac{\partial^2 c}{\partial z^2} \tag{C29}$$

So in calculating the differential equation in fractional occupancies instead of concentrations it is inherently assumed that the relation between concentration and fractional occupancies is linear and thus the volumetric expansion is not taken into account in their model.

C.5 - Verification of temperature calculation

The temperature calculation can be verified by comparing with the analytical solution, testing the case where there is a constant temperature of 200K at the surface and a temperature of 0K in the specimen to begin with.

The analytical solution to the heat conduction equation

$$\frac{\partial T}{\partial t} = \alpha \frac{\partial^2 T}{\partial z^2} \tag{C30}$$

is given by

$$\frac{T(x,t) - T_s}{T_i - T_s} = \mathrm{erf}\left(\frac{z}{\sqrt{4\alpha t}}\right) \tag{C31}$$

where T_s is the surface temperature, T_i the initital temperature of the material, z is the distance from the surface, t is the time and α is the thermal diffusivity which can be calculated by eq. 176. $\mathrm{erf}(x)$ is the error-function of x.

In this case where $T_i = 0$ this gives

$$T(x,t) = T_s - T_s \cdot \mathrm{erf}\left(\frac{z}{\sqrt{4\alpha t}}\right) \tag{C32}$$

which is a similar expression to the obtained analytical solution for the concentration.

Running this test assuming zero resistance in the air-cell, and plotting the analytically and numerically found solutions it is seen that the same temperature profiles are obtained.

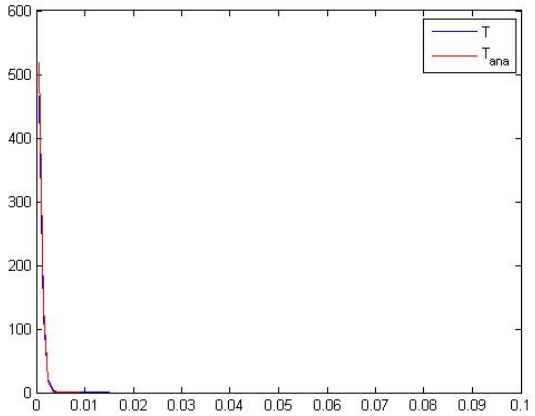

Figure 68 - temperature-depth profiles

Appendix D – Uneven loading

When the stresses can no longer be assumed to be the same in both in-plane directions, as is the case if the sample was subjected to uniaxial stressing, the assumption that $\sigma_{11} = \sigma_{22}$ is no longer valid. Below it is attempted to expand the model, beyond its limits, and calculate the stresses for the case of uneven loading The theoretical foundation for calculating stresses is discussed in section D1 and the results of applying this model is discussed in section D2.

D.1 - Calculation of elastic-plastic stresses with uneven loading

Applying the assumptions similar to the unloaded case, but with the difference that $\sigma_{11} \neq \sigma_{22}$ when uniaxial loading of the specimen applies, the assumptions are now

- Since the surface of the nitride specimen is free $\sigma_{33} = 0$,
- assuming no bending of the specimen, and hence uniform expansion through the material gives total strains $\varepsilon_{11}^{tot}, \varepsilon_{22}^{tot}$ constant in space and varying in time, $\varepsilon_{12} = \varepsilon_{13} = \varepsilon_{23} = 0$, and thus $\sigma_{12} = \sigma_{13} = \sigma_{23} = 0$

Since $\sigma_{33} = 0$

$$s_{11} = \sigma_{11} - \frac{\sigma_{11} + \sigma_{22}}{3} \tag{D1}$$

$$s_{22} = \sigma_{22} - \frac{\sigma_{11} + \sigma_{22}}{3} \tag{D2}$$

$$s_{33} = -\frac{\sigma_{11} + \sigma_{22}}{3} \tag{D3}$$

and having no shear stresses, von Mises stress can be described by

$$\sigma_e^2 = \frac{3}{2}({s_{11}}^2 + {s_{22}}^2 + {s_{33}}^2) \tag{D4}$$
$$= \frac{3}{2}\left(\left(\sigma_{11} - \frac{\sigma_{11}+\sigma_{22}}{3}\right)^2 + \left(\sigma_{22} - \frac{\sigma_{11}+\sigma_{22}}{3}\right)^2 + \left(-\frac{\sigma_{11}+\sigma_{22}}{3}\right)^2\right)$$
$$= {\sigma_{11}}^2 + {\sigma_{22}}^2 - \sigma_{22}\sigma_{11}$$

The von Mises stress increment is then

$$\dot{\sigma}_e = \frac{3(s_{11}\dot{\sigma}_{11} + s_{22}\dot{\sigma}_{22} + s_{33}\dot{\sigma}_{33})}{2\cdot\sigma_e} = \frac{3\left(\left(\sigma_{11} - \frac{\sigma_{11}+\sigma_{22}}{3}\right)\dot{\sigma}_{11} + \left(\sigma_{22} - \frac{\sigma_{11}+\sigma_{22}}{3}\right)\dot{\sigma}_{22}\right)}{2\cdot\sqrt{{\sigma_{11}}^2 + {\sigma_{22}}^2 - \sigma_{22}\sigma_{11}}} \tag{D5}$$

For concentration dependent yield strength the plasticity criterion is not only formulated in terms of the von Mises stress increment, but on the plastic strain increment and the parameter $\dot{\lambda}$, (see section 9.2). Now when the inplane stresses are not equal the expressions used to calculate the plastic strain increment should be modified. eqs. 149-150 gives the expressions

$$\dot{\lambda} = \left(\frac{1}{E_T} - \frac{1}{E}\right)\frac{3}{2\sigma_Y}\left(\frac{3s_{ij}\dot{\sigma}_{ij}}{2\sigma_Y} - \frac{\partial\sigma_Y}{\partial T}\dot{T} - \frac{\partial\sigma_Y}{\partial c}\dot{c}\right) \tag{D6}$$

$$\dot{\varepsilon}_{kl}^{pl} = \left(\frac{1}{E_T} - \frac{1}{E}\right)\frac{3}{2\sigma_Y}\left(\frac{3s_{ij}\dot{\sigma}_{ij}}{2\sigma_Y} - \frac{\partial\sigma_Y}{\partial T}\dot{T} - \frac{\partial\sigma_Y}{\partial c}\dot{c}\right)s_{kl} \tag{D7}$$

Combining with eqs. D1- D2 and since $\sigma_{12} = \sigma_{13} = \sigma_{23} = 0$, and $\sigma_{33} = 0$ gives

$$\dot{\lambda} = \left(\frac{1}{E_T} - \frac{1}{E}\right)\frac{3}{2\sigma_Y}\left(\frac{(2\sigma_{11} - \sigma_{22})\dot{\sigma}_{11} + (2\sigma_{22} - \sigma_{11})\dot{\sigma}_{22}}{2\sigma_Y} - \frac{\partial\sigma_Y}{\partial T}\dot{T} - \frac{\partial\sigma_Y}{\partial c}\dot{c}\right) \tag{D8}$$

and

$$\dot{\varepsilon}_{kl}^{pl} = \left(\frac{1}{E_T} - \frac{1}{E}\right)\frac{3}{2\sigma_Y}\left(\frac{(2\sigma_{11} - \sigma_{22})\dot{\sigma}_{11} + (2\sigma_{22} - \sigma_{11})\dot{\sigma}_{22}}{2\sigma_Y} - \frac{\partial\sigma_Y}{\partial T}\dot{T} - \frac{\partial\sigma_Y}{\partial c}\dot{c}\right)s_{kl} \tag{D9}$$

The expressions for the increments of the stress components are given by (see eq. 88-90)

$$\dot{\sigma}_{11} = \frac{E}{1+\nu}\left[1+\frac{\nu}{1-2\nu}-\beta\frac{3}{2}\frac{E/E_t-1}{E/E_t-(1-2\nu)/3}\frac{s_{11}s_{11}}{\sigma_e^2}\right]\dot{\varepsilon}_{11} + \frac{E}{1+\nu}\left[\frac{\nu}{1-2\nu}-\beta\frac{3}{2}\frac{E/E_t-1}{E/E_t-(1-2\nu)/3}\frac{s_{11}s_{22}}{\sigma_e^2}\right]\dot{\varepsilon}_{22} + \frac{E}{1+\nu}\left[\frac{\nu}{1-2\nu}-\beta\frac{3}{2}\frac{E/E_t-1}{E/E_t-(1-2\nu)/3}\frac{s_{11}s_{33}}{\sigma_e^2}\right]\dot{\varepsilon}_{33} \tag{D10}$$

$$\dot{\sigma}_{22} = \frac{E}{1+\nu}\left[\frac{\nu}{1-2\nu}-\beta\frac{3}{2}\frac{E/E_t-1}{E/E_t-(1-2\nu)/3}\frac{s_{22}s_{11}}{\sigma_e^2}\right]\dot{\varepsilon}_{11} + \frac{E}{1+\nu}\left[1+\frac{\nu}{1-2\nu}-\beta\frac{3}{2}\frac{E/E_t-1}{E/E_t-(1-2\nu)/3}\frac{s_{22}s_{22}}{\sigma_e^2}\right]\dot{\varepsilon}_{22} + \frac{E}{1+\nu}\left[\frac{\nu}{1-2\nu}-\beta\frac{3}{2}\frac{E/E_t-1}{E/E_t-(1-2\nu)/3}\frac{s_{22}s_{33}}{\sigma_e^2}\right]\dot{\varepsilon}_{33} \tag{D11}$$

$$\dot{\sigma}_{33} = \frac{E}{1+\nu}\left[\frac{\nu}{1-2\nu}-\beta\frac{3}{2}\frac{E/E_t-1}{E/E_t-(1-2\nu)/3}\frac{s_{33}s_{11}}{\sigma_e^2}\right]\dot{\varepsilon}_{11} + \frac{E}{1+\nu}\left[\frac{\nu}{1-2\nu}-\beta\frac{3}{2}\frac{E/E_t-1}{E/E_t-(1-2\nu)/3}\frac{s_{33}s_{22}}{\sigma_e^2}\right]\dot{\varepsilon}_{22} + \frac{E}{1+\nu}\left[1+\frac{\nu}{1-2\nu}-\beta\frac{3}{2}\frac{E/E_t-1}{E/E_t-(1-2\nu)/3}\frac{s_{33}s_{33}}{\sigma_e^2}\right]\dot{\varepsilon}_{33} \tag{D12}$$

Inserting the expressions for s_{11}, s_{22}, s_{33} (eqs. D1-D3) and σ_e^2 (eq. D4) gives

$$\dot{\sigma}_{11}(i) = \frac{E}{1+\nu}\left[1+\frac{\nu}{1-2\nu}-\beta\frac{3}{2}\frac{E/E_t-1}{E/E_t-(1-2\nu)/3}\frac{\frac{1}{9}\left(4{\sigma_{11}}^2+{\sigma_{22}}^2-4\sigma_{22}\sigma_{11}\right)}{{\sigma_{11}}^2+{\sigma_{22}}^2-\sigma_{22}\sigma_{11}}\right]\dot{\varepsilon}_{11} + \frac{E}{1+\nu}\left[\frac{\nu}{1-2\nu}-\beta\frac{3}{2}\frac{E/E_t-1}{E/E_t-(1-2\nu)/3}\frac{\frac{1}{9}\left(-2{\sigma_{11}}^2-2{\sigma_{22}}^2+5\sigma_{22}\sigma_{11}\right)}{{\sigma_{11}}^2+{\sigma_{22}}^2-\sigma_{22}\sigma_{11}}\right]\dot{\varepsilon}_{22} + \frac{E}{1+\nu}\left[\frac{\nu}{1-2\nu}-\beta\frac{3}{2}\frac{E/E_t-1}{E/E_t-(1-2\nu)/3}\frac{\frac{1}{9}\left(-2{\sigma_{11}}^2+{\sigma_{22}}^2-\sigma_{22}\sigma_{11}\right)}{{\sigma_{11}}^2+{\sigma_{22}}^2-\sigma_{22}\sigma_{11}}\right]\dot{\varepsilon}_{33} \tag{D13}$$

$$\dot{\sigma}_{22}(i) = \frac{E}{1+\nu}\left[\frac{\nu}{1-2\nu} - \beta\frac{3}{2}\frac{E/E_t - 1}{E/E_t - (1-2\nu)/3}\frac{\frac{1}{9}\left(-2{\sigma_{11}}^2 - 2{\sigma_{22}}^2 + 5\sigma_{22}\sigma_{11}\right)}{{\sigma_{11}}^2 + {\sigma_{22}}^2 - \sigma_{22}\sigma_{11}}\right]\dot{\varepsilon}_{11}$$
$$+ \frac{E}{1+\nu}\left[1 + \frac{\nu}{1-2\nu} - \beta\frac{3}{2}\frac{E/E_t - 1}{E/E_t - (1-2\nu)/3}\frac{\frac{1}{9}\left({\sigma_{11}}^2 + 4{\sigma_{22}}^2 - 4\sigma_{22}\sigma_{11}\right)}{{\sigma_{11}}^2 + {\sigma_{22}}^2 - \sigma_{22}\sigma_{11}}\right]\dot{\varepsilon}_{22}$$
$$+ \frac{E}{1+\nu}\left[\frac{\nu}{1-2\nu} - \beta\frac{3}{2}\frac{E/E_t - 1}{E/E_t - (1-2\nu)/3}\frac{\frac{1}{9}\left({\sigma_{11}}^2 - 2{\sigma_{22}}^2 - \sigma_{22}\sigma_{11}\right)}{{\sigma_{11}}^2 + {\sigma_{22}}^2 - \sigma_{22}\sigma_{11}}\right]\dot{\varepsilon}_{33} \quad \text{(D14)}$$

$$\dot{\sigma}_{33}(i) = \frac{E}{1+\nu}\left[\frac{\nu}{1-2\nu} - \beta\frac{3}{2}\frac{E/E_t - 1}{E/E_t - (1-2\nu)/3}\frac{\frac{1}{9}\left(-2{\sigma_{11}}^2 + {\sigma_{22}}^2 - \sigma_{22}\sigma_{11}\right)}{{\sigma_{11}}^2 + {\sigma_{22}}^2 - \sigma_{22}\sigma_{11}}\right]\dot{\varepsilon}_{11}$$
$$+ \frac{E}{1+\nu}\left[\frac{\nu}{1-2\nu} - \beta\frac{3}{2}\frac{E/E_t - 1}{E/E_t - (1-2\nu)/3}\frac{\frac{1}{9}\left({\sigma_{11}}^2 - 2{\sigma_{22}}^2 - \sigma_{22}\sigma_{11}\right)}{{\sigma_{11}}^2 + {\sigma_{22}}^2 - \sigma_{22}\sigma_{11}}\right]\dot{\varepsilon}_{22}$$
$$+ \frac{E}{1+\nu}\left[1 + \frac{\nu}{1-2\nu} - \beta\frac{3}{2}\frac{E/E_t - 1}{E/E_t - (1-2\nu)/3}\frac{\frac{1}{9}\left({\sigma_{11}}^2 + {\sigma_{22}}^2 + 2\sigma_{22}\sigma_{11}\right)}{{\sigma_{11}}^2 + {\sigma_{22}}^2 - \sigma_{22}\sigma_{11}}\right]\dot{\varepsilon}_{33} \quad \text{(D15)}$$

Because of the free surface $\sigma_{33} = 0$ at all times, thus $\dot{\sigma}_{33} = 0$, giving

$$0 = \frac{E}{1+\nu}\left[\frac{\nu}{1-2\nu} - \beta\frac{3}{2}\frac{E/E_t - 1}{E/E_t - (1-2\nu)/3}\frac{\frac{1}{9}\left(-2{\sigma_{11}}^2 + {\sigma_{22}}^2 - \sigma_{22}\sigma_{11}\right)}{{\sigma_{11}}^2 + {\sigma_{22}}^2 - \sigma_{22}\sigma_{11}}\right]\dot{\varepsilon}_{11}$$
$$+ \frac{E}{1+\nu}\left[\frac{\nu}{1-2\nu} - \beta\frac{3}{2}\frac{E/E_t - 1}{E/E_t - (1-2\nu)/3}\frac{\frac{1}{9}\left({\sigma_{11}}^2 - 2{\sigma_{22}}^2 - \sigma_{22}\sigma_{11}\right)}{{\sigma_{11}}^2 + {\sigma_{22}}^2 - \sigma_{22}\sigma_{11}}\right]\dot{\varepsilon}_{22}$$
$$+ \frac{E}{1+\nu}\left[1 + \frac{\nu}{1-2\nu} - \beta\frac{3}{2}\frac{E/E_t - 1}{E/E_t - (1-2\nu)/3}\frac{\frac{1}{9}\left({\sigma_{11}}^2 + {\sigma_{22}}^2 + 2\sigma_{22}\sigma_{11}\right)}{{\sigma_{11}}^2 + {\sigma_{22}}^2 - \sigma_{22}\sigma_{11}}\right]\dot{\varepsilon}_{33} \quad \text{(D16)}$$

and from this $\dot{\varepsilon}_{33}$ can be found as a function of $\dot{\varepsilon}_{11}$ and $\dot{\varepsilon}_{22}$:

$$\dot{\varepsilon}_{33} = -\frac{\left[\frac{\nu}{1-2\nu} - \beta\frac{3}{2}\frac{\frac{E}{E_t}-1}{\frac{E}{E_t}-\frac{(1-2\nu)}{3}}\frac{\frac{1}{9}\left(-2{\sigma_{11}}^2+{\sigma_{22}}^2-\sigma_{22}\sigma_{11}\right)}{{\sigma_{11}}^2+{\sigma_{22}}^2-\sigma_{22}\sigma_{11}}\right]}{\left[1+\frac{\nu}{1-2\nu} - \beta\frac{3}{2}\frac{\frac{E}{E_t}-1}{\frac{E}{E_t}-\frac{(1-2\nu)}{3}}\frac{\frac{1}{9}({\sigma_{11}}^2+{\sigma_{22}}^2+2\sigma_{22}\sigma_{11})}{{\sigma_{11}}^2+{\sigma_{22}}^2-\sigma_{22}\sigma_{11}}\right]}\dot{\varepsilon}_{11} - \frac{\left[\frac{\nu}{1-2\nu} - \beta\frac{3}{2}\frac{\frac{E}{E_t}-1}{\frac{E}{E_t}-\frac{(1-2\nu)}{3}}\frac{\frac{1}{9}({\sigma_{11}}^2-2{\sigma_{22}}^2-\sigma_{22}\sigma_{11})}{{\sigma_{11}}^2+{\sigma_{22}}^2-\sigma_{22}\sigma_{11}}\right]}{\left[1+\frac{\nu}{1-2\nu} - \beta\frac{3}{2}\frac{\frac{E}{E_t}-1}{\frac{E}{E_t}-\frac{(1-2\nu)}{3}}\frac{\frac{1}{9}({\sigma_{11}}^2+{\sigma_{22}}^2+2\sigma_{22}\sigma_{11})}{{\sigma_{11}}^2+{\sigma_{22}}^2-\sigma_{22}\sigma_{11}}\right]}\dot{\varepsilon}_{22} \quad \text{(D17)}$$

Inserting this expression for $\dot{\varepsilon}_{33}$ in the equations for $\dot{\sigma}_{11}$ and $\dot{\sigma}_{22}$ (eqs. D13-D14) gives

$$\dot{\sigma}_{11}(i) = \frac{E}{1+\nu}\left[1+\frac{\nu}{1-2\nu}-\beta\frac{3}{2}\frac{E/E_t-1}{E/E_t-(1-2\nu)/3}\frac{\frac{1}{9}\left(4{\sigma_{11}}^2+{\sigma_{22}}^2-4\sigma_{22}\sigma_{11}\right)}{{\sigma_{11}}^2+{\sigma_{22}}^2-\sigma_{22}\sigma_{11}}\right]\dot{\varepsilon}_{11} \tag{D18}$$

$$+\frac{E}{1+\nu}\left[\frac{\nu}{1-2\nu}-\beta\frac{3}{2}\frac{E/E_t-1}{E/E_t-(1-2\nu)/3}\frac{\frac{1}{9}\left(-2{\sigma_{11}}^2-2{\sigma_{22}}^2+5\sigma_{22}\sigma_{11}\right)}{{\sigma_{11}}^2+{\sigma_{22}}^2-\sigma_{22}\sigma_{11}}\right]\dot{\varepsilon}_{22}$$

$$+\frac{E}{1+\nu}\left[\frac{\nu}{1-2\nu}-\beta\frac{3}{2}\frac{E/E_t-1}{E/E_t-(1-2\nu)/3}\frac{\frac{1}{9}\left(-2{\sigma_{11}}^2+{\sigma_{22}}^2-\sigma_{22}\sigma_{11}\right)}{{\sigma_{11}}^2+{\sigma_{22}}^2-\sigma_{22}\sigma_{11}}\right]$$

$$\cdot\left(-\frac{\left[\frac{\nu}{1-2\nu}-\beta\frac{3}{2}\frac{\frac{E}{E_t}-1}{\frac{E}{E_t}-\frac{(1-2\nu)}{3}}\frac{\frac{1}{9}\left(-2{\sigma_{11}}^2+{\sigma_{22}}^2-\sigma_{22}\sigma_{11}\right)}{{\sigma_{11}}^2+{\sigma_{22}}^2-\sigma_{22}\sigma_{11}}\right]}{\left[1+\frac{\nu}{1-2\nu}-\beta\frac{3}{2}\frac{\frac{E}{E_t}-1}{\frac{E}{E_t}-\frac{(1-2\nu)}{3}}\frac{\frac{1}{9}\left({\sigma_{11}}^2+{\sigma_{22}}^2+2\sigma_{22}\sigma_{11}\right)}{{\sigma_{11}}^2+{\sigma_{22}}^2-\sigma_{22}\sigma_{11}}\right]}\dot{\varepsilon}_{11}\right.$$

$$\left.-\frac{\left[\frac{\nu}{1-2\nu}-\beta\frac{3}{2}\frac{\frac{E}{E_t}-1}{\frac{E}{E_t}-\frac{(1-2\nu)}{3}}\frac{\frac{1}{9}\left({\sigma_{11}}^2-2{\sigma_{22}}^2-\sigma_{22}\sigma_{11}\right)}{{\sigma_{11}}^2+{\sigma_{22}}^2-\sigma_{22}\sigma_{11}}\right]}{\left[1+\frac{\nu}{1-2\nu}-\beta\frac{3}{2}\frac{\frac{E}{E_t}-1}{\frac{E}{E_t}-\frac{(1-2\nu)}{3}}\frac{\frac{1}{9}\left({\sigma_{11}}^2+{\sigma_{22}}^2+2\sigma_{22}\sigma_{11}\right)}{{\sigma_{11}}^2+{\sigma_{22}}^2-\sigma_{22}\sigma_{11}}\right]}\dot{\varepsilon}_{22}\right)$$

$$\dot{\sigma}_{22}(i) = \frac{E}{1+\nu}\left[\frac{\nu}{1-2\nu} - \beta\frac{3}{2}\frac{E/E_t - 1}{E/E_t - (1-2\nu)/3}\frac{\frac{1}{9}\left(-2{\sigma_{11}}^2 - 2{\sigma_{22}}^2 + 5\sigma_{22}\sigma_{11}\right)}{{\sigma_{11}}^2 + {\sigma_{22}}^2 - \sigma_{22}\sigma_{11}}\right]\dot{\varepsilon}_{11} \tag{D19}$$

$$+ \frac{E}{1+\nu}\left[1 + \frac{\nu}{1-2\nu} - \beta\frac{3}{2}\frac{E/E_t - 1}{E/E_t - (1-2\nu)/3}\frac{\frac{1}{9}\left({\sigma_{11}}^2 + 4{\sigma_{22}}^2 - 4\sigma_{22}\sigma_{11}\right)}{{\sigma_{11}}^2 + {\sigma_{22}}^2 - \sigma_{22}\sigma_{11}}\right]\dot{\varepsilon}_{22}$$

$$+ \frac{E}{1+\nu}\left[\frac{\nu}{1-2\nu} - \beta\frac{3}{2}\frac{E/E_t - 1}{E/E_t - (1-2\nu)/3}\frac{\frac{1}{9}\left({\sigma_{11}}^2 - 2{\sigma_{22}}^2 - \sigma_{22}\sigma_{11}\right)}{{\sigma_{11}}^2 + {\sigma_{22}}^2 - \sigma_{22}\sigma_{11}}\right]$$

$$\cdot\left(-\frac{\left[\frac{\nu}{1-2\nu} - \beta\frac{3}{2}\frac{\frac{E}{E_t} - 1}{\frac{E}{E_t} - \frac{(1-2\nu)}{3}}\frac{\frac{1}{9}\left(-2{\sigma_{11}}^2 + {\sigma_{22}}^2 - \sigma_{22}\sigma_{11}\right)}{{\sigma_{11}}^2 + {\sigma_{22}}^2 - \sigma_{22}\sigma_{11}}\right]}{\left[1 + \frac{\nu}{1-2\nu} - \beta\frac{3}{2}\frac{\frac{E}{E_t} - 1}{\frac{E}{E_t} - \frac{(1-2\nu)}{3}}\frac{\frac{1}{9}\left({\sigma_{11}}^2 + {\sigma_{22}}^2 + 2\sigma_{22}\sigma_{11}\right)}{{\sigma_{11}}^2 + {\sigma_{22}}^2 - \sigma_{22}\sigma_{11}}\right]}\dot{\varepsilon}_{11}\right.$$

$$\left. -\frac{\left[\frac{\nu}{1-2\nu} - \beta\frac{3}{2}\frac{\frac{E}{E_t} - 1}{\frac{E}{E_t} - \frac{(1-2\nu)}{3}}\frac{\frac{1}{9}\left({\sigma_{11}}^2 - 2{\sigma_{22}}^2 - \sigma_{22}\sigma_{11}\right)}{{\sigma_{11}}^2 + {\sigma_{22}}^2 - \sigma_{22}\sigma_{11}}\right]}{\left[1 + \frac{\nu}{1-2\nu} - \beta\frac{3}{2}\frac{\frac{E}{E_t} - 1}{\frac{E}{E_t} - \frac{(1-2\nu)}{3}}\frac{\frac{1}{9}\left({\sigma_{11}}^2 + {\sigma_{22}}^2 + 2\sigma_{22}\sigma_{11}\right)}{{\sigma_{11}}^2 + {\sigma_{22}}^2 - \sigma_{22}\sigma_{11}}\right]}\dot{\varepsilon}_{22}\right)$$

where for plasticity $\beta = 1$. For elasticity $\beta = 0$ and $\dot{\sigma}_{11}$ and $\dot{\sigma}_{22}$ reduces to

$$\dot{\sigma}_{11}(i) = \frac{E}{1+\nu}\left(\left(\left[1 + \frac{\nu}{1-2\nu}\right] - \frac{\left[\frac{\nu}{1-2\nu}\right]^2}{\left[1 + \frac{\nu}{1-2\nu}\right]}\right)\dot{\varepsilon}_{11} + \left(\left[\frac{\nu}{1-2\nu}\right] - \frac{\left[\frac{\nu}{1-2\nu}\right]^2}{\left[1 + \frac{\nu}{1-2\nu}\right]}\right)\dot{\varepsilon}_{22}\right) \tag{D20}$$

$$\dot{\sigma}_{22}(i) = \frac{E}{1+\nu}\left(\left(\left[\frac{\nu}{1-2\nu}\right] - \frac{\left[\frac{\nu}{1-2\nu}\right]^2}{\left[1 + \frac{\nu}{1-2\nu}\right]}\right)\dot{\varepsilon}_{11} + \left(\left[1 + \frac{\nu}{1-2\nu}\right] - \frac{\left[\frac{\nu}{1-2\nu}\right]^2}{\left[1 + \frac{\nu}{1-2\nu}\right]}\right)\dot{\varepsilon}_{22}\right) \tag{D21}$$

The mechanical strain, $\dot{\varepsilon}_{22}$, was equal to $\dot{\varepsilon}_{22}^{tot} - \dot{\varepsilon}_{22}^{th} - \dot{\varepsilon}_{22}^{ch}$

and since the total strains are assumed constant in space and varying in time, they can be found using equilibrium of the stress over the cross-section from the surface to the depth z_{max} giving

$$\int_0^{z_{max}} \dot{\sigma}_{11} dz = 0 \tag{D22}$$

$$\int_0^{z_{max}} \dot{\sigma}_{22} dz = 0 \tag{D23}$$

For elasticity this gives

$$\begin{aligned}\int_0^{z_{max}} \frac{E}{1+\nu}\Bigg(&\left(\left[1+\frac{\nu}{1-2\nu}\right]-\frac{\left[\frac{\nu}{1-2\nu}\right]^2}{\left[1+\frac{\nu}{1-2\nu}\right]}\right)\dot{\varepsilon}_{11}^{tot}\\ &-\left(\left[1+\frac{\nu}{1-2\nu}\right]-\frac{\left[\frac{\nu}{1-2\nu}\right]^2}{\left[1+\frac{\nu}{1-2\nu}\right]}\right)\left(\dot{\varepsilon}_{11}^{th}+\dot{\varepsilon}_{11}^{ch}\right)\\ &+\left(\left[\frac{\nu}{1-2\nu}\right]-\frac{\left[\frac{\nu}{1-2\nu}\right]^2}{\left[1+\frac{\nu}{1-2\nu}\right]}\right)\dot{\varepsilon}_{22}^{tot}\\ &-\left(\left[\frac{\nu}{1-2\nu}\right]-\frac{\left[\frac{\nu}{1-2\nu}\right]^2}{\left[1+\frac{\nu}{1-2\nu}\right]}\right)\left(\dot{\varepsilon}_{22}^{th}+\dot{\varepsilon}_{22}^{ch}\right)\Bigg)dz=0\end{aligned} \tag{D24}$$

and

$$\int_0^{z_{max}} \frac{E}{1+\nu}\Bigg(\left(\left[\frac{\nu}{1-2\nu}\right]-\frac{\left[\frac{\nu}{1-2\nu}\right]^2}{\left[1+\frac{\nu}{1-2\nu}\right]}\right)\dot{\varepsilon}_{11}^{tot} \tag{D25}$$

$$-\left(\left[\frac{\nu}{1-2\nu}\right]-\frac{\left[\frac{\nu}{1-2\nu}\right]^2}{\left[1+\frac{\nu}{1-2\nu}\right]}\right)\left(\dot{\varepsilon}_{11}^{th}+\dot{\varepsilon}_{11}^{ch}\right)$$

$$+\left(\left[1+\frac{\nu}{1-2\nu}\right]-\frac{\left[\frac{\nu}{1-2\nu}\right]^2}{\left[1+\frac{\nu}{1-2\nu}\right]}\right)\dot{\varepsilon}_{22}^{tot}$$

$$-\left(\left[1+\frac{\nu}{1-2\nu}\right]-\frac{\left[\frac{\nu}{1-2\nu}\right]^2}{\left[1+\frac{\nu}{1-2\nu}\right]}\right)\left(\dot{\varepsilon}_{22}^{th}+\dot{\varepsilon}_{22}^{ch}\right)\Bigg)dz=0$$

Isolating $\dot{\varepsilon}_{11}^{tot}$ in the first equation gives

$$\dot{\varepsilon}_{11}^{tot}=\Bigg(\int_0^{z_{max}} \frac{E}{1+\nu}\left(\left[1+\frac{\nu}{1-2\nu}\right]-\frac{\left[\frac{\nu}{1-2\nu}\right]^2}{\left[1+\frac{\nu}{1-2\nu}\right]}\right)\left(\dot{\varepsilon}_{11}^{th}+\dot{\varepsilon}_{11}^{ch}\right)dz \tag{D26}$$

$$-\int_0^{z_{max}} \frac{E}{1+\nu}\left(\left[\frac{\nu}{1-2\nu}\right]-\frac{\left[\frac{\nu}{1-2\nu}\right]^2}{\left[1+\frac{\nu}{1-2\nu}\right]}\right)dz\cdot\dot{\varepsilon}_{22}^{tot}$$

$$+\int_0^{z_{max}} \frac{E}{1+\nu}\left(\left[\frac{\nu}{1-2\nu}\right]-\frac{\left[\frac{\nu}{1-2\nu}\right]^2}{\left[1+\frac{\nu}{1-2\nu}\right]}\right)\left(\dot{\varepsilon}_{22}^{th}+\dot{\varepsilon}_{22}^{ch}\right)dz\Bigg)$$

$$/\int_0^{z_{max}} \frac{E}{1+\nu}\left(\left[1+\frac{\nu}{1-2\nu}\right]-\frac{\left[\frac{\nu}{1-2\nu}\right]^2}{\left[1+\frac{\nu}{1-2\nu}\right]}\right)dz$$

Setting

$$A_{El}=\int_0^{z_{max}} \frac{E}{1+\nu}\left(\left[1+\frac{\nu}{1-2\nu}\right]-\frac{\left[\frac{\nu}{1-2\nu}\right]^2}{\left[1+\frac{\nu}{1-2\nu}\right]}\right)\left(\dot{\varepsilon}_{11}^{th}+\dot{\varepsilon}_{11}^{ch}\right)dz \tag{D27}$$

$$B_{El} = \int_0^{z_{max}} \frac{E}{1+\nu}\left(\left[\frac{\nu}{1-2\nu}\right] - \frac{\left[\frac{\nu}{1-2\nu}\right]^2}{\left[1+\frac{\nu}{1-2\nu}\right]}\right)dz \tag{D28}$$

$$C_{El} = \int_0^{z_{max}} \frac{E}{1+\nu}\left(\left[\frac{\nu}{1-2\nu}\right] - \frac{\left[\frac{\nu}{1-2\nu}\right]^2}{\left[1+\frac{\nu}{1-2\nu}\right]}\right)\left(\dot{\varepsilon}_{22}^{th} + \dot{\varepsilon}_{22}^{ch}\right)dz \tag{D29}$$

$$D_{El} = \int_0^{z_{max}} \frac{E}{1+\nu}\left(\left[1+\frac{\nu}{1-2\nu}\right] - \frac{\left[\frac{\nu}{1-2\nu}\right]^2}{\left[1+\frac{\nu}{1-2\nu}\right]}\right)dz \tag{D30}$$

The expression for $\dot{\varepsilon}_{11}^{tot}$ can be written as

$$\dot{\varepsilon}_{11}^{tot} = (A_{El} - B_{El} \cdot \dot{\varepsilon}_{22}^{tot} + C_{El})/D_{El} \tag{D31}$$

Inserting this in the second equation and isolating $\dot{\varepsilon}_{22}^{tot}$ gives

$$\dot{\varepsilon}_{22}^{tot} = \frac{-\frac{E_{El} \cdot (A_{El} + C_{El})}{D_{El}} + F_{EL} + H_{El}}{G_{El} + \frac{E_{El} \cdot B_{El}}{D_{El}}} \tag{D32}$$

where

$$E_{El} = \int_0^{z_{max}} \frac{E}{1+\nu}\left(\left[\frac{\nu}{1-2\nu}\right] - \frac{\left[\frac{\nu}{1-2\nu}\right]^2}{\left[1+\frac{\nu}{1-2\nu}\right]}\right)dz \tag{D33}$$

$$F_{El} = \int_0^{z_{max}} \frac{E}{1+\nu}\left(\left[\frac{\nu}{1-2\nu}\right] - \frac{\left[\frac{\nu}{1-2\nu}\right]^2}{\left[1+\frac{\nu}{1-2\nu}\right]}\right)\left(\dot{\varepsilon}_{11}^{th} + \dot{\varepsilon}_{11}^{ch}\right)dz \tag{D34}$$

$$G_{El} = \int_0^{z_{max}} \frac{E}{1+\nu}\left(\left[1+\frac{\nu}{1-2\nu}\right] - \frac{\left[\frac{\nu}{1-2\nu}\right]^2}{\left[1+\frac{\nu}{1-2\nu}\right]}\right)dz \tag{D35}$$

$$H_{El} = \int_0^{z_{max}} \frac{E}{1+\nu}\left(\left[1+\frac{\nu}{1-2\nu}\right] - \frac{\left[\frac{\nu}{1-2\nu}\right]^2}{\left[1+\frac{\nu}{1-2\nu}\right]}\right)\left(\dot{\varepsilon}_{22}^{th} + \dot{\varepsilon}_{22}^{ch}\right)dz \tag{D36}$$

For plasticity the equilibrium of stress over the cross-section gives:

$$\begin{aligned}
&\int_0^{z_{max,plastic}} \frac{E}{1+\nu}\Bigg\{\Bigg(\Bigg[1+\frac{\nu}{1-2\nu}-\frac{3}{2}\frac{E/E_t-1}{E/E_t-(1-2\nu)/3}\frac{\frac{1}{9}\left(4{\sigma_{11}}^2+{\sigma_{22}}^2-4\sigma_{22}\sigma_{11}\right)}{{\sigma_{11}}^2+{\sigma_{22}}^2-\sigma_{22}\sigma_{11}}\Bigg] \\
&\quad -\frac{\left[\frac{\nu}{1-2\nu}-\frac{3}{2}\frac{\frac{E}{E_t}-1}{\frac{E}{E_t}-\frac{(1-2\nu)}{3}}\frac{\frac{1}{9}\left(-2{\sigma_{11}}^2+{\sigma_{22}}^2-\sigma_{22}\sigma_{11}\right)}{{\sigma_{11}}^2+{\sigma_{22}}^2-\sigma_{22}\sigma_{11}}\right]\left[\frac{\nu}{1-2\nu}-\frac{3}{2}\frac{\frac{E}{E_t}-1}{\frac{E}{E_t}-\frac{(1-2\nu)}{3}}\frac{\frac{1}{9}\left(-2{\sigma_{11}}^2+{\sigma_{22}}^2-\sigma_{22}\sigma_{11}\right)}{{\sigma_{11}}^2+{\sigma_{22}}^2-\sigma_{22}\sigma_{11}}\right]}{\left[1+\frac{\nu}{1-2\nu}-\frac{3}{2}\frac{\frac{E}{E_t}-1}{\frac{E}{E_t}-\frac{(1-2\nu)}{3}}\frac{\frac{1}{9}\left({\sigma_{11}}^2+{\sigma_{22}}^2+2\sigma_{22}\sigma_{11}\right)}{{\sigma_{11}}^2+{\sigma_{22}}^2-\sigma_{22}\sigma_{11}}\right]}\Bigg) \\
&\quad \cdot\left(\dot{\varepsilon}_{11}^{tot}-\dot{\varepsilon}_{11}^{th}-\dot{\varepsilon}_{11}^{ch}\right) \\
&\quad +\Bigg(\Bigg[\frac{\nu}{1-2\nu}-\frac{3}{2}\frac{E/E_t-1}{E/E_t-(1-2\nu)/3}\frac{\frac{1}{9}\left(-2{\sigma_{11}}^2-2{\sigma_{22}}^2+5\sigma_{22}\sigma_{11}\right)}{{\sigma_{11}}^2+{\sigma_{22}}^2-\sigma_{22}\sigma_{11}}\Bigg] \\
&\quad -\frac{\left[\frac{\nu}{1-2\nu}-\frac{3}{2}\frac{\frac{E}{E_t}-1}{\frac{E}{E_t}-\frac{(1-2\nu)}{3}}\frac{\frac{1}{9}\left(-2{\sigma_{11}}^2+{\sigma_{22}}^2-\sigma_{22}\sigma_{11}\right)}{{\sigma_{11}}^2+{\sigma_{22}}^2-\sigma_{22}\sigma_{11}}\right]\left[\frac{\nu}{1-2\nu}-\frac{3}{2}\frac{\frac{E}{E_t}-1}{\frac{E}{E_t}-\frac{(1-2\nu)}{3}}\frac{\frac{1}{9}\left({\sigma_{11}}^2-2{\sigma_{22}}^2-\sigma_{22}\sigma_{11}\right)}{{\sigma_{11}}^2+{\sigma_{22}}^2-\sigma_{22}\sigma_{11}}\right]}{\left[1+\frac{\nu}{1-2\nu}-\frac{3}{2}\frac{\frac{E}{E_t}-1}{\frac{E}{E_t}-\frac{(1-2\nu)}{3}}\frac{\frac{1}{9}\left({\sigma_{11}}^2+{\sigma_{22}}^2+2\sigma_{22}\sigma_{11}\right)}{{\sigma_{11}}^2+{\sigma_{22}}^2-\sigma_{22}\sigma_{11}}\right]}\Bigg) \\
&\quad \cdot\left(\dot{\varepsilon}_{22}^{tot}-\dot{\varepsilon}_{22}^{th}-\dot{\varepsilon}_{22}^{ch}\right)\Bigg\}dz \\
&\quad +\int_{z_{max,plastic}}^{z_{max}} \frac{E}{1+\nu}\Bigg(\left(\left[1+\frac{\nu}{1-2\nu}\right]-\frac{\left[\frac{\nu}{1-2\nu}\right]^2}{\left[1+\frac{\nu}{1-2\nu}\right]}\right)\left(\dot{\varepsilon}_{11}^{tot}-\dot{\varepsilon}_{11}^{th}-\dot{\varepsilon}_{11}^{ch}\right) \\
&\quad +\left(\left[\frac{\nu}{1-2\nu}\right]-\frac{\left[\frac{\nu}{1-2\nu}\right]^2}{\left[1+\frac{\nu}{1-2\nu}\right]}\right)\left(\dot{\varepsilon}_{22}^{tot}-\dot{\varepsilon}_{22}^{th}-\dot{\varepsilon}_{22}^{ch}\right)\Bigg)dz = 0
\end{aligned} \tag{D37}$$

and

$$\int_0^{z_{max,plastic}} \frac{E}{1+\nu}\left\{\left(\left[\frac{\nu}{1-2\nu}-\frac{3}{2}\frac{E/E_t-1}{E/E_t-(1-2\nu)/3}\frac{\frac{1}{9}\left(-2{\sigma_{11}}^2-2{\sigma_{22}}^2+5\sigma_{22}\sigma_{11}\right)}{{\sigma_{11}}^2+{\sigma_{22}}^2-\sigma_{22}\sigma_{11}}\right]\right.\right. \tag{D38}$$

$$-\frac{\left[\frac{\nu}{1-2\nu}-\frac{3}{2}\frac{E/E_t-1}{E/E_t-(1-2\nu)/3}\frac{\frac{1}{9}\left({\sigma_{11}}^2-2{\sigma_{22}}^2-\sigma_{22}\sigma_{11}\right)}{{\sigma_{11}}^2+{\sigma_{22}}^2-\sigma_{22}\sigma_{11}}\right]\left[\frac{\nu}{1-2\nu}-\frac{3}{2}\frac{\frac{E}{E_t}-1}{\frac{E}{E_t}-\frac{(1-2\nu)}{3}}\frac{\frac{1}{9}\left(-2{\sigma_{11}}^2+{\sigma_{22}}^2-\sigma_{22}\sigma_{11}\right)}{{\sigma_{11}}^2+{\sigma_{22}}^2-\sigma_{22}\sigma_{11}}\right]}{\left[1+\frac{\nu}{1-2\nu}-\frac{3}{2}\frac{\frac{E}{E_t}-1}{\frac{E}{E_t}-\frac{(1-2\nu)}{3}}\frac{\frac{1}{9}\left({\sigma_{11}}^2+{\sigma_{22}}^2+2\sigma_{22}\sigma_{11}\right)}{{\sigma_{11}}^2+{\sigma_{22}}^2-\sigma_{22}\sigma_{11}}\right]}\right)\cdot\left(\dot{\varepsilon}_{11}^{tot}-\dot{\varepsilon}_{11}^{th}-\dot{\varepsilon}_{11}^{ch}\right)$$

$$+\left(\left[1+\frac{\nu}{1-2\nu}-\frac{3}{2}\frac{E/E_t-1}{E/E_t-(1-2\nu)/3}\frac{\frac{1}{9}\left({\sigma_{11}}^2+4{\sigma_{22}}^2-4\sigma_{22}\sigma_{11}\right)}{{\sigma_{11}}^2+{\sigma_{22}}^2-\sigma_{22}\sigma_{11}}\right]\right.$$

$$\left.\left.-\frac{\left[\frac{\nu}{1-2\nu}-\frac{3}{2}\frac{E/E_t-1}{E/E_t-(1-2\nu)/3}\frac{\frac{1}{9}\left({\sigma_{11}}^2-2{\sigma_{22}}^2-\sigma_{22}\sigma_{11}\right)}{{\sigma_{11}}^2+{\sigma_{22}}^2-\sigma_{22}\sigma_{11}}\right]\left[\frac{\nu}{1-2\nu}-\frac{3}{2}\frac{\frac{E}{E_t}-1}{\frac{E}{E_t}-\frac{(1-2\nu)}{3}}\frac{\frac{1}{9}\left({\sigma_{11}}^2-2{\sigma_{22}}^2-\sigma_{22}\sigma_{11}\right)}{{\sigma_{11}}^2+{\sigma_{22}}^2-\sigma_{22}\sigma_{11}}\right]}{\left[1+\frac{\nu}{1-2\nu}-\frac{3}{2}\frac{\frac{E}{E_t}-1}{\frac{E}{E_t}-\frac{(1-2\nu)}{3}}\frac{\frac{1}{9}\left({\sigma_{11}}^2+{\sigma_{22}}^2+2\sigma_{22}\sigma_{11}\right)}{{\sigma_{11}}^2+{\sigma_{22}}^2-\sigma_{22}\sigma_{11}}\right]}\right)\right.$$

$$\left.\cdot\left(\dot{\varepsilon}_{22}^{tot}-\dot{\varepsilon}_{22}^{th}-\dot{\varepsilon}_{22}^{ch}\right)\right\}dz$$

$$+\int_{z_{max,plastic}}^{z_{max}} \frac{E}{1+\nu}\left(\left(\left[\frac{\nu}{1-2\nu}\right]-\frac{\left[\frac{\nu}{1-2\nu}\right]^2}{\left[1+\frac{\nu}{1-2\nu}\right]}\right)\left(\dot{\varepsilon}_{11}^{tot}-\dot{\varepsilon}_{11}^{th}-\dot{\varepsilon}_{11}^{ch}\right)+\left(\left[1+\frac{\nu}{1-2\nu}\right]-\frac{\left[\frac{\nu}{1-2\nu}\right]^2}{\left[1+\frac{\nu}{1-2\nu}\right]}\right)\left(\dot{\varepsilon}_{22}^{tot}-\dot{\varepsilon}_{22}^{th}-\dot{\varepsilon}_{22}^{ch}\right)\right)dz=0$$

From these two equations with two unknown, expressions for the total strains can be found, as seen in Appendix B.2, to be

$$\dot{\varepsilon}_{11}^{tot}=-\frac{(C_{int}+G_{int})}{(A_{int}+E_{int})}\cdot\dot{\varepsilon}_{22}^{tot}-\frac{B_{int}+D_{int}+F_{int}+H_{int}}{(A_{int}+E_{int})} \tag{D39}$$

and

$$\varepsilon_{22}^{tot} = \frac{\frac{(I_{int} + M_{int}) \cdot (B_{int} + D_{int} + F_{int} + H_{int})}{(A_{int} + E_{int})} - J_{int} - L_{int} - N_{int} - P_{int}}{\left(-\frac{(I + M) \cdot (C_{int} + G_{int})}{(A_{int} + E_{int})} + K_{int} + O_{int}\right)} \tag{D40}$$

where

A_{int}

$$= \int_0^{z_{max,plastic}} \frac{E}{1+\nu} \left\{ \left(\left[1 + \frac{\nu}{1-2\nu} - \frac{3}{2} \frac{E/E_t - 1}{E/E_t - (1-2\nu)/3} \frac{\frac{1}{9}\left(4{\sigma_{11}}^2 + {\sigma_{22}}^2 - 4\sigma_{22}\sigma_{11}\right)}{{\sigma_{11}}^2 + {\sigma_{22}}^2 - \sigma_{22}\sigma_{11}} \right] \right. \right. \tag{D41}$$

$$\left. \left. - \frac{\left[\frac{\nu}{1-2\nu} - \frac{3}{2} \frac{\frac{E}{E_t} - 1}{\frac{E}{E_t} - \frac{(1-2\nu)}{3}} \frac{\frac{1}{9}\left(-2{\sigma_{11}}^2 + {\sigma_{22}}^2 - \sigma_{22}\sigma_{11}\right)}{{\sigma_{11}}^2 + {\sigma_{22}}^2 - \sigma_{22}\sigma_{11}} \right] \left[\frac{\nu}{1-2\nu} - \frac{3}{2} \frac{\frac{E}{E_t} - 1}{\frac{E}{E_t} - \frac{(1-2\nu)}{3}} \frac{\frac{1}{9}\left(-2{\sigma_{11}}^2 + {\sigma_{22}}^2 - \sigma_{22}\sigma_{11}\right)}{{\sigma_{11}}^2 + {\sigma_{22}}^2 - \sigma_{22}\sigma_{11}} \right]}{\left[1 + \frac{\nu}{1-2\nu} - \frac{3}{2} \frac{\frac{E}{E_t} - 1}{\frac{E}{E_t} - \frac{(1-2\nu)}{3}} \frac{\frac{1}{9}\left({\sigma_{11}}^2 + {\sigma_{22}}^2 + 2\sigma_{22}\sigma_{11}\right)}{{\sigma_{11}}^2 + {\sigma_{22}}^2 - \sigma_{22}\sigma_{11}} \right]} \right) \right\} dz$$

B_{int}

$$= -\int_0^{z_{max,plastic}} \frac{E}{1+\nu} \left\{ \left(\left[1 + \frac{\nu}{1-2\nu} - \frac{3}{2} \frac{E/E_t - 1}{E/E_t - (1-2\nu)/3} \frac{\frac{1}{9}\left(4{\sigma_{11}}^2 + {\sigma_{22}}^2 - 4\sigma_{22}\sigma_{11}\right)}{{\sigma_{11}}^2 + {\sigma_{22}}^2 - \sigma_{22}\sigma_{11}} \right] \right. \right. \tag{D42}$$

$$\left. \left. - \frac{\left[\frac{\nu}{1-2\nu} - \frac{3}{2} \frac{\frac{E}{E_t} - 1}{\frac{E}{E_t} - \frac{(1-2\nu)}{3}} \frac{\frac{1}{9}\left(-2{\sigma_{11}}^2 + {\sigma_{22}}^2 - \sigma_{22}\sigma_{11}\right)}{{\sigma_{11}}^2 + {\sigma_{22}}^2 - \sigma_{22}\sigma_{11}} \right] \left[\frac{\nu}{1-2\nu} - \frac{3}{2} \frac{\frac{E}{E_t} - 1}{\frac{E}{E_t} - \frac{(1-2\nu)}{3}} \frac{\frac{1}{9}\left(-2{\sigma_{11}}^2 + {\sigma_{22}}^2 - \sigma_{22}\sigma_{11}\right)}{{\sigma_{11}}^2 + {\sigma_{22}}^2 - \sigma_{22}\sigma_{11}} \right]}{\left[1 + \frac{\nu}{1-2\nu} - \frac{3}{2} \frac{\frac{E}{E_t} - 1}{\frac{E}{E_t} - \frac{(1-2\nu)}{3}} \frac{\frac{1}{9}\left({\sigma_{11}}^2 + {\sigma_{22}}^2 + 2\sigma_{22}\sigma_{11}\right)}{{\sigma_{11}}^2 + {\sigma_{22}}^2 - \sigma_{22}\sigma_{11}} \right]} \right) \cdot \left(\dot{\varepsilon}_{11}^{th} + \dot{\varepsilon}_{11}^{ch}\right) \right\} dz$$

C_{int}

(D43)

$$= \int_0^{z_{max,plastic}} \frac{E}{1+\nu} \left\{ \left(\left[\frac{\nu}{1-2\nu} - \frac{3}{2} \frac{E/E_t - 1}{E/E_t - (1-2\nu)/3} \frac{\frac{1}{9}\left(-2{\sigma_{11}}^2 - 2{\sigma_{22}}^2 + 5\sigma_{22}\sigma_{11}\right)}{{\sigma_{11}}^2 + {\sigma_{22}}^2 - \sigma_{22}\sigma_{11}} \right] \right. \right.$$

$$\left. \left. - \frac{\left[\frac{\nu}{1-2\nu} - \frac{3}{2} \frac{\frac{E}{E_t} - 1}{\frac{E}{E_t} - \frac{(1-2\nu)}{3}} \frac{\frac{1}{9}\left(-2{\sigma_{11}}^2 + {\sigma_{22}}^2 - \sigma_{22}\sigma_{11}\right)}{{\sigma_{11}}^2 + {\sigma_{22}}^2 - \sigma_{22}\sigma_{11}} \right] \left[\frac{\nu}{1-2\nu} - \frac{3}{2} \frac{\frac{E}{E_t} - 1}{\frac{E}{E_t} - \frac{(1-2\nu)}{3}} \frac{\frac{1}{9}\left({\sigma_{11}}^2 - 2{\sigma_{22}}^2 - \sigma_{22}\sigma_{11}\right)}{{\sigma_{11}}^2 + {\sigma_{22}}^2 - \sigma_{22}\sigma_{11}} \right]}{\left[1 + \frac{\nu}{1-2\nu} - \frac{3}{2} \frac{\frac{E}{E_t} - 1}{\frac{E}{E_t} - \frac{(1-2\nu)}{3}} \frac{\frac{1}{9}\left({\sigma_{11}}^2 + {\sigma_{22}}^2 + 2\sigma_{22}\sigma_{11}\right)}{{\sigma_{11}}^2 + {\sigma_{22}}^2 - \sigma_{22}\sigma_{11}} \right]} \right) \right\} dz$$

D_{int}

(D44)

$$= -\int_0^{z_{max,plastic}} \frac{E}{1+\nu} \left\{ \left(\left[\frac{\nu}{1-2\nu} - \frac{3}{2} \frac{E/E_t - 1}{E/E_t - (1-2\nu)/3} \frac{\frac{1}{9}\left(-2{\sigma_{11}}^2 - 2{\sigma_{22}}^2 + 5\sigma_{22}\sigma_{11}\right)}{{\sigma_{11}}^2 + {\sigma_{22}}^2 - \sigma_{22}\sigma_{11}} \right] \right. \right.$$

$$\left. \left. - \frac{\left[\frac{\nu}{1-2\nu} - \frac{3}{2} \frac{\frac{E}{E_t} - 1}{\frac{E}{E_t} - \frac{(1-2\nu)}{3}} \frac{\frac{1}{9}\left(-2{\sigma_{11}}^2 + {\sigma_{22}}^2 - \sigma_{22}\sigma_{11}\right)}{{\sigma_{11}}^2 + {\sigma_{22}}^2 - \sigma_{22}\sigma_{11}} \right] \left[\frac{\nu}{1-2\nu} - \frac{3}{2} \frac{\frac{E}{E_t} - 1}{\frac{E}{E_t} - \frac{(1-2\nu)}{3}} \frac{\frac{1}{9}\left({\sigma_{11}}^2 - 2{\sigma_{22}}^2 - \sigma_{22}\sigma_{11}\right)}{{\sigma_{11}}^2 + {\sigma_{22}}^2 - \sigma_{22}\sigma_{11}} \right]}{\left[1 + \frac{\nu}{1-2\nu} - \frac{3}{2} \frac{\frac{E}{E_t} - 1}{\frac{E}{E_t} - \frac{(1-2\nu)}{3}} \frac{\frac{1}{9}\left({\sigma_{11}}^2 + {\sigma_{22}}^2 + 2\sigma_{22}\sigma_{11}\right)}{{\sigma_{11}}^2 + {\sigma_{22}}^2 - \sigma_{22}\sigma_{11}} \right]} \right)$$

$$\left. \cdot \left(\dot{\varepsilon}_{22}^{th} + \dot{\varepsilon}_{22}^{ch} \right) \right\} dz$$

$$E_{int} = \int_{z_{max,plastic}}^{z_{max}} \frac{E}{1+\nu} \left(\left[1 + \frac{\nu}{1-2\nu} \right] - \frac{\left[\frac{\nu}{1-2\nu} \right]^2}{\left[1 + \frac{\nu}{1-2\nu} \right]} \right) dz \quad \text{(D45)}$$

$$F_{int} = -\int_{z_{max,plastic}}^{z_{max}} \frac{E}{1+\nu}\left(\left[1+\frac{\nu}{1-2\nu}\right]-\frac{\left[\frac{\nu}{1-2\nu}\right]^2}{\left[1+\frac{\nu}{1-2\nu}\right]}\right)\left(\dot{\varepsilon}_{11}^{th}+\dot{\varepsilon}_{11}^{ch}\right)dz \tag{D46}$$

$$G_{int} = \int_{z_{max,plastic}}^{z_{max}} \frac{E}{1+\nu}\left(\left[\frac{\nu}{1-2\nu}\right]-\frac{\left[\frac{\nu}{1-2\nu}\right]^2}{\left[1+\frac{\nu}{1-2\nu}\right]}\right)dz \tag{D47}$$

$$H_{int} = -\int_{z_{max,plastic}}^{z_{max}} \frac{E}{1+\nu}\left(\left[\frac{\nu}{1-2\nu}\right]-\frac{\left[\frac{\nu}{1-2\nu}\right]^2}{\left[1+\frac{\nu}{1-2\nu}\right]}\right)\left(\dot{\varepsilon}_{22}^{th}+\dot{\varepsilon}_{22}^{ch}\right)dz \tag{D48}$$

$$I_{int} = \int_{0}^{z_{max,plastic}} \frac{E}{1+\nu}\left\{\left(\left[\frac{\nu}{1-2\nu}-\frac{3}{2}\frac{E/E_t-1}{E/E_t-(1-2\nu)/3}\frac{\frac{1}{9}\left(-2{\sigma_{11}}^2-2{\sigma_{22}}^2+5\sigma_{22}\sigma_{11}\right)}{{\sigma_{11}}^2+{\sigma_{22}}^2-\sigma_{22}\sigma_{11}}\right]\right.\right. \tag{D49}$$

$$\left.\left.-\frac{\left[\frac{\nu}{1-2\nu}-\frac{3}{2}\frac{E/E_t-1}{E/E_t-(1-2\nu)/3}\frac{\frac{1}{9}\left({\sigma_{11}}^2-2{\sigma_{22}}^2-\sigma_{22}\sigma_{11}\right)}{{\sigma_{11}}^2+{\sigma_{22}}^2-\sigma_{22}\sigma_{11}}\right]\left[\frac{\nu}{1-2\nu}-\frac{3}{2}\frac{\frac{E}{E_t}-1}{\frac{E}{E_t}-\frac{(1-2\nu)}{3}}\frac{\frac{1}{9}\left(-2{\sigma_{11}}^2+{\sigma_{22}}^2-\sigma_{22}\sigma_{11}\right)}{{\sigma_{11}}^2+{\sigma_{22}}^2-\sigma_{22}\sigma_{11}}\right]}{\left[1+\frac{\nu}{1-2\nu}-\frac{3}{2}\frac{\frac{E}{E_t}-1}{\frac{E}{E_t}-\frac{(1-2\nu)}{3}}\frac{\frac{1}{9}\left({\sigma_{11}}^2+{\sigma_{22}}^2+2\sigma_{22}\sigma_{11}\right)}{{\sigma_{11}}^2+{\sigma_{22}}^2-\sigma_{22}\sigma_{11}}\right]}\right)\right\}dz$$

J_{int}

(D50)

$$= -\int_0^{z_{max,plastic}} \frac{E}{1+\nu}\left\{\left(\left[\frac{\nu}{1-2\nu} - \frac{3}{2}\frac{E/E_t - 1}{E/E_t - (1-2\nu)/3}\frac{\frac{1}{9}\left(-2{\sigma_{11}}^2 - 2{\sigma_{22}}^2 + 5\sigma_{22}\sigma_{11}\right)}{{\sigma_{11}}^2 + {\sigma_{22}}^2 - \sigma_{22}\sigma_{11}}\right]\right.\right.$$

$$\left.\left. - \frac{\left[\frac{\nu}{1-2\nu} - \frac{3}{2}\frac{E/E_t - 1}{E/E_t - (1-2\nu)/3}\frac{\frac{1}{9}\left({\sigma_{11}}^2 - 2{\sigma_{22}}^2 - \sigma_{22}\sigma_{11}\right)}{{\sigma_{11}}^2 + {\sigma_{22}}^2 - \sigma_{22}\sigma_{11}}\right]\left[\frac{\nu}{1-2\nu} - \frac{3}{2}\frac{\frac{E}{E_t} - 1}{\frac{E}{E_t} - \frac{(1-2\nu)}{3}}\frac{\frac{1}{9}\left(-2{\sigma_{11}}^2 + {\sigma_{22}}^2 - \sigma_{22}\sigma_{11}\right)}{{\sigma_{11}}^2 + {\sigma_{22}}^2 - \sigma_{22}\sigma_{11}}\right]}{\left[1 + \frac{\nu}{1-2\nu} - \frac{3}{2}\frac{\frac{E}{E_t} - 1}{\frac{E}{E_t} - \frac{(1-2\nu)}{3}}\frac{\frac{1}{9}\left({\sigma_{11}}^2 + {\sigma_{22}}^2 + 2\sigma_{22}\sigma_{11}\right)}{{\sigma_{11}}^2 + {\sigma_{22}}^2 - \sigma_{22}\sigma_{11}}\right]}\right)\right.$$

$$\left.\cdot\left(\dot{\varepsilon}_{11}^{th} + \dot{\varepsilon}_{11}^{ch}\right)\right\} dz$$

K_{int}

(D51)

$$= \int_0^{z_{max,plastic}} \frac{E}{1+\nu}\left\{\left(\left[1 + \frac{\nu}{1-2\nu} - \frac{3}{2}\frac{E/E_t - 1}{E/E_t - (1-2\nu)/3}\frac{\frac{1}{9}\left({\sigma_{11}}^2 + 4{\sigma_{22}}^2 - 4\sigma_{22}\sigma_{11}\right)}{{\sigma_{11}}^2 + {\sigma_{22}}^2 - \sigma_{22}\sigma_{11}}\right]\right.\right.$$

$$\left.\left. - \frac{\left[\frac{\nu}{1-2\nu} - \frac{3}{2}\frac{E/E_t - 1}{E/E_t - (1-2\nu)/3}\frac{\frac{1}{9}\left({\sigma_{11}}^2 - 2{\sigma_{22}}^2 - \sigma_{22}\sigma_{11}\right)}{{\sigma_{11}}^2 + {\sigma_{22}}^2 - \sigma_{22}\sigma_{11}}\right]\left[\frac{\nu}{1-2\nu} - \frac{3}{2}\frac{\frac{E}{E_t} - 1}{\frac{E}{E_t} - \frac{(1-2\nu)}{3}}\frac{\frac{1}{9}\left({\sigma_{11}}^2 - 2{\sigma_{22}}^2 - \sigma_{22}\sigma_{11}\right)}{{\sigma_{11}}^2 + {\sigma_{22}}^2 - \sigma_{22}\sigma_{11}}\right]}{\left[1 + \frac{\nu}{1-2\nu} - \frac{3}{2}\frac{\frac{E}{E_t} - 1}{\frac{E}{E_t} - \frac{(1-2\nu)}{3}}\frac{\frac{1}{9}\left({\sigma_{11}}^2 + {\sigma_{22}}^2 + 2\sigma_{22}\sigma_{11}\right)}{{\sigma_{11}}^2 + {\sigma_{22}}^2 - \sigma_{22}\sigma_{11}}\right]}\right)\right\} dz$$

$$L_{int}$$

$$= -\int_0^{z_{max,plastic}} \frac{E}{1+\nu}\left\{\left(\left[1+\frac{\nu}{1-2\nu}-\frac{3}{2}\frac{E/E_t-1}{E/E_t-(1-2\nu)/3}\frac{\frac{1}{9}({\sigma_{11}}^2+4{\sigma_{22}}^2-4\sigma_{22}\sigma_{11})}{{\sigma_{11}}^2+{\sigma_{22}}^2-\sigma_{22}\sigma_{11}}\right]\right.\right. \tag{D52}$$

$$\left.\left.-\frac{\left[\frac{\nu}{1-2\nu}-\frac{3}{2}\frac{E/E_t-1}{E/E_t-(1-2\nu)/3}\frac{\frac{1}{9}({\sigma_{11}}^2-2{\sigma_{22}}^2-\sigma_{22}\sigma_{11})}{{\sigma_{11}}^2+{\sigma_{22}}^2-\sigma_{22}\sigma_{11}}\right]\left[\frac{\nu}{1-2\nu}-\frac{3}{2}\frac{\frac{E}{E_t}-1}{\frac{E}{E_t}-\frac{(1-2\nu)}{3}}\frac{\frac{1}{9}({\sigma_{11}}^2-2{\sigma_{22}}^2-\sigma_{22}\sigma_{11})}{{\sigma_{11}}^2+{\sigma_{22}}^2-\sigma_{22}\sigma_{11}}\right]}{\left[1+\frac{\nu}{1-2\nu}-\frac{3}{2}\frac{\frac{E}{E_t}-1}{\frac{E}{E_t}-\frac{(1-2\nu)}{3}}\frac{\frac{1}{9}({\sigma_{11}}^2+{\sigma_{22}}^2+2\sigma_{22}\sigma_{11})}{{\sigma_{11}}^2+{\sigma_{22}}^2-\sigma_{22}\sigma_{11}}\right]}\right)\right.$$

$$\left.\cdot\left(\dot{\varepsilon}_{22}^{th}+\dot{\varepsilon}_{22}^{ch}\right)\right\}dz$$

$$M_{int} = \int_{z_{max,plastic}}^{z_{max}} \frac{E}{1+\nu}\left(\left[\frac{\nu}{1-2\nu}\right]-\frac{\left[\frac{\nu}{1-2\nu}\right]^2}{\left[1+\frac{\nu}{1-2\nu}\right]}\right)dz \tag{D53}$$

$$N_{int} = -\int_{z_{max,plastic}}^{z_{max}} \frac{E}{1+\nu}\left(\left[\frac{\nu}{1-2\nu}\right]-\frac{\left[\frac{\nu}{1-2\nu}\right]^2}{\left[1+\frac{\nu}{1-2\nu}\right]}\right)\left(\dot{\varepsilon}_{11}^{th}+\dot{\varepsilon}_{11}^{ch}\right)dz \tag{D54}$$

$$O_{int} = \int_{z_{max,plastic}}^{z_{max}} \frac{E}{1+\nu}\left(\left[1+\frac{\nu}{1-2\nu}\right]-\frac{\left[\frac{\nu}{1-2\nu}\right]^2}{\left[1+\frac{\nu}{1-2\nu}\right]}\right)dz \tag{D55}$$

$$P_{int} = -\int_{z_{max,plastic}}^{z_{max}} \frac{E}{1+\nu}\left(\left[1+\frac{\nu}{1-2\nu}\right]-\frac{\left[\frac{\nu}{1-2\nu}\right]^2}{\left[1+\frac{\nu}{1-2\nu}\right]}\right)\left(\dot{\varepsilon}_{22}^{th}+\dot{\varepsilon}_{22}^{ch}\right)dz \tag{D56}$$

D.2 – Results and discussion of modelling of uneven loading

Incorporating the calculation of stresses for uneven loading described above instead of the ones where even loading is assumed, provides the opportunity for applying for example uniaxial tensile stressing of the sample.

The calculations were tested with no loading, for both a thin sample and a sample where semi-infinity was assumed ($\varepsilon^{tot} = 0$), to verify the model and in both cases these tests gave the same simulation results as when applying the simpler model where even loading is assumed.

Testing the response of uniaxial pre-stressing was then done assuming a semi-infinite sample. The results are shown in Figure 69. As for the case of biaxial pre-stressing discussed in section 10, pre-stressing does not affect the composition profile much when semi-infinite samples are assumed.

Testing uniaxial pre-stressing of thin samples resulted in unstable calculations of the stress, even for very small time steps, and thus this is reaching the limits of reasonable applicability of this model. This is probably the time to use a full 3D finite element model instead. An example of the unstable behaviour is seen in Figure 70.

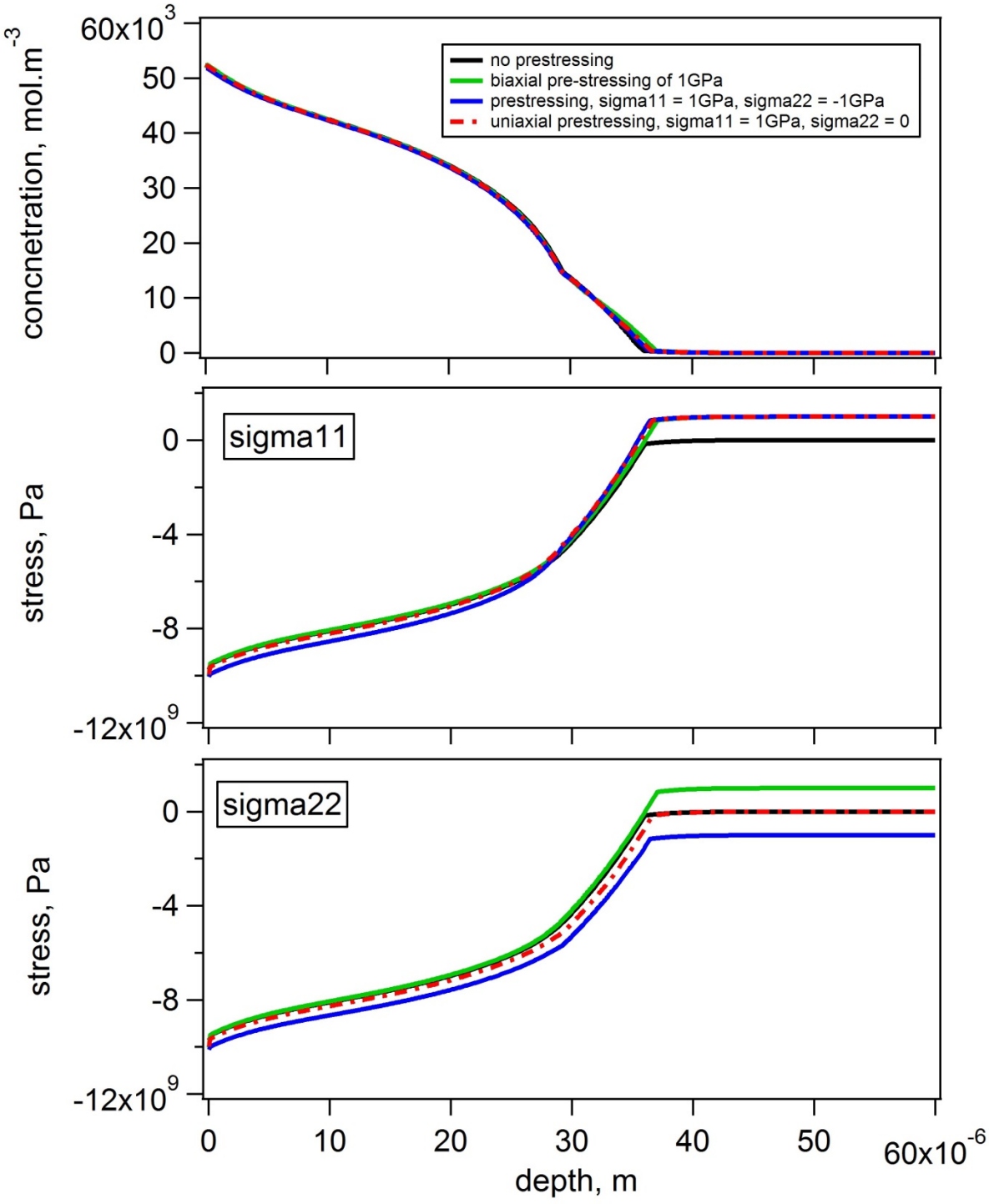

Figure 69 - Predicted composition and stress profiles after 22h nitriding for a sample of thickness 2L = 300µm with various even and uneven pre-stressing

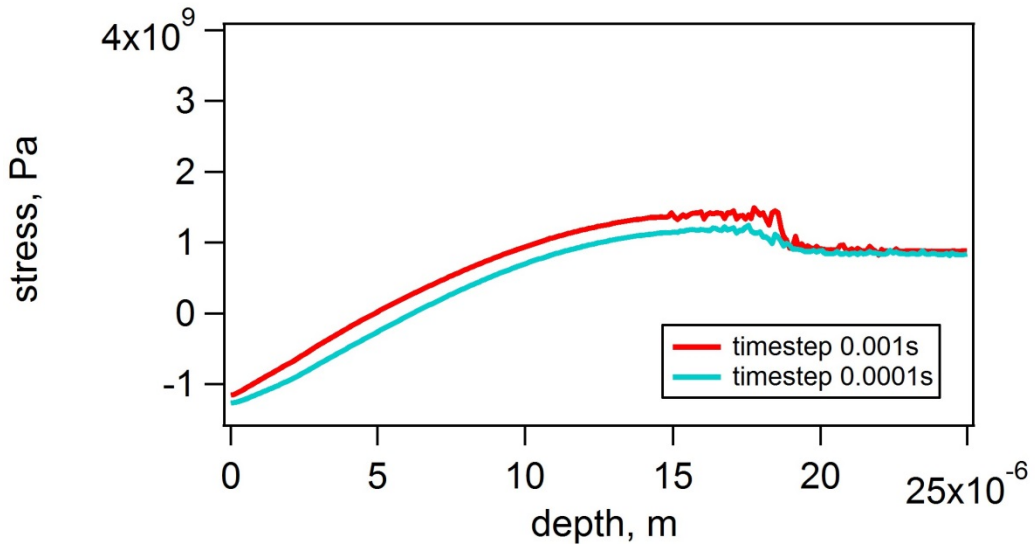

Figure 70 - Calculated stress profiles (σ_{11}) uneven loading of σ_{11} = 100MPa and σ_{22} = 0, for 10h nitriding of 25µm thin samples with no trapping

Appendix E- Articles

E.1 Article 1

The subsequent article has been submitted to the journal Modelling and Simulation in Materials Science and Engineering.

Modelling the evolution of composition- and stress-depth profiles in austenitic stainless steels during low-temperature nitriding

Freja N. Jespersen*, J.H. Hattel, M.A.J. Somers

Technical University of Denmark, Department of Mechanical Engineering, Produktionstorvet b. 425, 2800 Kgs. Lyngby, Denmark, *corresponding author: frnj@mek.dtu.dk

Abstract

Nitriding of stainless steel causes a surface zone of expanded austenite, which improves the wear resistance of the stainless steel while preserving the stainless behavior. During nitriding huge residual stresses are introduced in the treated zone, arising from the volume expansion that accompanies the dissolution of high nitrogen contents in expanded austenite.

An intriguing phenomenon during low-temperature nitriding is that the residual stresses evoked by dissolution of nitrogen in the solid state, affect the thermodynamics and the diffusion kinetics of nitrogen dissolution. In the present paper solid mechanics was combined with thermodynamics and diffusion kinetics to simulate the evolution of composition-depth and stress-depth profiles resulting from nitriding. The model takes into account a composition-dependent diffusion coefficient of nitrogen in expanded austenite, short range ordering (trapping) of nitrogen atoms by chromium atoms, and the effect of composition-induced stress on surface concentration and diffusive flux. The effect of plasticity and concentration-dependence of the yield stress was also included.

Keywords: Nitriding, nitrogen diffusion, expanded austenite, modelling, stress induced diffusion, plasticity

Introduction

Austenitic stainless steels are widely applied in structural applications because of their corrosion resistance in combination with favourable manufacturing performance. Generally, austenitic stainless steels have poor tribological and wear performance. Low-temperature thermochemical surface engineering by nitriding, carburizing and nitrocarburizing provides a means to drastically improve the tribological/wear performance, without compromising the general corrosion performance and even improving the resistance against localized corrosion, as pitting and crevice corrosion [1,2,3].

In low-temperature nitriding, carburizing or nitrocarburizing large amounts of nitrogen and/or carbon are dissolved in the surface region. This brings about a zone of expanded austenite, which essentially is a supersaturated solution of nitrogen and/or carbon in austenite. The expanded austenite zone has a substantially higher hardness than the untreated steel and

provides drastically improved wear resistance. Furthermore, high compressive residual stresses are introduced, which result in enhanced fatigue performance. A zone of expanded austenite can be achieved by bringing the steel in contact with an environment providing nitrogen and/or carbon, as for example in plasma-assisted or gas-based processing [1,2,3]. The present work is concerned with gas-based nitriding of austenitic stainless steels and modelling the evolution of nitrogen-depth and residual stress-depth profiles in relation to the processing parameters. Even though the case investigated is specific for gaseous nitriding, the concepts of the mechanisms governing the evolution of composition and residual stress are claimed to be applicable to (nitro)carburizing and plasma-assisted and liquid processing, as in Kolsterizing®, as well.

1. State-of-the art of modelling low-temperature surface hardening of stainless steel.

Concentration-depth profiles developing during low temperature nitriding, measured in for example [1], are characterized by the shape shown in Fig. 1: an initially steep decrease in nitrogen content followed by a plateau and a steep decline at the case-core transition. This behaviour deviates from the classical example in textbooks on diffusion showing the composition profile expected for diffusion into a semi-infinite medium with a constant diffusion coefficient (as for example carbon into iron/steel) and constant surface concentration, which obeys the complementary error function. Different approaches have been presented in the literature to explain and model the evolution of such composition-profiles. Parascandola, et al. [4] explained the characteristic nitrogen-concentration profile developing during ion plantation of nitrogen from trapping and detrapping of nitrogen atoms at chromium sites (i.e. short range order of chromium and nitrogen [5]), assuming a constant diffusion coefficient. A satisfactory correspondence was obtained between measured and fitted composition profiles. This mechanism was adopted, extended to include sputtering, and applied to plasma-nitrided single crystals with various orientations by Martinavicius et al. [6]. The assumption of a constant diffusion coefficient in these models contrasts the strong dependence of the nitrogen diffusion coefficient in austenitic stainless steel as determined experimentally on homogeneous thin foils of expanded austenite with various nitrogen contents [7]. Qualitatively, the composition dependence of the diffusion coefficient of nitrogen in expanded austenite can explain the shape of the nitrogen concentration profile developing during nitriding, as demonstrated by calculating the concentration profile from Fick's 2^{nd} law [8,9,10]. A better correspondence between calculated and experimental composition-depth profiles was found when trapping of nitrogen atoms was taken into account, as this allows a steeper case-core transition [8,9,10]. Moreover, it was demonstrated that the finite rate of the surface reaction, i.e. the decomposition rate of gas species at the surface before incorporation in the solid, as well as the effects of a compressive stress on the solubility of nitrogen in expanded austenite and a compressive stress *gradient* on the diffusive flux also contribute to the evolution of the concentration-depth profile [10].

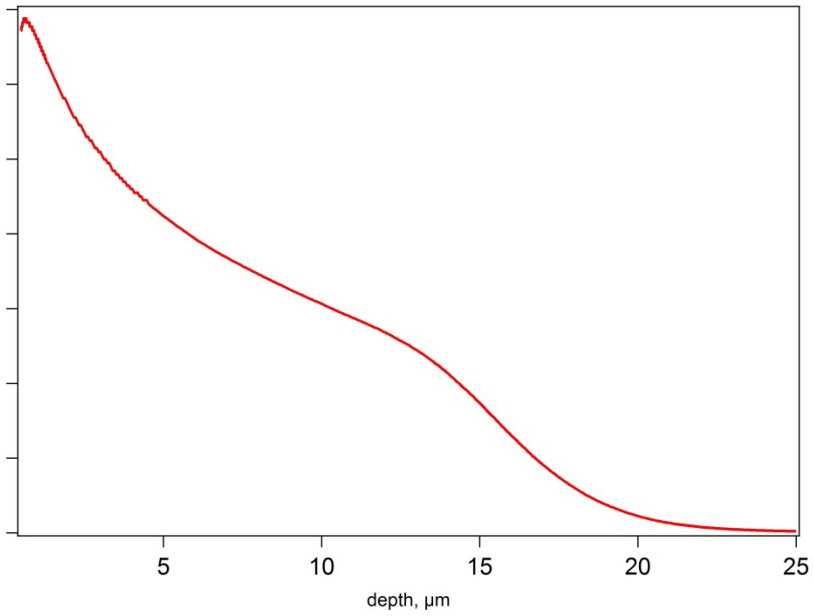

Figure 1 – Typical shape of measured concentration-depth profiles

It is well established that low-temperature nitriding of austenitic stainless steel leads to a composition-induced compressive residual stress depth-profile as a consequence of the lattice expansion associated with the dissolution of interstitial nitrogen and/or carbon. The compressive stresses developing are several GPa's in magnitude, as determined at room temperature after cooling [1,11,12]. Although the stresses at room temperature are mainly composition-induced, a contribution from a difference in linear expansion coefficient between austenite and expanded austenite cannot be excluded, because the expansion coefficient depends on the nitrogen content in expanded austenite [13].

Christiansen and Somers showed that the enormous residual stress gradient can augment the depth range of the expanded austenite zone by a factor of 2 [14]. The effect of residual stress on the nitrogen concentration profile was also recognized by Galdikas and Moskalioviene. They modelled the influence of a residual stress gradient on the concentration profile for the case of a constant as well as for a composition-dependent diffusion coefficient, assuming that the lattice misfit associated with nitrogen dissolution is elastically accommodated [15,16] . In their model a linear relation between residual stress and nitrogen concentration profile was assumed. For this purpose they adopted an unphysical proportionality parameter originally proposed by Christiansen and Somers [17] for the purpose of estimating artefacts on X-ray stress determination. In the pragmatic approach by Galdikas and Moskalioviene [15,16], no actual physical coupling occurs between the concentration-depth profile and mechanical equilibrium considerations. Furthermore, in [15,16] a diffusion coefficient continuously decreasing with nitrogen concentration was assumed (which approaches infinity for very low nitrogen contents!), rather than the dependence showing an *increase* with nitrogen content and a decrease as determined experimentally from diffusion in stress-free foils of uniform composition [7].

Experimentally, it has been demonstrated from lattice rotations and associated texture changes in expanded austenite as well as from enhanced surface roughness by grain push-out, that, at least part of the composition-induced stress is accommodated plastically during nitriding [18,19,20,21]. Biaxial compressive stress levels of several GPa's, as observed experimentally, clearly exceed by far the yield stress of austenitic stainless steel. The high compressive stresses measured are explained from solid-solution strengthening of austenite by the presence of nitrogen, which implies that the yield stress is augmented importantly by the dissolution of nitrogen. The occurrence of plastic accommodation of composition-induced stress is therefore the result of a competition between strengthening and stress build-up. Apparently, for nitriding (and nitro-carburizing) the stress build up exceeds the yield stress achievable by solid-solution strengthening. Note that the occurrence of plastic accommodation of composition-induced stresses has so far not been observed for carburizing of stainless steel. This indicates that in carbon-expanded austenite the strengthening effect dominates over the composition induced stress build-up for the (narrower) composition range under consideration.

A better understanding of the stress-assisted diffusion controlled growth of the expanded austenite case and the associated evolution of the substantial composition-induced stresses is crucial for an accurate prediction of the concentration-depth and stress-depth profiles.

In the present work the interdependent influences of composition and stress on the evolution of nitrogen concentration-depth profiles and stress-depth profiles in expanded austenite zones are modelled. The model includes:
a concentration-dependent diffusion coefficient of nitrogen in expanded austenite;
trapping of nitrogen atoms by chromium atoms;
the kinetics of the surface reaction;
the effect of composition-induced stress on the nitrogen solubility in expanded austenite;
the effect of a composition-induced stress gradient on the diffusive flux;
the effect of the competition between solid-solution strengthening and compressive stress build-up to account for the occurrence of plastic deformation.

In contrast with previous work by for example Christiansen et al. [10] or Galdikas and Moskalioviene [15] the model presented here calculates stress based on mechanical equilibrium principles and considers elasto-plasticity.

Apart from the kinetics of the surface reactions the concepts investigated here can be directly transferred to plasma nitriding as well, albeit that plasma nitriding requires a consideration of the sputtering effects at the surface. It is beyond the scope of the present work to discuss such peculiarities of plasma-surface interactions.

2. Basic equations of the model

The present work assumes 1-dimensional diffusion of nitrogen in the depth-direction, with reference to a flat surface. Consequently, the influence of corners and curved surfaces is not considered.

2.1 Basic diffusion equations

The diffusive flux of nitrogen atoms in the direction z under the influence of a chemical potential gradient of this species, $\frac{\partial \mu_N}{\partial z}$, is defined as [22]

$$J = -M_N c_N \frac{\partial \mu_N}{\partial z} \tag{1}$$

where c_N is the nitrogen concentration in mol.m^{-3}, μ_N is the chemical potential of nitrogen in J.mol^{-1} and M_N is the mobility of nitrogen in m^2.s^{-1} given by [22]

$$M_N = \frac{D_N}{RT} \tag{2}$$

where D_N is the intrinsic diffusion coefficient of nitrogen in m^2.s^{-1}, R is the gas constant in J.mol^{-1}.K^{-1} and T is the temperature in K.

Generally, the chemical potential is assumed to depend on the concentration only

$$\mu(c_N) = \mu_0 + RTln(c_N) \tag{3}$$

In which case Eq. 1 reduces to Fick's first law

$$J_N = -D_N \frac{\partial c_N}{\partial z} \tag{4}$$

More generally, the chemical potential is a function of the activity of nitrogen, a_N, and the hydrostatic stress (pressure), σ_H , and the temperature T [23,24]

$$\mu_N(a_N, \sigma_H, T) = \mu_{N,0} + RTln(a_N) - V_N \sigma_H \tag{5}$$

where $\mu_{N,0}$ is the chemical potential of nitrogen in the reference state with respect to which a_N is defined[3], V_N is the partial molar volume of nitrogen. It is noted that in principle a_N, V_N and σ_H depend on the temperature. Assuming that diffusion occurs at constant temperature and that no temperature gradients are present, the diffusive flux follows from inserting Eq. 5 into Eq. 1, which results in

$$J_N = -\frac{D_N c_N}{RT}\left(\frac{\partial \mu_N}{\partial c_N}\frac{\partial c_N}{\partial z} + \frac{\partial \mu_N}{\partial \sigma_H}\frac{\partial \sigma_H}{\partial z}\right) \tag{6}$$

[3] Usually, for nitrogen in solid solution the reference state is taken as nitrogen gas at 1 bar at the temperature under consideration.

In a Fe-N phase the activity is linearly proportional to the nitriding potential, $K_N = \frac{p_{NH_3}}{{p_{H_2}}^{3/2}}$, by [25]

$$a = K_T^{\varphi} K_N \tag{7}$$

where $K_T^{\varphi}(T,p)$ is the temperature and pressure dependent equilibrium constant for the reaction describing the dissolution of N into the solid phase φ from a gas containing NH_3 and H_2.

Since the activity depends on the concentration

$$\frac{\partial \mu_N}{\partial c_N} = RT\frac{\partial ln a_N}{\partial c_N} = \frac{RT}{c_N}\frac{\partial ln(a_N)}{\partial ln(c_N)} = \frac{RT}{c_N}\frac{\partial ln(K_T^{\varphi} K_N)}{\partial ln(c_N)} \tag{8}$$

Realizing that K_T^{φ} only depends on pressure and temperature and not on nitrogen concentration, it is obtained

$$\frac{\partial \mu_N}{\partial c_N} = \frac{RT}{K_N}\frac{\partial K_N}{\partial c_N} \tag{9}$$

Inserting Eq. 9 in Eq. 8, and inserting in Eq. 6 the following generalized form of Fick's 1st law is obtained

$$J_N = -\frac{D_N c_N}{RT}\left(\frac{RT}{K_N}\frac{\partial K_N}{\partial c_N}\frac{\partial c_N}{\partial z} - V_N\frac{\partial \sigma_H}{\partial z}\right) \tag{10}$$

Accordingly, the generalized form of Fick's 2nd law is

$$\frac{\partial c_N}{\partial t} = -\frac{\partial}{\partial z}\left(-D_N^{(c)}.\frac{\partial c_N}{\partial z} + \frac{D_N.c_N}{RT}.V_N.\frac{\partial \sigma_H}{\partial z}\right) \tag{11a}$$

where $D_N^{(c)}$ represents the concentration dependence of the diffusion coefficient of nitrogen, i.e. D_N times the thermodynamic factor $\left(\frac{c_N}{K_N}\frac{\partial K_N}{\partial c_N}\right)$. When $D_N^{(c)}$ is a known explicit function of the concentration the equation can be rewritten to

$$\frac{\partial c_N}{\partial t} = -\frac{\partial}{\partial z}\left(-D_N^{(c)}.\frac{\partial c_N}{\partial z} + \frac{D_N^{(c)}}{\frac{\partial K_N}{\partial c_N}}.\frac{K_N}{RT}.V_N.\frac{\partial \sigma_H}{\partial z}\right) \tag{11b}$$

and then the differentiation with respect to z gives

$$\frac{\partial c_N}{\partial t} = \frac{\partial D_N^{(c)}}{\partial c_N}\cdot\left(\frac{\partial c_N}{\partial z}\right)^2 + D_N^{(c)}\cdot\frac{\partial^2 c_N}{\partial z^2} - \frac{\partial}{\partial z}\left(D_N^{(c)}\cdot\frac{K_N}{\frac{\partial K_N}{\partial c_N}}\right)\cdot\frac{V_N}{RT}\frac{\partial \sigma_H}{\partial z} - D_N^{(c)}\cdot\left(\frac{K_N}{\frac{\partial K_N}{\partial c_N}}\frac{V_N}{RT}\frac{\partial^2 \sigma_H}{\partial z^2}\right) \tag{12}$$

2.2 Trapping

The short-range ordering of nitrogen atoms by chromium is referred to as trapping and is mathematically treated analogously to nitrogen precipitation as in [10,26,27]. It is assumed that trapping first occurs above a certain threshold probability for finding a Cr-N pair of atoms. Analogous to the solubility product of nitrogen and chromium contents above which CrN precipitation occurs, the thermodynamic solubility constant, K_e, is introduced to describe the solubility product of nitrogen and chromium contents above which trapping of nitrogen atoms occurs. Suppression of the actual precipitation of chromium nitride through sluggish diffusion kinetics of chromium diffusion is the very essence of supersaturated, metastable expanded austenite during low temperature nitriding (and/or carburizing) of stainless steel. Prolonged nitriding or subsequent ageing will eventually lead to the unintentional but unavoidable precipitation of CrN.

The equilibrium constant of trapping nitrogen by chromium is described by:

$$K_e = \frac{1}{c_{Cr} \cdot c_N^n} = \frac{1}{K_{MeN}} \rightarrow K_{MeN} = c_{Cr} \cdot c_N^n \tag{13}$$

where c_j is the concentration of the dissolved element *j* and K_{MeN} is the solubility product of Cr and N with *n* being the number of nitrogen atoms per chromium atom, which is about Cr:N=1:0.9 for strong binding of nitrogen to chromium in AISI 316L [21].

2.3 Diffusion boundary condition at the gas/solid interface

The concentration of nitrogen at the surface of expanded austenite during gaseous nitriding depends on the balance of the fluxes of nitrogen atoms at the surface [28]. The flux of nitrogen atoms arriving at the surface can usually be assumed to be governed by the dissociation kinetics of nitrogen-containing species at the surface (as ammonia). The fluxes of nitrogen atoms leaving from the surface are the diffusive flux of nitrogen into the solid state and the flux of N_2 molecules desorbing from the surface after association of adsorbed N atoms. The latter can be omitted for low temperature nitriding of stainless steel (T< 723 K), but has been observed to play an important role at higher temperatures and high ammonia contents [29]. The flux of nitrogen atoms arriving at the surface J_N^s is given by [28,30]

$$J_{surf} = k \cdot \left(c_N^{eq} - c_N^s\right) \tag{14}$$

where c_N^s is the concentration of nitrogen just below the surface, c_N^{eq} is the nitrogen concentration in the solid phase at the surface that would prevail if imposed equilibrium would be attained between nitrogen in the gas phase and nitrogen in solid solution, i.e. the chemical potentials of nitrogen in the gas-phase and in solid solution are equal; *k* is the reaction-rate constant of the slowest step in the ammonia dissociation [30].

At the surface the concentration can then be found from the continuity equation for balancing the arriving and leaving nitrogen fluxes:

$$\frac{\partial c_N^S}{\partial t} = -\frac{\partial J_N^S}{\partial z} = -\left(\frac{\partial J_N^{s,diff}}{\partial z} - \frac{\partial J_N^{s,diss}}{\partial z}\right) \tag{15}$$

where $J_N^{s,diss}$ and $J_N^{s,diff}$ are the fluxes of nitrogen atoms arriving at the surface (from dissociation) and leaving from the surface by diffusion, respectively.

2.4 Calculation of stress

The strain arising from the expansion of the austenite lattice as caused by the dissolution of interstitial nitrogen, i.e. the chemical-induced strain, ε_{ij}^{ch}, is defined as

$$for\ i = j: \quad \varepsilon_{ij}^{ch}(c) = \frac{V(c)^{1/3} - V_{ref}^{1/3}}{V_{ref}^{1/3}} \tag{16}$$

$$for\ i \neq j: \quad \varepsilon_{ij}^{ch} = 0$$

where V(c) in the concentration-dependent volume of (expanded) austenite per metal atom in m^3 and V_{ref} indicates the volume per metal atom of the interstitial-free lattice of austenite.

The total strain, ε_{ij}^{tot}, is then given by [31]

$$\varepsilon_{ij}^{tot} = \varepsilon_{ij}^{mech} + \varepsilon_{ij}^{ch} + \varepsilon_{ij}^{th} \tag{17}$$

where ε_{ij}^{th} is the thermal strain and ε_{ij}^{mech} is the mechanical strain which is the sum of the elastic and plastic strain.

A simple description of the stress state in the surface can be found by applying a method equivalent to that described by Hattel and Hansen [31,32], with the following assumptions:

- the surface of the sample is homogeneous and can move freely: $\sigma_{33} = \sigma_{\perp} = 0$ ($\sigma_{\perp}$ is the stress normal to the surface);
- the stress state in the surface is rotationally symmetric, hence the normal stresses in the surface plane are equal $\sigma_{11} = \sigma_{22} = \sigma_{\parallel}$ ($\sigma_{\parallel}$ is the stress parallel to the surface);
- the specimen does not bend, hence uniform expansion at all depths: $\varepsilon_{11}^{tot} = \varepsilon_{22}^{tot} = \varepsilon_{\parallel}^{tot}$ and $\varepsilon_{12}^{tot} = \varepsilon_{13}^{tot} = \varepsilon_{23}^{tot} = 0$, and thus $\sigma_{12} = \sigma_{13} = \sigma_{23} = 0$
- there are no temperature gradients in the sample, hence no thermal strains.

Using these assumptions and assuming, for the time being, purely elastic stresses, the following relation can be found between the in-plane stresses and strain in the surface region

$$\sigma_{\parallel}^{el} = \frac{E}{1-\nu}\left(\varepsilon_{\parallel}^{tot} - \varepsilon_{\parallel}^{ch}\right) \tag{18}$$

where E is Young's modulus and ν is Poisson's ratio. The total strain $\varepsilon_{\parallel}^{tot}$ can be found from considering mechanical equilibrium over the cross-section of the sample, which for the case that the stress state is mirror-symmetrical with respect to the plane at half the sample thickness (total sample thickness is 2L). Note that nitrogen is assumed to diffuse from two parallel surfaces on either side of the sample towards the centre of the sample, and thus mirror-symmetry is assumed and considering one side suffices for the calculations. Hence,

$$\int_0^L \sigma_{\parallel} dz = 0 \tag{19}$$

Inserting Eq. 18 into Eq. 19, and assuming that Young's modulus, E, and the Poisson ratio, ν, are independent of depth, yields

$$\frac{E}{1-\nu}\int_0^L \left(\varepsilon_{\parallel}^{tot} - \varepsilon_{\parallel}^{ch}\right) dz = 0 \tag{20}$$

Since it was assumed that $\varepsilon_{22}^{tot} = \varepsilon_{11}^{tot}$ is constant in space and varies in time, this gives

$$\varepsilon_{\parallel}^{tot} = \frac{1}{L}\int_0^L \left(\varepsilon_{\parallel}^{ch}\right) dz \tag{21}$$

It is noted that a similar method was applied in [10,33,34], albeit that the total strain was taken equal to zero. This is a reasonable assumption, provided that the depth range where chemical strains apply is infinitely thin as compared to the depth range of the sample (cf. section 4.3). This assumption drastically simplifies the mathematical equations, resulting in the following equation for calculating the stress

$$\sigma_{\parallel} = -\frac{E}{1-\nu}\varepsilon_{\parallel}^{ch} \tag{22}$$

2.5 Plastic accommodation of stress

If the strains are no longer accommodated purely elastically, but lead to plastic deformation as well, the stresses can no longer be calculated directly, since the stress depends on the loading path. Thus an incremental formulation is used. The relation between the incremental stress $\dot{\sigma}_{ij}$ and the incremental mechanical strain $\dot{\varepsilon}_{kl}$ is

$$\dot{\sigma}_{ij} = L_{ijkl}\dot{\varepsilon}_{kl} \tag{23}$$

where L_{ijkl} is the incremental stiffness tensor which, according to J_2-flow theory [35], is given by

$$L_{ijkl} = \frac{E}{1+\nu}\left[\frac{1}{2}\left(\delta_{ik}\delta_{jl} + \delta_{il}\delta_{jk}\right) + \frac{\nu}{1-2\nu}\delta_{ij}\delta_{kl} - \beta\frac{3}{2}\frac{E/E_t - 1}{E/E_t - (1-2\nu)/3}\frac{s_{ij}s_{kl}}{\sigma_e^2}\right] \tag{24}$$

where E is Young's modulus, E_t is the tangent modulus, ν is Poisson's ratio and δ_{ij} is Kronecker's delta and β = 0 for elastic problems and β = 1 if there is plastic flow.

The stress deviator tensor, s_{ij}, is given by [35]

$$s_{ij} = \sigma_{ij} - \delta_{ij}\frac{\sigma_{kk}}{3} \tag{25}$$

and the von Mises yield surface is described by [35]

$$\sigma_e^2 = \frac{3}{2}s_{ij}s_{ij} \tag{26}$$

The maximal von Mises stress depends on the loading path and is changed if the actual von Mises stress exceeds the preceding maximum von Mises stress (strengthening):

$$if\ \sigma_e\ \geq\ \sigma_{e,max}\ then\ \sigma_{e,max} = \sigma_e \tag{27}$$

The von Mises stress increment $\dot{\sigma}_e$ is found from the incremental stresses ($\dot{\sigma}_{kl}$) [35]:

$$\dot{\sigma}_e = \frac{3 \cdot s_{kl} \cdot \dot{\sigma}_{kl}}{2 \cdot \sigma_e} \tag{28}$$

The values for β can now be determined from the flow criteria, in J_2 flow theory [35]:

$$for\ \sigma_e = \sigma_{e,max}\ and\ \dot{\sigma}_e \geq 0 \qquad \beta = 1$$

$$if\ \sigma_e < \sigma_{e,max}\ or\ \dot{\sigma}_e < 0 \qquad \beta = 0 \tag{29}$$

Since β depends on the stresses, in this work the β calculated in the preceding step is used to determine the state and hence stresses in the next step. This means that no equilibrium iterations are performed and thus a small overshoot will occur at the time of changing from elasticity to plasticity. For the monotone loading seen for nitriding, the overshoot can be minimized (neglected) using sufficiently small increments.

The tangent modulus is found using a power hardening law [35], which states that

$$for\ \sigma > \sigma_y, \varepsilon = \frac{\sigma_y}{E}\left(\frac{\sigma}{\sigma_y}\right)^n \tag{30}$$

Since $\frac{1}{E_t} = \frac{d\varepsilon}{d\sigma}$ this means that, using von Mises criterion of plasticity, the tangent modulus, E_t, is given by:

$$E_t = \frac{E}{n}\left(\frac{\sigma_y}{\sigma_e}\right)^{n-1} \tag{31}$$

The new stress is found by adding the incremental stress to the stress from the preceding step

$$\sigma_{ij}^{t+\Delta t} = \sigma_{ij}^t + \dot{\sigma_{ij}} \tag{32}$$

Analogous to the purely elastic case, assuming equal in-plane stresses, $\sigma_{11} = \sigma_{22}$, and no shear stresses, gives the following expression for the von Mises stress

$$\sigma_e^2 = \frac{3}{2}({s_{11}}^2 + {s_{22}}^2 + {s_{33}}^2) = {\sigma_{22}}^2 \tag{33}$$

Since the out of plane stress is zero, $\sigma_{33} = 0$, it follows immediately $\dot{\sigma}_{33} = 0$, and the von Mises stress increment is then

$$\dot{\sigma}_e = \frac{3(s_{11}\dot{\sigma}_{11} + s_{22}\dot{\sigma}_{22} + s_{33}\dot{\sigma}_{33})}{2 \cdot \sigma_e} = \frac{3\left(\frac{\sigma_{22}}{3}\dot{\sigma}_{22} + \frac{\sigma_{22}}{3}\dot{\sigma}_{22} - \frac{2\sigma_{22}}{3}0\right)}{2 \cdot |\sigma_{22}|} \tag{34}$$

and thus

$$for\ \sigma_{22} > 0, \quad \dot{\sigma}_e = \dot{\sigma}_{22}$$

$$for\ \sigma_{22} < 0, \quad \dot{\sigma}_e = -\dot{\sigma}_{22} \tag{35}$$

Since $\varepsilon_{11} = \varepsilon_{22}$ it holds that $\dot{\varepsilon}_{11} = \dot{\varepsilon}_{22}$ and then the expressions for the incremental stress components become

$$\begin{aligned}\dot{\sigma}_{\parallel} = \dot{\sigma}_{11} = \dot{\sigma}_{22} = {} & \frac{E}{1+\nu}\left[\frac{\nu}{1-2\nu} - \beta\frac{1}{6}\frac{E/E_t - 1}{E/E_t - (1-2\nu)/3}\right]\dot{\varepsilon}_{22} + \frac{E}{1+\nu}\left[1 + \frac{\nu}{1-2\nu} - \beta\frac{1}{6}\frac{E/E_t - 1}{E/E_t - (1-2\nu)/3}\right]\dot{\varepsilon}_{22} \\ & + \frac{E}{1+\nu}\left[\frac{\nu}{1-2\nu} + \beta\frac{1}{3}\frac{E/E_t - 1}{E/E_t - (1-2\nu)/3}\right]\dot{\varepsilon}_{33}\end{aligned}$$

$$\begin{aligned}\dot{\sigma}_{\perp} = \dot{\sigma}_{33} = {} & \frac{E}{1+\nu}\left[\frac{\nu}{1-2\nu} - \beta\frac{3}{2}\frac{E/E_t - 1}{E/E_t - (1-2\nu)/3}\frac{-2}{9}\right]\dot{\varepsilon}_{22} + \frac{E}{1+\nu}\left[\frac{\nu}{1-2\nu} - \beta\frac{3}{2}\frac{E/E_t - 1}{E/E_t - (1-2\nu)/3}\frac{-2}{9}\right]\dot{\varepsilon}_{22} \\ & + \frac{E}{1+\nu}\left[1 + \frac{\nu}{1-2\nu} - \beta\frac{3}{2}\frac{E/E_t - 1}{E/E_t - (1-2\nu)/3}\frac{4}{9}\right]\dot{\varepsilon}_{33}\end{aligned} \tag{36}$$

Because of the free surface $\sigma_{33} = 0$ at all times, thus $\dot{\sigma}_{33} = 0$ and restructuring Eq. 36 gives an expression for $\dot{\varepsilon}_{33}$ as a function of $\dot{\varepsilon}_{22}$

$$\dot{\varepsilon}_{33} = -\frac{\left[2\frac{\nu}{1-2\nu} + \beta\frac{2}{3}\frac{E/E_t - 1}{E/E_t - (1-2\nu)/3}\right]}{\left[1 + \frac{\nu}{1-2\nu} - \beta\frac{2}{3}\frac{E/E_t - 1}{E/E_t - (1-2\nu)/3}\right]}\dot{\varepsilon}_{22} \tag{37}$$

Inserting this interdependence of $\dot{\varepsilon}_{33}$ and $\dot{\varepsilon}_{22}$ in the expression for the in-plane incremental stress tensors, it follows for the case of plasticity, $\beta = 1$, that

$$\dot{\sigma}_{11} = \dot{\sigma}_{22} = \frac{E}{1+\nu}\left(\left[1 + 2\frac{\nu}{1-2\nu} - \frac{1}{3}\frac{E/E_t - 1}{E/E_t - (1-2\nu)/3}\right] + \frac{-2\left[\frac{\nu}{1-2\nu} + \frac{1}{3}\frac{E/E_t - 1}{E/E_t - (1-2\nu)/3}\right]^2}{\left[1 + \frac{\nu}{1-2\nu} - \frac{2}{3}\frac{E/E_t - 1}{E/E_t - (1-2\nu)/3}\right]}\right)\dot{\varepsilon}_{22} \tag{38}$$

and for elasticity, $\beta = 0$,

$$\dot{\sigma}_{11} = \dot{\sigma}_{22} = \frac{E}{1-\nu}\dot{\varepsilon}_{22} \tag{39}$$

where the mechanical incremental strain, $\dot{\varepsilon}_{22}$, is found by

$$\dot{\varepsilon}_{22}^{tot} = \dot{\varepsilon}_{22} + \dot{\varepsilon}_{22}^{ch} \tag{40}$$

The total strain increment $\dot{\varepsilon}_{22}^{tot}$ can be found using equilibrium of the stress increment $\dot{\sigma}_{22}$ over the cross-section from the surface to the depth L

$$\int_0^L \dot{\sigma}_{22} dz = 0 \tag{41}$$

Since there are now both a plastic region from the surface to a depth z_{pl} and an elastic region from z_{pl} to the maximum depth, L, the integral is split as follows

$$\int_0^L \dot{\sigma}_{22} dz = \int_0^{z_{pl}} \dot{\sigma}_{22} dz + \int_{z_{pl}}^L \dot{\sigma}_{22} dz \tag{42}$$

This results in the following form of the equilibrium equation

$$\int_0^{z_{pl}} \dot{\sigma}_{22} dz + \int_{z_{pl}}^L \dot{\sigma}_{22} dz = 0 \tag{43}$$

Assuming constant material parameters (E, ν) and inserting the expressions for the stress in elastic (Eq. 39) and the plastic regions (Eq.38) in Eq. 43 gives

$$\dot{\varepsilon}_{22}^{tot} = \left[\frac{E}{1+\nu} \left(\left[1 + 2\frac{\nu}{1-2\nu} - \frac{1}{3}\frac{\frac{E}{E_t} - 1}{\frac{E}{E_t} - \frac{(1-2\nu)}{3}} \right] + \frac{-2\left[\frac{\nu}{1-2\nu} + \frac{1}{3}\frac{\frac{E}{E_t} - 1}{\frac{E}{E_t} - \frac{(1-2\nu)}{3}} \right]^2}{\left[1 + \frac{\nu}{1-2\nu} - \frac{2}{3}\frac{\frac{E}{E_t} - 1}{\frac{E}{E_t} - \frac{(1-2\nu)}{3}} \right]} \right) \int_0^{z_{pl}} \dot{\varepsilon}_{22}^{ch} dz + \frac{E}{1-\nu} \int_{z_{pl}}^L \dot{\varepsilon}_{22}^{ch} dz \right] \Bigg/ \left[\frac{E}{1+\nu} \left(\left[1 + 2\frac{\nu}{1-2\nu} - \frac{1}{3}\frac{\frac{E}{E_t} - 1}{\frac{E}{E_t} - \frac{(1-2\nu)}{3}} \right] + \frac{-2\left[\frac{\nu}{1-2\nu} + \frac{1}{3}\frac{\frac{E}{E_t} - 1}{\frac{E}{E_t} - \frac{(1-2\nu)}{3}} \right]^2}{\left[1 + \frac{\nu}{1-2\nu} - \frac{2}{3}\frac{\frac{E}{E_t} - 1}{\frac{E}{E_t} - \frac{(1-2\nu)}{3}} \right]} \right) z_{pl} + \frac{E}{1-\nu}(L - z_{pl}) \right] \tag{44}$$

3. Computational Method

3.1 Computation of composition profiles

Composition profiles were computed with the finite difference method. Discretizing was done using the central explicit finite-difference method giving for Eq. 12:

$$\frac{c_i^{t+\Delta t}-c_i^t}{\Delta t}=\frac{\partial D_N^{(c_i^t)}}{\partial c}\left(\frac{c_{i+1}^t-c_{i-1}^t}{2\Delta z}\right)^2+D_N^{(c_i^t)}\cdot\frac{c_{i+1}^t-2c_i^t+c_{i-1}^t}{\Delta z^2}-\frac{\left(D_N^{(c_{i+1}^t)}\cdot\frac{K_{N_{i+1}}}{\frac{\partial K_{N_{i+1}}}{\partial c_N}}-D_N^{(c_{i-1}^t)}\cdot\frac{K_{N_{i-1}}}{\frac{\partial K_{N_{i-1}}}{\partial c_N}}\right)}{2\Delta z}\frac{\sigma_{H_{i+1}}^{\ t}-\sigma_{H_{i-1}}^{\ t}}{2\Delta z}$$
$$-D_N^{(c_i^t)}\left(\frac{K_{N_i}}{\frac{\partial K_{N_i}}{\partial c_N}}\frac{V_N}{RT}\frac{\sigma_{H_{i+1}}^{\ t}-2\sigma_{H_i}^{\ t}+\sigma_{H_{i-1}}^{\ t}}{\Delta z^2}\right) \tag{45}$$

where $D_N^{(c_i^t)}$ is a known explicit function of the concentration, giving the possibility of calculating $\frac{\partial D}{\partial c}$ for a known concentration c_i^t.

The continuity equation at the surface to balance the fluxes of nitrogen atoms arriving at and leaving from the surface cell to calculate the actual surface concentration of nitrogen, described by Eq. 15, can be discretized as

$$\frac{c_i^{t+\Delta t}-c_i^t}{\Delta t}=-\frac{J_{i\to i+1}-J_{surf}}{\Delta z} \tag{46}$$

Combining Eq. 46 with the expression for J_{surf}, given in Eq. 14 and the expression for the flux, (see Eq. 10 and 11b) the nitrogen concentration in the surface cell follows from

$$\frac{c_i^{t+\Delta t}-c_i^t}{\Delta t}=D_N^{(c_i^t)}\frac{c_{i+1}^t-c_i^t}{{\Delta z_i}^2}-D_N^{(c_i^t)}\frac{K_{N_i}}{\frac{\partial K_{N_i}}{\partial c_N}}\frac{V_N}{RT}\frac{\sigma_{H_{i+1}}^t-\sigma_{H_i}^t}{{\Delta z_i}^2}+\frac{k}{\Delta z_i}\cdot\left(c_{eq}-c_i^t\right) \tag{47}$$

A Flow chart of the computational sequence is shown in Fig. 2.

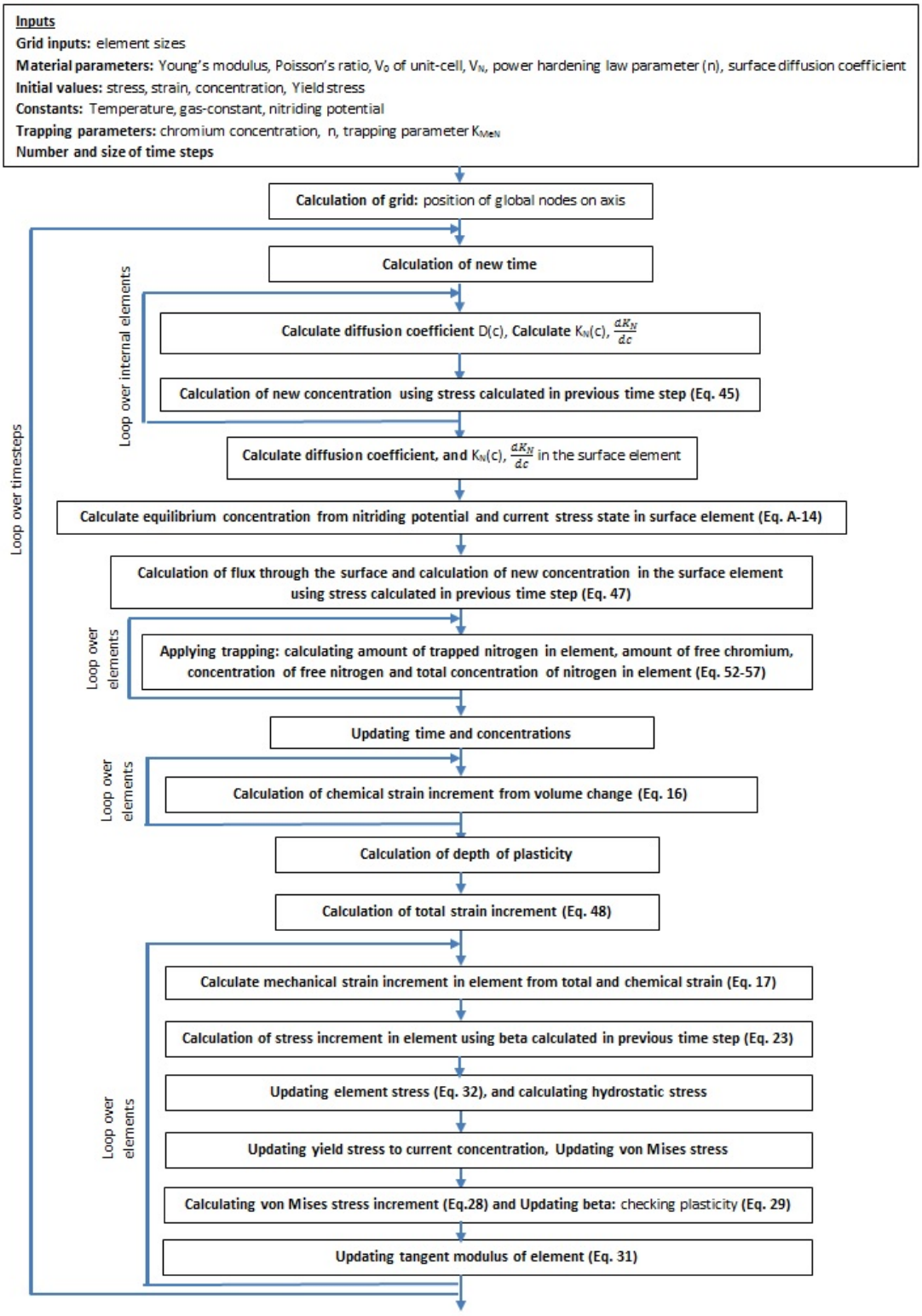

Figure 2 - Computational flowchart

3.2 Computation of strains and stresses

The computation of composition-induced strains and stresses is done straightforwardly for each element after the concentration is calculated in each time-step. However since β depends on the stresses, this work uses the beta calculated in the preceding step to determine the state and hence stresses. This means that a small overshoot will occur at the time of changing from elasticity to plasticity, but with the monotone loading and using sufficiently small increments the overshoot can be neglected.

The computation of the integrals used for finding the total strains as in for example Eq. 21 is done using the following numerical integration

$$\varepsilon_{\parallel}^{tot} = \frac{1}{L}\int_0^L \left(\varepsilon_{\parallel}^{ch}\right) dz = \frac{1}{L}\sum_1^{imax}[\varepsilon_{22}^{ch}(i)\cdot \Delta z(i)] \tag{48}$$

where *i*, is the element number and *imax*, is the number of the element ending at the depth *L*.

Similarly the integrals used for calculating the total strain when there is plasticity (Eq. 44)

is calculated using a similar numerical integration

$$\int_0^{z_{pl}} \dot{\varepsilon}_{22}^{ch} dz = \sum_1^{i_{max,plastic}}[\dot{\varepsilon}_{22}^{ch}(i)\cdot \Delta z(i)] \tag{49}$$

$$\int_{z_{pl}}^{L} \dot{\varepsilon}_{22}^{ch} dz = \sum_{i_{max,plastic}}^{imax}[\dot{\varepsilon}_{22}^{ch}(i)\cdot \Delta z(i)] \tag{50}$$

For the case of expanded austenite, where no nucleation or precipitation of a new phase occurs, the chemical strain can be calculated directly from the total nitrogen concentration by

$$for\ i = j \quad \varepsilon_{ij}^{che}(c_N^{tot}) = \frac{V(c_N^{tot})^{1/3} - V_{ref}^{1/3}}{V_{ref}^{1/3}}$$

$$for\ i \neq j \quad \varepsilon_{ij}^{che} = 0 \tag{51}$$

3.3 Computational implementation of trapping

The amount of free nitrogen after trapping, i.e. the concentration of residual nitrogen, c_N^{res}, can be found using Eq. 13 from

$$K_{MeN} = c_{Cr}^{res}\cdot (c_N^{res})^n \tag{52}$$

Computationally, the calculation of residual nitrogen and chromium is done sequentially by calculating the residual nitrogen assuming that residual chromium concentration in the equation above is equal to the free chromium concentration before trapping, so

$$c_{Cr}^{res}{}_{before\ trapping} \cdot \left(c_N^{res}{}_{after\ trapping}\right)^n = K_{MeN} \tag{53}$$

The concentration of trapped nitrogen, c_N^{tr}, is then found by

$$c_N^{tr} = c_N(t,z) - c_N^{res} \tag{54}$$

and the trapped chromium, c_{Cr}^{tr}, by

$$c_{Cr}^{tr} = \frac{c_N^{tr}}{n} \tag{55}$$

The concentration of residual chromium after trapping, c_{Cr}^{res}, is then found as

$$c_{Cr}^{res} = c_{Cr}(t,z) - c_{Cr}^{tr} \tag{56}$$

It is noted that this sequential modeling induces a slight error, but for small time steps it is deemed negligible.

On incorporating trapping in the model for nitrogen diffusion only residual nitrogen is considered to diffuse, while the surface flux depends on the total concentration of nitrogen in the surface:

$$c_N^{tot} = c_N^{tr} + c_N^{res} \tag{57}$$

It should be noted that the diffusion coefficient also depends on the total nitrogen concentration.

4. Results and discussion

4.1 Effects of trapping and concentration dependent diffusion coefficient

The combined effect of a composition-dependent diffusion coefficient of nitrogen and the role of trapping on the developing concentration profile is investigated in this section. For this purpose nitriding at 718 K for 22 hours is considered, using a nitriding potential of 1000 $atm^{-1/2}$. The concentration-dependent diffusion coefficient is given in Eq. A-1. For the calculations with a constant diffusion coefficient, the average value over the composition range is taken. For diffusion, in all cases the sample was considered infinitely thick, as compared to the diffusion depth range, i.e. diffusion into a semi-infinite solid can be considered. The nitrogen concentration-depth profiles were calculated for the case of no trapping, $K_{MeN} = \infty$, full trapping $K_{MeN} = 0$, and intermediate trapping for solubility products $K_{MeN} = 10^7$, $K_{MeN} = 10^8$ and $K_{MeN} = 10^9$. For these three cases of intermediate trapping, trapping occurs for nitrogen concentrations higher than approximately $700 \mathrm{mol.\,m^{-3}}$, $4600 \mathrm{mol.\,m^{-3}}$ and $41600 \mathrm{mol.\,m^{-3}}$, respectively. The concentration profiles were calculated under the assumption that no stress develops in the case.

The results of the calculations are presented in Fig. 3 a) and b) for constant diffusivity and concentration-dependent diffusivity, respectively. The effect of trapping is most easily observed in Fig. 3a for a constant diffusivity. No trapping

yields the usual complementary error-function profile, with a concentration gradient that decreases gradually with depth (black line in Fig. 3a). Full trapping leads to an abrupt transition to zero nitrogen concentration (dashed line in Fig. 3a). Intermediate trapping has as a consequence that a tail appears to the concentration profile beyond the depth where the solubility product is reached. The arrows in Fig. 3a indicate where this discontinuity in the slope to the concentration profile occurs, corresponding to the nitrogen concentrations given above, marking the combination of nitrogen concentration and the depth below which no trapping occurs. Furthermore, a smoothening of the aforementioned abrupt transition from high to low nitrogen concentration is obtained for intermediate trapping. This is most clearly reflected by the profile for $K_{MeN}=10^7$. The effect of a concentration-dependent diffusion coefficient that increases with nitrogen content, reaches a maximum and thereafter decreases with nitrogen content (see Appendix A1) is reflected in Fig. 3b. Analogous to the observations in Fig. 3a a discontinuity in the slope is observed (marked by arrows) for the concentration and depth below which no trapping occurs.

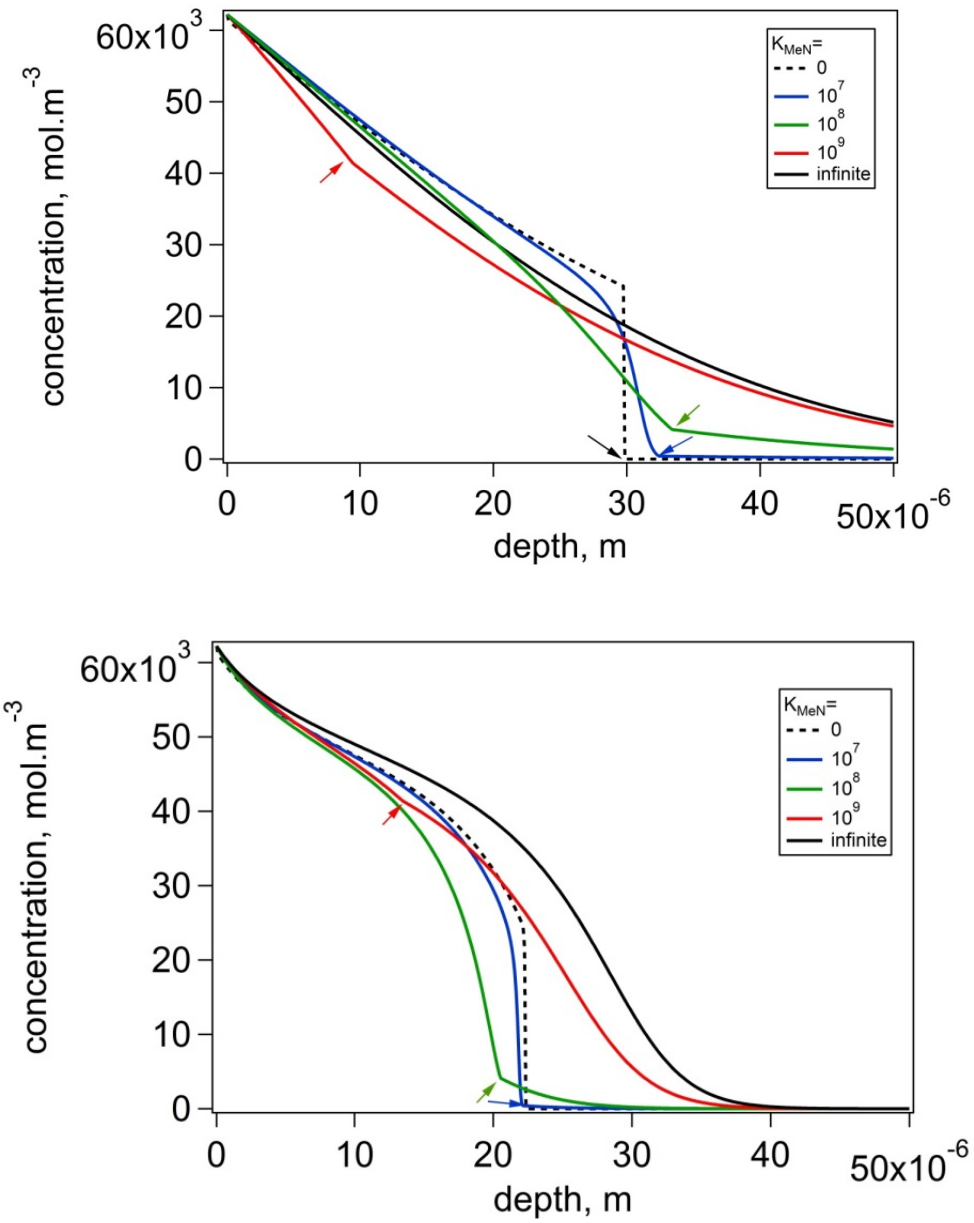

Figure 3 - Concentration-depth profiles calculated assuming a) constant diffusion coefficient and b) concentration dependent diffusion coefficient (cf. Appendix A1), for no trapping, $K_{MeN} = \infty$, full trapping $K_{MeN} = 0$, and intermediate trapping for solubility products $K_{MeN} = 10^7$, $K_{MeN} = 10^8$ and $K_{MeN} = 10^9$ of diffusing nitrogen atoms by chromium atoms. The arrows mark the concentrations (and depths) below which no trapping occurs.

4.2 The role of the surface reaction on evolution of composition-depth profiles

The competition of the fluxes of nitrogen arriving at and leaving from the surface was calculated for a concentration-dependent diffusivity, intermediate trapping $K_{MeN} = 10^7$and $K_{MeN} = 10^9$ (cf. Fig. 3b), and different values of the reaction-rate constant k in Eq. 14. Again nitriding at K_N= 1000 $atm^{-1/2}$ at 718 K is considered. The evolution of the concentration-depth profile with time for $k = 5 \cdot 10^{-7} \mathrm{m.s^{-1}}$ and $k = 5 \cdot 10^{-10} \mathrm{m.s^{-1}}$ is shown in Fig. 4, while the evolution of the surface concentration for various values of k is displayed in Fig. 5. As above, the role of stress is omitted.

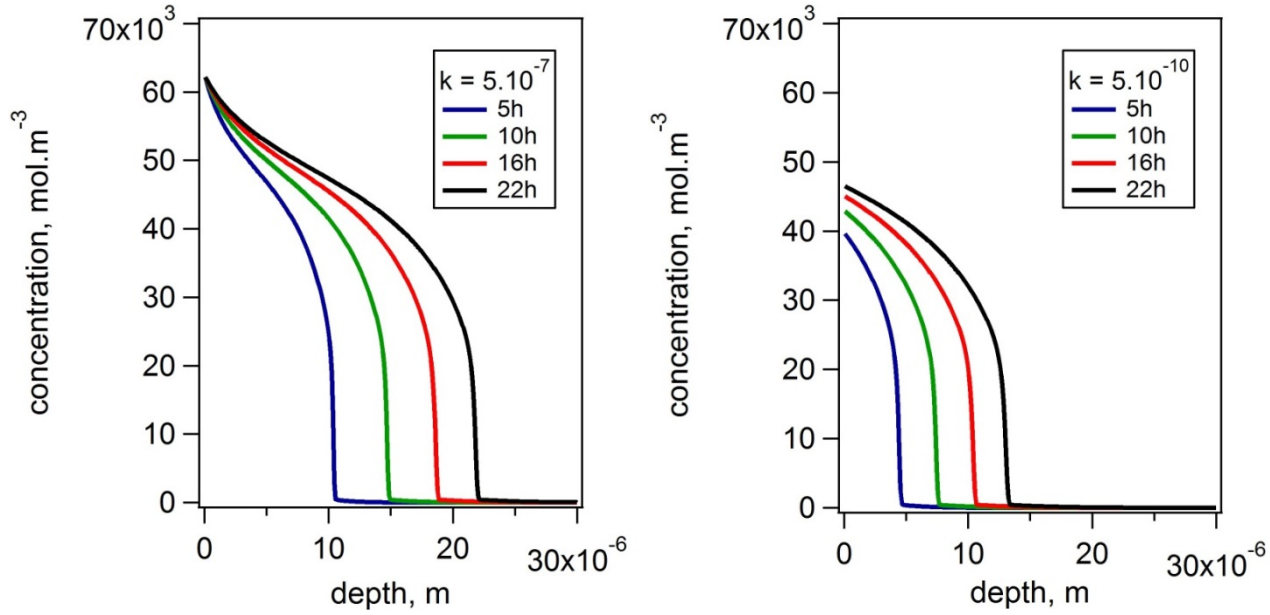

Figure 4 - evolution of the concentration-depth profile with time for $k = 5 \cdot 10^{-7} \mathrm{m.s^{-1}}$ and $k = 5 \cdot 10^{-10} \mathrm{m.s^{-1}}$, for nitriding with a nitriding potential of 1000 $atm^{-1/2}$.

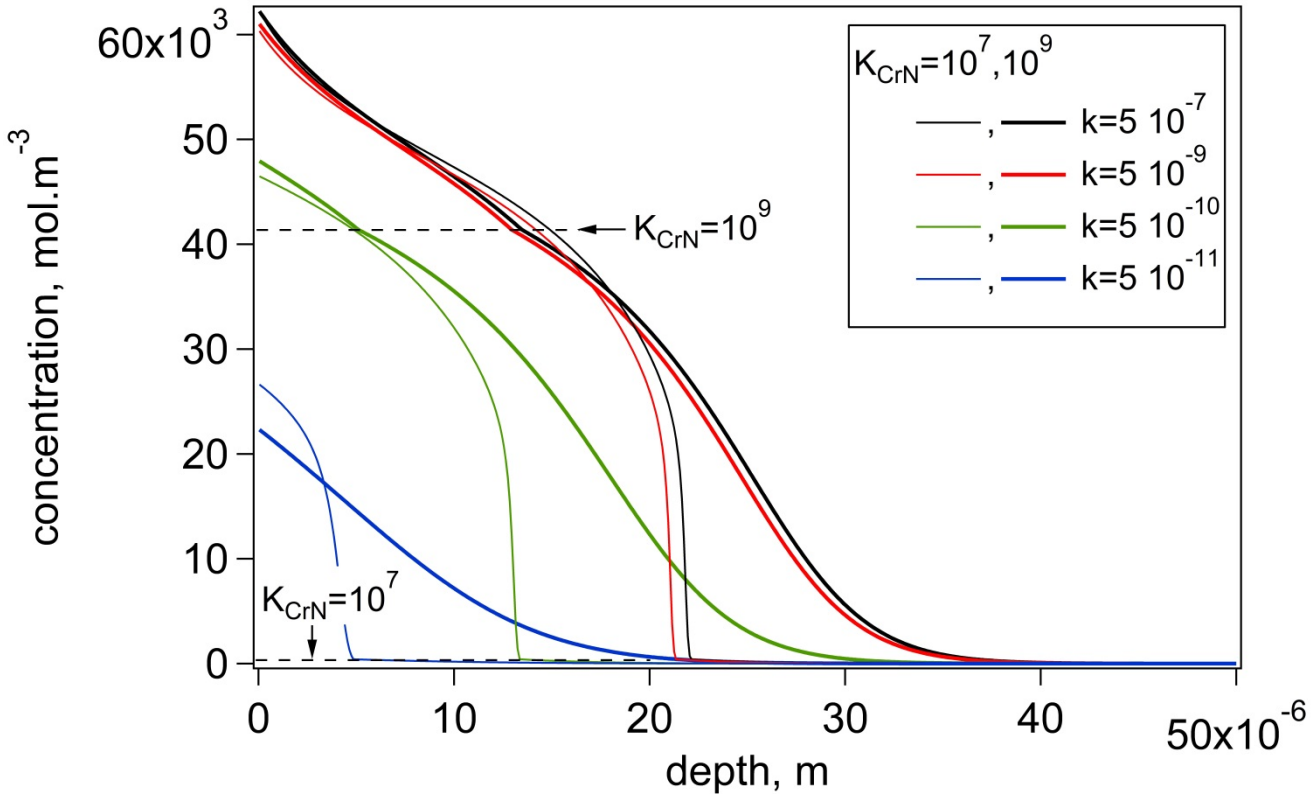

Figure 5 - Evolution of the surface concentration for various values of k, for $K_{CrN} = 10^7$ (thin lines) and $K_{CrN} = 10^9$ (thick lines) for nitriding of 22h at 718K at $K_N = 1000\ \text{atm}^{-1/2}$.

The evolution of the concentration profile in Fig. 4 shows that the reaction rate constant of the surface reaction leads to the same surface concentration for all investigated times if k=10^{-7} m.s^{-1}. This indicates that (imposed) local equilibrium between nitrogen in the gas phase and nitrogen in the solid phase is achieved at the surface. For a lower value of the reaction rate constant (k=5 10^{-10} m.s^{-1}), the surface concentration increases gradually with nitriding time. In Fig. 5 the concentration profiles obtained after nitriding for 22 h at 718 K are shown for various combinations of K_{MeN} and k. Clearly, the surface concentration of nitrogen attained after 22h decreases with a reduction of the reaction rate constant of the surface reaction. Moreover, the incorporation of trapping and the value of K_{MeN} have an important influence on the total amount of nitrogen incorporated in the material. Stronger trapping leads to a lower amount of incorporated nitrogen and a steeper case-core transition.

4.3 Composition induced stress-depth profiles

The dissolution of interstitials into the solid state is not associated with the nucleation of a new phase, but rather an expansion of the existing lattice. From the relation between lattice parameter and nitrogen concentration, the volumetric expansion of the lattice can be calculated, see Appendix A2. Accordingly, the composition-induced strains introduced into the lattice can be calculated with Eq. 16. Firstly, it is assumed that these strains are accommodated purely elastically. The stresses introduced under the assumption of an infinitely thick substrate, i.e. all stress is accumulated in the expanded region, were calculated with Eq. 22 and are shown in Fig. 6, for the composition profiles as displayed in Fig. 4. Not surprisingly, the elastic composition-induced compressive stress-depth profiles reflect the composition-depth profiles from which they were calculated. In this respect it is important to realize that in the present calculations the elastic constants were assumed to be independent of the composition of austenite, because no quantitative data are available of how Young's modulus and Poisson's ratio depend on nitrogen concentration in austenite. It is noted that the calculated stress values are unrealistically high and will never be possible to be supported by the austenitic stainless steels under consideration. Furthermore, the values of the elastic stresses are five times as high as found experimentally with X-ray diffraction stress analysis [37]. Clearly, accommodation of the volume misfit introduced by dissolving nitrogen into austenite should, at least partly, be accommodated by plastic deformation. This is in agreement with the experimental observations of grain rotation and stacking fault introduction in expanded austenite [18,19,20,21].

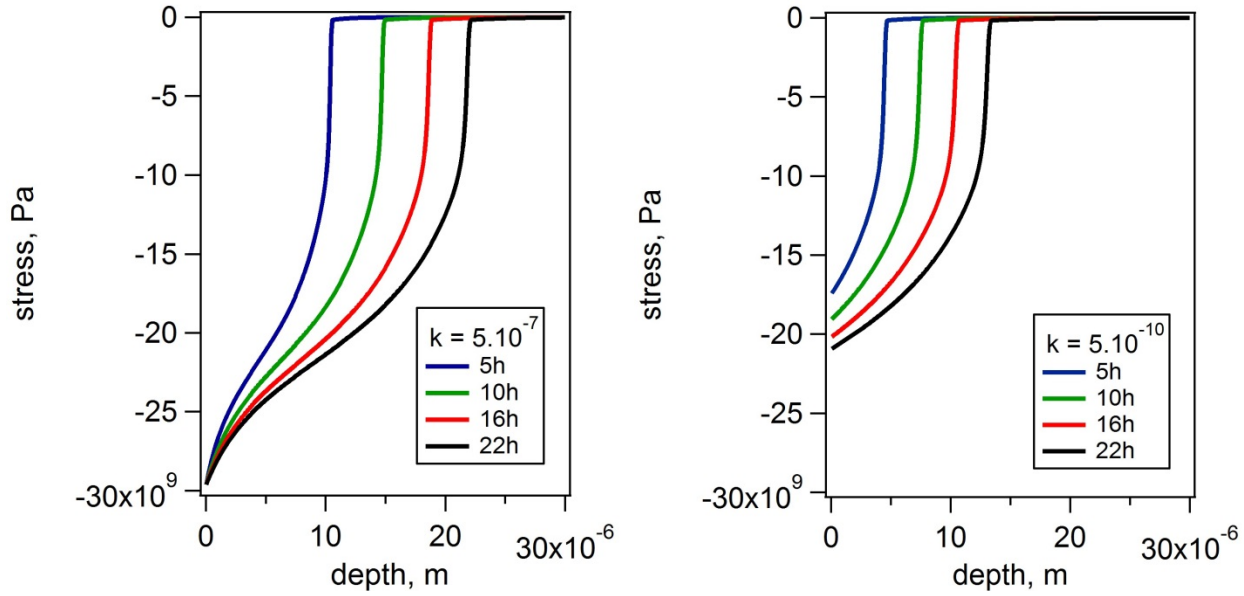

Figure 6 - Compressive composition-induced stress for an infinitely thick substrate, elastic accommodation of the volume expansion and $K_{CrN}=10^7$ and $k=5\ 10^{-7}$ m.s^{-1} and $k=5\ 10^{-10}$ m.s^{-1} for selected diffusion times. The corresponding nitrogen concentration-depth profiles are given in Fig. 4.

The effect of the sample thickness on the stress distribution as calculated with Eqs. 18-21 is shown in Fig. 7 for several sample thicknesses, 2L. Only for relatively thin samples substantial tensile stresses are present in the core to compensate for the high compressive stresses in the case. Realizing that the stresses in the case are grossly overestimated by the assumption of fully elastic accommodation, it is concluded that for practical situations the tensile stresses in the core can be neglected. This justified omission is therefore implemented in the sequel of this manuscript.

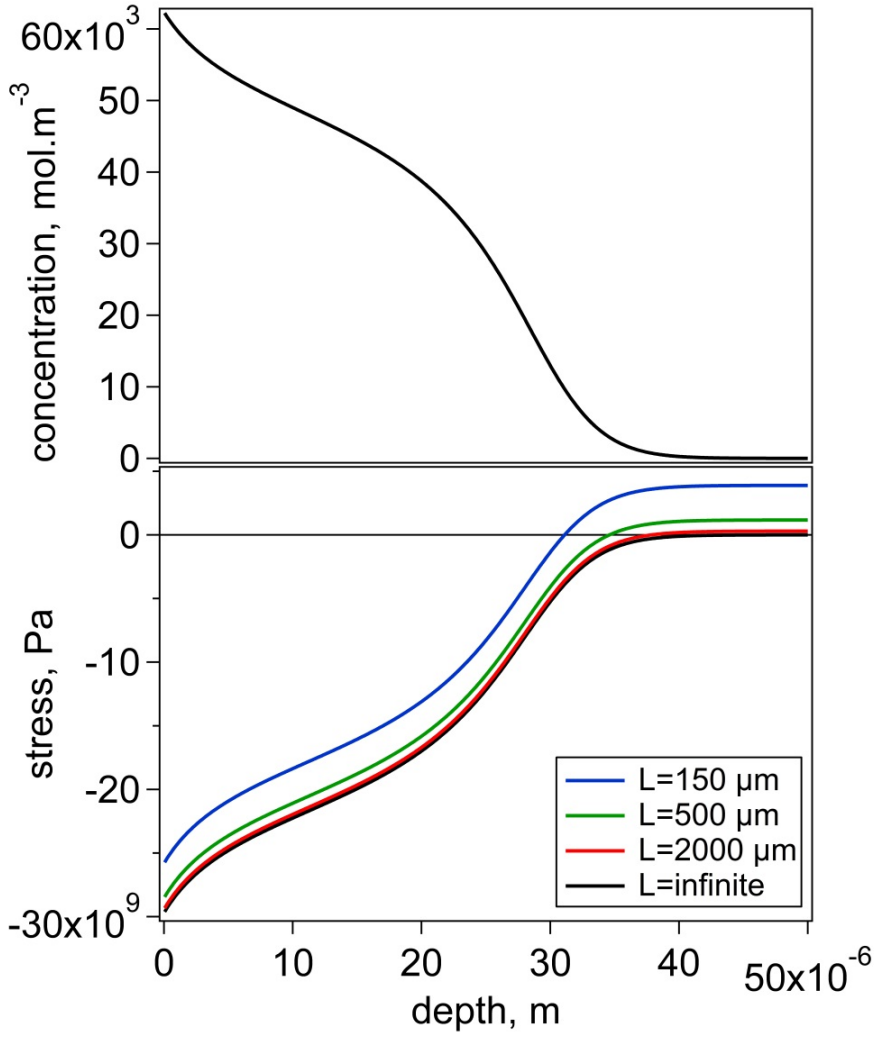

Figure 7 - Effect of thickness of the sample on the predicted stress profile, for 22h nitriding with a nitriding potential of 1000 $atm^{-1/2}$, k= $5 \cdot 10^{-7}$ $m.s^{-1}$ and no trapping (cf. Fig. 3b for $K_{CrN} = \infty$).

4.4 Influence of compressive stress on diffusive flux in the sample

The presence of a gradient in the composition-induced stress is equivalent to an additional (positive or negative) driving force for the diffusion of nitrogen. A compressive stress decreasing with depth, as for the present case (Fig. 6), would imply a positive additional driving force for diffusion. It should be noted that it is the stress *change* with depth that increases the diffusion, not the actual level of the stress.

In Fig. 8 the effect of a stress-gradient induced driving force is demonstrated for the same nitriding conditions as in Fig. 5a, i.e. 22h at 718 K at K_N=1000 $atm^{-1/2}$, while keeping the surface concentration constant. The lines obtained without considering an effect of the stress on the internal diffusion are reproduced from Fig. 4 and Fig. 6. Evidently, for the exorbitantly huge elastic stresses the stress-gradient induced driving force establishes a concentration profile that reaches about 3.5 times as deep as driven by the concentration gradient alone. This shows the potentially substantial contribution of stress-induced diffusion in expanded austenite, albeit for a grossly overestimated elastic stress.

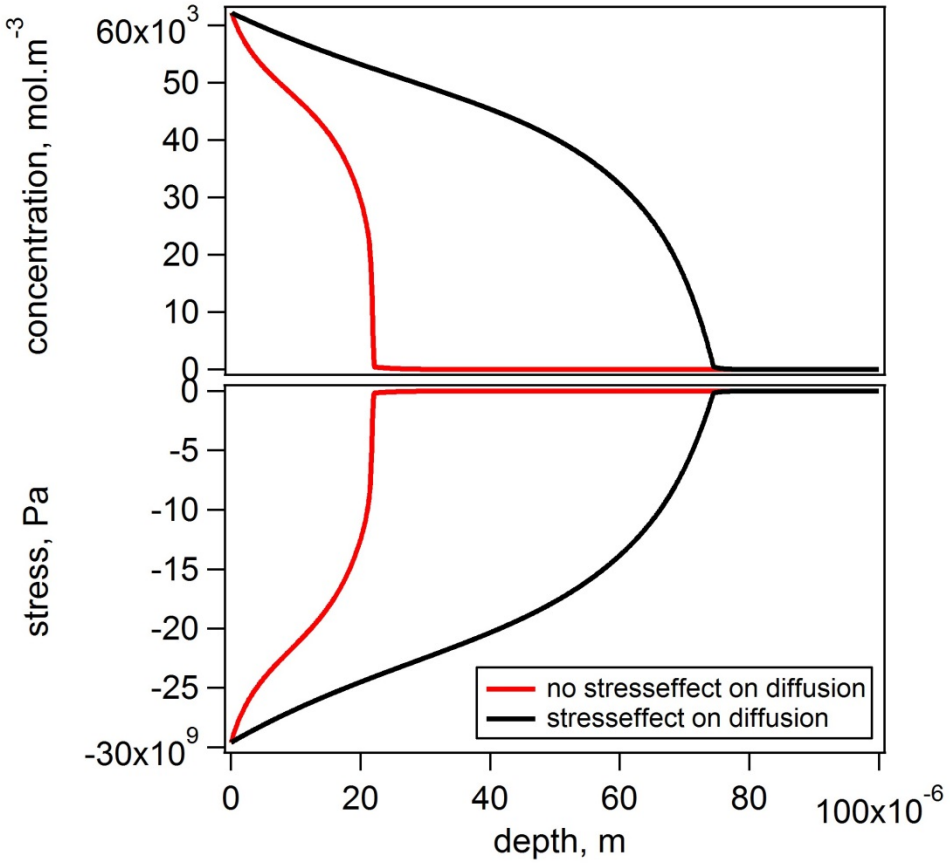

Figure 8 – Effect of taking into account stress on Predicted concentration-depth profiles and stress-depth profiles for nitriding of 316 austenitic stainless steel after 22 hours at 718K using a nitriding potential of 1000 $atm^{-1/2}$, $K_{CrN}=10^7$ and k=5 10^{-7} $m.s^{-1}$

4.5 Influence of compressive stresses on the surface flux

Compressive stress (or pressure) reduces the solubility of nitrogen in austenite under equilibrium conditions. This will be most clearly manifested by a reduction of the nitrogen concentration at the interface between the solid and gaseous phase, i.e. the surface, where local equilibrium is attempted to be imposed.

The dependence of the surface concentration on the hydrostatic component of the compressive stress is given in Fig. 9 for stainless steel AISI 316 at 718 K and selected values of the nitriding potential[4], using Eq. A-14 (for details of the quantitative data extracted from literature data, see Appendix A3 and A4). Evidently, the solubility of nitrogen depends sensitively on the (imposed or residual) stress. Since a lower equilibrium concentration leads to a lower maximum flux through the surface, this indicates that a compressive stress resulting from the chemical strain reduces the nitrogen flux through the surface.

This means, that even though the level of stress does not affect the internal diffusion, as discussed earlier, it does affect the flux through the surface. So even though a stress profile with higher compressive stresses at the surface compared to the centre increases the internal diffusion, it also decreases the flux through the surface.

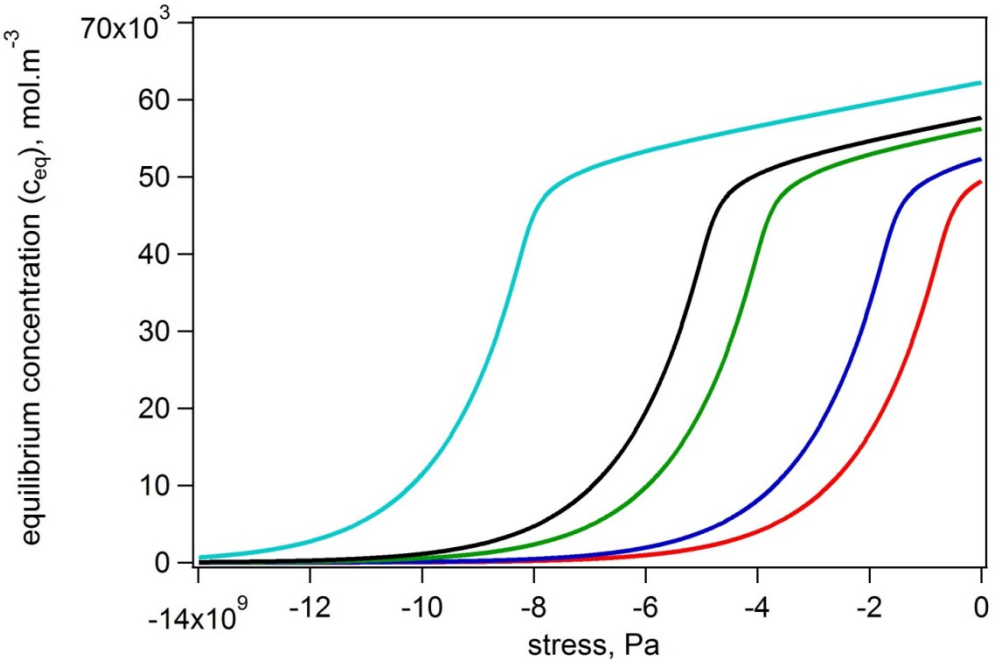

Figure 9 - Equilibrium concentrations as a function of surface stress for varying nitriding potentials, K_N, (Note that negative values of stress denotes compressive stress)

[4] The nitriding potential is proportional to the activity, and thus the chemical potential, of nitrogen in the gas phase (see Appendix A4).

Implementing the effect of compressive stress on the local equilibrium at the surface, combined with the additional stress-induced driving force for diffusion, leads to the predicted concentration-depth and stress-depth profiles shown in Fig. 10. A reduction by about a factor 2 in the local nitrogen concentration is seen compared to the profile predicted, when the effect of stress on the surface concentration is not taken into account. The lines obtained without considering an effect of the stress on the surface concentration are reproduced from Fig. 8. According to Eq. 14 a lower equilibrium concentration at the surface leads to a lower maximally possible flux through the surface. Nevertheless, the effect of a compressive stress gradient causes a penetration depth of the profile beyond the depth achieved without including the contribution of stress-induced diffusion, (see Fig. 8) despite the substantially smaller chemical contribution to the driving force for diffusion. This indicates that the net effect of the combination of the lower maximal flux through the surface and the larger diffusive flux postpones the establishment of local equilibrium at the surface to guarantee a sufficient uptake of nitrogen to maintain growth of the expanded austenite zone.

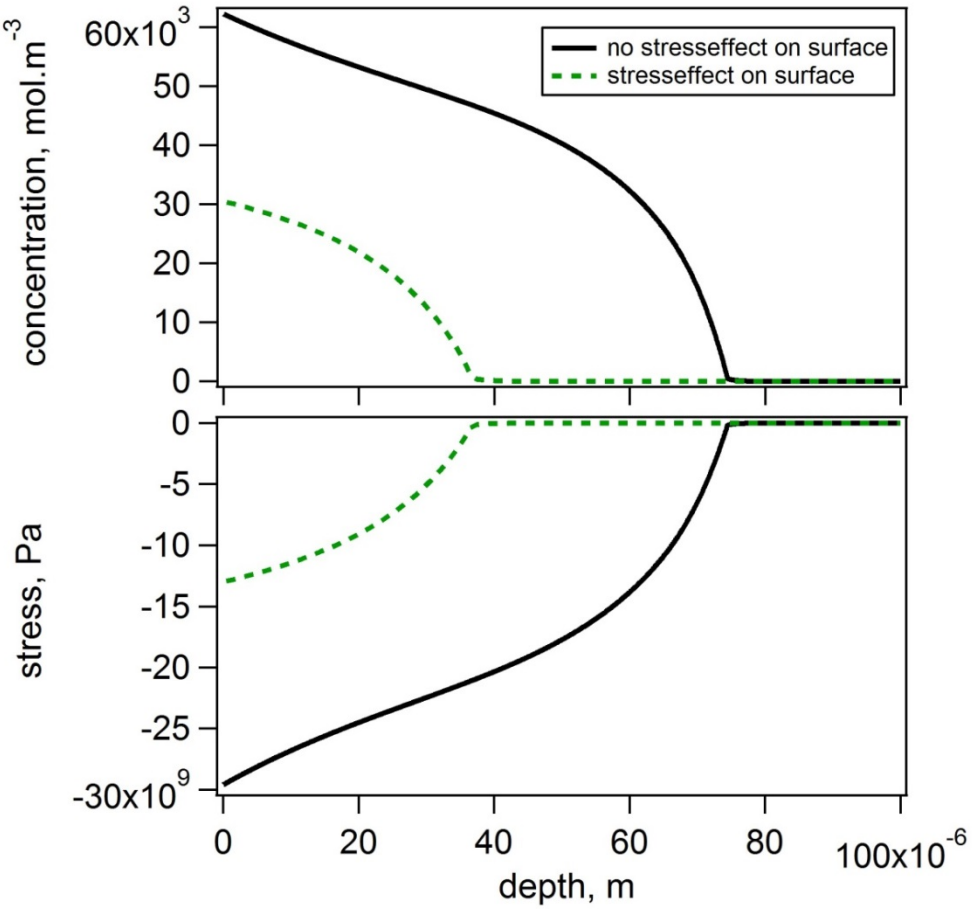

Figure 10 - Predicted concentration-depth profile and stress-depth profile for nitriding of 316 austenitic stainless steel after 22 hours at 718K using a nitriding potential of 1000 atm$^{-1/2}$ $K_{CrN}=10^7$ and $k = 5 \cdot 10^{-7}$ m.s^{-1}.

4.6 Effect of plasticity on predicted profiles

Assuming purely elastic accommodation of the lattice expansion of austenitic stainless steel associated with nitrogen dissolution is unrealistic, because the yield stress of austenite is as low as 290 MPa [38].

Concentration-depth and stress-depth profiles are shown for three distinct situations in Fig. 11: assuming purely elastic accommodation of the composition-induced expansion (cf. Fig. 10 for stress affected surface) indicated as "elastic", plastic accommodation for stress beyond the yield stress of the base material, indicated as "plastic (const. Yield stress)" and the situation where both plasticity and solid-solution hardening are taken into account, indicated as "plastic, Yield stress $= f(c_N)$", reflecting the composition-dependence of the yield stress. Details of the input parameters and computational method for incorporating the composition-dependent yield stress are described in Appendix A5. Comparison of the profiles for elastic and plastic accommodation shows that taking into account plasticity, the stress level in the expanded austenite zone is very low as compared to when assuming purely elastic accommodation; as was expected. Consequently, for the case of plasticity with constant yield stress, the nitrogen surface concentration and diffusion in expanded austenite would be largely unaffected by the stress and thus a composition-depth profile reminiscent of that for no stress is obtained (cf. Fig. 4). Consistently with the appreciably lower elastic stress in the case, the contribution of stress-induced diffusion is limited, as reflected by the relatively shallow diffusion depth reached. Assuming a concentration-dependent yield stress, implying that solid solution strengthening by nitrogen dissolution in austenite is accounted for, a high nitrogen content is obtained, whilst the compressive residual stresses reach a level of maximally 6 GPa at the surface (Fig. 11).

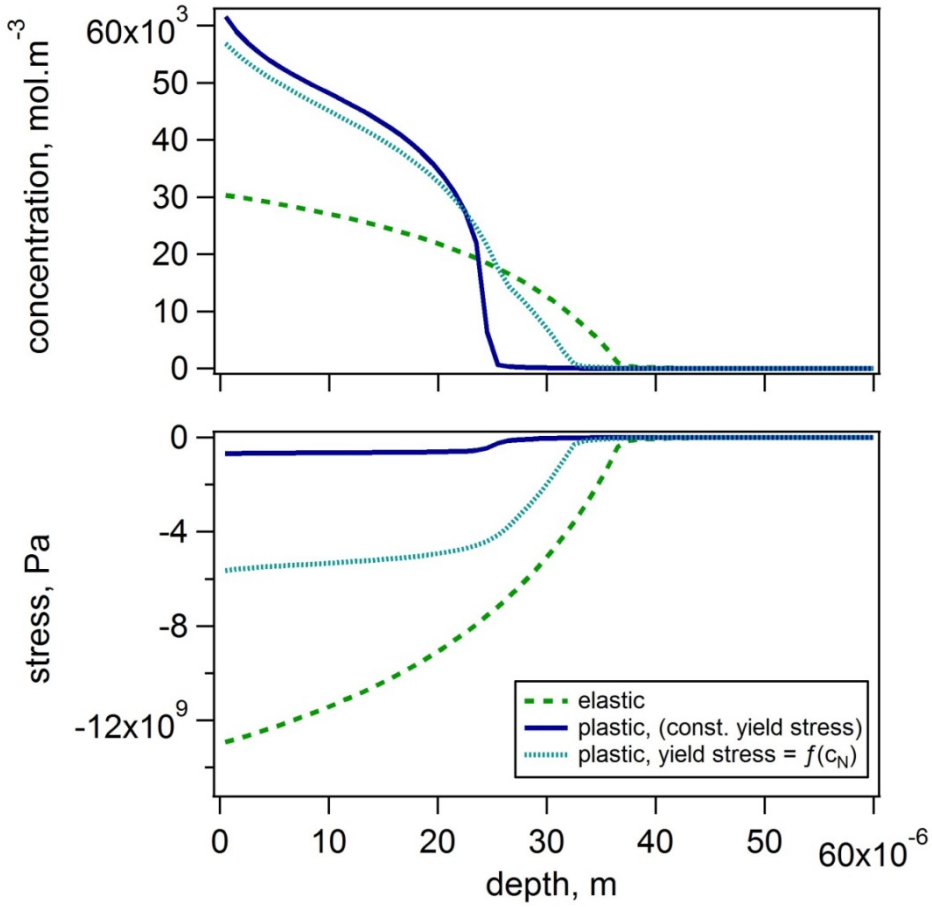

Figure 11 - Simulated concentration-depth profiles and stress-depth profiles using purely elastic accommodation (designated "elastic") of the lattice expansion or elastic-plastic accommodation. For a fixed yield stress the lines denoted "plastic, (const. Yield stress)" are obtained, while the assumption of a concentration-dependent yield stress results in the lines denoted "plastic, Yield stress $= f(c_N)$". In all cases the nitriding conditions are 22h at 718 K for K_N=1000 $atm^{-1/2}$, K_{CrN}=10^7 and k=5 10^{-7} $m.s^{-1}$.

5. Discussion

5.1 Evolution of composition and stress-depth profiles

In the preceding chapter it was demonstrated how the various parameters influence both the shape of the concentration-depth profile as well as its evolution with nitriding time. From the systematic analysis in this manuscript it is clear that from the concentration-depth profile alone it is not possible to discriminate between the various models that have so far been presented in the literature. On the one-hand, the adoption of a model presuming a constant diffusion coefficient and trapping of nitrogen atoms, as in Refs. [4,6], can yield concentration-depth profiles of a shape as given in Fig. 3a (in particular for $K_{MeN}=10^7$). Taking the diffusivity and solubility product, K_{MeNn} (including n), as fitting parameters will certainly allow a satisfactory mathematical description of concentration-depth profiles. On the other hand, the assumption of a concentration-dependent diffusivity as adopted in this work (cf. Appendix A1) also leads to concentration-profiles that resemble those determined experimentally, particularly after including trapping (cf. Fig. 3b). Simulation models like these do not account for the development of residual stress and its influence on the developing concentration-depth profiles. Although the consideration of residual stress was suggested to enhance nitrogen diffusion in expanded austenite, and demonstrated to be able to enhance the case depth by a factor two when the surface concentration was constant [14], further mathematical implementation has so far been pragmatic, assuming an unphysical linear relation between composition and stress and a continuously decreasing diffusion coefficient [36], which obviously is in conflict with the experimentally determined diffusion coefficient for nitrogen in expanded austenite. In the present work the actual lattice expansion of expanded austenite was taken into account and mechanical equilibrium considerations were used to estimate the stress. Moreover, the experimentally observed concentration-dependent diffusion coefficient (measured for stress-free expanded austenite!) were taken as input data in the model, while also the effect of stress on the surface flux and stress-enhanced diffusion was accounted for. Clearly, the present simulations demonstrate that elastic accommodation of the lattice expansion leads to residual stress values far beyond the yield stress of the material, which necessitates an elastic-plastic accommodation of the lattice expansion. Moreover, the residual stress values determined experimentally in expanded austenite are far beyond the yield stress of stainless steel, albeit not as high as the predicted elastic stress values (Fig. 6). Accordingly, solid-solution strengthening by the dissolution of high amounts of interstitials in expanded austenite has to be incorporated, yielding realistic simulations of both concentration-depth and stress-depth profiles over the expanded austenite case (Fig. 11).

The evolution of the case depth, taking a concentration of 5 $mol.m^{-3}$ as the minimum nitrogen concentration that belongs to the expanded austenite case, is shown in Fig. 12 for various values of the nitriding potential at a nitriding temperature of 718K. In these simulations all of the effects described in the previous chapter were included. Trapping was included by taking $K_{MeN}=10^7$, while the surface reaction was assumed to be in equilibrium ($k = 5 \cdot 10^{-7}\ \mathrm{m.s^{-1}}$). Also, stress-induced diffusion and stress effects at the surface were assumed as well as plasticity with a concentration-dependent yield strength. As follows from Fig. 12, increasing the nitriding potential beyond $K_N=100\ atm^{-1/2}$ has no further influence on the case depth. Note that a linear relation is obtained between squared depth and time, as expected for diffusion-controlled evolution of concentration profiles. The depth range of the expanded austenite case wherein plastic accommodation occurs for the same nitriding conditions, is shown in Fig. 13. Comparison of Fig. 12 and Fig. 13 shows that it is nearly unavoidable that plastic

accommodation occurs. Only for a very low nitriding potential and associated shallow case depths can plastic accommodation be avoided during nitriding of stainless steel. This is in excellent agreement with the results published in Ref. [20], where lattice rotation, as a consequence of plastic accommodation of residual stress, was observed from the case-core transition to the surface.

So far, carburizing has not been reported to lead to plastic accommodation of lattice expansion and leads to relatively low interstitial contents in the expanded austenite zone. Consistently, the experimental residual stress values reported for carbon-stabilized expanded austenite are below 3 GPa [1, 11] while the interstitial concentration is maximally 20.10^3 mol.m^{-3} [1]. For this combination of interstitial content and compressive residual stress, indeed purely elastic accommodation is predicted by Appendix A5 (Fig. A-3).

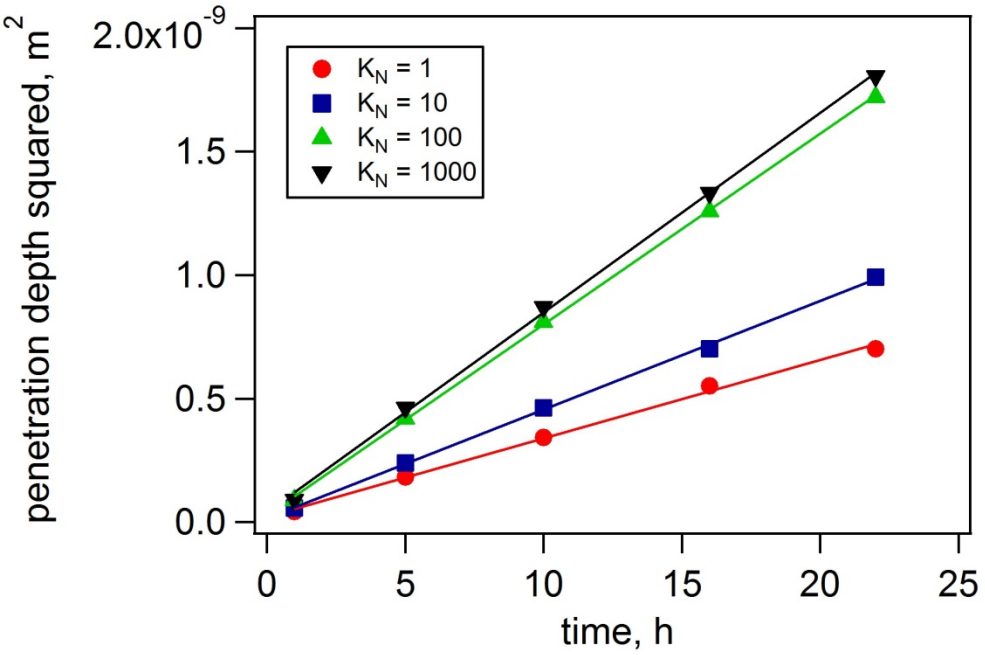

Figure 12 - Case depth (c_N>5 mol.m^{-3}) of expanded austenite as a function of nitriding time for various applied nitriding potentials, K_N, given in atm$^{-1/2}$ in the legend.

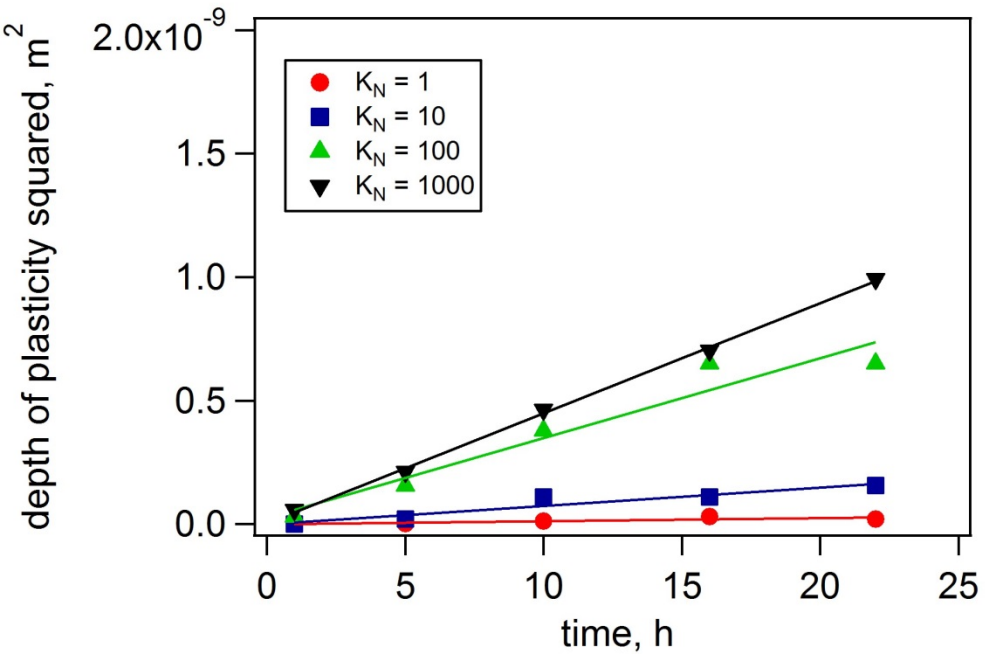

Figure 13 - depth of the plastic zone of expanded austenite as a function of nitriding time for various applied nitriding potentials, K_N, given in $atm^{-1/2}$ in the legend.

5.2 limitations of the model and comparison to experimental work

The most important novel approaches in the model presented are the coupling of composition and composition-induced stress (rather than a pragmatic linear relation between stress and concentration), and inclusion of plastic deformation, taking into account the occurrence of solid solution strengthening. While experimental data on the concentration-dependent diffusion coefficient was included in the current work, several simplifications and pragmatic approximations were adopted, which are listed below. Also, an anticipation of the effects that these simplifications may have caused are briefly described.

In the simulations, as an approximation for the elastic properties of expanded austenite those for austenitic stainless steel at room temperature were adopted. It was indicated very recently by nano-indentation observations [18] and X-ray residual stress measurements [37] that the elastic properties of expanded austenite vary with nitrogen content and that reversal of elastic anisotropy occurs as compared to austenite. As yet the absolute values of Young's modulus and Poisson constant are undetermined, a prediction of the effect of the approximate elastic constants can therefore not be given.

Elastic and plastic properties are also temperature dependent; both the Young's modulus and the yield stress decrease with temperature [38]. Thus, at the nitriding temperature, a lower Young's modulus and a lower yield stress prevail than the values adopted in the model. A lower Young's modulus would cause lower stress levels (for a certain imposed strain) and a lower yield stress would lead to an earlier introduction of plasticity. Both effects result in a lower surface stress.

Moreover, it should be noted that the updating of the plasticity criterion is based on a semi-coupled procedure in which the strengthening and the effect of the concentration-dependent yield stress is considered in a sequential manner. This may

affect the stress-predictions, but as a pragmatic approach this is deemed sufficient for the small elements and time-steps considered.

In this work the lattice expansion caused by the dissolution of nitrogen in the austenite lattice was taken from the lattice parameter applying at room temperature. Actually, for the calculation of the concentration (in $mol.m^{-3}$) and the lattice strain, the lattice parameters at the nitriding temperature should have been adopted. Thermal expansion of expanded austenite was recently determined experimentally and it was demonstrated that the linear expansion coefficient depends on the nitrogen content [13].

Thermally-induced stress from the heating and cooling cycle are not considered in the present work, and could lead to a modification of the stress profile that affects the diffusive flux and a modification of the stress-profile after cooling to room temperature. This should be considered in order to more realistically compare the experimental stress values with the calculated values. The influence of thermal stress will be the topic of future research.

Experimentally, no elastic compressive stresses exceeding 10 GPa have been reported and the highest experimentally determined compressive stresses of 7-8 GPa [1] were very recently shown to be a consequence of inappropriate elastic constants, which appear to depend strongly on the nitrogen concentration, such that a reversal of the elastic anisotropy occurs over the composition range [37]. Based on recent insights, the compressive stresses are estimated to be maximally about 5 GPa. In this respect the present calculations give an overestimation by 20%. Seen in the light of the limitations mentioned above, this is considered a good agreement

6. Conclusion

Nitriding of austenitic stainless steel was modelled taking into account a concentration-dependent diffusion coefficient and short-range ordering of chromium and nitrogen atoms (trapping). Stress-depth profiles were predicted from the lattice expansion caused by the interstitial nitrogen atoms. The interaction between the composition-induced stresses and the diffusion was examined for both purely elastic and elastic-plastic stresses. It can be concluded that:

- Solid state diffusion is enhanced by the compressive stress *gradient* resulting from the nitrogen concentration gradient;
- Assuming purely elastic accommodation of the composition-induced strain, the interaction between stresses and diffusion results in surface stresses in the order of 10GPa, which causes a significant decrease of predicted nitrogen concentration at the surface and faster growth of the expanded austenite case;
- Assuming elastic-plastic accommodation of the composition-induced strain, and a constant yield stress, equal to the yield stress of the austenitic stainless steel, decreases the predicted surface stresses to stresses in the order of 1 GPa, and the predicted surface concentration is significantly increased compared to when assuming purely elastic stresses;
- Taking into account the concentration dependent yield stress in the elastic-plastic approach, results in stresses up to 6GPa and a surface concentration value slightly lower than predicted using the constant yield stress of the austenitic stainless steel. The thus obtained composition-depth and stress-depth profiles are in favourable agreement with experimental results.

References

[1] T. L. Christiansen, M. A. J. Somers, Low-temperature gaseous surface hardening of stainless steel: The current status, Int. J. Mater. Res., 100 (2009) 1361–1377

[2] H. Dong, S-phase surface engineering of Fe-Cr, Co-Cr and Ni-Cr alloys, Int. Mater. Rev., 55 (2010) 65–98

[3] M.A.J. Somers and T.L. Christiansen, "Low-Temperature Surface Hardening og Stainless Steels," in ASM Handbook - Heat treating of Iron And Steels, vol. 4D, ASM International, 2014, pp. 439–450

[4] S. Parascandola, W. Möller D.L. Williamson, The nitrogen transport in austenitic stainless steel at moderate temperatures, Appl. Phys. Lett., 76 (2000) 2194–2196

[5] J. Oddershede, T.L. Christiansen, K. Ståhl, M.A.J. Somers, Extended X-ray absorption fine structure investigation of nitrogen stabilized expandend austenite, Scr. Mater., 62 (2010) 290–293

[6] A. Martinavicius, G. Abrasonis, W. Möller, Influence of crystal orientation and ion bombardment on thenitrogen diffusivity in single-crystalline austenitic stainless steel, J. Appl. Phys., 110 (2011) 074907

[7] T.L. Christiansen, M. A. J. Somers, Determination of the concentration dependent diffusion coefficient of nitrogen in expanded austenite, Int. J. Mater. Res., 99 (2008) 999–1008

[8] T.L. Christiansen, K. V. Dahl, M. A. J. Somers, Simulation of nitrogen concentration depth profiles in low temperature nitrided stainless steels, Defect Diffus. Forum, 258–260 (2006) 378–383

[9] T. Christiansen, M. A. J. Somers, Evaluation of diffusion coefficients from composition profiles - the influence of trapping, Defect Diffus. Forum, 258–260 (2006) 384–389

[10] T.L. Christiansen, K. V. Dahl, M. A. J. Somers, Nitrogen diffusion and nitrogen depth profiles in expanded austenite: Experimental assessment, numerical simulation and role of stress, Mater. Sci. Technol., 24 (2008) 159–167

[11] T.L. Christiansen, M. A. J. Somers, Stress and composition of carbon stabilized expanded austenite on stainless steel, Metall. Mater. Trans. A, 40A (2009) 1792–1798

[12] T. Christiansen, Ph. D. Thesis: Low temperature surface hardening of stainless steel. Technical University of Denmark, 2004

[13] B. Brink, K. Ståhl, T.L. Christiansen, M.A.J. Somers, Thermal expansion and phase transformations of nitrogen-expanded austenite studied with in situ synchotron x-ray diffraction, J. Appl. Crystallogr., 47 (2014) 819–826

[14] T. L. Christiansen, M.A.J. Somers, The influence of stress on interstitial diffusion- Carbon diffusion data in austenite revisited, Defect Diffus. Forum, 297–301 (2010) 1408–1413

[15] A. Galdikas, T. Moskalioviene, Stress induced nitrogen diffusion during nitriding of austenitic stainless steel, Comput. Mater. Sci., 50 (2010) 796–799,

[16] T. Moskalioviene, A. Galdikas, Modeling of nitrogen pentration in polycrystalline AISI 316L stainless steel, Surf. Coat. Technol., 205 (2011) 3301–3306

[17] T.L. Chistiansen, M.A.J. Somers, Avoiding ghost stress on reconstruction of stress- and compostion-depth profiles from destructive X-ray diffration depth profiling, Mater. Sci. Eng. A, 424 (2006) 181–189

[18] J.C. Stinville, C. Tromas, P. Villechaise, C. Templier, Anisotropy changes in hardness and indentation modulus induced by plasma nitriding of 316L polycrystalline stainless steel, Scr. Mater., 64 (2011) 37–40

[19] J.C. Stinville, P. Villechaise, C. Templier, J. P. Rivière, M. Drouet, Lattice rotation induced by plasma nitriding in a 316L polycrystalline stainless steel, Acta Mater., 58 (2010) 2814–2821

[20] C. Templier, J. C. Stinville, P. Villechaise, P. O. Renault, G. Abrasonis, J. P. Rivière, A. Martinavicius, M. Drouet, On lattice plane rotation and crystallographic structure of the expanded austenite in plasmanitrided AISI 316L steel, Surf. Coat. Technol., 204 (2010) 2551–2558

[21] T. Christiansen, M. A. J. Somers, Controlled Dissolution of Colossal Quantities of Nitrogen in Stainless Steel, Metall. Mater. Trans. A, 37A (2006) 675–682

[22] F. C. Larche, J. l. Cahn, The effect of self-stress on diffusion in solids, Acta Metall., 30 (1982) 1835–1845

[23] R. T. DeHoff, Thermodynamics in materials science. New York,N.Y.: McGraw-Hill, 1993
[24] J.C.M. Li, Physical Chemistry of some microstructural Phenomena, Metall. Mater. Trans. A, 9A (1978) 1353-1380
[25] M.A.J. Somers, IFHTSE Global 21: heat treatment and surface engineering in the twenty-first century, Part 14 - Development of compound layer during nitriding and nitrocarburising; current understanding and future challenges, Int. Heat Treat. Surf. Eng., 5, (2011) 7–16
[26] Y. Sun, T. Bell, A numerical model of plasma nitriding of low alloy steels, Mater. Sci. Eng. A, 224 (1997) 33–47
[27] R.E. Schacherl, P.C.J. Graat, E.J. Mittemeijer, The Nitriding Kinetics of Iron-Chromium Alloys; The Role of Excess Nitrogen: Experiments and Modelling, Metall. Mater. Trans. A, 35A (2004) 3387–3398
[28] E.J. Mittemeijer, M.A.J. Somers, Thermodynamics, kinetics, and process control of nitriding, Surf. Eng., 13 (1997) 483–497
[29] M.A.J. Somers, thermodynamics, Kinetics and microstructural evolution of the compound layer; a comparison of the states of knowledge of nitriding and nitrocarburising, Heat Treat. Met., 200. (2000) 92–102
[30] P.B. Friehling, F.W. Poulsen, M.A.J. Somers, Nucleation of iron nitrides during gaseous nitriding of iron; effect of a preoxidation treatment, Z. für Met., 92 (2001) 589–595
[31] J.H. Hattel, Fundamentals of numerical modelling of casting processes. Polyteknisk forlag, 2005
[32] J.H. Hattel, P.N. Hansen, A 1-D analytical model for the thermally induced stresses in the mold surface during die casting, Appl Math Model., 18 (1994)
[33] M.A.J. Somers, Modelling nitriding of iron: From thermodynamics to residual stress, J. Phys. IV Proc., 120 (2004) 13
[34] M.A.J. Somers, E.J. Mittemeijer, Development and relaxation of stress in surface layers; Composition and residual stress profiles in γ′-Fe4N1−x layers on α-Fe substrates, Metall. Trans. A, 21 (1990) 189–204
[35] V. Tvergaard, Plasticity and creep in structural materials. Kgs. Lyngby, Denmark: Department of mechanical engineering, Technical University of Denmark, 2001
[36] T. Moskalioviene, A. Galdikas, Stress induced and concentration dependent diffusion of nitrogen in plasma nitrided austenitic stainless steel, Vacuum, 86 (2012) 1552–1557
[37] F.A.P. Fernandes, T.L. Christiansen, G. Winther, M.A.J. Somers, On the determination of stress profiles in expanded austenite by grazing incidence X-ray diffraction and successive layer removal, Acta Mater., 94 (2015) 271–280
[38] 316-316L data bulletin – www.aksteel.com 20/7 -2014
[39] M.A.J. Somers, E.J. Mittemeijer, Layer-growth kinetics on gaseous nitriding of pure iron: Evaluation of diffusion coefficients for nitrogen in iron nitrides, Metall. Mater. Trans. A, 26 (1995) 57–74
[40] F. Bottoli, G. Winther, T.L. Christiansen, M.A.J. Somers, Influence of Plastic Deformation on Low-Temperature Surface Hardening of Austenitic Stainless Steel by Gaseous Nitriding, Metall. Mater. Trans. A, 46A (2015) 2579–2590
[41] F.A.P. Fernandes, M.A.J. Somers, and T. Christiansen, Determination of stress profiles in expanded austenite by combining successive layer removal and GI-XRD, Adv. Mater. Res., 996 (2014) 155–161

Appendix A – Input parameters to the model

A1 – Concentration dependent diffusion coefficient

The following Lorentzian type expression for diffusion coefficient as a function of concentration for the specific temperature of 718K was obtained using the data of Christiansen and Somers [34]

$$D(c) = 3.16 \cdot 10^{-15} \cdot \frac{1}{\pi} \cdot \frac{0.109}{(y_N - 0.4365)^2 + 0.109^2} \quad \text{(A-1)}$$

where y_N is the fractional occupancy of the octahedral interstices of the f.c.c. lattice with nitrogen atoms.

A2 – determination of volumetric expansion of the lattice with nitrogen concentration

To find the volume of the unit cell as a function of the concentration for expanded austenite $V(c_N)$, data from Christiansen and Somers [21] of the lattice parameter *a* corresponding to fractional occupancy, y_N, was used.

The relation between the nitrogen concentration, c_N, and the nitrogen occupancy, y_N, is [39]:

$$c_N = \frac{n}{N_{av}} \cdot y_N \cdot \frac{1}{V(y_N)} \quad \text{(A-2)}$$

where n is the number of atoms pr. unit-cell in the iron lattice (equal to 4 for f.c.c.), N_{av} is Avogadros number and $V(y_N)$ is the volume of the unit cell in [m^3] at the given y_N.

$$c_N = \frac{4}{6.022 \cdot 10^{23}[/mol]} \cdot y_N \cdot \frac{1}{V(y_N)} \quad \text{(A-3)}$$

A plot showing the calculated volumes as a function of the fractional occupancy are shown in Fig. A-1. Fitting a polynomium to the data gives a linear fit of

$$V(y_N) = 2.8147 \cdot 10^{-29} \cdot y_N + 4.7134 \cdot 10^{-29} \quad \text{(A-4)}$$

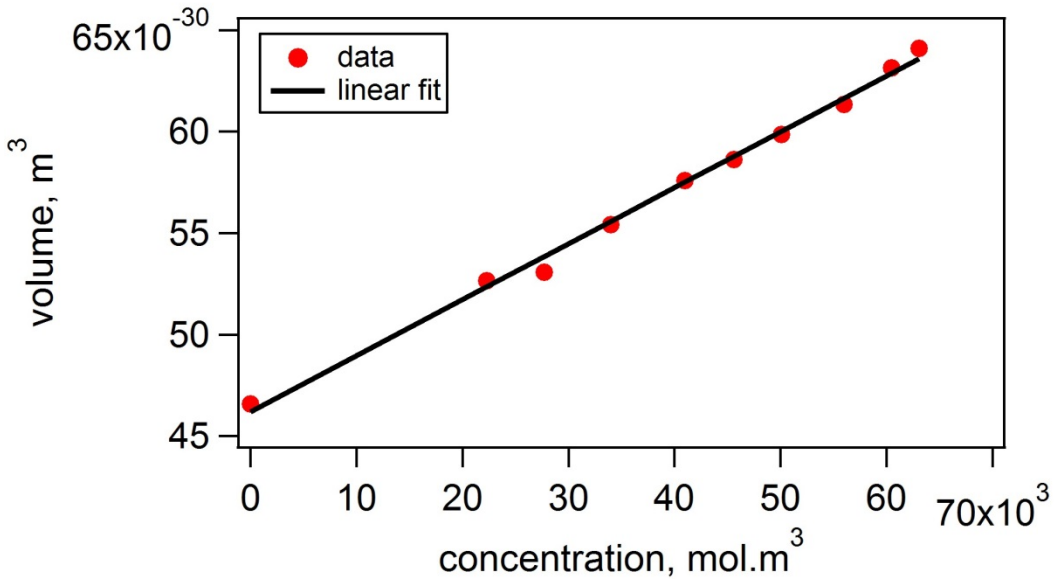

Figure A-1 - unit cell volume as function of nitrogen concentration expressed as fractional occupancy

Inserting the linear fit gives the following expression for calculating concentration as function of fractional occupancy

$$c_N[\mathrm{mol/m^3}] = \frac{4}{6.022\cdot10^{23}/\mathrm{mol}} \cdot \frac{y_N}{2.8147\cdot10^{-29}\mathrm{m^3}\cdot y_N + 4.7134\cdot10^{-29}\mathrm{m^3}} \tag{A-5}$$

Inverting and reducing gives the following expression for fractional occupancy as function of concentration

$$y_N = \frac{c_N}{140924\mathrm{mol/m^3} - c_N\cdot 0.59717} \tag{A-6}$$

Inserting Eq. (A-6) in the expression for volume as a function of fractional occupancy, Eq. (A-4) gives the unit cell volume as function of concentration

$$V(c_N) = 2.8147\cdot10^{-29}\mathrm{m^3}\cdot\frac{c_N}{140924\mathrm{mol/m^3} - c_N\cdot 0.59717} + 4.7134\cdot10^{-29}\mathrm{m^3} \tag{A-7}$$

A3 – Relation between activity and nitrogen content; nitrogen absorption isotherms

Absorption isotherms depict the relation between nitriding potential of an NH_3/H_2 gas mixture, i.e. $K_N = {p_{NH_3}}/{p_{H_2}^{\frac{3}{2}}}$, and the nitrogen concentration, c_N. The fractional occupancy of the nitrogen sub-lattice, y_N, in stress-free austenite was determined experimentally by Christiansen and Somers [21]. Converting the fractional occupancy, y_N, to concentration, c_N, Fig. A-2, is obtained. For equilibrium between nitrogen in solid state and imposed nitriding potential the activity of nitrogen in the solid state is linearly proportional to the nitriding potential, K_N by [25]

$$a_N = K_T K_N \tag{A-8}$$

where K_T is the equilibrium constant for the dissolution reaction of N into the solid state from the gas phase, and is a function of temperature and pressure. For dilute solutions Henrian behaviour can be assumed, implying linear proportionality between the nitrogen activity and the nitrogen concentration: $a_N = \gamma \cdot c_N$. This condition can be assumed only for nitrogen concentrations approaching nil. Since K_T is not a function of concentration, it follows from the above for small concentrations $K_N = \gamma \cdot \frac{c_N}{K_T}$. The raw data suggest an exponential relation between K_N and c_N. A function of the following form obeys Henrian behaviour for small c_N, and was used to parametrize the data

$$K_N = k1 \cdot \frac{c_N}{K_T} + k2 \cdot e^{\frac{c_N \cdot k3 + k4}{\ln(K_T)}} \quad \text{(A-9)}$$

where k1, k2, k3 and k4 are fitting parameters. Calculating K_T for 316 stainless steel the temperature of the measurements 445°C = 718.15K, and no hydrostatic stress gives $K_T = 2.4256 \cdot 10^4$.

For AISI 316 a satisfactory fit of the data at 718K was obtained with the following parameters; $k1 = 1.7524$, $k2 = 0.9346$, $k3 = 0.0051788$and $k4 = 251.9510$.

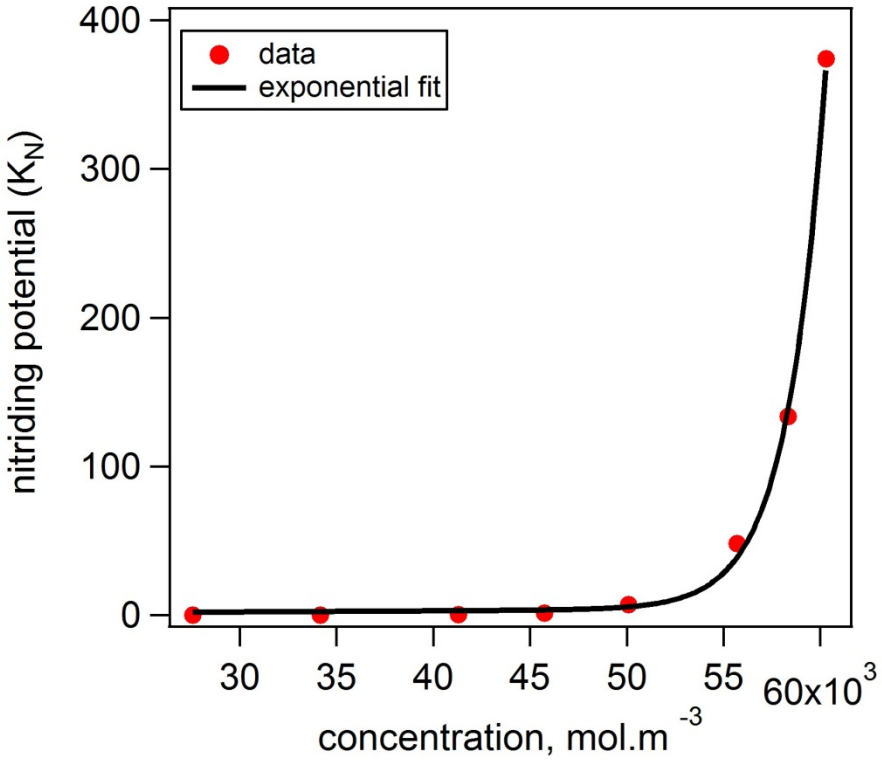

Figure A-2 – fit and - raw data of nitriding potential as function of concentration at 445°C

A4 - Determination of the effect of stress on the surface flux

The nitrogen content that can be dissolved in equilibrium with a chemical potential as imposed by a gas phase of known composition depends on the state of stress of the solid, as expressed by Eq. 5. Consequently, the value of c_N^{eq}, i.e. the nitrogen content in the solid in equilibrium with the gas phase, decreases with the invoked compressive stress in the surface element. At its turn the flux of nitrogen through the surface as given by Eq. 14 is affected as is the actual surface

concentration. The concentration of nitrogen in a stressed solid in equilibrium with nitrogen in a gas of known composition follows from equating the chemical potentials of nitrogen in solid and in gas:

$$\mu^{gas} = \mu^{\sigma} \tag{A-10}$$

The chemical potentials in the solid with and without stress ($\sigma=0$) are given by

$$\mu^{\sigma=0} = \mu_0 + RTln(a)$$

$$\mu^{\sigma} = \mu_0 + RTln(a) - V_N\sigma_H \tag{A-11}$$

Hence, comparing the chemical potential in a stressed and a stress-free solid in equilibrium with the same gas leads to

$$\mu_0 + RTln(a^{\sigma}) - V_N\sigma_H = \mu_0 + RTln(a^{\sigma=0})$$

$$\rightarrow a^{\sigma} = a^{\sigma=0} \cdot exp\left(\frac{V_N\sigma_H}{RT}\right) \tag{A-12}$$

Inserting $a_N = K_T K_N$ and realizing that K_T depends on pressure, it follows

$${K_T}^{\sigma} = {K_T}^{\sigma=0} \cdot exp\left(\frac{V_N\sigma_H}{RT}\right) \tag{A-13}$$

The relation between the nitrogen concentration and the nitriding potential for a stressed solid follows from inserting Eq. A-13 for K_T in Eq. A-9

$$K_N = k1 \cdot \frac{c^{eq}}{{K_T}^{\sigma=0} \cdot exp\left(\frac{V_N\sigma_H}{RT}\right)} + k2 \cdot e^{\frac{c^{eq} \cdot k3 - k4}{\ln({K_T}^{\sigma=0} \cdot exp\left(\frac{V_N\sigma_H}{RT}\right))}} \tag{A-14}$$

Since the equation is non-linear and cannot be inverted analytically, the equilibrium concentration was evaluated using Newton-Rhapson iterations.

A5- **Concentration dependent yield stress**

The dependence of yield stress on the nitrogen content for austenitic stainless steel is not precisely known, particularly not for the high nitrogen contents of relevance for expanded austenite. Bottoli, et al. [40] investigated two qualities of austenitic stainless steel deformed to various degrees of equivalent strain, and found that the Vickers hardness (HV) and yield stress (σ_y) obey the following relation:

$$\sigma_y[\text{in MPa}] = -396 + 3.73 \cdot \text{HV [in MPa]} \tag{A-15}$$

Realizing that hardness and yield stress both are a measure of the resistance against plastic deformation, it is attempted to obtain an estimate for the concentration dependence of the yield stress from the hardness. Correlating hardness-depth and concentration-depth profiles for nitrided AISI 316 austenitic stainless steel from [41] and converting hardness into yield

stress with Eq. A-15, the dependence displayed in Fig. A-3 was obtained. Obviously, the yield stress increases with the concentration until a plateau of constant yield stress is reached. Taking the yield stress of nitrogen free austenite as 290 MPa, a linear fit through the region ($c<14796$ mol.m^{-3}) where a steep increase in yield stress occurs, results in:

$$\sigma_y[\text{in MPa}] = 0.2424 \cdot c[\text{in mol.m}^{-3}] + 290 \tag{A-16}$$

For the plateau the average value is $\sigma_y = 3848$ MPa, which is considerably higher that the yield stress of the base material.

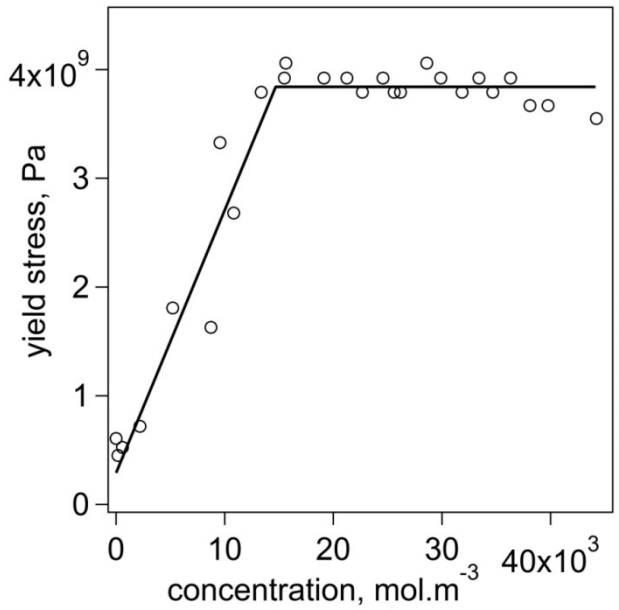

Figure A-3 - Relation between yield stress and nitrogen concentration for AISI 316 stainless steel

Computationally the changing yield stress was implemented by comparing the maximum von Mises stress with the current yield stress resulting from the current concentration, after each time-step. If the concentration dependent yield stress exceeded the maximum von Mises stress, it replaced the value of the maximum von Mises stress, when evaluating plasticity in the next time step.

E.2 article 2

The following article is accepted as a conference contribution at the Heat Treating Society Conference and Expo, being held October 20-22, 2015 in Detroit, Michigan.

Modelling of composition and stress profiles in low temperature surface engineered stainless steel

Freja N. Jespersen, Jesper H. Hattel, Marcel A.J. Somers
Technical University of Denmark, Kgs. Lyngby, Denmark

frnj@mek.dtu.dk, jhat@mek.dtu.dk, somers@mek.dtu.dk

Abstract

Thermochemical surface engineering by nitriding/carburizing of stainless steel causes a surface zone of expanded austenite, which improves the wear resistance of the stainless steel while preserving the stainless behavior. As a consequence of the thermochemical surface engineering, huge residual stresses are introduced in the developing case, arising from the volume expansion that accompanies the dissolution of high interstitial contents in expanded austenite.
Modelling of the composition *and* stress profiles developing during low temperature surface engineering from the processing parameters temperature, time and gas composition is a prerequisite for targeted process optimization. A realistic model to simulate the developing case has to take the following influences on composition *and* stress into account:

- a concentration dependent diffusion coefficient
- trapping of nitrogen by chromium atoms
- the effect of residual stress on diffusive flux
- the effect of residual stress on solubility of interstitials
- plastic accommodation of residual stress.

The effect of all these contributions on composition and stress profiles will be addressed.

Introduction

Austenitic stainless steels are widely applied in structural applications because of their corrosion resistance in combination with favourable manufacturing performance. Generally, austenitic stainless steels have poor tribological and wear performance. Low-temperature thermochemical surface engineering by nitriding, carburizing and nitrocarburizing provides a means to drastically improve the tribological/wear performance, without compromising the general corrosion performance and even improving the resistance against localized corrosion, as pitting and crevice corrosion [1],[2],[3]. In low-temperature nitriding, carburizing or nitrocarburizing large amounts of nitrogen and/or carbon are dissolved in the surface region. This brings about a zone of expanded austenite, which essentially is a supersaturated solution of nitrogen and/or carbon in austenite. The expanded austenite zone has a substantially higher hardness than the untreated steel and provides drastically improved wear resistance. Furthermore, high compressive residual stresses are introduced, which result in enhanced fatigue performance. A zone of expanded austenite, can be achieved by bringing the steel in contact with an environment providing nitrogen and/or carbon, as for example in plasma-assisted or gas-based processing. The concentration-depth profiles developing during low temperature nitriding are characterized by an initially steep decrease in nitrogen content followed by a plateau and a steep decline at the case-core transition [1]. This behaviour deviates from the composition profile expected for diffusion into a semi-infinite medium with a constant diffusion coefficient (as for example carbon into iron/steel) and constant surface concentration. It is well established that low-temperature nitriding/carburizing of austenitic stainless steel leads to a composition-induced compressive residual stress depth-profile as a consequence of the lattice expansion associated with the dissolution of interstitial nitrogen and/or carbon. The compressive stresses developing in the case are several GPa's in magnitude [1],[4],[5] and are largely composition induced.
In this contribution an attempt is made to simulate realistic composition-depth and stress-depth profiles during nitriding, taking into account the influences of trapping of nitrogen by chromium atoms, the concentration-dependence of diffusivity of nitrogen in expanded austenite, stress-affected nitrogen solubility, a stress-assisted diffusive flux and composition-induced volume expansion which is partly accommodated plastically. Details of the model and the input parameters used are provided in a separate publication [6].

Basic Equations

The equation describing the diffusive flux, J_N, in the direction z under the influence of a composition and a stress profile is:

$$J_N = -\frac{D_N c_N}{RT}\left(\frac{\partial \mu_N}{\partial c_N}\frac{\partial c_N}{\partial z} + \frac{\partial \mu_N}{\partial \sigma_H}\frac{\partial \sigma_H}{\partial z}\right) \quad (1)$$

where D_N, c_N and μ_N are the intrinsic diffusivity, the concentration and the chemical potential of nitrogen in expanded austenite, respectively. R and T are the gas constant and temperature and σ_H is the hydrostatic stress. The chemical potential of nitrogen is proportional to the nitrogen activity, which, for gasnitriding, is linearly proportional to the nitriding potential, $K_N = \frac{p_{NH_3}}{p_{H_2}^{3/2}}$, of the gas mixture. Then, after inserting the equation for the chemical potential of stressed solids [7]

$$\mu_N = \mu_{N,0} + RTln(a_N) - V_N\sigma_H \quad (2)$$

with a_N the nitrogen activity and V_N the partial molar volume of nitrogen in expanded austenite, Eq. 1 can be shown to obey [6]

$$J_N = -\frac{D_N c_N}{RT}\left(\frac{RT}{K_N}\frac{\partial K_N}{\partial c_N}\frac{\partial c_N}{\partial z} - V_N\frac{\partial \sigma_H}{\partial z}\right) \quad (3)$$

From experimental data available in the literature the dependence of c_N on K_N (a so-called absorption isotherm) [8], the composition-dependent D_N [9] and the dependence of lattice parameter on nitrogen content, and hence, V_N [8] are known. Then, in principle, the diffusive flux of nitrogen in expanded austenite can be calculated for the experimental conditions of temperature and nitriding potential, provided that assumptions for the accommodation of composition-induced stresses are done. In the present work it is assumed that the surface reaction by which nitrogen is transferred from the gas to the solid is always in equilibrium, implying that the surface reaction (adsorption/dissociation of ammonia and desorption of hydrogen) proceeds infinitely rapidly.
Another mechanism that affects the composition profile of nitrogen over the expanded austenite case is the occurrence of short-range order of nitrogen and chromium atoms, manifested as and often referred to as trapping of nitrogen. Analogous to [10], in the present work, trapping has pragmatically been accounted for by adopting a solubility product $K_{CrN_n} = c_{Cr} \cdot c_N^n$, with c_{Cr} the chromium concentration.

Accommodation of composition-induced stress

For simplicity, strains arising from externally imposed forces or thermal gradients are not included. Then, the strain in expanded austenite is the strain arising from the expansion of the austenite lattice as caused by the dissolution of interstitial nitrogen, i.e. the chemical-induced strain, ε_{ij}^{ch}, defined as

$$for\ i = j: \quad \varepsilon_{ij}^{ch}(c) = \frac{V(c)^{1/3} - V_{ref}^{1/3}}{V_{ref}^{1/3}} \quad (4)$$

$$for\ i \neq j: \quad \varepsilon_{ij}^{ch} = 0$$

where V(c) in the concentration-dependent volume of (expanded) austenite per metal atom and V_{ref} indicates the volume per metal atom of the interstitial-free lattice of austenite. A simple description of the stress state in the surface can be found under the following assumptions:

- the surface of the sample can move freely: $\sigma_{33} = \sigma_\perp = 0$ ($\sigma_\perp$ is the stress normal to the surface);
- the stress state is rotationally symmetric, hence $\sigma_{11} = \sigma_{22} = \sigma_\parallel$ ($\sigma_\parallel$ is the stress within the plane of the surface);
- the specimen does not bend, hence $\sigma_{12} = \sigma_{13} = \sigma_{23} = 0$;
- the depth range of the expanded austenite case is infinitely thin as compared to the total thickness of the sample. Accordingly, all stresses can be assumed to be accommodated in the case and the core is stress-free.

Under these conditions and assuming purely elastic stresses, it is obtained

$$\sigma_\parallel^{el} = -\frac{E}{1-\nu}\varepsilon_\parallel^{ch} \quad (5)$$

where E is Young's modulus, ν is the Poisson ratio and $\varepsilon_\parallel^{ch}$ is the chemical strain within the plane of the surface.

The assumption of fully elastic accommodation of the composition-induced strains leads to exorbitantly high, unrealistic residual stresses, as will be demonstrated. These huge compressive stresses have a large impact on the stress-gradient induced diffusive flux (cf. Eqs. 1 and 3) as well as on the solubility of nitrogen in the solid state for an imposed chemical potential (as dictated by the nitriding potential) by the gas phase (cf. Eq. 2). For elastic-plastic accommodation of the composition-induced strain, the stress depends on the loading path, and, thus, an incremental description has to be adopted: $\dot{\sigma}_{ij} = L_{ijkl}\dot{\varepsilon}_{kl}$, with L_{ijkl} the incremental stiffness tensor. Here, the J2 flow theory was implemented to evaluate L_{ijkl}. As a plastic stress criterion, the von Mises yield surface was adopted: $\sigma_e^2 = \frac{3}{2}s_{ij}s_{ij}$. The occurrence of strengthening was accounted for by evaluating the yield stress as a function of nitrogen concentration, adopting the experimental relation between hardness and yield stress [11] and an experimental relation between hardness and nitrogen concentration over a nitrided case [12].

Computational Method

Composition profiles were computed applying the central explicit finite difference method on the 1-dimensional version of Fick's 2nd law

$$\frac{\partial c_N}{\partial t} = -\frac{\partial}{\partial z}(J_N) \quad (6)$$

where J_N is given by Eq. 3.
Including trapping of nitrogen by chromium atoms only the non-trapped nitrogen atoms are considered to diffuse, while all nitrogen atoms are taken into account to describe the lattice expansion that leads to stress build-up in the diffusion zone. The computation of chemical strains and stresses is done straightforwardly for each element after the concentration is calculated in each time-step.
Full details of the calculations are given elsewhere [6].

Results and interpretation

The combined effect of a composition-dependent diffusion coefficient of nitrogen and the role of trapping on the developing concentration profile was simulated for nitriding at 718 K for 22 hours, using a nitriding potential of 1,000 $atm^{-1/2}$. The concentration-dependent diffusion coefficient is given by a Lorentzian fit to the diffusivity data from [9]:

$$D_N = 3.16 \cdot 10^{-15} \cdot \frac{1}{\pi} \cdot \frac{0.109}{\left(y_N - 0.4365\right)^2 + 0.109^2} \qquad (7)$$

where y_N is the fractional occupancy of the octahedral interstices of the f.c.c. lattice with nitrogen atoms. For the calculations with a constant diffusion coefficient, the average value over the composition range was taken. In Fig.1 simulation results are given for a constant diffusivity (Fig. 1a) and a diffusivity obeying Eq.7 (Fig. 1b), considering three degrees of trapping: no trapping (K_{CrN}=inf), infinitely strong trapping (K_{CrN}=0) and an intermediate level of trapping (K_{CrN}=10^8).

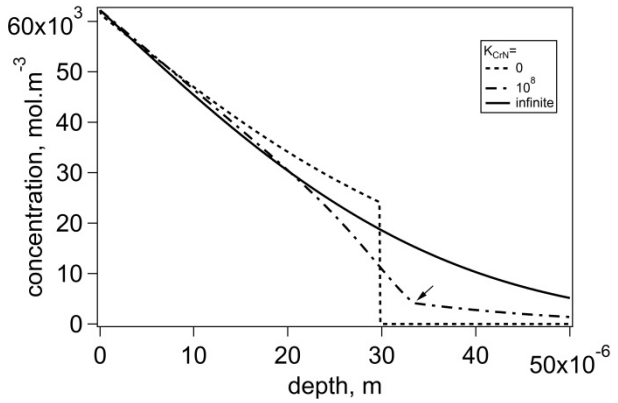

(a.)

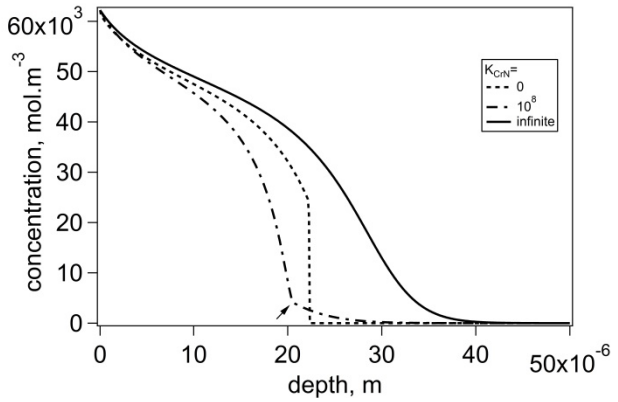

(b.)

Figure 1: Simulated nitrogen concentration-depth profiles for constant diffusivity (a.) and concentration-dependent diffusivity (b.) and three degrees of trapping: no trapping (K_{CrN}=inf), infinitely strong trapping (K_{CrN}=0) and an intermediate level of trapping (K_{CrN}=10^8). The nitriding conditions were T=718 K, t=22 h and K_N=1,000 atm$^{-1/2}$. Local equilibrium was assumed at the surface.

The effect of trapping is observed as follows: no trapping (K_{CrN}=inf) yields the usual complementary error-function profile for a constant diffusivity in Fig.1a, while the concentration dependence of the diffusivity is reflected by the profile in Fig.1b. Full trapping (K_{CrN}=0) leads to an abrupt transition to zero nitrogen concentration (dashed line in Fig. 3a). Intermediate trapping has as a consequence that a tail appears to the concentration profile beyond the depth where the solubility product is reached. The onset of the tail is indicated by arrows in Fig.1.

From the relation between lattice parameter and nitrogen concentration [8], the volume expansion of the lattice can be calculated according to Eq.4. The elastic constants were assumed to be independent of the composition of austenite, because no quantitative data are available of how Young's modulus and the Poisson ratio depend on nitrogen concentration. Under these assumptions, the elastic composition-induced compressive stress-depth profiles reflect the composition-depth profiles from which they were calculated. An example is given in Fig. 2.

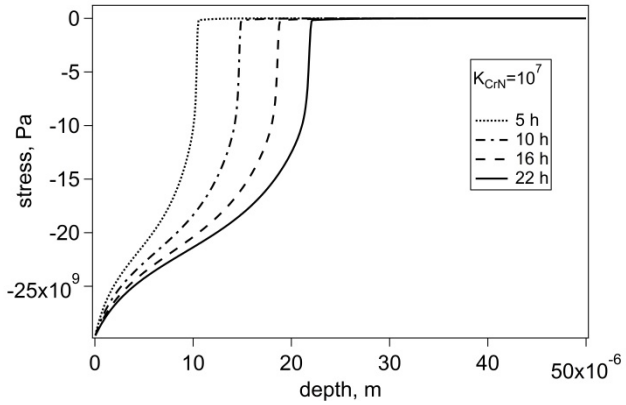

Figure 2: Simulated stress-depth profiles for concentration-dependent diffusivity and an intermediate level of trapping (K_{CrN}=10^7). The nitriding conditions were T=718 K and K_N=1,000 atm$^{-1/2}$ for various nitriding times. Local equilibrium was assumed at the surface.

Compressive stresses of close to 30 GPa are obviously impossible to be subtended by metals. Before introducing elastic-plastic accommodation of the lattice expansion, it is investigated how these enormous stress distributions affect the evolution of the concentration profile by stress-enhanced diffusion (cf. Eq. 3) and reduce the solubility of nitrogen in the solid state (cf. Eq. 2). Fig.3 shows the concentration and stress profiles simulated for the cases that (i) the stress affects neither the solubility nor the diffusive flux (dashed line), (ii) the stress influences the diffusive flux (drawn line) and (iii) the stress affects both the solubility of nitrogen in expanded austenite and the diffuse flux (dash-dot line). Evidently, for the exorbitantly huge elastic stress gradient, the additional driving force for diffusion induced by the stress gradient establishes a concentration profile that reaches about 3.5 times as deep as driven by the concentration gradient alone (cf. drawn line in Fig.3). This illustrates the potentially substantial contribution of stress-induced diffusion, albeit for a grossly overestimated elastic stress. Further, including the effect of residual stress on solubility (dash-dot line) shows that, for the assumption of local equilibrium at the surface, elastic accommodation of the composition-induced stress leads to a reduction of the solubility of nitrogen in austenite by a factor 2. The stress-gradient induced diffusive flux is still sufficiently large to establish a case depth beyond that reached without including the influence of stress (Fig.3).

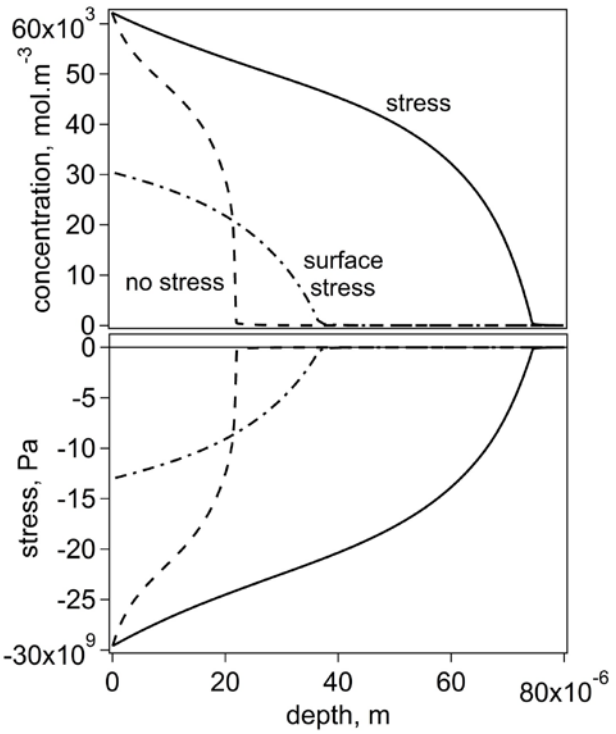

Figure 3: Simulated concentration-depth and stress-depth profiles for elastic accommodation of composition-induced stress, where (i) stress has no influence (dashed line), (ii) the stress-gradient induces an additional diffusive flux (drawn line) and (iii) stress affects both solubility of nitrogen in austenite and the diffusive flux (dash-dot line). The nitriding conditions were T=718 K and K_N=1,000 atm$^{-1/2}$ for 22 h and K_{CrN}=10^7. Local equilibrium was assumed at the surface. Note that the dashed stress line is identical to the drawn line in Fig. 2.

Assuming purely elastic accommodation of the composition-induced stress in austenitic stainless steel is unrealistic, because the yield stress of (interstitial-free) austenite is as low as 290 MPa [13]. The dissolution of interstitials in the f.c.c. lattice is most effective for strengthening of austenite, indicating that solid-solution strengthening has to be accounted for. Recently, it was found for the relation between Vickers hardness, HV, and the yield stress for uniaxial tension, σ_y, of austenite [11] $\sigma_y = -396 + 3.73 \cdot \mathrm{HV}$, where both σ_y and HV are given in MPa. Correlating hardness-depth and concentration-depth profiles for nitrided AISI 316 [12], it is obtained from implementing the above relation between hardness and yield stress $\sigma_y = 0.2424 \cdot c_N + 290$ where c_N is given in mol.m^{-3} (Fig.4). The maximum yield stress in expanded austenite thus found is $\sigma_y = 3.85$ GPa in uniaxial tension. This value compares favorably with the experimental residual stress values observed for nitrogen expanded austenite, which generally exceed 4 GPa in biaxial compression.

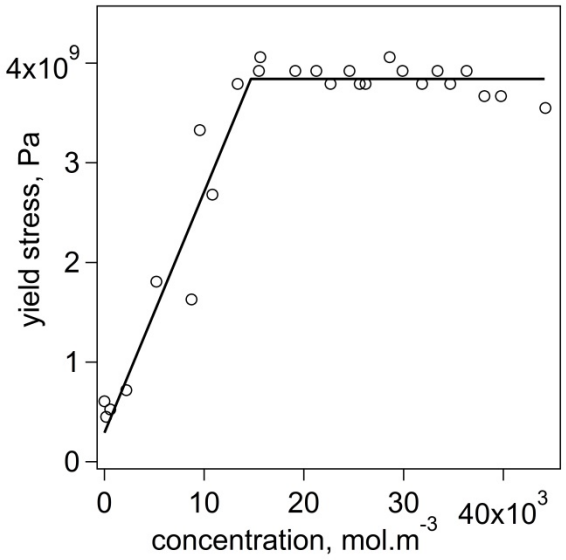

Figure 4: Relation between yield stress and nitrogen concentration for AISI 316 stainless steel as evaluated from experimental data in [11] and [12].

In Fig.5 simulated concentration-depth and stress-depth profiles are shown for: (i) purely elastic accommodation of the composition-induced expansion (cf. Fig.3) indicated as "elastic", (ii) elastic-plastic accommodation for stress beyond the yield stress of 290 MPa for the base material, indicated as "plastic (const. yield stress)" and (iii) elastic-plastic accommodation for a concentration-dependent yield stress, i.e., solid-solution strengthening, indicated as "plastic, yield stress =f(c_N)", using the composition-dependence of the yield stress in Fig.4. Comparison of the profiles for elastic and elastic-plastic accommodation shows that, in accordance with expectations, the elastic stress level in the expanded austenite zone is very low if plasticity as for austenitic stainless steel is taken into account. Consequently, for this case of plasticity with a constant yield stress, the nitrogen surface concentration and diffusion in expanded austenite would be largely unaffected by the stress and thus a composition-depth profile reminiscent of that for a stress-free case is obtained (cf. Fig. 3 "no stress"). Consistent with the appreciably lower stress in the case, the contribution of stress-induced diffusion is limited, as reflected by the relatively shallow diffusion depth reached. Assuming a concentration-dependent yield stress, implying that solid-solution strengthening by nitrogen dissolution in austenite is effectively accounted for, a high nitrogen content is obtained, whilst the (elastic) compressive residual stresses reach a level of approximately 5 GPa at the surface (Fig.5). This is in favourable agreement with the residual stresses found experimentally [1,12].

Discussion

In the preceding chapter it was demonstrated how concentration-dependence of the diffusivity, nitrogen trapping and elastic-plastic stress influence the shape of the concentration-depth profile. Evidently, it is not possible to

discriminate between the various models presented in the literature only on the basis of the shape of the concentration-depth profile.

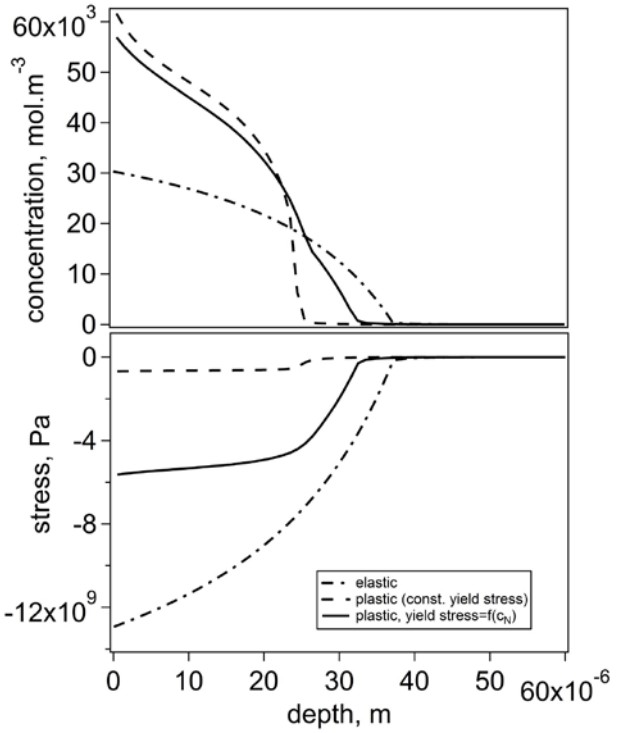

Figure 5: Simulated concentration-depth and stress-depth profiles using purely elastic accommodation (designated "elastic") of the lattice expansion or elastic-plastic accommodation. For a constant yield stress the lines denoted "plastic, (const. yield stress)" are obtained, while the assumption of a concentration-dependent yield stress results in the lines denoted "plastic, yield stress=f(c_N)". In all cases the nitriding conditions are 22h at 718 K for K_N=1000 atm$^{-1/2}$, K_{CrN}=10^7 and local equilibrium at the surface.

The adoption of a model presuming a constant diffusion coefficient and trapping of nitrogen atoms [14,15], can yield concentration-depth profiles of a shape as given in Fig. 1a (particularly for K_{CrN}=10^7; not shown here, but see [6]). Taking the diffusivity, D_N, and solubility product, K_{CrN_n}, as fitting parameters will certainly allow a satisfactory *mathematical* description of concentration-depth profiles. On the other hand, the assumption of a concentration-dependent diffusivity also leads to concentration-profiles that resemble those determined experimentally (cf. Fig. 1b). The simulation of concentration profiles omitting the role of composition-induced residual stress and its influence on the developing concentration profiles, appears an over-simplification of the case. In previous work it was estimated that a residual stress gradient enhances nitrogen diffusion in expanded austenite, such that the case depth is increased by a factor two [16]. Further mathematical implementation has so far been pragmatic, assuming an unphysical linear relation between composition and stress and a continuously decreasing diffusion coefficient [17], which obviously is in conflict with the experimentally determined diffusion coefficient for nitrogen in expanded austenite (cf. Eq.7). The present work adopts the actual lattice expansion of expanded austenite to estimate the stress, and the experimentally observed stress-free concentration-dependent diffusion coefficient were included in the model, while also the effect of stress on the nitrogen solubility and stress-enhanced diffusion were taken into account. Clearly, the present simulations demonstrate that elastic accommodation of the lattice expansion leads to residual stress values far beyond the yield stress of the material, which necessitates the incorporation of plasticity. Moreover, the residual stress values determined experimentally in expanded austenite are far beyond the yield stress of stainless steel (Fig. 5). It is necessary to take solid-solution strengthening of expanded austenite by the dissolution of high amounts of interstitials into account. This provides realistic simulations of concentration-depth and stress-depth profiles over the expanded austenite case (Fig. 5). It is noted that plastic deformation in expanded austenite induced by the dissolution of nitrogen has been reported by several research groups [8,19]. Simulations of the depth range where plasticity occurs with the present model (not shown here) indicated that plastic deformation occurs over the entire case depth of expanded austenite [6], which is reflected by the steep increase in nitrogen concentration and compressive stress at the core-case transition.

In this respect it is mentioned that after carburizing no plastic deformation in the expanded austenite zone has been observed. In order to understand this significant difference between nitriding and carburizing of stainless steel, it is important to realize that the interstitial content introduced by carburizing is appreciably lower than for nitriding, maximally 20.10^3 mol.m^{-3} [1], while the level of compressive residual stress is generally below, say, 3 GPa [19]. For this combination of interstitial content and compressive residual stress, indeed purely elastic accommodation is predicted by Fig.4.

Conclusions

Nitriding of austenitic stainless steel was modelled taking into account a concentration-dependent diffusion coefficient and short-range ordering of chromium and nitrogen atoms (trapping). Stress-depth profiles were predicted from the lattice expansion caused by the interstitial nitrogen atoms. The interaction between stress (gradients) and solid-state diffusion was examined for purely elastic and for elastic-plastic accommodation of the composition-induced strain. It can be concluded that:

- solid-state diffusion is enhanced by the compressive stress gradient resulting from the nitrogen concentration gradient;
- for *elastic* accommodation of composition-induced strain, the interaction between stresses and diffusion results in compressive surface stresses exceeding 10 GPa, which causes a significant decrease of the equilibrium nitrogen concentration;
- for *elastic-plastic* accommodation of composition-induced strains, the predicted compressive surface stresses are below 1 GPa, if a constant yield stress is

assumed, while the nitrogen concentration at the surface approaches that for the stress-free condition;

- for a concentration-dependent yield stress in the elastic-plastic approach, compressive stresses up to 5 GPa are predicted. The thus obtained composition-depth and stress-depth profiles are in good agreement with experimental results;
- the elastic-plastic approach including the composition-dependent yield stress shows that no plastic deformation occurs for low-temperature surface hardening by carburizing instead of nitriding. This is consistent with experimental observations.

References

[1] Christiansen, T.L. and Somers, M.A.J., "Low-temperature gaseous surface hardening of stainless steel: The current status," *Int. J. Mater. Res.*, vol. 100, no. 10 (2009), pp. 1361–1377.

[2] Dong, H., "S-phase surface engineering of Fe-Cr, Co-Cr and Ni-Cr alloys," *Int. Mater. Rev.*, no. 55 (2010), pp. 65–98.

[3] Somers, M.A.J. and Christiansen, T.L., "Low-Temperature Surface Hardening of Stainless Steels," in *ASM Handbook - Heat treating of Iron And Steels, vol. 4D*, (Metals Park OH, 2014), pp. 439–450.

[4] Christiansen, T.L. and Somers, M.A.J., "Stress and composition of carbon stabilized expanded austenite on stainless steel," *Metall. Mater. Trans. A*, vol. 40A, (2009), pp. 1792–1798,

[5] Christiansen, T., "Low temperature surface hardening of stainless steel." Ph.D. Thesis, Technical University of Denmark, 2004.

[6] Jespersen, F.N., Hattel, J.H. and Somers, M.A.J., "Modelling the evolution of composition- and stress-depth profiles in austenitic stainless steels during low-temperature nitriding", submitted to *Modelling and Simulation in Materials Science and Engineering*.

[7] Li, J.C.M., "Physical Chemistry of Some Microstructural Phenomena", *Metall. Trans. A*, vol. 9A, 1978, pp. 1353-1380.

[8] Christiansen, T. and Somers, M.A.J., "Controlled Dissolution of Colossal Quantities of Nitrogen in Stainless Steel," *Metall. Mater. Trans. A*, vol. 37A, (2006), pp. 675–682.

[9] Christiansen, T.L. and Somers, M.A.J., "Determination of the concentration dependent diffusion coefficient of nitrogen in expanded austenite," *Int. J. Mater. Res.*, vol. 99, (2008), pp. 999–1008.

[10] Christiansen, T.L., Dahl, K.V. and Somers, M.A.J., "Nitrogen diffusion and nitrogen depth profiles in expanded austenite: Experimental assessment, numerical simulation and role of stress," *Mater. Sci. Technol.*, vol. 24, no. 2 (2008), pp. 159–167.

[11] Bottoli, F., Winther, G., Christiansen, T.L. and Somers, M.A.J., "Influence of Plastic Deformation on Low-Temperature Surface Hardening of Austenitic Stainless Steel by Gaseous Nitriding," *Metall. Mater. Trans. A*, vol. 46A, 2015, pp. 2579–2590.

[12] Fernandes, F.A.P., Christiansen, T.L., Winther, G. and Somers, M.A.J., "On the determination of stress profiles in expanded austenite by grazing incidence X-ray diffraction and successive layer removal," *Acta Mater.*, vol. 94, (2015), pp. 271–280.

[13] "316-316L data bulletin - aksteel.com 20/7 -2014." and "Stainless 316 datasheet - Farnell.com 24/1-2014."

[14] S. Parascandola, W. Möller, and D. L. Williamson, "The nitrogen transport in austenitic stainless steel at moderate temperatures," *Appl. Phys. Lett.*, vol. 76, no. 16 (2000), pp. 2194–2196.

[15] Martinavicius, A., Abrasonis, G. and Möller, W., "Influence of crystal orientation and ion bombardment on the nitrogen diffusivity in single-crystalline austenitic stainless steel," *J. Appl. Phys.*, vol. 110, (2011), p. 074907.

[16] Christiansen, T.L. and Somers, M.A.J., "The influence of stress on interstitial diffusion- Carbon diffusion data in austenite revisited," *Defect Diffus. Forum*, vol. 297–301, (2010), pp. 1408–1413.

[17] Moskalioviene, T. and Galdikas, A., "Stress induced and concentration dependent diffusion of nitrogen in plasma nitrided austenitic stainless steel," *Vacuum*, vol. 86, (2012), pp. 1552–1557.

[18] Stinville, J.C., Villechaise, P. Templier, C., Rivière, J.P. and Drouet, M., "Lattice rotation induced by plasma nitriding in a 316L polycrystalline stainless steel," *Acta Mater.*, vol. 58, (2010), pp. 2814–2821.

[19] Christiansen, T.L. and Somers, M.A.J., "Stress and composition of carbon stabilized expanded austenite on stainless steel," *Metall. Mater. Trans. A*, vol. 40A, (2009), pp. 1792–1798.

DTU Mechanical Engineering
Section of Materials and Surface Engineering
Technical University of Denmark

Produktionstorvet, Bld. 425
DK-2800 Kgs. Lyngby
Denmark
Phone (+45) 4525 2205
Fax (+45) 4593 6213
www.mek.dtu.dk
ISBN: 978-87-7475-435-0